# CAVITY RINGDOWN SPECTROSCOPY STUDIES OF ATMOSPHERIC REACTIONS: PEROXYNITROUS ACID FORMATION AND ALKOXY RADICAL ISOMERIZATION

Thesis by

Andrew Keeler Mollner

In Partial Fulfillment of the Requirements

for the Degree of

Doctor of Philosophy


California Institute of Technology

Pasadena, California

2007

(Defended May 18, 2007)

# Acknowledgements

My graduate career has been a wonderfully rewarding experience. Caltech as an institution is ideal for graduate work, with minimal bureaucracy, skilled and caring support staff, and brilliant faculty, graduate students, and undergraduates. I have been particularly blessed to be supported by an amazing group of mentors, colleagues, friends and family.

First and foremost I would like to thank my advisors Drs. Mitchio Okumura and Stan Sander. Our weekly meetings have been a wonderful opportunity for me to tap into their wealth of knowledge and learn strategies for attacking scientific problems. As scientific advisors, they managed to provide me with both the freedom to develop my skills as an independent researcher and the guidance and support I needed to be productive. In addition to being wonderful teachers and mentors, Mitchio and Stan are also kind and generous people. I have never doubted that they sincerely care about me, both as a scientist and a person, and I will always consider them both mentors and friends.

I also owe a great deal of thanks to the many people I have had the pleasure of working with in 17 Noyes who contributed immensely to the work described in this thesis. Many of my lab skills were passed down from Drs. Sergey Nizkorodov and Brian Bean, who showed me the ropes my first year in lab. They shared with me not only their scientific knowledge, but also their enthusiasm for the research. They were both wonderful teachers and treated me from day one as colleague rather than a subordinate. In particular, Brian spent many patient days forcing me to align lasers, ringdown cavities,

and detectors so that I could learn these skills, when I'm sure he could have done it all himself in a fraction of the time. Later in my career, I was fortunate to have three other experienced researchers, Drs. Leah-Nani Alconcel, Lin Feng, and Eva Garland, as co-workers in lab. Each of them shared with me knowledge gained from their graduate experiences and helped immensely in progressing my research.

My graduate career was also greatly enriched by several opportunities I have had to act as a mentor. I have had three undergraduates work with me as part of the Summer Undergraduate Fellowship Program, Gautham Nair, Terry Yen, and Alex Padilla as well as one high school student Da Lin. All of them were enthusiastic, hard working, and wonderful people to spend summers with. I also must express my gratitude to my latest apprentice, Matthew Sprague, who has taken over for me as the graduate student in 17 Noyes. He has been a joy to work with and his efforts the past year have contributed greatly to this thesis. I hope that I have been able to give him the same quality tutelage I received from my mentors.

I have also benefited greatly from the support of the Okumura group as a whole. The group office is a friendly, happy, and collaborative place to work where you can always find advice and support when problems arise. I like to think the incoming class of 2001 (myself, Julie Fry and David Robichaud) is partly responsible for fostering this wonderful group dynamic. I must give special thanks to the group Labview guru David Robichaud. David not only wrote the program which collected nearly all the data contained in this thesis, but had the skill and patience to walk me through understanding how it works and how to modify it. I would also like to thank current members of the

group David Robichaud, Aaron Noell, Laurence Yeung, Kana Takematsu, Matthew Sprage, and Kathleen Spencer, for their feedback on my propositions and this thesis.

I would also like to thank several staff and faculty for their contributions to my work. Dave Natzic of the Sander group was tremendously helpful in getting my lab running again several times when things went awry. Rick Gerhart in the Caltech glass shop and Mike Roy in the Caltech machine shop have also been instrumental, not only through their wonderful craftsmanship but also through their knowledge and advice. Thanks also to my committee members for their feedback on my Candidacy, Propositions, and Thesis: Pat Collier, Mitchio Okumura, Stan Sander, Nate Lewis, and Paul Wennberg.

Finally, I firmly believe that a happy graduate student is a productive graduate student and I owe thanks to many people outside of my research for helping keep me happy. Bill Bing and the Caltech-Occidental Concert Band provided me with a wonderful outlet for my inner musician. My various intramural sports teams, in particular Team Justice, Imperial Palace, and FBOD were a great group of friends and ensured I exercised regularly. It has also been wonderful to be near my family. I am fortunate to have had them provide me with unconditional love (as well as occasional food and laundry) during my graduate career.

Finally I would like to try and express my gratitude to my wife Rebecca. She has been a constant source of love, joy, and inspiration. No matter how well or how poorly things went in lab, I could always count on being happy when I went home and I cannot thank Rebecca enough for that.

# Abstract

This thesis describes laboratory experiments investigating atmospheric reactions using cavity ringdown spectroscopy (CRDS). The reactions studied were the formation of peroxynitrous acid (HOONO) in the termolecular association reaction OH + $NO_2$ (R1) and the isomerization of alkoxy radicals. Experiments were conducted in a gas flow cell combining UV photolysis to initiate reactions with infrared CRDS for the detection of products.

Formation of the weakly bound HOONO in the atmosphere reduces the yield of nitric acid ($HONO_2$) from R1 and lowers the efficiency of R1 as a sink for radicals. The *cis-cis* conformer of HOONO was detected through its fundamental $\nu_1$(OH-stretch) spectrum centered at 3306 $cm^{-1}$. The integrated absorbance of the $\nu_1$ bands for HOONO and $HONO_2$ were measured with CRDS and used to calculate the branching ratio (BR = $k_{HOONO}$ / $k_{HONO2}$) of R1. Initial experiments using a microwave discharge to initiate R1 measured BR at 298 K and 14 torr, but were limited to low pressures by the discharge. BR was then reinvestigated using pulsed laser photolysis to initiate R1. BR was measured over the range 20–760 torr at 298 K.

In support of these branching ratio measurements, a detailed study of the spectroscopy of $HONO_2$ was conducted. CRDS experiments with moderate resolution (1 $cm^{-1}$) are known to give incorrect absorbances and line shaes when measuring spectral features with much narrower linewidths. However, the magnitude of these CRDS errors when probing a highly congested spectrum such as that of $HONO_2$ was unknown. We

observed reductions in the $HONO_2$ integrated intensity up to 60% and quantified these errors as a function of concentration and pressure.

Alkoxy radicals (RO) are an important class of intermediates in the oxidation of hydrocarbons, and they react via several mechanisms. For longer chain RO isomerization (forming HOR) becomes a major pathway, but isomerization rates have never been directly measured. Continuing work described in Eva Garland's thesis, we measured the infrared spectrum of alkoxy radical isomerization products (HOR and $HORO_2$) formed within 100 μs. We then used this spectrum to measure the relative rate of isomerization to reaction with oxygen for n-butoxy and 2-pentoxy radicals.

**TABLE OF CONTENTS**

# List of Figures

# List of Tables

# 1 Introduction

## *1.1 Atmospheric Chemistry*

The atmosphere is composed of mostly stable gases. Over 99.9% of the gas molecules are nitrogen (78%), oxygen (21%), and argon (1%). The next three most-abundant molecules are carbon dioxide (400 ppm), methane (2 ppm), and nitrous oxide (315 ppb). All the molecules listed so far are closed-shell molecules and, as such, are relatively unreactive [1, 2].

The chemistry of the atmosphere is instead dominated by free radicals (molecules containing an unpaired electron). Despite being present in very low concentrations, these molecules are highly reactive and stimulate the majority of chemical transformation in the atmosphere. Two important families of radicals are odd-hydrogen ($HO_x$ = H + OH + $HO_2$) and odd-nitrogen ($NO_x$ = NO + $NO_2$). These radicals are grouped into families because they rapidly cycle between members in the atmosphere.

These families of radicals are of particular importance because of their roles in the destruction and formation of ozone. In the stratosphere, the photolysis of molecular oxygen in the ultraviolet ($\lambda < 240$ nm) produces relatively high concentrations of atomic oxygen. This atomic oxygen combines with molecular oxygen to form stratospheric ozone, but also enables $HO_x$ and $NO_x$ to participate in catalytic cycles that destroy ozone [2].

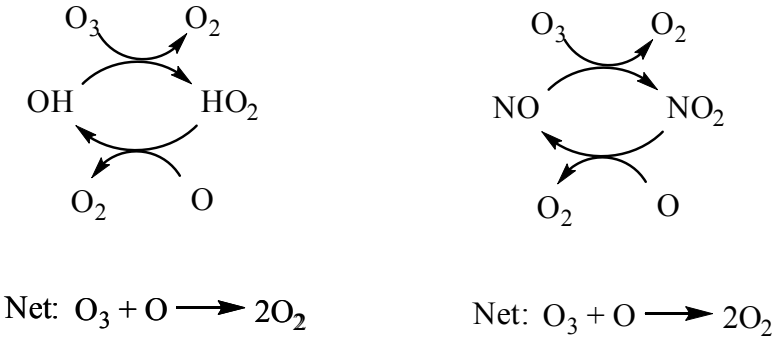


**Figure 1.1. Catalytic $HO_x$ and $NO_x$ cycles that destroy ozone in the stratosphere.**

Due to the filtering of short-wavelength ultraviolet by the stratosphere, atomic oxygen concentrations are much lower in the troposphere, and the cycles shown above do not apply. Instead, $HO_x$ and $NO_x$ participate in the production of ozone as a component of photochemical smog. Photochemical smog requires three chemical ingredients: hydrocarbons (RH), an oxidizer (typically OH), and NOx. A representative reaction scheme for the production of photochemical ozone is shown in Figure 1.2.

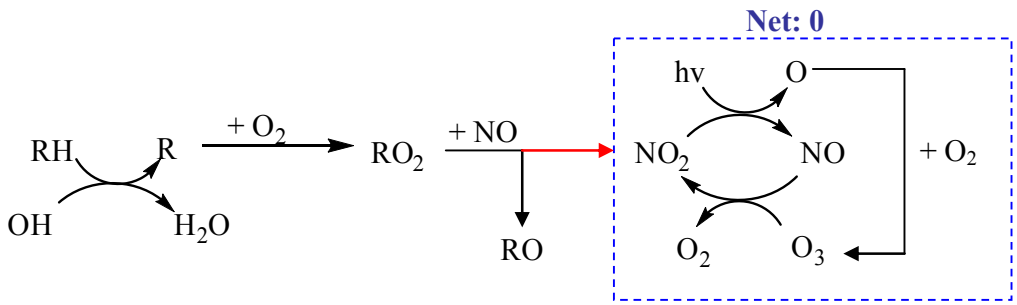


**Figure 1.2. Reaction scheme for the production of tropospheric ozone.**

The oxidation of hydrocarbons emitted to the atmosphere is predominantly initiated by reaction with the hydroxyl radical (OH). For unsaturated hydrocarbons, this would be hydrogen abstraction to form water and an alkyl radical (as shown in Figure 1.2); For alkenes and alkynes this would be OH addition to form a hydroxyl alkyl radical.

Alkyl radicals then add oxygen to form an alkyl peroxy radical. In the presence of $NO_x$, these alkyl peroxy radicals then react with NO to form $NO_2$ and alkoxy radicals (RO). During the daytime, $NO_x$ in the troposphere rapidly cycles between NO and $NO_2$ via photolysis and reaction with $O_3$. This cycle (dashed box) results in no net chemical change. $NO_2$ produced from the reaction of NO with alkyl peroxy radicals short-circuits the normal tropospheric $NO_x$ cycle and leads to the net production of ozone.

### 1.1.1 Peroxynitrous Acid

One of the most important free radical chain termination reactions is the gas phase reaction of hydroxyl radical (OH) with nitrogen dioxide ($NO_2$) to form nitric acid ($HONO_2$).

$$OH + NO_2 + M \xrightarrow{k_{1a}} HONO_2 + M \qquad \text{Reaction 1.1a}$$

Reaction 1.1a sequesters reactive OH and $NO_2$ radicals as long-lived nitric acid, shortening their atmospheric lifetimes and slowing the catalytic cycles responsible for formation of photochemical air pollution in the troposphere and depletion of stratospheric $O_3$. The rate constant $k_{1a}$ therefore affects not only $HO_x$ and $NO_x$ concentrations throughout the atmosphere, but also the formation of air pollutants including $O_3$, nitric acid, and fine particulate nitrate.

Reaction 1.1a is particularly important in polluted urban environments airsheds with high ratios of $NO_x$ to volatile organic compounds (VOC). At high enough $NO_x$ levels, urban ozone levels decrease with increasing $NO_x$, because elevated $NO_x$ levels reduce OH concentrations through reaction 1.1a and lead to reduced VOC oxidation rates. Tonnesen [3] has shown that model predictions of ozone production can be almost

inversely proportional to changes in $k_{1a}$. Recent sensitivity analyses have shown that modeled ozone concentrations can be more sensitive to changes in $k_{1a}$ than changes in any other rate constant [4, 5]. The link between $k_{1a}$ and photochemical ozone production is discussed further in appendix C.

Despite extensive studies over a wide range of temperatures and pressures, significant uncertainties remain at atmospherically relevant pressures and temperatures. Reaction 1.1a is a termolecular association reaction that requires a collision with a third body to stabilize the energetically excited initially formed complex. Such reactions can be thought of as a two-step process:

$$A + B \rightleftarrows [AB]^* \xrightarrow{M} AB .$$

The effective bimolecular rate constants of such reactions can be highly pressure-dependent. At very low pressures, almost every complex formed re-dissociates. The rate-limiting step to forming AB is therefore collision with a third body, and the effective bimolecular rate constant varies linearly with pressure. At very high pressures, every complex formed is immediately stabilized by a third body. As a result, the rate-limiting step is the initial formation of the AB complex and the effective bimolecular rate constant is independent of pressure. Between these two extremes, the reaction is said to be in the falloff regime and the dependence of the effective bimolecular rate constant on pressure is more complicated.

The effective bimolecular rate constant for reaction 1.1, $k_1$, has an anomalous fall-off curve; observed rate constants over the full range of pressures cannot be fit with a single set of falloff parameters. Robertshaw and Smith [6] first proposed that the

existence of a second product channel producing peroxynitrous acid (HOONO) could explain this anomaly.

$$OH + NO_2 + M \rightarrow HOONO + M \qquad \text{Reaction 1.1b}$$

The discrepancy between the high- and low-pressure observed rate constants can be removed if the HOONO channel is insignificant at low pressures, but becomes comparable to the $HONO_2$ channel at high pressures. A significant branching fraction into channel 1.1b is of importance in the atmosphere. HOONO is less stable than nitric acid and is expected to rapidly dissociate or photolyze back to reactants. Formation of HOONO would therefore reduce the efficiency of the $OH + NO_2 + M$ reaction as a sink for OH and $NO_2$ radicals.

I was fortunate to participate in the first direct spectroscopic detection of HOONO and measurement of the HOONO branching ratio from reaction 1.1, $k_{1b}/k_{1a}$ [7]. The spectra of HOONO and $HONO_2$ were measured in the mid-infrared by cavity ringdown spectroscopy. These spectra were then combined with the ratio of *ab initio* cross sections to derive $k_{1b}/k_{1a}$ at 14 torr. These published results are included in appendix A.

The microwave discharge method used to generate OH radicals in Bean et al. limited that study to low pressures and gas mixtures of mostly $H_2$ and He. This left the branching ratio under conditions relevant to the lower atmosphere highly uncertain. We have since used a coupled pulsed laser photolysis/cavity ringdown apparatus to measure the pressure dependence of the reaction 1.1 branching ratio. These results are described in Chapter 3. In the process of making these new measurements, we have gained an improved understanding of the spectroscopy of both HOONO and $HONO_2$. Chapter 3 therefore also presents revisions to the results published in Bean et al.

Chapter 2 describes investigations of the spectroscopy of nitric acid. Nitric acid spectra measured in our studies of reaction 1.1 underrepresent the true nitric acid absorbance due to a cavity ringdown artifact. The main focus of Chapter 2 is a detailed analysis of this artifact to derive correction factors to be used in the branching ratio measurements. Nitric acid cross sections in the ultraviolet and infrared are also reported. These cross sections are important for researchers monitoring nitric acid concentrations either in a laboratory environment or in the atmosphere.

### 1.1.2 Alkoxy Radicals

Alkoxy radicals are key intermediates formed during the oxidation of hydrocarbons. Once formed, alkoxy radicals can further react via one of three pathways: decomposition, isomerization, or reaction with $O_2$. The end products of oxidation for a given hydrocarbon depend on the relative yield of these reaction pathways. In order to better understand the kinetics of these processes, we have studied the fate of two relatively simple alkoxy radicals, *n*-butoxy and 2-pentoxy. Chapter 5 describes the first detection of the primary isomerization products of these radicals by their infrared spectra. These spectra were then used to measure the relative rates of isomerization and reaction with $O_2$ for these molecules. These are the first such measurements to be made without the use of a secondary reaction product.

## *1.2 Experimental Technique*

The atmosphere is a very complex chemical reactor. Thousands of reactions involving free radicals, photolysis, short-lived intermediates and long-lived reservoir species are constantly occurring. Our ability to understand and model this complex

system depends on an accurate knowledge of the kinetics and products of individual reaction pathways. To reduce the complexity of the problem, studies of individual reactions are most easily conducted in carefully controlled laboratory experiments. The experiments described in this thesis were conducted by initiating reactions in a gas flow cell and then spectroscopically detecting products. The use of a flow cell gave us control over precursor gas concentrations and ensured that molecules detected were those of the initial products. Infrared spectroscopy enabled us to make direct and unambiguous *in situ* measurements of the products.

### 1.2.1 Cavity Ringdown Spectroscopy

Optical spectroscopy is one of the most powerful tools for the direct detection of gas-phase molecules. Spectroscopy relies on measuring the interaction of electromagnetic radiation with atoms or molecules. The absorbance, $A$, is related to the change in radiation intensity by the Beer-Lambert Law,

$$A = -\ln\left(\frac{I}{I_0}\right) = \sigma[\mathrm{X}]L, \qquad \text{Equation 1.1}$$

where $I_0$ and $I$ are the light intensity before and after interacting with species X, $\sigma$ is the cross section and $L$ is the path length of the radiation through a sample with concentration [X]. The cross section is a measure of the probability a photon will be absorbed by a molecule of X and is highly dependent on the frequency of the radiation and the molecule. The variation in cross section with frequency defines a spectrum that can be used to uniquely identify molecules and quantify their concentration with eq 1.1.

The experiments described here were conducted in the mid-infrared, where spectra are predominantly due to molecular C-H and O-H stretches. These spectra

provide unique fingerprints to identify molecules. The reactions we study form products in low concentrations ([x] < 0.01 torr or $10^{14}$ molecules×cm$^{-3}$) and cross sections in the infrared are typically less than $1\times10^{-18}$ cm$^2$×molecule$^{-1}$. Detecting products at these low concentrations therefore requires spectroscopic detection with high sensitivity. We obtain this sensitivity with cavity ringdown spectroscopy (CRDS).

CRDS is an increasingly common technique to measure absorption spectra with high sensitivity. The technique uses a high-finesse optical cavity to create very long effective path lengths and several reviews of its applications are now available [8-12]. While CRDS can be accomplished with either continuous-wave or pulsed laser sources, the discussion here will be limited pulsed CRDS systems such as ours.

In CRDS, laser light is coupled into a high-finesse optical cavity formed by two high-reflectivity ($R$ > 99.9%) mirrors. As the light travels within the cavity, the intensity gradually decreases with time due to various loss processes: transmission and scattering at the mirrors and absorption and scattering be species within the cavity.

$$I(t) = I_0 \exp\left[-\left(\#\text{ of passes}(t)\right)\times\frac{\text{loss}}{\text{pass}}\right] = I_0 \exp\left[-\frac{tc}{L_{cav}}(A+(1-R))\right] \qquad \text{Equation 1.2}$$

In eq 1.2, $c$ is the speed of light, $L_{\text{cav}}$ is the mirror-to-mirror length of the cavity, and it has been assumed that the dominant loss processes per pass are molecular absorption and transmission through the mirrors [13-18].

The light transmitting from the cavity at time $t$ is proportional to the light still trapped inside the cavity. This is recorded and fit to a single exponential decay. The time it takes for the intensity to decay to $I_0/e$ is the ringdown lifetime, $\tau$.

$$\tau = \frac{L_{cav}}{c\left(A + \left(1 - R\right)\right)}$$

By comparing the ringdown lifetime with and without the absorber present, the Beer-Lambert absorbance can be obtained.

$$A = \frac{L_{cav}}{c}\left(\frac{1}{\tau} - \frac{1}{\tau_0}\right)$$

Due to the thousands of round-trips within the cell, the laser light interacts with the sample over very long effective path lengths (>1 km). In addition, because only the decay rate is measured, CRDS measurements are insensitive to fluctuations in laser power. As a result, per-pass absorbances smaller than $10^{-6}$ can be detected.

These equations only technically apply when the absorbance is constant over the linewidth of the laser. The consequences when this condition is not met are discussed in detail in Chapter 2.

### 1.2.2 CRDS Apparatus

Experiments were conducted in a pulsed mid-infrared CRDS spectrometer coupled to a gas flow cell. The apparatus was originally built by Garland and Fuelberth and detailed descriptions of the design and construction can be found in their theses [19, 20]. What follows is a general description of the experimental components common to all following chapters. Details such as the specific dimensions of flow cells, gas concentrations, and timing schemes are contained in experimental sections of individual chapters.

#### 1.2.2.1 Laser System

Pulsed infrared radiation from 2.7 to 3.7 μm was produced by difference-frequency generation with an optical parametric amplifier (OPA), based on the configuration reported by Reid and Tang [21]. With typical input energies of 110 mJ of pump radiation (532 nm) and 1 mJ of signal radiation (620-660 nm), the OPA produced idler (infrared) radiation with energy $E \approx 1$ mJ/pulse, linewidth $\Gamma \approx 1$ cm$^{-1}$ and diameter $d \approx 2$ mm after transmission through three filters to remove the residual 532 and 630 nm light. Potassium titanyl phosphate (KTP) crystals were used for the OPA because of their relatively high damage threshold (>250 MW/cm$^2$). The crystals were cut at 44° off the *z*-axis in the *xz* plane, with 7 mm × 7 mm crystal faces, and length of 15 mm (Crystal Technologies). Two KTP crystals were used in series in order to obtain a higher conversion of pump to signal and idler radiation and to compensate for beam displacement as the crystals were angle tuned. The angle of each KTP crystal was controlled with a stepper motor (Superior Electric Slo Syn MO61-LSO2E) mounted on a translation stage to maintain phase matching as the dye wavelength was scanned.

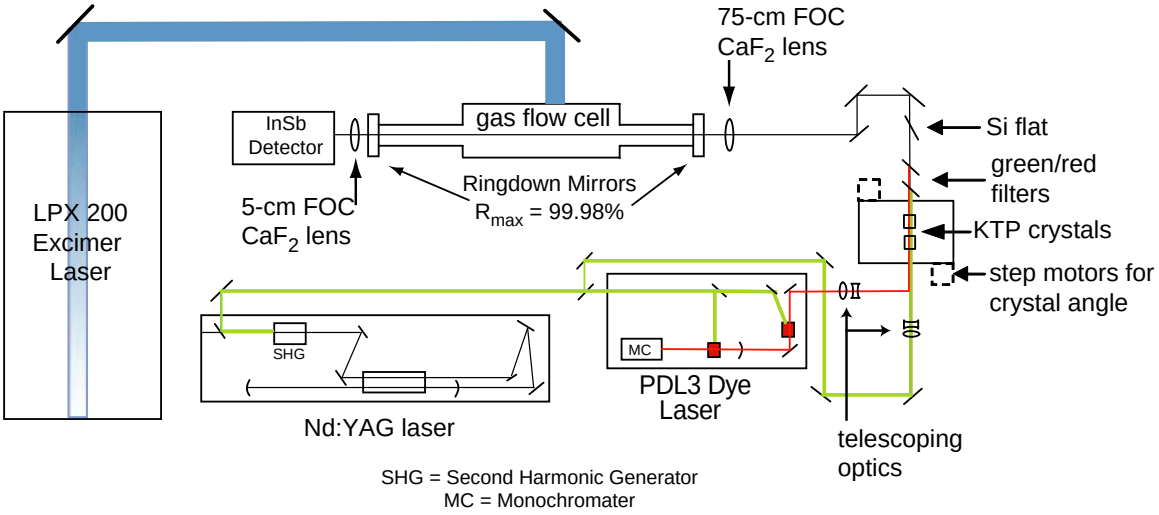


**Figure 1.3. Schematic of laser system.**

A schematic of the laser system and its arrangement on the laser table is shown in Figure 1.3. Schematic of laser system.Figure 1.3. The pump beam consisted of 532 nm radiation produced by doubling the output of a Nd:YAG laser (Spectra Physics GCR 130 or Continuum YG 661) operating at 10 Hz. Approximately 30% was diverted to pump a dye laser (Spectra Physics PDL3), to produce the signal radiation. The pump beam then passed through a delay line, the length of which was adjusted to optimize the temporal overlap of the pump and probe beams at the OPA. The polarization of the pump beam was then adjusted with a half-wave plate so that it entered the OPA horizontal to the plane of the laser table. The dye laser produced the signal beam with vertical polarization, and the output wavelength could be varied from 600 to 660 nm with DCM dye. Both the pump and signal beams were reduced with telescoping optics to approximately half of their original size ($d \approx 3$ mm) before being combined and sent into the OPA.

After passing through the OPA, the green and red beams were picked off with sapphire optics with antireflective coatings centered at 532 nm and 630 nm. Remaining

traces of the red and green light were eliminated by passing the beams through a polished silicon optic placed at Brewster's angle ($74^0$) so as to allow for maximum transmission of the IR radiation. The resulting IR energy varied from 0.1 to 1.0 mJ depending on frequency. The IR radiation had a beam diameter of $d \approx 2$ mm and a linewidth of $\Gamma_L \approx 1$ cm$^{-1}$. The linewidth was estimated by the measured width of water and methane transitions. See chapter 2 for further discussion.

The IR beam was then sent through a series of turning mirrors to allow for alignment with the CRDS cavity. The IR beam was found to be slightly diverging, and so a 75-cm focal length $CaF_2$ lens was placed in front of the CRDS cell to improve coupling into the ringdown cavity. For experiments requiring UV photolysis (Chapters 3 and 4) the output of an LPX 200 excimer was aligned into the gas flow cell perpendicular to the ringdown axis.

#### 1.2.2.2 CRDS Flow Cells

Conducting experiments in a gas flow cell provided several important benefits. Gas concentrations could be precisely determined and rapidly varied by introducing flow through calibrated flow meters. For kinetics experiments, the entire gas sample could be replaced faster than the laser repetition rate (10 Hz) to avoid the buildup and photolysis of products. Using a flow cell instead of a static gas cell also prevents the reactant and product gases from interacting with the ringdown mirrors. Due to the reactive nature of the gases used, this was critical to prevent degradation of mirror performance during the course of an experiment.

A general schematic of the flow cell system is shown in Figure 1.4. Ringdown mirrors were coupled to the gas flow cell via home-built mounts [20]. A vacuum seal is made by pressing the mirrors against O-rings. The O-rings sit in grooves machined into 2″ Conflat flanges. Fine adjustments to the mirror alignment are made by changing the position of threaded rods pressing against a washer around the outside of the mirror. The Conflat flanges with mounted mirrors are then attached to another pair of Conflat flanges fixed to the laser table. The first of these flanges has a feedthrough for inert purge gas (Ar or $N_2$). The second flange was welded to a ¾″ Ultratorr adapter used to connect the mirror mount assembly to the gas flow cell.

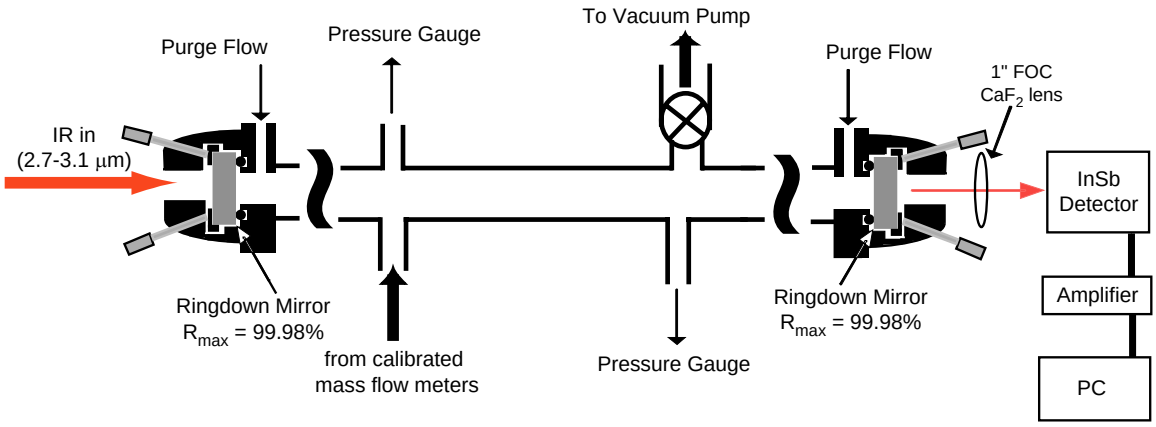


**Figure 1.4. Diagram of CRDS-coupled gas flow cell.**

Gas flow cells of various dimensions and materials were used. In addition to connectors on the ends to couple to the mirror mounts, all cells used had at least three ports: one for the input of reactant gas mixtures, one for the pumping out of the cell, and one for measuring the cell pressure. Most cells had a second port for measuring pressure so that pressure gradients within the cell could be quantified. All gases were flowed

through calibrated mass flow meters and then mixed prior to entering the cell. The cell was pumped by high-throughput mechanical pumps to facilitate the rapid flushing of the cell. The pressure in the cell was controlled by adjusting a valve between the cell and the vacuum line.

#### 1.2.2.3 CRDS Measurements

Because of the large losses at the mirrors, measuring the infrared radiation leaking from the CRDS cavity required a sensitive detection method. The ringdown cavity output was tightly focused with a 1″-focal length $CaF_2$ mirror onto the sensor of a liquid nitrogen-cooled InSb photodiode (Judson Technologies J10D-M204-R01M-60). Accurate measurements of ringdowns require a fast detector, so a photodiode with a small (1 mm) active area was used. The detector was then amplified, filtered to reduce high-frequency noise, and digitized.

Each ringdown trace was amplified and then accumulated with a 50 MHz bandwidth digital oscilloscope card with 14-bit digitizer (GageScope 1450). For each point in a spectrum, 16 ringdown traces were averaged and fit to a single-exponential function and constant baseline by a nonlinear Levenberg-Marquardt algorithm. Due to noise in the ringdowns at early times, the earliest part of the recorded decays was removed before fitting. This was accomplished by making an initial log-linear fit to estimate the lifetime, then cutting data points corresponding to the first half lifetime before the decay was fit with the Levenberg-Marquardt algorithm. The first half lifetime was cut from each decay before fitting. Scanning of the OPA system, collection of the

spectra, and the fitting of accumulated ringdown traces were controlled by a Labview PC program.

The CRDS mirrors (Los Gatos Research), with R=99.98%, have their maximum reflectivity at 2.8 μm. Typical background ringdown times were about 7 μs and about 5 lifetimes are collected and fit at 50 MSamples $s^{-1}$. The quality of the single-exponential fits depended on the alignment of the optical cavity, the alignment of the IR beam into the cavity, and the alignment of the focused IR output on the detector active area. As a result, the shot-to-shot fitting variance in the measured empty cell ringdown lifetime varied over the range $\Delta\tau/\tau = 0.3\% - 2.0\%$. For a typical cavity length of $L_{cav}$ = 50 cm ($1/\tau$ = 120,000) this corresponds to a minimum detectable absorbance of 0.6–2 ppm averaging 16 shots or 0.75-5.0 ppm $Hz^{-1/2}$.

# 2 Quantitative Integrated Intensity Measurements by Pulsed Cavity Ringdown Spectroscopy: The $\nu_1$ Band of Nitric Acid

## *2.1 Introduction*

### 2.1.1 Spectroscopy of Nitric Acid

Nitric acid plays a critical role throughout the atmosphere as a reservoir for odd nitrogen species. In the troposphere, the formation of nitric acid from the reaction

$$OH + NO_2 \xrightarrow{M} HONO_2 \qquad \text{Reaction 2.1}$$

leads to radical chain termination and removal of nitrogen oxides through precipitation of nitric acid. In the stratosphere, the competition of nitric acid formation by reaction 2.1 and its destruction through reaction with OH or photolysis

$$OH + HONO_2 \longrightarrow H_2O + NO_3 \qquad \text{Reaction 2.2}$$

$$h\nu + HONO_2 \longrightarrow HO + NO_2 \qquad \text{Reaction 2.3}$$

largely determines the fraction of total nitrogen oxides that exist as the more reactive odd nitrogen species. As a result of its importance in the atmosphere nitric acid has been, and continues to be, the target of much research.

#### 2.1.1.1 Infrared

The spectrum of nitric acid in the infrared has been studied by a number of groups to assist in atmospheric monitoring of nitric acid concentrations. The reported integrated intensities of the strongest band, the $\nu_1$ O-H stretch, differ from each other by greater than 30% [22-24] leading to significant uncertainty in atmospheric $HNO_3$ measurements.

The $\nu_1$ band has also been used in the studies of reaction 2.1 described in detail in chapters three and four. Reaction 2.1 has two possible products:

$$OH + NO_2 \xrightarrow{M} HONO_2 \qquad \text{Reaction 2.1a}$$

$$OH + NO_2 \xrightarrow{M} HOONO \qquad \text{Reaction 2.1b}$$

The yield of reaction 2.1b is pressure dependent and has important implications for our understanding of nitrogen oxides in the atmosphere. We measured this yield spectroscopically by measuring the $\nu_1$ bands of HOONO and $HONO_2$ produced in reaction 2.1 with cavity-ringdown spectroscopy (CRDS). The high sensitivity of CRDS was critical to detecting and quantifying the low concentrations of the minor HOONO product. As described in the next section, however, the use of CRDS to measure the much higher concentrations resulted in systematic errors in retrieved nitric acid absorbances.

To understand and quantify these errors, we have measured the integrated absorbance of the nitric acid with IR-CRDS while simultaneously measuring the nitric acid concentration by direct absorption in the ultraviolet. The observed integrated cross section derived from our CRDS spectra was observed to vary as a function of pressure and nitric acid concentration. By extrapolating to conditions under which we expect no systematic error from CRDS, we make a new measurement of the nitric acid $\nu_1$ integrated intensity.

#### 2.1.1.2 Ultraviolet

The UV spectrum from 195 to 350 nm has been carefully studied, as photodissociation in this spectral region is the predominant loss process for nitric acid in

the stratosphere [25-31]. In addition to the large number of cross-section measurements at these wavelengths, the data sets are in very good agreement.

Due to absorption by molecular oxygen, the nitric acid cross section at wavelengths shorter than 195 nm is not relevant to the atmosphere and has not been as extensively studied [25, 32, 33]. However, the large value of the cross section at 184.9 nm ($\sigma_{185}$) and convenient Hg-lamp emission line at this wavelength provide a useful analytical tool for monitoring nitric acid concentrations. Absorption at 184.9 nm has been used previously in laboratory experiments of nitric acid, primarily for measurements of the rate constant for reaction 2.1 [32, 33].

We use the large cross section at 184.9 nm to measure the low nitric acid concentrations needed in our IR integrated intensity measurements. Due to the critical nature of $\sigma_{185}$ to our IR CRDS experiments and the sparsity of reported values, we have re-measured $\sigma_{185}$.

### 2.1.2 Cavity Ringdown Spectroscopy

CRDS is an increasingly popular method for making measurements of very weak absorption spectra. A general description of the CRDS can be found in Chapter 1. Pulsed lasers with low resolution (0.1 to 1.0 $cm^{-1}$ FWHM) are commonly used due to their wide tunability and ease of CRDS implementation, and the discussion here will be limited to pulsed systems. In an ideal CRDS experiment, subsequent to injection of a pulse of radiation to the optical cavity, the intensity of radiation in the cavity decays exponentially in time according to

$$I(t) = I_0 \exp\left[ -\frac{tc}{L_{cav}}(A + (1-R)) \right], \qquad \text{Equation 2.1}$$

where $t$ is time, $c$ is the speed of light, $L_{cav}$ is the length of the cavity, $R$ is the reflectivity of the ringdown mirrors, and $A$ is the absorbance by species $X$ at concentration [$X$] molecules×cm$^{-3}$ occupying length $l_{abs}$ in the cavity. By fitting the observed decay to an exponential, the 1/e decay lifetime, $\tau$, is obtained,

$$\tau = \frac{L_{cav}}{c}\left( \frac{1}{(1-R)+A} \right). \qquad \text{Equation 2.2}$$

The absorbance can then calculated by subtracting the background decay rate,

$$\frac{1}{\tau} - \frac{1}{\tau_0} = \frac{c}{L_{cav}} A, \qquad \text{Equation 2.3}$$

where $\tau_0$ is ringdown time measured in the absence of the absorber. Generally, in a pulsed CRDS apparatus, $\tau_0$ varies smoothly as the laser frequency is scanned with no influence from transverse modes of the cavity, as the short coherence length of the laser prevents the buildup of cavity mode structure in the ringdown cavity [13, 16].

The sensitivity and tunability of CRDS has been exploited by our group to simultaneously measure the infrared absorption of the $\nu_1$ (OH stretch) bands of HOONO and $HONO_2$ formed in reaction 2.1 (chapters 3 and 4). While the high sensitivity of CRDS was necessary for detection and quantification of HOONO, the use of a low-resolution CRDS to make quantitative measurements introduces potential errors, particularly for the strongly absorbing, highly structured spectrum of nitric acid. With the broad frequency envelope of pulsed lasers ($\Gamma_L$ = 0.1 – 1.0 cm$^{-1}$ FWHM), the absorbance may vary within the frequency envelope of the laser. In this case, eq 2.1 no

longer describes the time profile of the cavity radiation, and the ringdown signal does not decay as a single exponential. For a frequency-dependent absorption, $A(\tilde{\nu})$, the observed ringdown is actually the combination of many different exponential decays described by

$$I(t,\tilde{\nu}_L) = I_0 \int_0^{\infty} L(\tilde{\nu}-\tilde{\nu}_L) \exp\left[\frac{tc}{l}\left[A(\tilde{\nu})+(1-R)\right]\right] d\tilde{\nu}, \qquad \text{Equation 2.4}$$

where $L(\tilde{\nu}-\tilde{\nu}_L)$ is a normalized function representing the laser profile centered at $\tilde{\nu}_L$. Attempts to fit an observed multi-exponential decay to a single decay lifetime $\tau$ lead to erroneous absorption results.

This is shown graphically for the simple case of a broad laser pulse interacting with a single sharp absorption feature in Figure 2.1. This specific case was thoroughly studied in the early days of CRDS to investigate the impact of fitting errors on retrieved CRDS spectra [14, 15, 18, 34]. Zalicki and Zare found that deviations occur when the laser linewidth $\Gamma_{\mathrm{L}}$ meets the condition $\Gamma_{\mathrm{L}} > \Gamma_{\mathrm{Abs}}/400$. Errors include incorrect line shapes and peak heights, incorrect integrated absorbance, and a dependence of the apparent absorption cross section on the size of the fitting window. At very low absorbance, while the line shape of a single feature is still not correctly determined, the absorbance is recovered "to within 10%" [18]. Zalicki and Zare propose that in order to obtain accurate absorbance measurements with low resolution lasers, the criterion $A < 0.1(1\text{-}R)$ must be met.

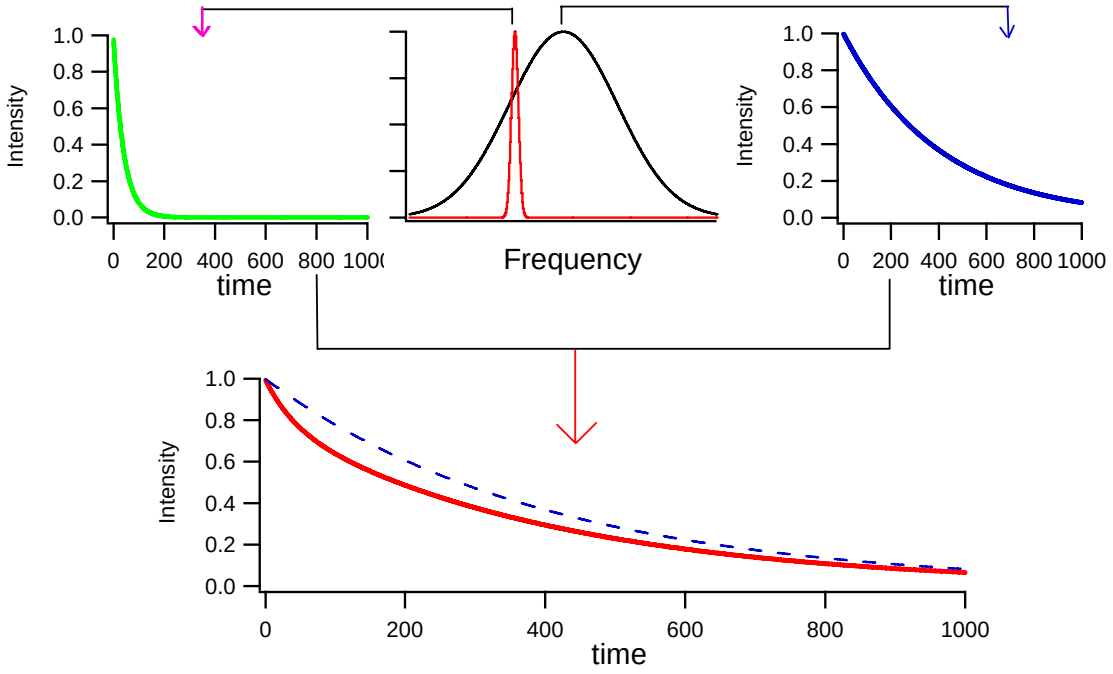


**Figure 2.1. Representative ringdown decays for the case of a broad laser profile (black, top) probing a single narrow absorption feature (red, top). Frequencies corresponding to absorption will have fast decays (green), others will have slow decays (blue) identical to the empty cell. The observed decay is multi-exponential (red, bottom). The single-exponential empty-cell decay is shown as a dashed line for comparison.**

While previous studies focused on the investigation of a single spectral line, there are no quantitative studies on a typical spectroscopy experiment of a small polyatomic molecule in which a low resolution laser scans a congested rovibrational spectrum. In this case, many lines that would be resolvable at high resolution are contained within the spectral bandwidth of the probe. It is not known how well CRDS measures the rotational envelope of congested spectra when using conventional nanosecond pulsed lasers with resolutions of 0.1 – 1.0 $cm^{-1}$. Figure 2.2 shows a high resolution FTIR spectrum of the $\nu_1$ OH stretch of nitric acid [35].

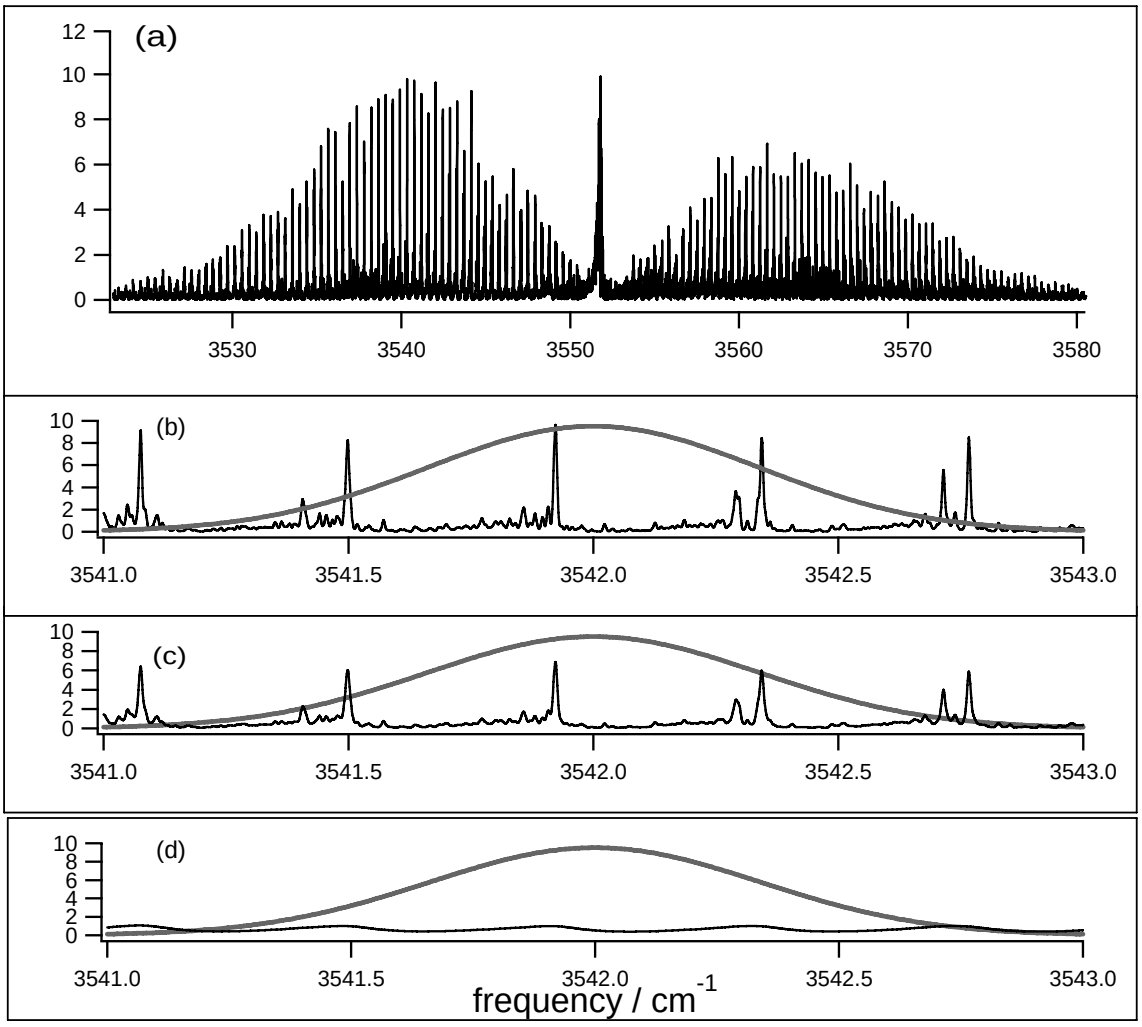


**Figure 2.2. High resolution FTIR spectrum of the $\nu_1$ band of nitric acid (panel a) in arbitrary units. (b)-(d) show a subset of the FTIR data (thin black line) with an approximation of our laser profile (thick grey line): (b) is the Doppler-limited spectrum, (c) is Lorentzian broadened to 0.0033 cm$^{-1}$ FWHM (20 torr), (d) is Lorentzian broadened to 0.125 cm$^{-1}$ FWHM (760 torr).**

This is a congested band consisting of a small number of very sharp and intense features superimposed over a background of many weak, partially resolved lines. Panel (b) of Figure 2.2 compares a small portion of the FTIR spectrum with an assumed Gaussian laser profile ($\Gamma_L$ = 1.0 cm$^{-1}$) superimposed in grey. For such a broad laser

width, the observed decay at each laser frequency, $\tilde{\nu}_L$, will be a multi-exponential; specifically the sum of a large number of exponentials each weighted by the intensity of the laser profile as described by eq 2.4. In general, the component decays that comprise the multi-exponential fall into two regimes: the very sharp features with large absorbance result in fast decay lifetimes and the broad background absorption results in much longer decay lifetimes.

Fits of a single exponential to these observed multi-exponential tend to give too much weight to the slow-decay component. This leads to measured CRDS absorbances from eq 2.3 lower than the true absorbance. These errors will depend on frequency, pressure and concentration, as the various component decays vary. As a result, we expect CRDS measurements of the $v_1$ band to have significant variations in the $v_1$ band shape and integrated absorbance, $IA(v_1)$.

In certain limiting cases, we would expect the error in our CRDS spectra to be negligible. At very high pressures, pressure broadening of the sharp features produces a more homogeneous underlying spectrum. As a result, fluctuations in $A(\tilde{\nu})$ over the laser profile are small, the decay is nearly a single exponential, and the observed integrated intensity should be accurate. At low concentrations, all components of the absorption contribute decays with long decay lifetimes. In this case, Zalicki and Zare's $A < 0.1\times(1\text{-}R)$ criterion is met for all components of the spectrum and again the integrated intensity should be accurate.

When not in the high-pressure or low-concentration limit, however, the observed CRDS spectrum will underrepresent the true molecular absorption, as the sharp features will contribute decays that are too fast to be captured by the single exponential fit. The

measured lifetime, $\tau$, will therefore be dominated by the broad background absorption. CRDS errors should be the most dramatic at the peaks of the *P*, *Q* and *R* branches where the sharp features are the most intense. As a result we expect the nitric acid $v_1$ band shape and $IA(v_1)$ observed with CRDS to be both pressure and concentration dependent. The main goal of these experiments was to quantify these dependencies over a range of pressures and absorbances, paying particular attention to the conditions similar to those found in the relative kinetics measurements of reaction 2.1 (Chapters 3 and 4). To this end, three experiments were conducted: (1) experimental CRDS measurements of the nitric acid $v_1$ band shape and $IA(v_1)$ as a function of pressure and [HNO3], (2) CRDS simulations to reproduce the experimental $v_1$ band shape and $IA(v_1)$ data, and (3) CRDS measurements of $IA(v_1)$/ $IA(2v_2)$ as a function of pressure. From these experiments, corrections for CRDS $IA(v_1)$ measurements are derived and integrated cross sections for the nitric acid $v_1$, $S(v_1)$, and $2v_2$, $S(2v_2)$, bands are reported.

## *2.2 Cross Section at 184.9 nm*

### 2.2.1 Experiment

A schematic of the apparatus is shown in Figure 2.3 with the setup labeled (a). Nitric acid was introduced by flowing He through a temperature-controlled bubbler containing pure nitric acid. The nitric acid flow was diluted with $N_2$ before entering the first flow cell (Cell A), where the concentration was measured, then further diluted with $N_2$ before entering the second flow cell (Cell B), where the absorption at 184.9 nm was measured.

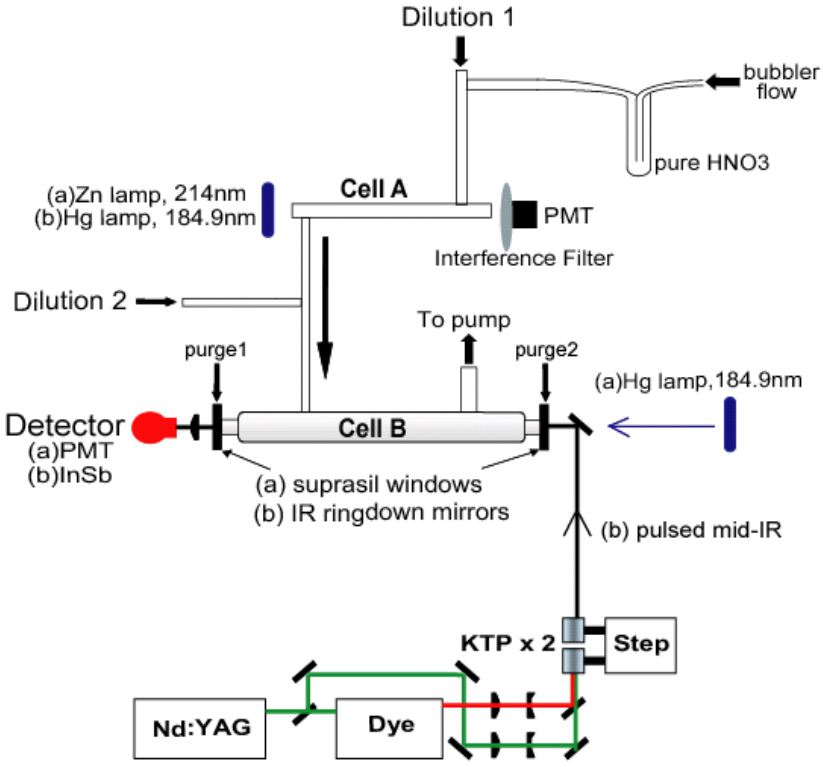


**Figure 2.3. Schematic of the flow cell apparatus used for (a) measuring the nitric acid 184.9 nm UV cross section and (b) measuring the $\nu_1$ and $2\nu_2$ integrated absorption by IR-CRDS.**

#### 2.2.1.1 UV Absorbance

The nitric acid concentration was measured in Cell A by UV absorption at 214 nm. Cell A was 30.2 cm long with an inside diameter of 1.0 cm and UV-grade quartz windows. 214 nm radiation was produced by a Zn lamp (UVP), collimated through a series of lenses and irises, passed through cell A and detected with a bialkali PMT equipped with a 214 nm interference filter. For each 184.9 nm absorption measurement, the concentration of nitric acid in Cell B, $[HNO_3]_{185}$, was calculated using eq 2.5.

$$[HNO_3]_{185} = \frac{-\ln\left(\frac{I_{214}}{I_{0,214}}\right)}{L_{214}\sigma_{214}}\left(\frac{P_{185}}{P_{214}}\right)\left(\frac{f_{214}}{f_{185}}\right), \qquad \text{Equation 2.5}$$

where $-\ln\left(\frac{I_{214}}{I_{0,214}}\right)$ is the Beer's Law absorption in Cell A, $\sigma_{214}$ is the cross section at 214 nm ($\sigma_{214} = 4.33\times10^{-19}$ cm$^2$ molecule$^{-1}$) [36], $L_{214}$ is the length of Cell A ($L_{214}$), and the last two factors are the ratios of flows and pressures in the two cells. Nitric acid concentrations in Cell A were typically on the order of $10^{16}$ molecules×cm$^{-3}$, leading to 214 nm absorbances of about 0.1. The total pressure in the system was kept at about 40 torr and $P_{185}/P_{214}$ was typically between 0.9 and 1. The total flow in the system varied from 200 to 2000 sccm, with $f_{214}/f_{185}$ ranging from 0.05 to 0.3, resulting in Cell B nitric acid concentrations of 4-50×$10^{14}$ molecules×cm$^{-3}$.

Cell B had a total length of 47 cm, with suprasil windows mounted to either end. The sample was confined to the center of Cell B by purge flows of UHP Ar over the ends, as discussed below. 184.9 nm radiation was produced by a Hg Pen-Ray lamp (UVP), collimated through a series of lenses and irises, passed through cell B and detected with a bi-alkali PMT equipped with two 184.9 nm interference filters. Leakage of 254 nm light through the 185 nm interference filter was quantified each day by saturating the absorption at 185 nm with $N_2O$ ($\sigma_{185} > 10^4\times\sigma_{254}$). The 254 nm intensity, on the order of 1% to 3% of the empty cell intensity, was subtracted from all intensity measurements. Leakage from the nearby Hg emission line at 195 nm was measured by absorption of $CO_2$ to be 9.5% of the of the empty cell intensity, and was also subtracted from all intensity measurements. The uncertainty of individual intensity measurements were 0.7% for 184.9 nm and 0.5% for 214 nm. Background UV readings were measured before and after each point. The background drifted slightly over the course of the data collection, so the average of the background readings surrounding each point was used.

### 2.2.1.2 Sample Path Length

The effective path length of sample in Cell B, $l_s$, was measured by flowing pure $N_2O$ through the center of Cell B and measuring the absorbance at 214 nm as a function of purge flow. The UV apparatus was first tested by measuring the $N_2O$ absorbance of the cell filled completely to a given pressure of pure $N_2O$. We measured a cross section of $\sigma_{214} = 3.48\times10^{-21}$ cm$^2$ molecule$^{-1}$, within 2% of the literature value [36], using $l_s = L_{tot}$ = 53 cm (Figure 2.4).

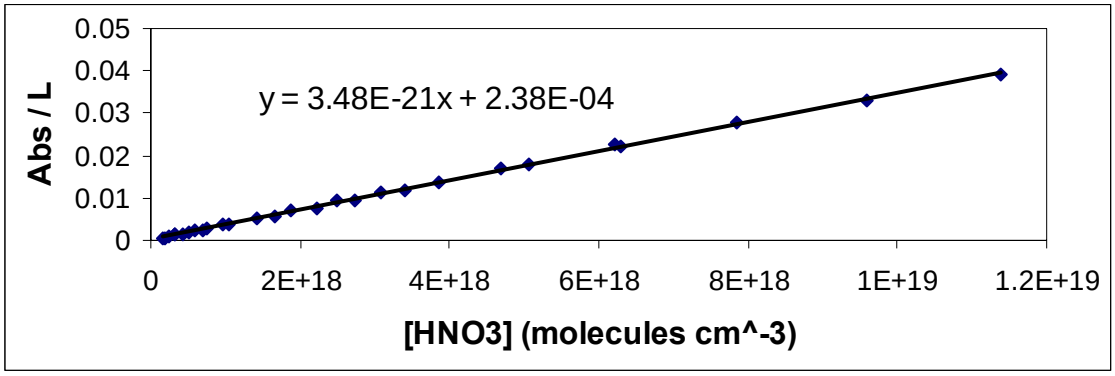


**Figure 2.4. Static cell measurements of $N_2O$ absorbance at 214 nm.**

Figure 2.5 shows the variation in $l_s$ with purge flow. When the purge flows were small $l_s$ varied rapidly with purge, dropping to 23 cm at purge flows 3% of the total flow ($0.03F_{tot}$). The dependence of $l_s$ upon purge at higher purge flows was much more gradual, with $l_s$ = 17 cm at $0.13F_{tot}$. We found that $l_s$ was also weakly dependent upon pressure. As a result of the dependence upon purge flow, an attempt was made conduct all subsequent experiments keeping the purge flow over each end at $0.07F_{tot}$ to keep $l_s \approx$ 19.5 cm. The dependence of $l_s$ upon purge and pressure was parameterized and the specific flow conditions for each measurement were used to calculate $l_s$. Calculated $l_s$ values are estimated to have a $2\sigma$ uncertainty of 3%.

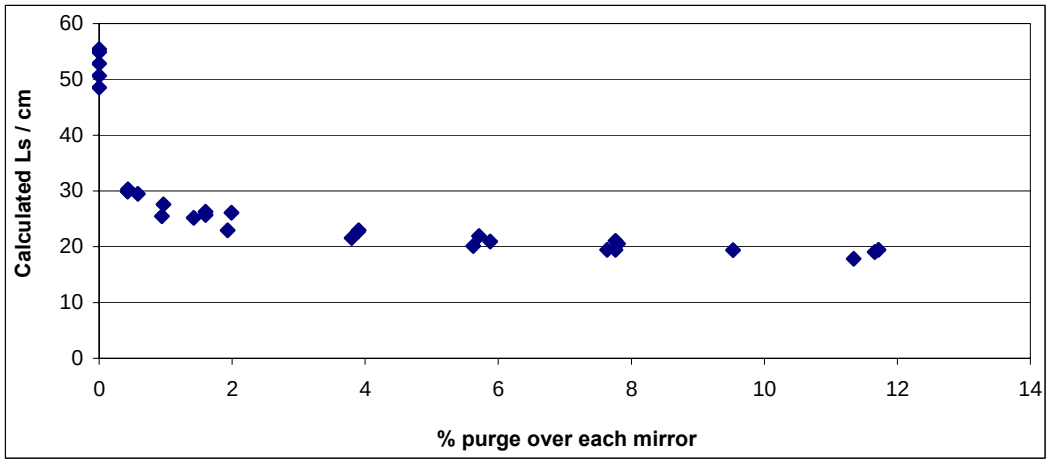


**Figure 2.5. Variation in sample path length as a function of purge flow. *Ls* was calcuated using $\sigma_{214}$ = $3.48\times10^{-21}$ $cm^2$ $molecule^{-1}$**

### 2.2.1.3 Gases

All flows were measured with Edwards or Omega mass flow transducers, calibrated volumetrically and were accurate to 0.5%. The pressure was measured from ports in the center of both cells using MKS Baratrons, calibrated with a JPL calibration system consisting of MKS 10 torr and 1000 torr calibration heads accurate to within 0.05% from a recent factory calibration. Corrections to our pressure readouts were generally less than 5% and corrected values should be accurate to 0.5% over the range of pressures used in this study. The pressures and flows remained constant for the duration of each data point.

Nitric acid was synthesized by adding concentrated $H_2SO_4$ to $NaNO_3$ under vacuum, collecting the nitric acid vapor in a liquid $N_2$ cold trap. When not being used the sample was stored in a liquid $N_2$ dewar. After storage, the sample would contain small quantities of the decomposition product $NO_2$. After bubbling for about 5 minutes, the $NO_2$ would completely evolve leaving pure nitric acid. This process was confirmed by

connecting our flow system to a Nicolet FTIR spectrometer and monitoring the $NO_2$ absorption in time. All tubing, valves, and joints between and including Cell A and Cell B were either glass or teflon to minimize surface decomposition.

### 2.2.2 Results

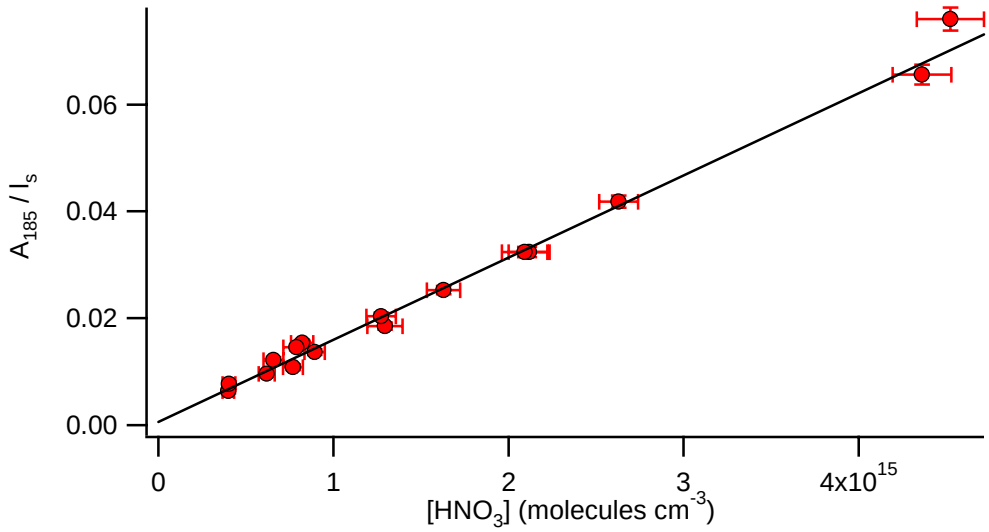


**Figure 2.6. ($A_{185}$ / $l_s$) as a function of nitric acid concentration. Nitric acid concentration is calculated from eq 2.5. The slope of the fit yields a 184.9 nm cross section of 1.55±09×10$^{-17}$ cm$^2$×molecule$^{-1}$**

The 184.9 nm Beer's Law absorbance $A_{185}$ divided by $l_s$ at room temperature is plotted as a function of nitric acid concentration in Figure 2.6. The error bars on each point represent propagated 2σ uncertainties. Uncertainties in the *y*-axis are dominated by the 0.7% uncertainty in $I_{185}$, which lead to 2%-6% uncertainties in $A_{185}$, and the 3% uncertainty in $l_s$. The uncertainty in $l_s$ stems from the scatter in measurements of $l_s$ (see Figure 2.5 above) and thus has been treated as a random uncertainty. Ucertainties in the *x*-axis are dominated by the 0.5% uncertainty in $I_{214}$, which leads to 5%-9% uncertainties in $A_{214}$. Other sources of uncertainty in [$HNO_3$], such as in the literature value of $\sigma_{214}$

and uncertainties in the pressure and flow measurements, are less than 1% and therefore contribute little to the overall uncertainty.

A weighted fit of the data yields $\sigma_{185} = 1.55 \pm 0.09(2\sigma) \times 10^{-17}$ cm$^2$ molecule$^{-1}$. The intercept of $0.0006 \pm 0.0009$ is of the same order as our uncertainty in an individual measurement of the absorbance, indicating no significant systematic error.

### 2.2.3 Discussion

Table 2.1 lists our value of $\sigma_{184.9}$ along with the most recently reported values in the literature [25, 32, 33]. The previous studies differ from each other and this study in many ways, making assessment of their relative merits difficult. The most significant difference stems from the nature of the gas handling in each experiment. This study uses a diluted flow of nitric acid, Connell continuously flows pure nitric acid through the cell, while Biaume and Wine et al. fill static cells. Using a constant flow of nitric acid as in this study and Connell reduces possible complications from decomposition of nitric acid to form $NO_2$. Wine et al. report a significant variation in their measured cross section depending on the how many fills they have done between extensive pumping on the cell. They attribute this variation to conditioning of their cell and this leads to their wide range of reported values. Biaume does not report any such effect. Wine and Connell use small cells (2.5 cm) and measure low pressures of nitric acid directly in the cell while Biaume, for wavelengths shorter than 200 nm, measures the pressure of nitric acid in a small volume and then expands it into a larger cell.

**Table 2.1. $HNO_3$ 184.9 nm cross section measured in this work compared to literature data. Reported uncertainties are 2σ. Wine et al. report only a range of observed values.**

| Study | year | static/flow | $[HNO_3]$ measurement | $\sigma_{184.9}$ / $cm^2 \times molecule^{-1}$ |
|---|---|---|---|---|
| this work | 2004 | flow | 214 nm UV absorption/dilution | $1.55 \pm 0.09 \times 10^{-17}$ |
| Biaume [25] | 1998 | static | $HNO_3$ pressure/expansion | $1.63 \pm 0.05 \times 10^{-17}$ |
| Connell / Howard [32] | 1985 | flow | $HNO_3$ pressure | $1.64 \pm 0.03 \times 10^{-17}$ |
| Wine et al. [33] | 1981 | static | $HNO_3$ pressure | $1.45\text{-}1.70 \times 10^{-17}$ |

The procedure used in this experiment of measuring the nitric acid concentration with a well-known UV cross section is unique among the measurements of $\sigma_{184.9}$. Using a continuous and fairly rapid flow has several advantages, primarily a reduced potential influence of nitric acid decomposing or sticking to the walls of the cell. The main drawback of this technique is the increase in measurement uncertainties, such as the doubling of the number of intensity measurements and the uncertainty in $l_s$. Overall, our value for $\sigma_{185}$ is about 5% lower and has slightly larger error bars than the most commonly used value of Biaume; The two measurements do agree within their uncertainties. The agreement between our value and the previous literature indicates that our flow-cell apparatus, where $[HNO_3]$ is determined by UV absorption, can yield accurate cross-section measurements. The IR experiments described below utilize our value for $\sigma_{185} = 1.55 \times 10^{-17}$ $cm^2 \times molecule^{-1}$.

## 2.3 IR Integrated Intensities

### 2.3.1 Experiments

A schematic of the apparatus is shown in Figure 2.3 with the setup labeled (b). The concentration of nitric acid carried in $N_2$ was measured by 184.9 nm absorption in Cell A. The details of Cell A and 184.9 nm absorption measurements are given above. The flow was then further diluted with $N_2$ before entering Cell B, where the IR-CRDS spectrum was taken. The concentration of nitric acid in Cell B was calculated using eq 2.6.

$$[HNO_3]_{IR} = \frac{-\ln\left(\frac{I_{185}}{I_{0,185}}\right)}{L_{185}\sigma_{185}}\left(\frac{P_{IR}}{P_{185}}\right)\left(\frac{f_{185}}{f_{IR}}\right), \qquad \text{Equation 2.6}$$

where $-\ln\left(\frac{I_{185}}{I_{0,185}}\right)$ is the Beer's Law absorption in Cell A, $L_{185}$ = 20.2 cm is the length of Cell A, $\frac{P_{IR}}{P_{185}}$ and $\frac{f_{185}}{f_{IR}}$ are the ratio of flows and pressures in the two cells, and $\sigma_{185}$ = $1.55\times10^{-17}$ $cm^2\times molecule^{-1}$ (Section 2.2). Nitric acid concentrations in Cell A were in the range $2\text{-}14\times10^{14}$ $molecules\times cm^{-3}$, leading to 185 nm absorbances ranging from 0.1 to 0.7. The total pressure in the system varied from 18 to 760 torr. At higher pressures, $P_{185}/P_{214}$ was typically very close to 1, whereas at low pressures and high dilution flows was as small as 0.6. The total flow in the system varied from 500 to 4000 sccm, with $f_{214}/f_{185}$ ranging from 0.03 to 0.2, resulting in Cell B nitric acid concentrations of $(7\text{-}500)\times10^{12}$ $molecules\times cm^{-3}$. Cell B was the same as that described above, but with the suprasil windows replaced with ringdown mirrors ($L_{cav}$ = 45 cm). As described above (Section 2.2.1.2), the sample path in Cell B, $l_s$, was calculated from the pressure and flows for

each experiment, with $l_s \approx 19$ cm. Gases, flowmeters, and pressure transducers were all the same as described in Section 2.2.1.3.

Infrared spectra were collected in Cell B using moderate resolution (1 $cm^{-1}$) IR-CRDS. Details of the laser system and CRDS apparatus are given in Chapter 1. For these experiments, typical background ringdown times were about 7 μs and about 5 lifetimes were collected and fit. Scanning of the OPA system, collection of the spectra, and the fitting of accumulated ringdown traces were controlled by a Labview PC program.

Scans investigating changes in our observed $v_1$ spectral shape were taken from 3490-3610 $cm^{-1}$ at 0.2 $cm^{-1}$ step size. Scans measuring $IA(v_1)$ as a function of pressure and [$HNO_3$], were taken in pairs: from 3480 to 3620 $cm^{-1}$ at 4 $cm^{-1}$ step size and from 3530 to 3570 $cm^{-1}$ at 1 $cm^{-1}$ step size. Scanning in this manner enabled us to capture the shape surrounding the Q-branch, while significantly reducing the time needed to scan over the entire $v_1$ band. The agreement of the 4 $cm^{-1}$ and 1 $cm^{-1}$ scans at all overlapping points assured us there was no drift in nitric acid concentration on the time scale of the scans (10 minutes). Scans measuring the relative integrated absorption of the $v_1$ and $2v_2$ bands were taken over the range 3330-3620 $cm^{-1}$ at 1.5 $cm^{-1}$ step size.

Background CRDS scans were taken before and after at most every 4 scans of the nitric acid peak. Background scans showed no sign of outgassing from residual nitric acid adsorbed to the walls. Additionally, each nitric acid scan extended 10 $cm^{-1}$ beyond the nitric acid band on either side, serving as an inherent measure of the background $\tau_0$ with each scan. The integrated absorbance was calculated from the measured ringdown

lifetimes with ($\tau$) and without ($\tau_0$) an absorber by integrating the standard ringdown equation (eq 2.3) for absorbance over the entire band profile.

$$IA(\nu_1) = \int_{3490\ \mathrm{cm}^{-1}}^{3610\ \mathrm{cm}^{-1}} \mathrm{Abs}(\tilde{\nu})\mathrm{d}\nu = \frac{L_{cav}}{c} \int_{3490\ \mathrm{cm}^{-1}}^{3610\ \mathrm{cm}^{-1}} \left( \frac{1}{\tau(\tilde{\nu})} - \frac{1}{\tau_0(\tilde{\nu})} \right) \mathrm{d}\tilde{\nu}\,.$$

$IA(2\nu_2)$ was calculated similarly, with the bounds of integration changed to 3350-3450 $cm^{-1}$.

### 2.3.2 Simulations

The IR-CRDS nitric acid spectrum was also investigated using a CRDS simulation program. The program convolved an assumed high resolution spectrum and laser profile (Figure 2.2) into multi-exponential CRDS decays. This was accomplished by first broadening the high-resolution spectrum with Lorentzians to the pressure of interest ($\gamma$ = 0.125 $cm^{-1}\times atm^{-1}$ was used, discussed below). The pressure-broadened spectrum was then scaled to the desired absorbance and each point converted from absorbance units to a ringdown lifetime, $\tau$. These $\tau$ were then added to an assumed background $\tau_0$ (set to 7 μs as in the experiments), converted to exponential decays, and summed over a normalized Gaussian centered at $\tilde{\nu}_\mathrm{L}$, $L(\tilde{\nu} - \tilde{\nu}_L)$, representing the laser profile ($\Gamma_\mathrm{L}$ = 1.0 $cm^{-1}$ was used, discussed below)

$$I(t, \tilde{\nu}_L) = I_0 \sum^{\text{all points}} L(\tilde{\nu}_i - \tilde{\nu}_L) \exp -\left[ \tau(\tilde{\nu}_i) + \tau_0 \right] \qquad \text{Equation 2.7}$$

To expedite the simulations, the above sum was carried out only over points within $\tilde{\nu}_\mathrm{L} \pm \Gamma_\mathrm{L}$ (98% of laser profile intensity), rather than for all points. Tests using $\tilde{\nu}_\mathrm{L} \pm 1.5\Gamma_\mathrm{L}$ showed no change in simulation results. The decays generated by eq 2.7 were then fit

using the same nonlinear Levenberg-Marquardt algorithm used to fit our experimentally observed decays. The center frequency of the laser profile, $\tilde{\nu}_L$, was then scanned over the entire band profile. In this way, changes in the $\nu_1$ band shape and $IA(\nu_1)$ were investigated as a function of pressure and [$HNO_3$] in the same manner as in the experiments described above.

In addition to the absorbance derived from our fits to these multi-exponentials, the true absorbance with no CRDS fitting error, $IA(\nu_1)_{Ture}$, was also obtained by summing the lifetimes over the laser profile prior to converting to exponential decays. In order to compare the simulation results to the experimental results, $IA(\nu_1)_{True}$ was converted to a nitric acid concentration using an assumed value for the integrated cross section $S(\nu_1)$ = $1.22\times10^{-17}$ cm molecule$^{-1}$ [22].

$IA(\nu_1)_{True}$ was also used to calculate the magnitude of the CRDS error, $E_{CRDS}$, from the simulations where

$$E_{CRDS} = \frac{IA(\nu_1)_{CRDS}}{IA(\nu_1)_{True}},$$

Due to the limited range of the high-resolution FTIR spectrum used for the simulations, the simulated CRDS and true absorbance spectra are limited to the range 3525-3579 cm$^{-1}$. It was assumed that the missing absorbance in the far wings was well approximated by the experimentally observed spectra. Any error in this assumption was likely small and had a negligible impact on simulated $IA(\nu_1)_{CRDS}$ since the far wings contribute <2% to the total integrated absorbance.

Calculated $E_{CRDS}$ were then used to correct the low-[$HNO_3$] experimental $IA(\nu_1)$ to eliminate the impact of CRDS fitting errors prior to deriving $S(\nu_1)$ from the

experimental data. Due to the low concentrations involved, variations in $E_{CRDS}$ for these data were small. As a result, our derived integrated cross section was insensitive to the value of $S(\nu_1)$ used to calculate [$HNO_3$] for the simulation data, varying by less than 1% over the range $S(\nu_1) = (1.0–1.5)\times10^{-17}$ cm molecule$^{-1}$.

Assumed values for the laser linewidth, $\Gamma_L$, and the pressure-broadening coefficient, γ, were critical inputs to the CRDS simulations. As a result, both $\Gamma_L$ and γ were systematically varied to determine the sensitivity of simulated outputs to these parameters and confirm the validity of our assumed values. Since previous measurements using our OPA system had indicated $\Gamma_L \approx 1.0$ cm$^{-1}$, the range $\Gamma_L = 0.5$-2.0 cm$^{-1}$ was used to generate simulated spectra. Simulated $IA(\nu_1)$ showed a negligible dependence upon $\Gamma_L$. The change was largest at the highest concentrations, but even at $2800\times10^{-12}$ molecules×cm$^{-3}$, doubling $\Gamma_L$ led to only a 0.7% decrease in $IA(\nu_1)$. Similarly, halving $\Gamma_L$ led to only a 1.5% increase in $IA(\nu_1)$. Changes in the simulated $\nu_1$ band shape with $\Gamma_L$, particularly in the region around the $Q$ branch at low pressures, were more pronounced. Only Gaussian line shaes in the range $\Gamma_L$ = 0.8-1.2 cm$^{-1}$ produced reasonable matches to the experimentally observed spectra, with the best fit coming with $\Gamma_L = 1.0$ cm$^{-1}$.

Literature measurements of pressure broadening coefficients for pure rotational transitions in nitric acid (γ = 0.11 cm$^{-1}$×atm$^{-1}$ in $N_2$ [37]) and $\nu_1$ rovibrational transitions of OH (γ = 0.146 cm$^{-1}$×atm$^{-1}$ in $N_2$ [38]) led to testing the range γ = 0.09-1.70 cm$^{-1}$×atm$^{-1}$ in our simulations. While any values of γ > 0.10 cm$^{-1}$×atm$^{-1}$ were able to match the observed spectral shape at 1 atm, only the very small range of γ = 0.120-0.130 cm$^{-1}$×atm$^{-1}$ were successfully able to match both the high- and low-pressure experimental spectra.

The quantitative impact of changing γ over this range was largest at the lowest pressures studied and less than 2% under all conditions.

### 2.3.3 Results

Four scans of the $\nu_1$ band of nitric acid taken at 0.2 $cm^{-1}$ step size for various concentrations and pressures are shown in Figure 2.7. Both experimental and simulated spectra are shown for four conditions: 750 torr at $6.0\times10^{13}$ and $1.0\times10^{15}$ molecules$\times cm^{-3}$ and 20 torr at $4.2\times10^{13}$ and $1.0\times10^{15}$ molecules$\times cm^{-3}$. For comparison, the simulated true absorbance with no CRDS fitting error is also shown. In the bottom panel the experimental scans have been normalized to $1.0\times10^{14}$ molecules$\times cm^{-3}$ in order to emphasize the change in spectral shape. The experimental and simulated spectra agree quite well in both shape and intensity under all conditions. As expected, the absorbance loss due to CRDS fitting errors is much more dramatic in the 20 torr spectra, with considerable loss in the most intense regions of the spectrum even at the lower concentration. While the 750 torr exhibits much smaller CRDS effects, changes in the spectral shape from the data to the true absorbance and between the two concentrations are still apparent in the heights of the Q-branch.

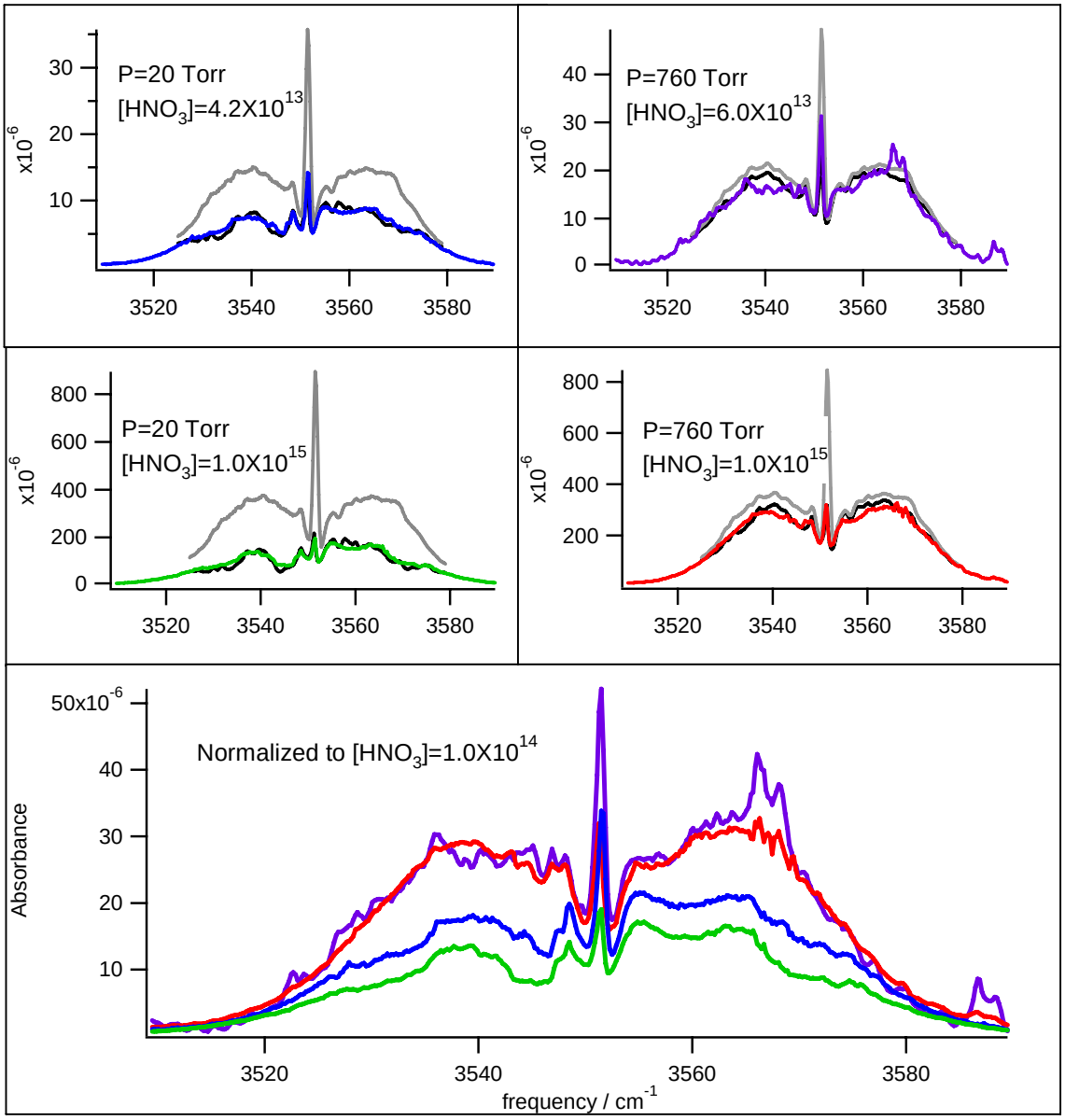


**Figure 2.7. Experimental and simulated IR-CRDS spectra of the $\nu_1$ OH stretch of nitric acid. Colored spectra are experimental data, CRDS simulations are shown in black, and the grey spectra represent the expected spectral shape with no CRDS error. All concentrations in molecules×cm$^{-3}$. The bottom panel shows the four experimental spectra from the upper panels normalized to 1×10$^{14}$ molecules×cm$^{-3}$.**

Figure 2.8 shows collected ringdown traces at two frequencies from the low pressure, high concentration spectrum shown in Figure 2.7 along with the fits and residuals for those traces.

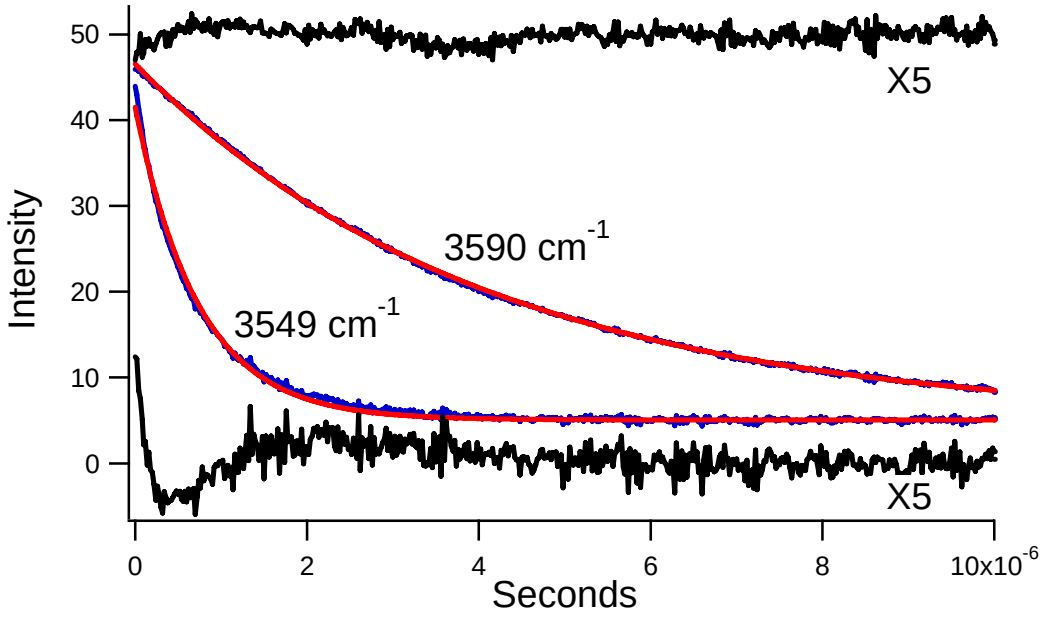


**Figure 2.8. Two measured ringdowns (blue) along with the Levenberg-Marquardt fits (red) and residuals. The residuals have been multiplied by 5 for clarity. The residual for the 3549 cm$^{-1}$ trace is shown at the bottom, while the residual for the 3590 cm$^{-1}$ trace has been offset by 50.**

The mechanism for the dramatic reduction in absorbance in the intense regions of the low pressure CRDS spectra is evidenced by the poor fit to the 3549 cm$^{-1}$ trace. The observed multi-exponential decay is poorly fit by a single exponential, particularly at early times, when the contribution of the sharp, intense features is rapidly changing. As expected, the fit to the trace taken at 3590 cm$^{-1}$ is much better, as the spectrum is more homogeneous and all absorbances are much smaller in this region. Residuals such as that shown in the bottom of Figure 2.8 are found, to varying degrees, for all regions of nitric acid spectra where a reduction in CRDS spectral intensity is observed.

$IA(\nu_1)/l_s$ data taken at 20 and 630 torr are plotted as a function of nitric acid concentration in Figure 2.9. Again, both experimental and simulated CRDS data are shown along with the simulated true $IA(\nu_1)/l_s$ in the absence of CRDS error. The

uncertainties in individual experimental $IA(\nu_1)/l_s$, on the order of the scatter in the data, have been omitted for clarity.

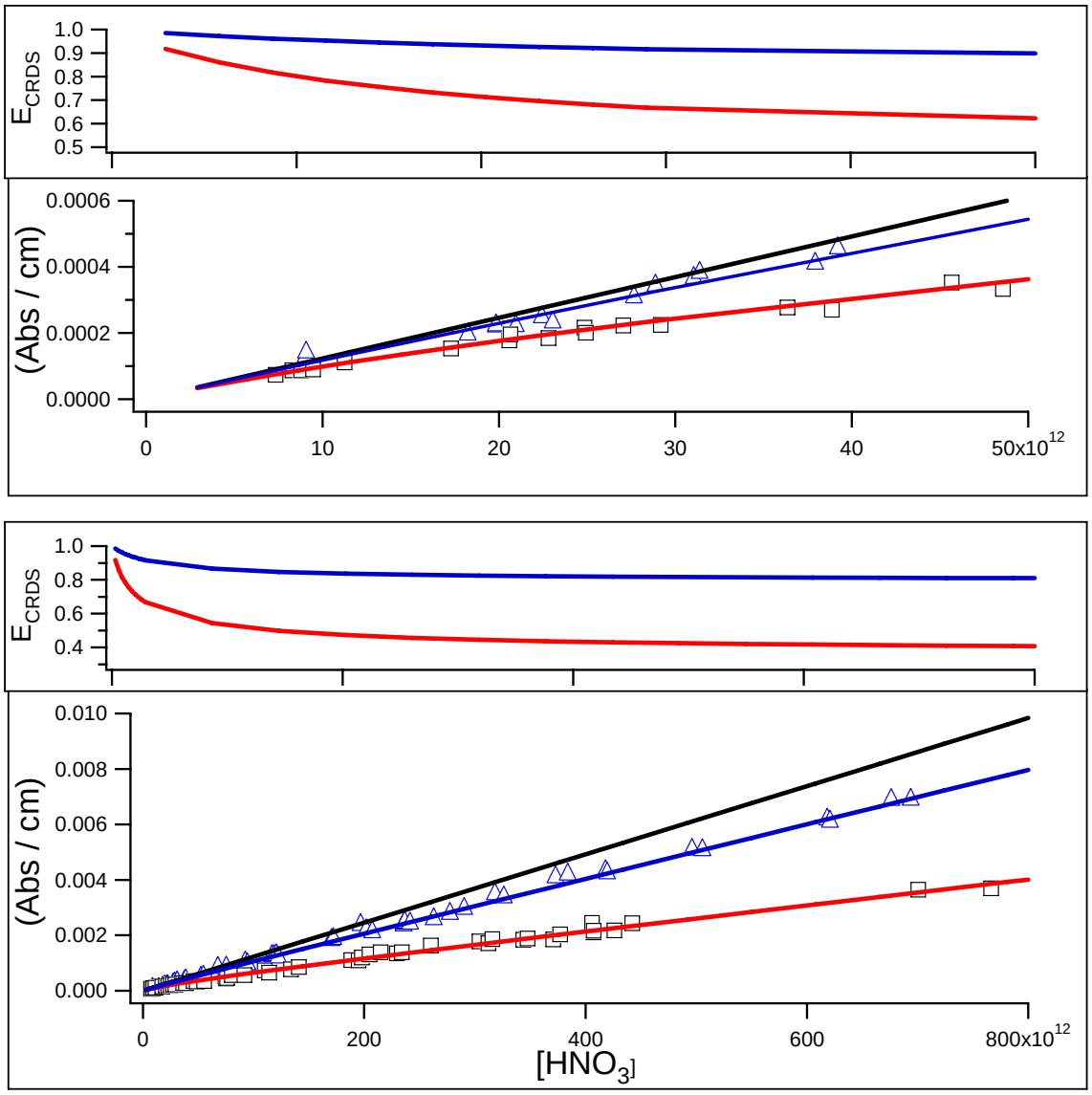


**Figure 2.9. ($IA(\nu_1)/l_s$) as a function of nitric acid concentration. Triangles are data taken at 630 torr, squares are data taken at 20 torr. The blue line is the CRDS simulation at 630 torr, the red line is the CRDS simulation at 20 torr, and the black line represents the integrated absorbance with no CRDS artifact as derived from our simulations. The top panel shows the lowest concentration data. Above each graph is also shown $E_{CRDS}$ from the simulations are plotted for 20 torr (red) and 630 torr (blue).**

Additionally, $E_{CRDS}$ data from the simulations are plotted for both pressures. The experimental and simulated data agree quite well for both pressures over the entire concentration range studied. While $IA(\nu_1)/l_s$ at the two pressures approach each other and the $IA(\nu_1)/l_s$ in the absence of CRDS error at low [$HNO_3$], the three have not yet converged at the lowest concentrations achieved in this study ($8.0\times10^{12}$ molecules×$cm^{-3}$).

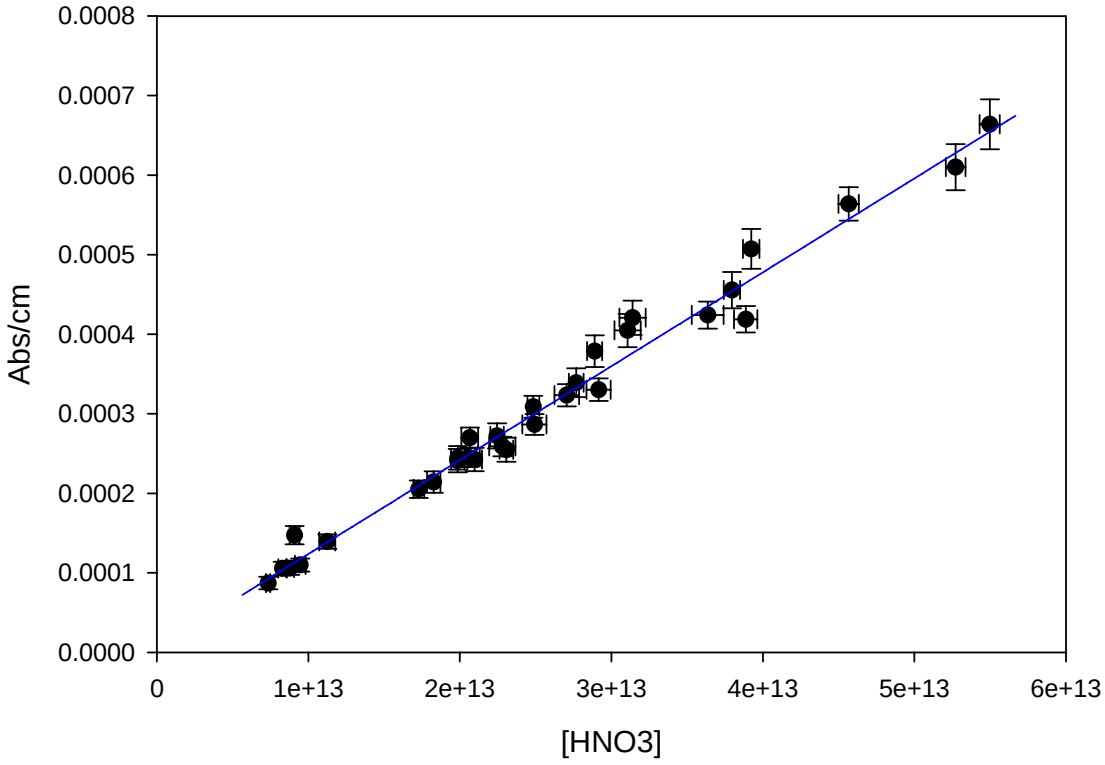


**Figure 2.10. Fit to integrated nitric acid $\nu_1$ absorbance data taken at low concentrations (20 and 620 torr). The data is that shown in Figure 2.9 divided by $E_{CRDS}$ to eliminate CRDS fitting errors. The slope of the fit yields a $\nu_1$ integrated cross section of $1.18(08)\times10^{-17}$ cm×molecule$^{-1}$.**

The data used to calculate our measured $\nu_1$ integrated cross section are shown in Figure 2.10. These are the low concentration data shown in Figure 2.9 (both pressures) divided by $E_{CRDS}$ as calculated from the simulations. $E_{CRDS}$ values range from 0.69 to 0.94 for the 20 torr data and from 0.89 to 0.98 for the 630 torr data. The error bars on

each point represent propagated 2σ uncertainties. Uncertainties in the *y*-axis are dominated by the 3% uncertainty in $l_s$ and, for very low-[$HNO_3$] data, integrated spectral noise, which can contribute up to 5% uncertainty in $IA(\nu_1)$. As described in Section 2.2.3, $l_s$ has been treated as a random error. Uncertainties in [$HNO_3$] are dominated by the 0.7% uncertainty in $I_{185}$, which leads to 1%-5% uncertainties in $A_{185}$ and the 6% systematic uncertainty in $\sigma_{185}$. Other sources of uncertainty in [$HNO_3$], uncertainties in the pressure and flow measurements, are less than 1% and therefore contribute little to the overall uncertainty. A weighted fit to the data yields an integrated cross section of $S(\nu_1) = 1.18\pm05(2\sigma)\times10^{-19}$ cm×molecule$^{-1}$. The *y*-intercept of $5.5\pm10.4\times10^{-6}$ cm$^{-1}$ is within the uncertainty in a single absorbance measurement. We estimate that systematic uncertainties, such as errors in $E_{CRDS}$, $\Gamma_L$, and γ combine to give about 2% additional uncertainty. We therefore report $S(\nu_1) = 1.18\pm08(2\sigma)\times10^{-19}$ cm×molecule$^{-1}$.

A representative spectrum used to measure $IA(\nu_1)/IA(2\nu_2)$, along with measured and simulated $IA(\nu_1)/IA(2\nu_2)$ data as a function of pressure (at $4\times10^{14}$ molecules×cm$^{-3}$) are shown in Figure 2.11. The data show an increase in $IA(\nu_1)/IA(2\nu_2)$ with pressure that appears to be converging, but not yet flat, as the pressure approaches 760 torr. The simulated data assume that the $2\nu_2$ band is in the low-signal limit and that the integrated cross section $S(2\nu_2)$ is independent of pressure. Given the excellent agreement between simulations and experiments for the $\nu_1$ band and the poor agreement for $IA(\nu_1)/IA(2\nu_2)$, it appears this assumption is not valid. It is likely that the $2\nu_2$ band, like the $\nu_1$ band, has rovibrational structure that leads to CRDS fitting errors and a pressure dependent apparent cross section. As a result, we have scaled $IA(\nu_1)/IA(2\nu_2)$ assumed in limit of infinite pressure for the simulations to match the data at 760 torr, where the CRDS error

in $2\nu_2$ should be a minimum. There may still be significant CRDS error in $2\nu_2$ at 760 torr, but it is likely smaller than the 15% our simulations predict for the $\nu_1$ band under these conditions. As a result, we add a 10% uncertainty to the 3% uncertainty in our $IA(\nu_1)/IA(2\nu_2)$ at 760 torr to give $S(\nu_1)/S(2\nu_2) = 44\pm5(2\sigma)$, leading to a $2\nu_2$ integrated cross section of $S(2\nu_2) = 2.68\pm.35(2\sigma)\times10^{-19}$ cm×molecule$^{-1}$.

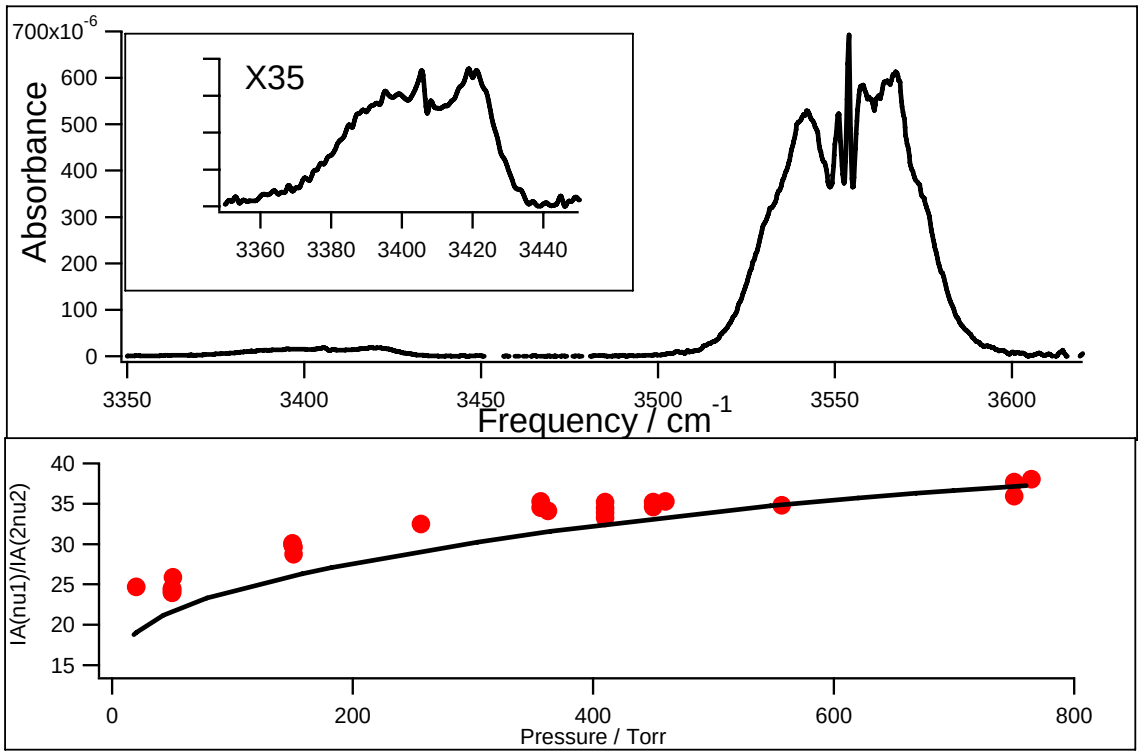


**Figure 2.11. Experimentally measured and simulated $S(\nu_1)/S(2\nu_2)$ a function of pressure; data and simulations are both at 4e14 molecules×cm$^{-3}$. Observed data are shown as diamonds. The line represents simulated data. A representative spectrum used to measure $S(\nu_1)/S(2\nu_2)$ is shown in the top panel.**

We have also observed a third nitric acid band at 3220 cm$^{-1}$. This band was reported previously by Feierabend, Havey and Vaida, but was unassigned [39]. This spectrum of this band along with the $2\nu_2$ is shown in Figure 2.12. The peak at 3220 only has a signal-to-noise ratio of about 8 and has no discernable rovibrational structure. We

measure the ratio of the integrated area of the $2\nu_2$ band to that of this band to be $IA(2\nu_2)/IA(3220) = 7\pm1$, where the uncertainty stems mostly from the uncertainty in the baseline subtraction for the smaller peak. Feierabend et al. report an intensity ratio of 0.029/0.003 = 9.7. If we assume an uncertainty of ±1 in their last reported digits, this ratio is 9.7±3.4. These values agree reasonably well considering the absorbance of this band was near the detection limit in both studies.

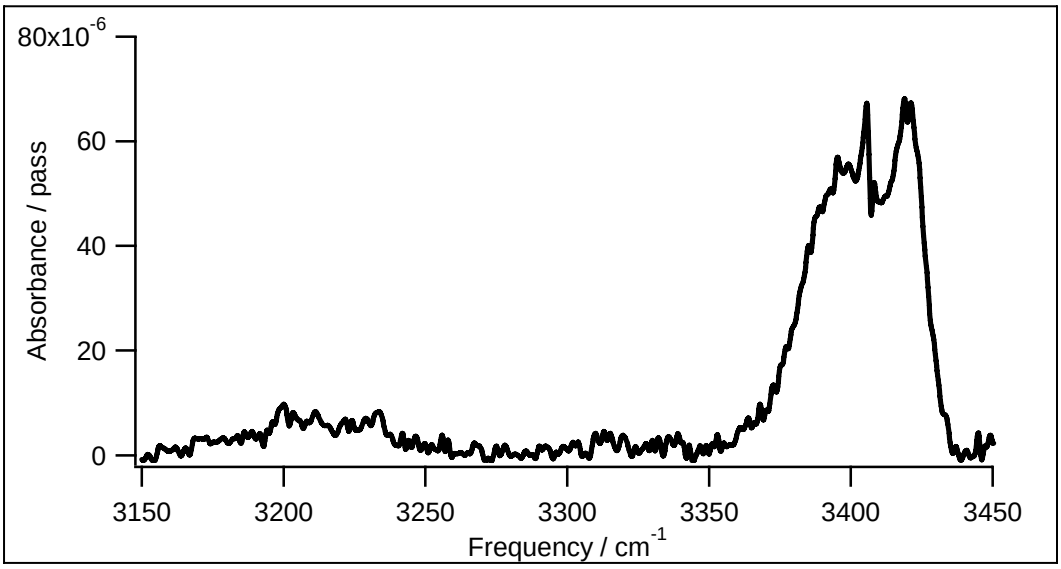


**Figure 2.12. Nitric acid $2\nu_2$ band (3400 $cm^{-1}$) and small unassigned band (3220 $cm^{-1}$).**

While the nitric acid band at 3220 $cm^{-1}$ is quite weak, the high sensitivity of CRDS can magnify the importance of such weak transition. For example, the fitting of HOONO spectra in Chapter 4 was greatly improved once the spectrum shown in Figure 2.12 was used as the nitric acid reference spectrum. Prior to our accounting for the nitric acid peak at 3220 $cm^{-1}$, we consistently had problems fitting the baseline to the red of HOONO.

## 2.3.4 Discussion

### 2.3.4.1 $HNO_3$ $\nu_1$ Cross Section

The previously reported measurements of $S(\nu_1)$ are listed in Table 2.2. The two previously reported experimental measurements differ significantly despite similarities in methods. Both synthesize nitric acid by addition of nitric acid to a nitrate salt and both use static cells, although Chackerian fills the cell with a small quantity of nitric acid and then charges their cell to 1013 hPa, while Lange does their measurements all at less than 100 torr of pure nitric acid. Both use FTIR, although the resolution for Chackerian, 0.112 $cm^{-1}$, is much smaller than the 4 $cm^{-1}$ resolution of Lange. The Chackerian study is a detailed study of many different nitric acid bands and carefully measures impurities in the FTIR and subtracts their contributions from the total pressure. If impurities were contributing significantly to the pressure in the Lange study, this might account for their significantly lower value for the cross section. However, the Lange study includes measurements of integrated cross sections for many other molecules as well as overtones and no systematic error appears over their data as a whole.

**Table 2.2. $HNO_3$ $\nu_1$ integrated intensity measured in this work compared to existing literature data.**

| Study | year | method | integrated intensity / cm molecule$^{-1}$ |
|---|---|---|---|
| this work | 2004 | flow cell IR-CRDS (1 $cm^{-1}$ resolution) | $1.18\pm0.08\times10^{-17}$ |
| Chackerian et al. [22] | 2003 | static cell FTIR (0.112 $cm^{-1}$) | $1.238\pm0.024\times10^{-17}$ |
| Lange et al. [23] | 2001 | static cell FTIR (4 $cm^{-1}$ resolution) | $9.46\pm0.47\times10^{-18}$ |
| Phillips et al. [24] | 1998 | scaling calculated intensities | $1.40\pm0.20\times10^{-17}$ |

The procedure used in this experiment of measuring the nitric acid concentration with UV absorption is unique among the measurements of $S(\nu_1)$. Using a continuous and fairly rapid flow has several advantages, primarily a reduced potential influence of nitric acid decomposing or sticking to the walls of the cell. The main drawbacks of this experiment are the uncertainty in the $l_s$ for the IR absorbance and the uncertainty in the correction for CRDS errors. Our measured value of $1.18\pm08(2\sigma)\times10^{-19}$ cm×molecule$^{-1}$ agrees within 5% with the Chackerian et al. value, but deviates significantly from that by Lange et al. and Phillips et al.

#### 2.3.4.2 $HNO_3$ $2\nu_2$ cross section

There is some discrepancy between the two previous measurements of the nitric acid $2\nu_2$ band. The study by Feierabend et al. does not quote absolute cross sections, but give two values for $S(\nu_1)/S(2\nu_2)$: 38.5 (0.1 cm$^{-1}$ resolution) and 34.5 (1 cm$^{-1}$ resolution). Chackerian et al. report $S(2\nu_2) = 2.82\pm69\times10^{-19}$ cm×molecule$^{-1}$. This, combined with their value for $S(\nu_1)$ yields $S(\nu_1)/S(2\nu_2) = 44\pm10$. While the Chackerian et al. measurement carefully quantified errors in their nitric acid concentration, their uncertainty in $S(2\nu_2)$ is quite high, presumably due to low signal for this band. The Feierabend et al. paper only measures relative band strengths, so errors in the nitric acid concentration cancel, but the difference between their two measurements is on the same order as the uncertainty in the Chackerian et al. ratio.

Since the focus of this study was the nitric acid $\nu_1$ band, only a narrow range of concentrations were probed in which the $2\nu_2$ band was large enough to measure. As a result, similar to the Fierabend et al. paper, we only directly measure $S(\nu_1)/S(2\nu_2)$ and

then extrapolate $S(2\nu_2)$ from our $S(\nu_1)$ measurement. Because we are measuring the ratio, uncertainties in the nitric acid concentration and $l_s$ cancel. Additionally, our $2\nu_2$ signal is quite large at the concentrations studied. Due to our poor understanding of CRDS errors in the $2\nu_2$ band, our measured $S(\nu_1)/S(2\nu_2)$ and $S(2\nu_2)$ have error bars similar in magnitude to the previous measurements. Our measurement, $S(\nu_1)/S(2\nu_2) = 44\pm5(2\sigma)$, agrees with that of Chackerian et al. and is consistent with the higher value reported by Fierabend et al., but not their lower value.

## *2.4 Conclusions*

The experiments and simulations described in this paper show that using low resolution pulsed ringdown to scan congested spectra can retrieve accurate integrated cross sections, but only under certain conditions. In the limit of high pressure and low concentration, our system yields quantitatively accurate measurements of the nitric acid $\nu_1$ integrated cross section to within 5%. If only one of these conditions is met, measured integrated absorbances can still be reasonably close to the true value. At low concentrations all components of the observed multi-exponential are in the fairly long (microsecond) decay regime and the Zalicki and Zare criterion is met for most of the spectrum. We measure integrated absorbances accurate to better than 20% at 20 torr and $[HNO_3]<1.0\times10^{13}$ molecules$\times$cm$^{-3}$. At high pressures, pressure broadening causes the molecular spectrum to become homogeneous and the observed ringdowns are well fit by a single exponential. We measure integrated absorbances accurate to better than 20% at 760 torr even at $[HNO_3]>5.0\times10^{15}$ molecules$\times$cm$^{-3}$.

When neither of these conditions is met, the loss in observed integrated absorbance can be quite dramatic and is strongly concentration and pressure dependent. As shown in Figure 2.9, as concentration increases, the CRDS error increases rapidly and then converges to a constant at high concentrations. We attribute this constant error at high concentrations to a complete loss of contribution from the most intense features in the $HNO_3$ spectrum to the single exponential fit. At a certain point, while the absorbance due to sharp features contribute decays with such fast lifetimes they are completely missed by the single exponential fits, the rest of the spectrum continues to scale linearly with concentration. The concentration at which the CRDS converges and the magnitude of the error at this concentration both depend on pressure. This convergence of the CRDS error leads to the appearance of linearity in $IA(\nu_1)$ as a function of $[HNO_3]$ if all data is taken in the high-concentration limit. This data can be well fit by a line, but with an offset significantly larger than zero.

When making quantitative measurements of congested spectra using low-resolution CRDS, care must be taken to ensure this is not the operating regime. As shown in this study, if a high-resolution spectrum of the feature being investigated is available, it is possible to correct rovibrational spectra taken by low-resolution CRDS and derive accurate absorbances to within 5% through the use of CRDS simulations. However, if a high-resolution spectrum is not available, quantitative measurements should be accompanied by demonstrations that the experiment is being carried out in a regime where such measurements are accurate. We suggest two such demonstrations: (1) Show that the absorbance as measured by CRDS is not only linear with concentration,

but has an intercept very close to zero. (2) Show that the apparent integrated intensity for the band is independent of pressure over a wide range.

The $HOONO/HONO_2$ branching ratio measurements we published in Bean et al. [7] (Chapter 3) recognized that CRDS errors may have impacted measurements of $HONO_2$ absorbances, but had a poor understanding of the magnitude of these errors. We previously assumed $E_{CRDS} = 0.9$, but now estimate for those conditions that $E_{CRDS}$ should be 0.4. This dramatically reduces the reported branching ratio by more than a factor of two. The later CRDS measurements of the $HOONO/HONO_2$ branching ratio (chapter 3) have used the results of this chapter to correct integrated absorbances as a function of concentration and pressure to derive accurate $HOONO/HONO_2$ branching ratios.

# 3 Pressure Dependence of the HOONO/$HONO_2$ Branching Ratio in the Reaction OH+$NO_2$+M; Pulsed Laser Photolysis Studies

## *3.1 Introduction*

The reaction of the reactive hydroxyl (OH) and nitrogen dioxide ($NO_2$) radicals to produce the stable molecule nitric acid ($HONO_2$) plays a critical role throughout the atmosphere. The yield of nitric acid from this reaction is reduced due to a competing minor channel producing peroxynitrous acid (HOONO).

$$OH + NO_2 + M \xrightarrow{k_{1a}} HONO_2 + M \qquad \text{Reaction 3.1a}$$

$$OH + NO_2 + M \xrightarrow{k_{1b}} HOONO + M \qquad \text{Reaction 3.1b}$$

An introduction to the importance of these reactions in the atmosphere can be found in chapter 1.

Appendix A describes the absorption spectroscopy of HOONO and first direct measurement of the branching ratio $k_{1b}/k_{1a}$. This was my first project as a graduate student. While those results were a significant contribution to our understanding of reaction 3.1, the discharge flow method used to generate OH radicals suffered some significant drawbacks: (1) the impact of collisions with the reactor wall and secondary chemistry were unknown, (2) the gas composition was predominantly He and therefore did not reflect our atmosphere, and (3) measurements could only be made at pressures below 40 torr. As a result, while the branching ratio measured with the discharge-flow apparatus help constrain the HOONO yield in the low-pressure limit, the yield under conditions relevant to the lower atmosphere remained highly uncertain.

### 3.1.1 HOONO: What Do We Know?

HOONO has been a molecule of considerable interest to the physical chemistry community over the past two decades. This stems from the potential atmospheric impact of a significant HOONO yield, but also from the complexity the multiple conformers and intramolecular hydrogen bond give to its potential energy surface and spectroscopy. As a result, HOONO has now been studied from many different angles: *ab initio* calculations, condensed phase spectroscopy [40-43], gas phase vibrational spectroscopy (fundamental and overtones, jet cooled and room temperature), rotational spectroscopy, biexponential $OH + NO_2$ kinetics, and statistical rate modeling.

Taking the literature data set as a whole, portions of the ground state potential energy surface connecting $OH + NO_2$, $HONO_2$, HOONO, and $HO_2 + NO$ can now be described in considerable detail (Figure 3.1). Unless otherwise specified, all stated energies are relative to $OH + NO_2$.

The most accurate measurement of the HOONO binding energy comes from the jet-cooled action spectroscopy conducted in Marsha Lester's group at the University of Pennsylvania. By measuring the overtone spectrum of *trans-perp* HOONO and the internal energy of the OH dissociation fragments, they measured the dissociatioin energy of *trans-perp* HOONO to be -16.2±0.1 kcal $mol^{-1}$ [44].

The dissociation energy of *cis-cis* HOONO has also been estimated experimentally. Matthews and Sinha, working with *cis-cis* HOONO at room temperature, measured the OH rotational distributions using action spectroscopy. From this, they measured $D_0$ (*c-c*) = -19.9±0.5 kcal $mol^{-1}$ [45]. In a similar experiment, McCoy et al. found the OH quantum yield in the action spectroscopy of the *cis-cis* HOONO $2\nu_1$

band to be consistent with $D_0$ (*c-c*) = -19.6 kcal $mol^{-1}$ [46]. In a very different experiment, Hippler et al. analyzed observed bi-exponential OH decays to derive equilibrium constants for *cis-cis* HOONO. From this they estimated $D_0$(*c-c*) = -19.2±0.5 kcal $mol^{-1}$ [47]. *Ab initio* calculations of the *cis-cis* HOONO dissociation energy, even at high levels of theory, vary from 18.4 to 19.8 kcal $mol^{-1}$ [48-51]. These calculations are further complicated by errors in the calculated enthalpies of OH and $NO_2$. A more consistent and accurate *ab initio* result is the energy of the *trans-perp* isomer relative to *cis-cis* HOONO, calculated to be $\Delta H^0(0) = 3.4$ kcal $mol^{-1}$ [7, 51]. This can be combined with the measured *trans-perp* dissociation energy to yield $D_0$ (*c-c*) = -19.6 kcal $mol^{-1}$.

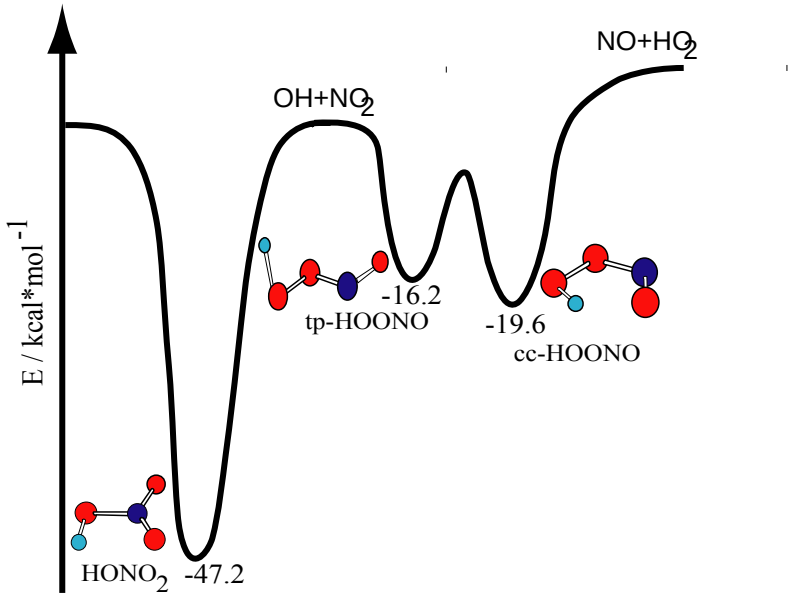


**Figure 3.1. Potential energy surface for the reaction of OH + $NO_2$ + M. Energies are in reference to OH + $NO_2$ and corrected for zero-point energy. *trans-perp* HOONO energy from Konen et al. [44]. *cis-cis* HOONO energy from calculated ΔH(0) relative to *trans-perp* HOONO.**

One prolonged debate in the HOONO community has surrounded the possible third stable conformer, *cis-perp* HOONO. While initial *ab initio* predicted this geometry to be a stable conformer [52] subsequent calculations at higher levels of theory indicated

that the *cis-perp* HOONO minimum may [51] or may not [7, 49] be a stable minimum on the potential energy surface. Infrared spectra of HOONO trapped in Ar matrices by Y. P. Lee's group contained bands corresponding to *trans-perp* and *cis-cis* HOONO, but not *cis-perp* [43]. While *cis-perp* HOONO is likely not a stable minimum on the potential surface, there is considerable evidence that *cis-perp*-like geometries are accessed through the torsional excitation of *cis-cis* HOONO [45, 46, 53, 54]. This will be discussed in more detail in Section 3.1.3.

The only experimental determination of the *trans-perp* to *cis-cis* isomerization barrier was made by measuring the temperature-dependent disappearance of *trans-perp* HOONO using overtone action spectroscopy [55]. This barrier was measured to lie 7.9±2.9 kcal $mol^{-1}$ above *trans-perp* HOONO; in agreement with *ab initio* calculations of 9.6-10.8 kcal $mol^{-1}$ [49, 52, 55-57]. The *trans* to *cis* isomerization barrier is thus 6-7 kcal $mol^{-1}$ below the dissociation energy and so the dominant fate of *trans-perp* HOONO should be isomerization to the *cis-cis* conformer.

It should be noted that a recent RRKM master equation modeling study has challenged this conclusion, suggesting that instead *trans-perp* HOONO may have a concerted mechanism to isomerize preferentially to nitric acid [58]. It was hypothesized that a low-energy barrier was necessary to account for recent experimental observations of nitric acid formation from the reaction $HO_2$ + NO. *Ab initio* studies have consistently been unable to find such a low-energy transition state. Calculalted transition states for concerted isomerization of *trans-perp* HOONO to $HONO_2$ instead lie 12.5-14 kcal $mol^{-1}$ above the barrier for isomerization to *cis-cis* HOONO (1.5-3 kcal $mol^{-1}$ above dissociation to OH + $NO_2$) [48, 56, 57].

With the potential energy surface shown in Figure 3.1, we can begin to tell the story of the reaction 3.1. The initial interaction forms both [HOONO]* and [$HONO_2$]* with considerable internal energy. Under atmospheric conditions, most of these nascent molecules re-dissociate before they can be stabilized by collisions with a third body. Due to its larger binding energy, [$HONO_2$]* has a longer lifetime and reaction 3.1a dominates. At higher pressures, as the rate of collisions with a third body increases, the relative HOONO yield will increase.

Collisionally stabilized [HOONO]* initially fall into the wells corresponding to the various HOONO conformers. At very low (200 K) temperatures, these various conformers can be stable long enough to be observed. At room temperature, however, all HOONO molecules are predicted to isomerize to the lowest-energy *cis-cis* conformer on the timescale of ≈300 μs even at 20 torr [7, 55].

*Cis-cis* HOONO then undergoes unimolecular decomposition back to OH + $NO_2$ with a time constant on the order of 1 s in the lower troposphere. Because HOONO is likely to be re-dissociate to OH and $NO_2$ and has a much shorter lifetime than $HONO_2$, production of HOONO by reaction 3.1b reduces the efficiency of reaction 3.1 to sequester $HO_x$ and $NO_x$. This leads us back to our need to know the branching ratio for reaction 3.1 under atmospheric conditions.

There have been several previous measurements and calculations of the branching ratio, but only at conditions quite removed from those found in the atmosphere. At very high temperatures and pressures the HOONO dissociation lifetime is much shorter. This has been observed in the form of bi-exponential OH decays by the Hippler and Hynes groups [47, 59, 60]. These decays can then be fit to extract the rate constants $k_{1a}$ and $k_{1b}$

as well as the equilibrium constant $K_{1b}$. Hippler et al. measured $k_{1b}/k_{1a} = 0.15$ at 430 K and 5 bar He, with a HOONO dissociation rate of 20 μs [60]. D'Ottone et al. measured $k_{1b}/k_{1a} = 0.10\pm0.03$ at 413 K and 400 torr He, with a HOONO dissociation rate of 200 μs [59].

At lower temperatures, there have also only been a few estimates of the branching ratio, all at very low pressures. Donahue et al. measured the rate of $^{18}OH$ scrambling in the OH + $NO_2$ reaction. From this, they estimated the branching ratio in the low-pressure limit to be $k_{1b}/k_{1a} = 0.17$ [61]. Nizkorodov and Wennberg in their first spectroscopic detection of HOONO estimated a HOONO yield of 5±3% at 253 K and 20 torr [62]. The only direct measurement of the reaction 3.1 branching ratio remains those made by cavity ringdown spectroscopy as described in appendix A [7]. The published branching ratio has been revised (see section 3) to $k_{1b}/k_{1a} = 0.048\pm0.013$ at 298 K and 14 torr. While not a laboratory experiment, a recent time-dependent capture theory calculation produced a branching ratio of $k_{1b}/k_{1a} = 0.051$ at 20 torr and 300 K and produced a similar temperature-dependence to that shown in our early discharge-flow experiments [63].

Several studies have calculated values of the branching ratio [47, 49, 58, 63-67]. Early calculations, either pure RRKM calculations or RRKM calculations modified to fit the existing data, produced widely varying estimates of the branching ratio at 1 atm: >1% [66], 2.5% [67], and 30% [65]. More recent calculations that take advantage of the more detailed knowledge of the potential energy surface and new additions to the kinetics data set, are more consistent. The results of Golden et al. and Hippler et al. along with other branching ratio determinations below 1 atm are shown in Figure 3.2. We see that, with

the exception of the Donahue et al. value, the qualitative agreement is reasonable, but there remains a dearth of experimental data on the branching ratio in this pressure range.

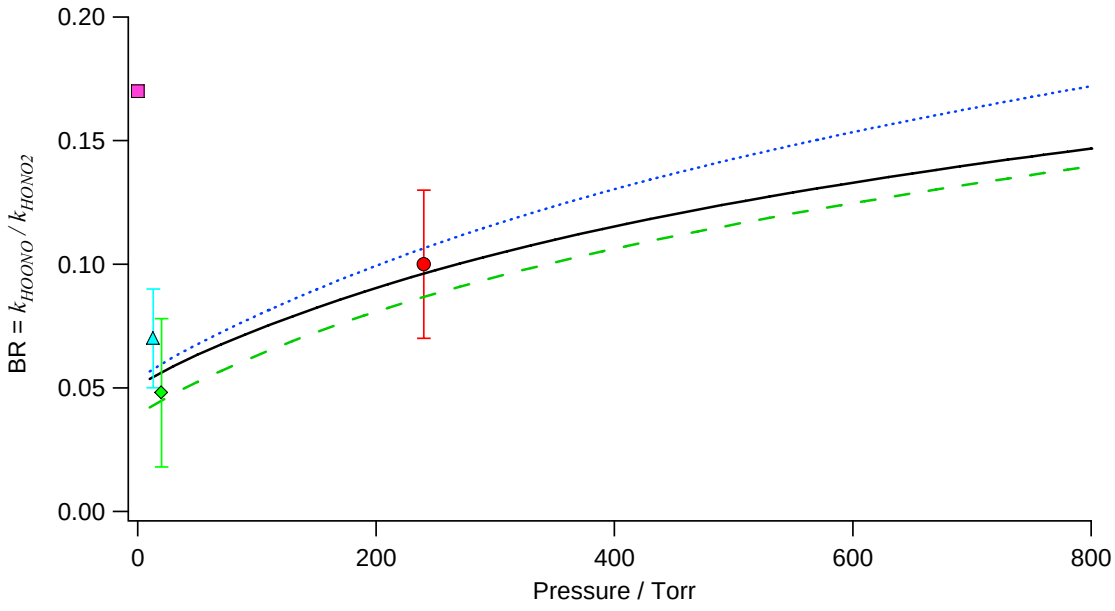


**Figure 3.2. Calculated and measured values of the branching ratio below 1 atm. Hippler (green dashed line), Golden (dotted line), the JPL 2006 recommendation (solid line), Donahue (pink square), Nizkorodov (green diamond), D'Ottone (red circle), and Bean (blue triangle). Experimental pressures from Bean and D'Ottone have been scaled to reflect an effective $N_2$ pressure. No corrections have been made for temperature.**

The NASA-JPL 2006 kinetics data evaluation (also shown in Figure 3.2) recommends rate constants that yield branching ratios between those of Golden and Hippler. The IUPAC kinetics data evaluation still contains no recommendation for the inclusion of reaction 3.1b.

### 3.1.2 Branching Ratio Pressure Dependence

It was shown in Bean et al. that *cis-cis* HOONO can be detected using infrared cavity ringdown spectroscopy (CRDS) [7]. The infrared spectra of HOONO and $HONO_2$ can then be used to measure the branching ratio $k_{1b}/k_{1a}$. Those measurements were limited to low pressures by the microwave discharge used to generate OH radicals. Thus,

the main challenge in extending branching ratio measurements to higher pressures was the development of a method for the generation of OH radicals at pressures up to 1 atm. This was accomplished through the use of a coupled laser photolysis-CRDS apparatus.

OH radicals were produced by the photolysis of ozone to produce excited-state oxygen atoms $O(^1D)$ in the presence of hydrogen or methane. After allowing complete reaction with $NO_2$, IR spectra of the products were recorded with CRDS. The branching ratio was then measured by integrating the $\nu_1$ OH-stretch bands of *cis-cis* HOONO and $HONO_2$ and converting these to product concentrations with *ab initio* ratio of cross sections.

By generating OH radicals through laser photolysis, reaction 3.1 could be initiated over a wide range of pressures up to 1 atm. While the generation of product by photolysis decreased our overall signal by reducing the sample path length, this technique had several major advantages over microwave discharge: (1) Products were measured in a mostly nitrogen environment, more closely resembling the atmosphere. (2) Products were probed shortly after they are produced (100 μs) to minimize the influence of secondary chemistry. (3) Products were formed and probed in the center of the cell, minimizing the impact of wall reactions. (4) The product spectrum and the background were collected simultaneously, eliminating uncertainty due to changes in mirror properties. The most significant advantage of the laser photolysis method, however, is that it allowed access to a much wider range of pressures.

We therefore measured the pressure-dependence of the HOONO yield from reaction 3.1 from 20 to 760 torr and report the first measurement of the HOONO yield from reaction 3.1 at 1 atm.

### 3.1.3 Stretch-Torsion Coupling

A critical step in our branching ratio measurements was the integration of the *cis-cis* HOONO $\nu_1$ band. This was accomplished by fitting the observed product spectrum with reference spectra for HOONO, HONO, and $HONO_2$. The reference spectrum used to fit the *cis-cis* HOONO band is shown in Figure 3.3. This spectrum was generated during the discharge-flow studies by subtracting the $2\nu_2$ bands of *cis*- and *trans*-HONO from the observed product spectrum [7]. The HONO subtraction on the blue side was difficult and, for lack of a better option, the spectral profile used for integration was assumed to be linear for the R-branch edge. The resulting band shape was clearly asymmetric, with appreciable intensity spread to the blue.

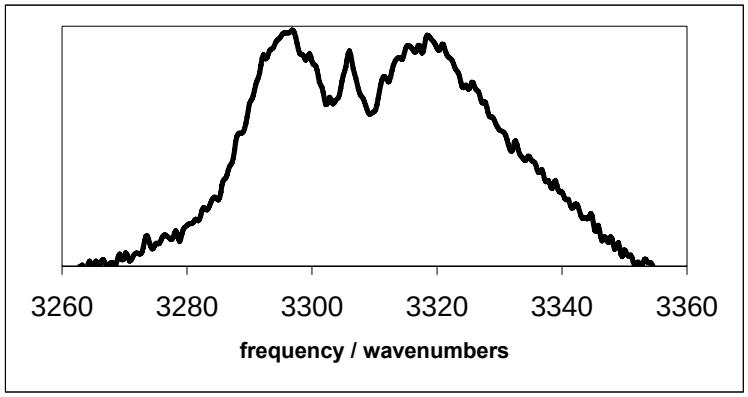


**Figure 3.3. *Cis-cis* HOONO spectrum used to fit experimental data.**

Originally, the blue shading in the spectrum was assumed to be the result of two processes: (1) intramolecular hydrogen bond tightening in the vibrationally excited state leading to a more compact geometry and slightly larger upper state rotational constants and (2) population in low-frequency vibrational modes such as the *a″* HOON torsion ($\nu_9$), the *a″* ONOO torsion ($\nu_8$), and the *a′* NOO bend. In particular, excitation of the HOON

torsion would be expected to break the intramolecular hydrogen bond and lead to substantially shifted sequence bands. Any shifts in spectral intensity larger than 30-40 $cm^{-1}$ would have been obscured by spectral interference of the HONO and $HONO_2$ bands. As a result, we were concerned that *cis-cis* HOONO integrated absorbance obtained with the spectral shape shown in Figure 3.3 may under-represent the total $\nu_1=1\leftarrow0$ absorption.

As mentioned above, the coupling of the OH stretch to the HOON torsion has been studied previously [45, 46, 54, 68]. The action spectrum of the $2\nu_1$ band of *cis-cis* HOONO has an unusual shape, with a large amount of intensity in bands blue-shifted from the band origin. The blue-shifted bands could be understood through coupling of the HOON torsion to the OH stretch. The overtone spectrum was simulated by calculating the two-dimensional *ab initio* potential energy and dipole moment surfaces for *cis-cis* HOONO as functions of the HOON torsional angle and OH bond length. The calculated minimum-energy potential as a function of the HOONO torsional angle showed a shelf that opened up about 700 $cm^{-1}$ above the zero-point energy (Figure 3.4). This shelf leads to a pileup of torsional states in the 700-800 $cm^{-1}$ energy region. The wave functions of these states lead to geometries with the OH predominantly out of the plane. As a result, $2\nu_1$ transitions from these excited torsional states lead to absorptions that are significantly blue-shifted and more intense than absorptions from the ground state.

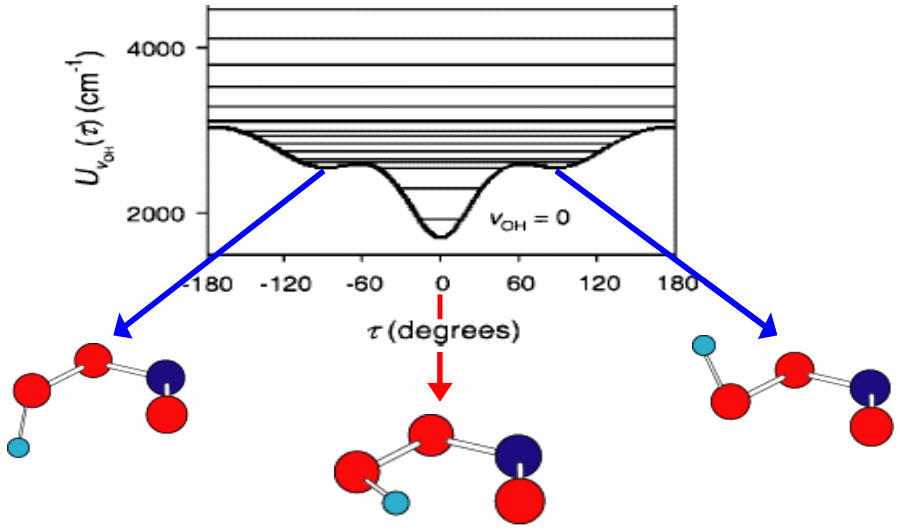


**Figure 3.4. Vibrationally adiabatic potential energy surface as a function of the HOON torsion angle. The location of $\nu_9$ states are shown as lines. Adapted from [46].**

The two-dimensional calculations also yielded a predicted spectrum for the $\nu_1$ fundamental. The impact of this shelf upon the fundamental OH stretch was predicted to be much less than that for the overtone, but still led to a prediction that 25% of the *cis-cis* HOONO absorption intensity may be blue-shifted outside of our reference spectrum. These calculations only considered one of the low-frequency modes of *cis-cis* HOONO. To better understand the positions and frequencies of important sequence bands, we felt it necessary to repeat these calculations including both low-frequency torsional modes.

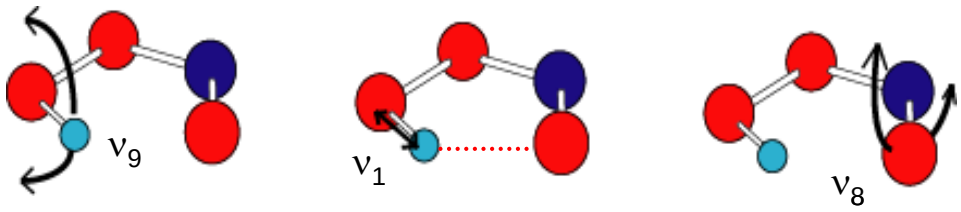


**Figure 3.5. *cis-cis* HOONO vibrational bands: OH stretch ($\nu_1$), HOON torsion ($\nu_9$) and ONOO torsion ($\nu_8$). The intramolecular hydrogen bond (red dashed line) red-shifts the OH stretch.**

If we picture the most stable planar *cis-cis* HOONO geometry and the HOON and OONO torsional motions (Figure 3.5) we would expect both torsions to influence the

intramolecular hydrogen bond and for the two modes to be coupled. Additionally the two-dimensional results of McCoy et al. and Matthews et al. agree qualitatively but obtain different energies for the lowest HOON torsional state. McCoy et al., who froze the ONOO into a planar arrangement, calculate 382 $cm^{-1}$, while Matthews et al, who let the heavy atoms relax in their calculations, calculate 290 $cm^{-1}$. This is a fairly large difference, indicating that the heavy atoms have a significant impact on the details of the HOONO potential and the OH stretch.

To better understand the influence of the two torsional modes and their coupling on the fundamental OH stretch spectrum of *cis-cis* HOONO, we calculated the 3D *ab initio* potential energy surface for HOONO surrounding the *cis-cis* minimum as functions of the HOON torsional angle ($\nu_9$), ONOO torsional angle ($\nu_8$), and OH bond length ($R_{OH}$). By calculating a potential energy surface of HOONO with enough detail, we aimed to derive the energies of the low-frequency torsional modes associated with the $\nu_1$=0 and $\nu_1$=1 states to the highest accuracy possible. From these energies the frequencies and relative intensities of sequence bands can be calculated and the *cis-cis* HOONO absorption intensity that falls outside our assumed band shape can be calculated and corrected for.

In support of these calculations, we also re-measured the HOONO spectrum. With improved HONO and $HONO_2$ reference spectra, we have tried to resolve spectral features corresponding to torsionally excited HOONO transitions.

## 3.2 Experimental Methods

### 3.2.1 Generation of Reactants

Spectra were taken in a reaction flow cell combining UV excimer laser photolysis for production of radicals and IR-CRDS for the detection of products. A schematic of the experimental apparatus is shown in Figure 3.6.

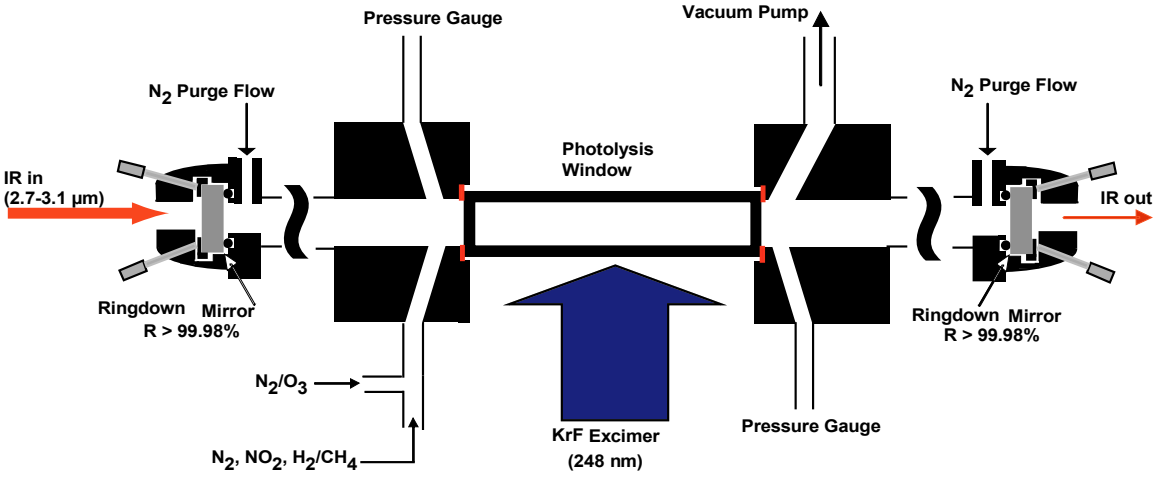


**Figure 3.6. Photolysis/CRDS flow cell. Length of the photolysis cells were 3.6, 6.0, and 12.0 cm. Typical photolysis beam width was 2 mm.**

The design uses a rectangular photolysis cell coupled on both ends to Teflon blocks. These blocks provide feed throughs for gas inputs, a pump out port and pressure gauges, and they serve to link the photolysis cell to the ringdown mirrors. Dimensions and assembly of the photolysis cells are described in appendix B. We initiated the reaction $OH + NO_2 + M$ via the following reaction scheme.

$$O_3 + h\nu(248\ nm) \rightarrow O(^1D) + O_2 \qquad \text{Reaction 3.2}$$
$$O(^1D) + H_2 \rightarrow OH + H \qquad \text{Reaction 3.3}$$
$$H + NO_2 \rightarrow OH + NO \qquad \text{Reaction 3.4}$$
$$OH + NO + M \rightarrow HONO + M \qquad \text{Reaction 3.5}$$
$$OH + NO_2 + M \rightarrow HONO_2 + M \qquad \text{Reaction 3.1a}$$
$$\rightarrow HOONO + M \qquad \text{Reaction 3.1b}$$

While this overall reaction scheme was an efficient and clean way to make OH with few unwanted by-products, it required a system free of $O_2$ to prevent the rapid formation of $HO_2$ from the H atoms produced in reaction 3.3. As a result, the branching ratio measurements were all done in a gas mixture of mostly $N_2$ (>90%) with the remainder essentially all $H_2$.

While these measurements could not be carried out in air, the branching ratio is not expected to have a significant dependence upon the nature of the bath gas. In particular, the lack of $O_2$ in our gas mixtures should have a minimal effect on the branching ratio due to the similar collision efficiencies, $\beta$, of $N_2$ and $O_2$. The presence of a significant fraction of $H_2$ in our measurements does impact the branching ratio, due to the much lower collision efficiency of $H_2$. A first-order correction for this was made by calculating an effective pressure for each experiment,

$$P_{\text{effective}} = P_{\text{baratron}} \times \left( f_{N_2} \beta_{N_2} + f_{H_2} \beta_{H_2} \right),$$

where $f_{N2}$ and $f_{H2}$ are the fractions of total flow consisting of $N_2$ and $H_2$ respectively. For this calculation we assumed the collision efficiency for $H_2$ to be that given by Golden et al. for He, $\beta_{H2}/\beta_{N2}$=0.4 [49]. This correction had the largest impact on data taken at low pressures, when the fraction of $H_2$ was highest.

Both reaction 3.3 and reaction 3.4 are known to produce OH with a high degree of vibrational excitation. As a result, some experiments were carried out with the OH production from the reaction

$$O(^1D) + CH_4 \rightarrow OH + CH_3. \qquad \text{Reaction 3.3b}$$

It was assumed that the collision efficiency of $CH_4$ was the same as for $N_2$.

Ozone was delivered to the cell by flowing nitrogen through silica gel saturated with ozone. Ozone was generated by an ozonizer (Osmonics V10-0) and collected by flowing through a U-tube containing silica gel (6-12 mesh) kept at -78 $^0$C. Silica gel saturated with ozone turned deep purple. Filling the trap could be accomplished in under an hour. Ozone was then delivered to the cell by flowing nitrogen through the silica gel trap still at -78 $^0$C. The trap was always kept at about 1 atm with a needle valve after the trap. The ozone concentration would stabilize after 10-15 min as an equilibrium between ozone diffusion within the silica gel and the nitrogen flow was established. If the flow through the trap and the cold bath were left undisturbed, a constant flow of 300 sccm containing about $1\times10^{17}$ molecules$\times$cm$^{-3}$ could be sustained for over 12 hours. To prevent ozone from reaching our mechanical pump, an ozone scrubber was inserted into the vacuum line. The scrubber consisted of approximately two feet of 1-inch tubing filled with copper mesh and heated to >100 $^0$C.

Hydrogen and methane were introduced as pure gas flows. $NO_2$ was introduced as a 4% mixture in nitrogen (Matheson). All reactant gases and a nitrogen dilution flow were mixed in a glass cross about 5 cm from the photolysis region. All gas flows were through mass flow transducers (Edwards Model 831 and Omega Model 1700) calibrated volumetrically so that final concentrations in the photolysis cell could be calculated. Typical concentrations used for the pressure-dependent measurements are listed in Table 3.1.

**Table 3.1. Concentrations used in $HOONO/HONO_2$ branching ratio measurements.**

| Gas | Concentration range / molecules×$cm^{-3}$ |
|---|---|
| $O_3$ | $(1\text{-}10)\times10^{15}$ |
| $NO_2$ | $(1\text{-}10)\times10^{16}$ |
| $H_2$ / $CH_4$ | $(1\text{-}10)\times10^{17}$ |
| $N_2$ | balance to pressure |

Photolysis was initiated with the 248 nm pulse from a KrF excimer laser. The output beam was a slightly diverging 1 cm × 2.5 cm rectangle. The excimer beam was sent through a +50 cm focal-length cylindrical lens and -30 cm focal-length circular lens such that the beam entering our cell matched the width of our photolysis window on the long axis of the beam and 2-5 mm along the short axis. The laser flux was varied over the range $1\text{-}50\times10^{15}$ photons $cm^{-2}$ to test for any possible dependence of the measured branching ratio on the photolysis energy.

### 3.2.2 Detection of Products

Absorption spectra of the reaction products were recorded by pulsed cavity ringdown spectroscopy. The details of our CRDS apparatus have been described in detail in Chapter 1 and will only be described briefly here. A mid-infrared laser pulse (2.7-3.3 μm) was injected into an optical cavity made by two high-reflectivity infrared mirrors (R=99.98%). Spectra of reaction products were typically recorded by scanning the spectral region of interest alternating 16 shots with the excimer on and then 16 shots with the excimer off and then subtracting the two. This subtraction eliminated background due to species present in the absence of reaction, as well as to the wavelength-dependent

ringdown loss of the mirrors. By comparing the ringdown lifetime with and without the photolysis laser, the absorbance of the photolysis products was measured,

$$A = \frac{L_{cav}}{c}\left(\frac{1}{\tau_{\text{Photolysis}}} - \frac{1}{\tau_0}\right),$$

with a minimum-detectable absorbance of $A = 10^{-6}$. The frequency of the infrared laser was then scanned over the fundamental $v_1$ (OH stretch) spectral region to obtain the partially rotationally-resolved spectra of HOONO (3306 $cm^{-1}$) and $HONO_2$ (3350 $cm^{-1}$) as well as the by-product nitrous acid (HONO, 3275 $cm^{-1}$ and 3370 $cm^{-1}$). The production of HONO from reaction 3.6 was unavoidable, but did not impact our ability to integrate the HOONO and $HONO_2$ spectra.

It should be stated that, unlike the absolute measurements described in Chapter 2, these experiments only require accurate *relative* absorbances. The mirror-to-mirror length and path length occupied by the sample therefore did not influence our results since these values were the same for both HOONO and $HONO_2$. As a result, data analysis was conducted using the raw data values of $1/\tau$ rather than the true absorbance. Where appropriate, data will be shown in units of "absorbance per pass," but this was an unnecessary step that was omitted in the general data analysis.

### 3.2.3 3D Potential and Energy Levels

These calculations have primarily been the work of Matthew Sprague and Anne McCoy and will only be described briefly here. Optimized geometries and energies were calculated by Sprague at various geometries using the GAUSSIAN98 and 2003 programs [69]. A 3D potential energy surface was computed in two steps. First a fully-optimized

2D surface over the HOON torsional angle ($\tau_9$) and OONO torsional angle ($\tau_8$) was computed in which the torsional angles were held fixed while all other angles and all bond lengths were allowed to relax. Second, for each pair of torsional angles, single-point energy calculations were run at various values of the OH bond length.

In order to decrease the time required for each calculation, the geometries were optimized in a sequence of progressively more costly levels of theory and basis sets. The initial optimization was done with Møller-Plesset perturbation theory truncated at second order with correlation consistent polarized double ζ basis set (MP2/cc-pVDZ). The geometry from this calculation was then re-optimized at coupled cluster doubles level of theory with the same basis set (CCD/cc-pVDZ) and then re-optimized again at coupled cluster with singles and doubles with perturbative triples level of theory (CCSD(T)/cc-pVDZ), and again with the larger consistent polarized triple ζ basis set (CCSD(T)/cc-pVTZ). This final geometry was then used for energy calculations done at the CCSD(T)/cc-pVTZ level of theory/basis set.

These calculations were run at many different geometries to generate a two-dimensional minimum energy potential as a function of $\tau_9$ and $\tau_8$. Since the final level of theory was the same as used in McCoy et al., their results for $\tau_8$=0° were used. The values of $\tau_9$ and $\tau_8$ were selectively chosen to help map out critical areas of the potential with a minimum of points, as the calculations were quite time consuming. For each optimized geometry, single-point energy calculations were carried out as the OH bond length ($R_{OH}$) was varied about its minimum-energy length ($R_{min}$). $R_{OH}$ was varied from $R_{min}$-0.15 Å to $R_{min}$+0.25 Å at 0.05 Å intervals. All other angles and bond lengths were

held constant and the calculations were performed at the same CCSD(T)/cc-pVTZ level of theory as the final geometry optimization.

All of the calculated energies were then given to Anne McCoy for further analysis. The single-point energies were used to calculate a three-dimensional analytical potential energy surface, fitting to an expansion of the three coordinates, $\tau_9$, $\tau_8$, and $R_{OH}$, 79 terms in all. The $R_{OH}$-dependence was expressed as a quartic expansion in $(1-\exp(-\alpha * \Delta R_{OH}))$; the angular dependence was fit to a high-order expansion in $(1-\cos\tau)$ and the explicit HOON torsion dependence of the effective mass associated with the HOON torsion as a function of $R_{OH}$ was included.

McCoy then used this three-dimensional potential energy surface to solve the Schrödinger equation in the vibrationally adiabatic approximation, separating $\nu_1$ from $\nu_8$ and $\nu_9$, to obtain the frequencies of the torsional states of *cis-cis* HOONO with $\nu_1$=0, $\nu_1$=1, and $\nu_1$=2. The wave functions associated with each of these states were also generated.

This study has not yet been finished. Several calculations of energies and the final 3D potential energy surface remain incomplete. While the results presented here should be treated as preliminary, they include all of the points that will be calculated near the bottom of the well. Since the Botzmann correction factor derived below is dominated by these states, I expect the future refining of the potential energy surface to have only a small impact on this result.

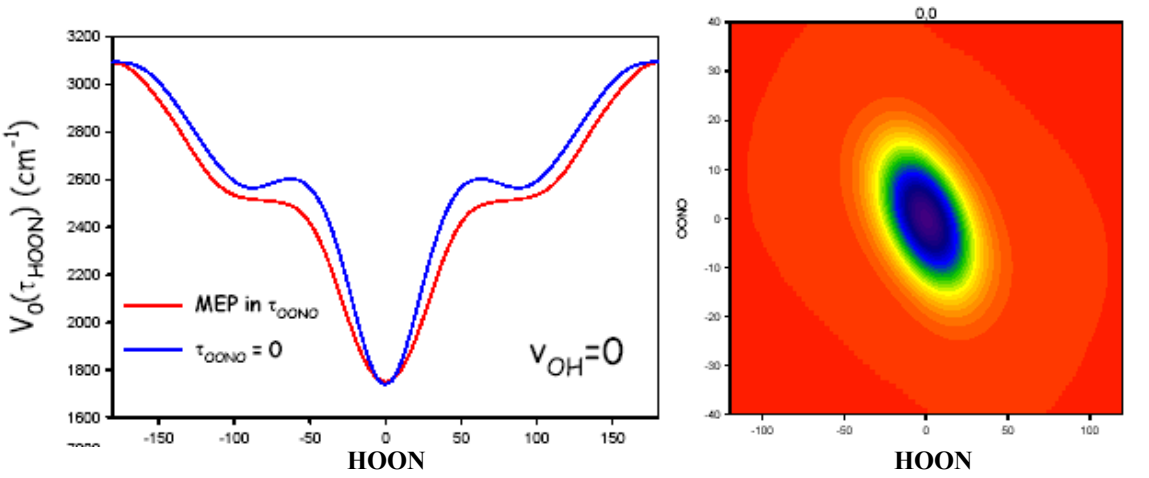


**Figure 3.7. The 2D potential energy surface for HOONO as a function of the OONO (vertical) and HOON(horizontal) torsional angles. Red is high energy and purple is low. The 1D potential of the HOON torsion along the minimum-energy path is also shown and compared to the 1D potential obtained with the OONO torsion fixed at 0.**

The ground state wavefunction and the one-dimensional adiabatic potential along the minimum energy path are shown in Figure 3.7. We see that the two torsional modes are clearly coupled, leading to a shift in the ground state wave function to lie along the diagonal between the two torsions (this effect is exaggerated by the plot shown, since the axes are on different scales). We see that the one-dimensional potential along the minimum energy path is significantly wider and has its shelf at slightly lower energy than that obtained by holding the OONO torsion at 0. The expected result of this is that the $\nu_9$ states will be shifted to lower energy and the pileup of states at the shelf will also be at slightly lower energy.

The calculated frequencies for the two states of interest to our measurements, $\nu_1$=0 and $\nu_1$=1 are shown in Table 3.2. The assignments were made based on the wavefunctions and the average kinetic energy of each torsion.

**Table 3.2. Calculated torsional states of *cis-cis* HOONO. The relative ground-state populations at 298 K and the v1=0→1 transition frequencies associated with each state are also shown. Energies and frequencies are both given in $cm^{-1}$.**

| | | $\nu_{OH}=0$ | | | $\nu_{OH}=1$ | | | |
|---|---|---|---|---|---|---|---|---|
| **n-HOON** | **n-OONO** | **energy** | **E-ZPE** | $P_{Rel}$ | **energy** | **E-ZPE** | **transition freq** | **blue shift** |
| 0 | 0 | 2174.19 | 0.00 | 1.000 | 5546.25 | 0.00 | 3372.06 | 0.00 |
| 1 | 0 | 2481.65 | 307.45 | 0.227 | 5897.99 | 351.74 | 3416.35 | 44.29 |
| 0 | 1 | 2659.93 | 485.74 | 0.096 | 6046.14 | 499.89 | 3386.21 | 14.15 |
| 2 | 0 | 2687.65 | 513.46 | 0.084 | 6174.41 | 628.16 | 3486.76 | 114.71 |
| 3 | 0 | 2767.79 | 593.60 | 0.057 | 6314.99 | 768.74 | 3547.19 | 175.14 |
| 4 | 0 | 2827.44 | 653.25 | 0.043 | 6396.30 | 850.05 | 3568.86 | 196.80 |
| 5 | 0 | 2924.94 | 750.75 | 0.027 | 6472.36 | 926.11 | 3547.42 | 175.36 |
| 1 | 1 | 2940.52 | 766.33 | 0.025 | 6358.44 | 812.19 | 3417.92 | 45.86 |
| 6 | 0 | 3022.74 | 848.55 | 0.017 | 6572.06 | 1025.81 | 3549.32 | 177.26 |
| 2 | 1 | 3094.61 | 920.42 | 0.012 | 6611.61 | 1065.36 | 3517.00 | 144.94 |
| 0 | 2 | 3122.12 | 947.92 | 0.010 | 6529.22 | 982.97 | 3407.10 | 35.04 |
| 7 | 0 | 3132.87 | 958.68 | 0.010 | 6679.30 | 1133.05 | 3546.43 | 174.37 |
| 3 | 1 | 3163.90 | 989.71 | 0.008 | 6712.07 | 1165.83 | 3548.17 | 176.11 |
| 3 | 2 | 3229.19 | 1055.00 | 0.006 | 6771.08 | 1224.83 | 3541.88 | 169.82 |
| 8 | 0 | 3237.30 | 1063.11 | 0.006 | 6794.21 | 1247.96 | 3556.91 | 184.85 |
| | ? | 3319.54 | 1145.35 | 0.004 | | | | |
| 9 | 0 | 3343.60 | 1169.41 | 0.004 | | | | |
| | ? | 3379.65 | 1205.46 | 0.003 | | | | |
| | ? | 3412.30 | 1238.11 | 0.003 | | | | |
| | ? | 3422.77 | 1248.58 | 0.002 | | | | |

I have used these frequencies to generate a simulated room temperature spectrum of the *cis-cis* HOONO OH-stretch coupled to the two torsional modes. Frequencies of transitions from levels containing quanta in $\nu_8$ or $\nu_9$ were obtained by comparing the frequencies of these states in $\nu_1$=0 and $\nu_1$=1. The Boltzmann populations of these states were calculated to weight the various transitions. The populations and frequencies were then combined to generate a simulated spectrum and calculate what percentage of the $\nu_1$ band was blue-shifted outside of the HOONO spectrum used for fitting.

A careful experimental investigation of the HOONO band profile was also conducted to search for features characteristic of torsionally excited HOONO. Three scans were taken covering the range 3245-3445 $cm^{-1}$ in 0.2 $cm^{-1}$ step sizes. Scans were taken at 250 torr and room temperature. An attempt was made to minimize the HONO produced by reducing the concentrations of $H_2$ and $O_3$ and increasing the concentration of $NO_2$.

### 3.2.4 Vibrationally Excited OH

The possible influence of vibrationally excited OH (OH*) on the HOONO branching ratio measurements was a concern. OH produced from both reactions 3a and 4 are known to produce OH*. While collisional deactivation of OH* is fairly efficient collisions of hot OH with $NO_2$ undoubtedly occur. $NO_2$ is known to be an efficient quencher ($k = 4.8\times10^{-11}$ $cm^3$ $molecule^{-1}$ $s^{-1}$) for excited OH [70].

$$OH^* + NO_2 \rightarrow OH + NO_2^* \qquad \text{Reaction 3.6}$$

In two cases the presence of OH* would not concern us. If the only result of reaction 3.6 is quenching, then nitric acid and HOONO are only produced from OH + $NO_2$ and clearly the branching ratio we measure is not influenced by OH*. If some of our measured product does result from OH* + $NO_2$ + M, but the branching ratio is unaffected by the vibrational excitation, then again this would not influence our result.

If, however, a significant fraction of our measured products does come from OH*,

$$OH^* + NO_2 + M \rightarrow HONO_2 + M, \qquad \text{Reaction 3.7a}$$

$$OH^* + NO_2 + M \rightarrow HOONO + M, \qquad \text{Reaction 3.7b}$$

then reactions 3.7a and 3.7b compete with reactions 3.1a and 3.1b. If the branching ratio is not the same as for these two sets of reactions, perhaps favoring the more stable nitric acid product in reactions 3.7, then our measured branching ratio may be influenced by the degree of OH vibrational excitation. Experimentally, we have tried to address this by altering the initial OH* distribution and by adding an efficient quencher.

We varied the initial OH* distribution by switching our OH generation from reaction 3.3a and reaction 3.4 to reaction 3.3b. While $O(^1D)$ + $CH_4$ also produces OH*, the yield with $v > 2$ is less than from reaction with $H_2$ [71, 72]. A careful examination of our observed HOONO/$HONO_2$ yields over the full pressure range showed no correlation between the source chemistry and the branching ratio.

We also tried to investigate the role of OH* by introducing an efficient quencher. $SF_6$ is the classic quencher for vibrational excitation due to its large mass and number of vibrational modes. The introduction of $SF_6$ to our experiments should increase the rate of OH* quenching and increase the percentage of our product coming from reaction of $NO_2$ with OH in the ground state. A series of branching ratio measurements were made at 330

torr at concentrations of $SF_6$ in the range $[SF_6] = (0\text{-}7.5)\times10^{15}$ $cm^{-3}$. All other conditions such as precursor concentrations and excimer power were kept constant during the experiment. A clear trend was seen in the ratio of HOONO to $HONO_2$ areas with $[SF_6]$ as shown in Figure 3.8.

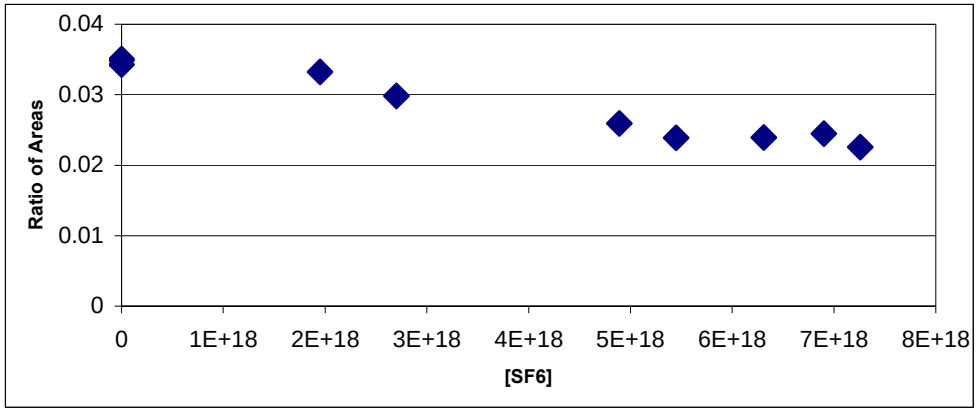


**Figure 3.8. Ratio HOONO/$HONO_2$ areas measured at 300 torr total pressure as a function of $SF_6$ concentration.**

While the presence of $SF_6$ clearly decreased the HOONO/$HONO_2$ ratio, the trend was opposite what we would expect if this was due to changes in the OH vibrational-state distribution. An increase in $[SF_6]$ should increase the rate of quenching for hot OH. If this impacts the branching ratio at all, I would expect a reduction in hot OH to increase formation of the more weakly bound HOONO product.

The stronger evidence that this trend with $[SF_6]$ is unrelated to vibrationally hot OH is in the raw HOONO and $HONO_2$ areas shown in Figure 3.9. If the presence of $SF_6$ was influencing the branching ratio, we would expect the two to trend in opposite directions. Instead, the HOONO absorbance remains constant, while the nitric acid absorbance increases steadily with $[SF_6]$. This is indicative of a change in CRDS detection of nitric acid and is likely the result of a change in the pressure broadening of

the nitric acid band by $SF_6$. This was supported by observed changes in the observed nitric acid band shape at higher [$SF_6$] also indicative of pressure broadening. The impact of pressure broadening on the CRDS detection of nitric acid is discussed in detail in chapter 2.

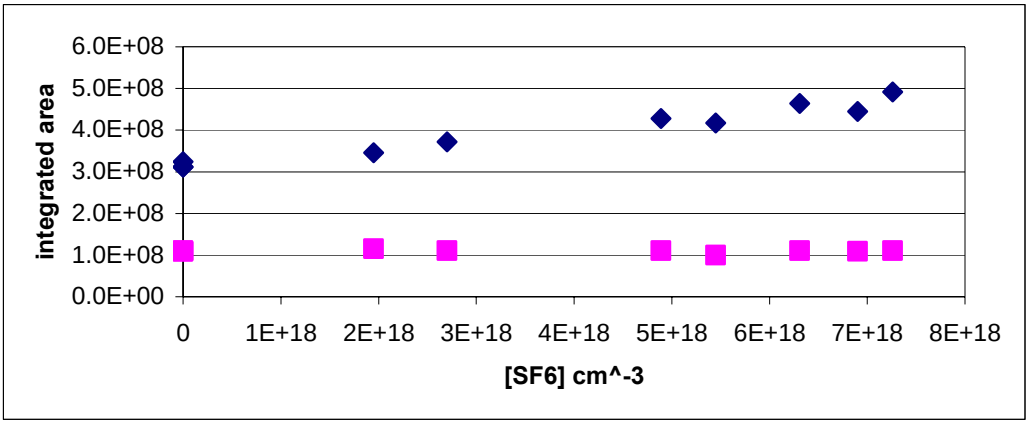


**Figure 3.9. Integrated areas of HOONO (pink squares) and $HONO_2$ (blue diamonds) measured at 300 torr as a function of $SF_6$ concentration. The HOONO integrated areas have been multiplied by 10 to be on the same scale.**

This large change in the nitric acid area makes interpreting the branching ratio data in Figure 3.8 with respect to the role of OH vibrational excitation difficult. The most reliable data is the HOONO area as a function of [$SF_6$] shown in Figure 3.9. From this, we cconclude that there is no evidence that adding $SF_6$ to the cell impacted the production of HOONO in our cell.

In summary, we have tried to evaluate the possible influence of OH* on our branching ratio measurements in two ways: changing the initial vibrational distribution of OH and adding an efficient quencher. Neither experiment showed evidence of a change in the HOONO yield. This result seems to indicate that the influence of OH* on the branching ratio is not large, but does not prove the lack of influence. Conclusive proof

would require a method for generating uniformly cold OH without introducing large spectral interference in our detection region.

### 3.2.5 Branching Ratio Measurements

Several steps were involved in measuring the branching ratio from reaction 3.1: (1) measuring the infrared spectrum of the reaction products, (2) fitting the data spectrum with reference spectra, (3) integration of the $\nu_1$ bands of HOONO and $HONO_2$, (4) correcting measured integrated absorbances for known errors, and (5) conversion from relative absorbance to relative concentrations using the ratio of *ab initio* calculated cross sections.

Excimer on-off spectra collected as described in Section 3.2.2 were then fit with reference spectra of all known bands in the region of interest: HOONO (3306 $cm^{-1}$), $HONO_2$ (3350 $cm^{-1}$), HONO (3260 $cm^{-1}$, 3372 $cm^{-1}$, and 3590 $cm^{-1}$) and, formaldehyde (3472 $cm^{-1}$, only when $CH_4$ was used as an OH precursor). The $\nu_1$ bands of HOONO and $HONO_2$ in their respective reference spectra were then integrated:

$$\int Abs_{\mathrm{HOONO}} = \int_{3250\ \mathrm{cm^{-1}}}^{3370\ \mathrm{cm^{-1}}} \left( \frac{1}{\tau} - \frac{1}{\tau_0} \right) d\nu ,$$

$$\int Abs_{\mathrm{HONO_2}} = \int_{3480\ \mathrm{cm^{-1}}}^{3620\ \mathrm{cm^{-1}}} \left( \frac{1}{\tau} - \frac{1}{\tau_0} \right) d\nu .$$

Errors in the measured $HONO_2$ and HOONO absorbances were then corrected. As described in detail in Chapter 2, the correction factor in nitric acid absorbances stems from nonlinearities in the CRDS spectra: $E_{\mathrm{HONO_2}} = \frac{A_{\mathrm{CRDS}}}{A_{\mathrm{True}}}$. The magnitude of this correction factor was highly pressure dependent and ranged from 0.4 at 20 torr to 0.85 at

1 atm. A correction factor for our HOONO integrated absorbances was introduced to account for blue-shifted intensity from torsionally excited HOONO. This correction factor, $f_{Boltz}$, was derived from the calculated Boltzmann population of torsional states as described in Section 3.3.3.

In order to convert from the integrated absorbances of the two species to relative concentrations, we rely on calculations of the ratio of their integrated absorption cross sections. When calculating ratios, significant cancellations of systematic errors occur when comparing similar vibrations. Even in calculations we have done in the harmonic approximation comparing nitric acid and peroxynitrous acid, despite errors in absolute intensities of nearly a factor two, the calculated ratios agreed with experiment within 20% [7]. We have been collaborating with Professor John F. Stanton on calculations of HOONO and related species. He has completed a high-level (CCSD(T)/ANO) calculation of the full quartic force field of $HONO_2$ and of all isomers of HOONO within the second-order vibrational perturbation theory (VPT2). For small molecules with nearly complete basis sets these calculations have been found to be robust [73, 74]. The $HONO_2$ intensities for $\nu_1$ and $2\nu_2$ from these calculations as well as all HOONO and $HONO_2$ frequencies agree with experiment to better than 5%, giving us considerable confidence in the calculated ratio of intensities: $I_{HONO2}/I_{HOONO} = 2.71$.

**Table 3.3. Comparison of HOONO and $HONO_2$ frequency and intensity calculations.**

| | | Harmonic CCSD(T)/ AUG-cc-pVTZ Francisco | Harmonic CCSD(T)/ ANO Stanton | Anharmonic CCSD(T)/ ANO Stanton | Experiment |
|---|---|---|---|---|---|
| HOONO | | | | | |
| | $\omega_1$, $cm^{-1}$ | 3521 | NA | 3320 | 3306[a] |
| | $2\omega_1$, $cm^{-1}$ | 7042 | NA | 6415 | 6350[c] |
| | $I_1$, km/mol | 33.2 | 33.4 | 27.0 | NA |
| $HONO_2$ | | | | | |
| | $\omega_1$, $cm^{-1}$ | 3753 | NA | 3560 | 3550 |
| | $I_1$, km/mol | 95.4 | 88.6 | 73.2 | 75[b] |
| | $2\omega_2$, $cm^{-1}$ | NA | NA | 3436 | 3406 |
| | $I_{2v2}$ | NA | NA | 2.2 | 1.7[b] |
| | $I_{1,HONO2}/I_{1,HOONO}$ | 2.87 | 2.65 | 2.71 | |

a.Bean et al. [7]
b.Chackerian et al. [22]
c. Fry et al. [55]

The branching ratio from reaction 3.1, $k_{1b}/k_{1a}$, was therefore calculated from each measured spectrum by

$$\mathrm{BR} = \frac{k_{1b}}{k_{1a}} = \frac{\int Abs_{\mathrm{HOONO}}}{\int Abs_{\mathrm{HONO_2}}} \times E_{\mathrm{HONO_2}} \times f_{Boltz} \times \frac{I_{\mathrm{HONO_2}}}{I_{\mathrm{HOONO}}}. \qquad \text{Equation 3.1}$$

## *3.3 Results*

### 3.3.1 CRDS Data

Typical CRDS spectra of the products of reactions 3.1-3.5 following excimer photolysis are shown in Figure 3.10 and Figure 3.11. Spectra shown were collected with a photolysis-probe delay of 1 ms and with a pressure of 200 torr. The background CRDS signal with the excimer off has been subtracted and the resulting signal has been converted to units of absorbance per pass. Figure 3.10 shows the spectrum of products formed using $H_2$ as the OH precursor. Features due to $HONO_2$, HOONO and HONO are all clearly identifiable.

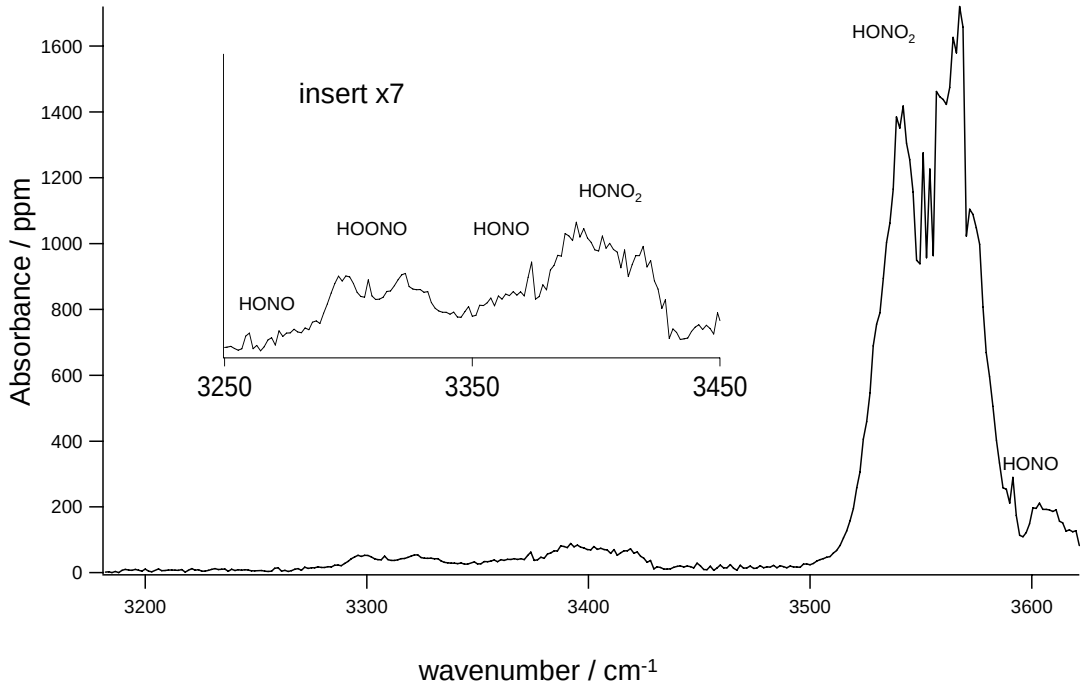


**Figure 3.10. IR-CRDS spectrum of the products of the reaction OH + $NO_2$ using $O(^1D)$ + $H_2$ as the OH source. The spectrum shown has the background with the no excimer photolysis subtracted and has been converted to absorbance units assuming $L_{cav}$ = 50 cm and $L_s$ = 6 cm.**

Figure 3.11 shows the spectrum of products formed using $CH_4$ as the OH precursor. In addition to the features present in Figure 3.10, a peak due to formaldehyde ($CH_2O$) is also clearly visible. The signal-to-noise ratio for HOONO in Figure 3.11 is worse than in Figure 3.10. This is largely because the total OH yield is lower due to the absence of secondary OH formation via reaction 3.4, thus decreasing the concentration of products. Background absorption of $CH_4$ to the red of HOONO also acts to increase the noise in the subtracted spectra.

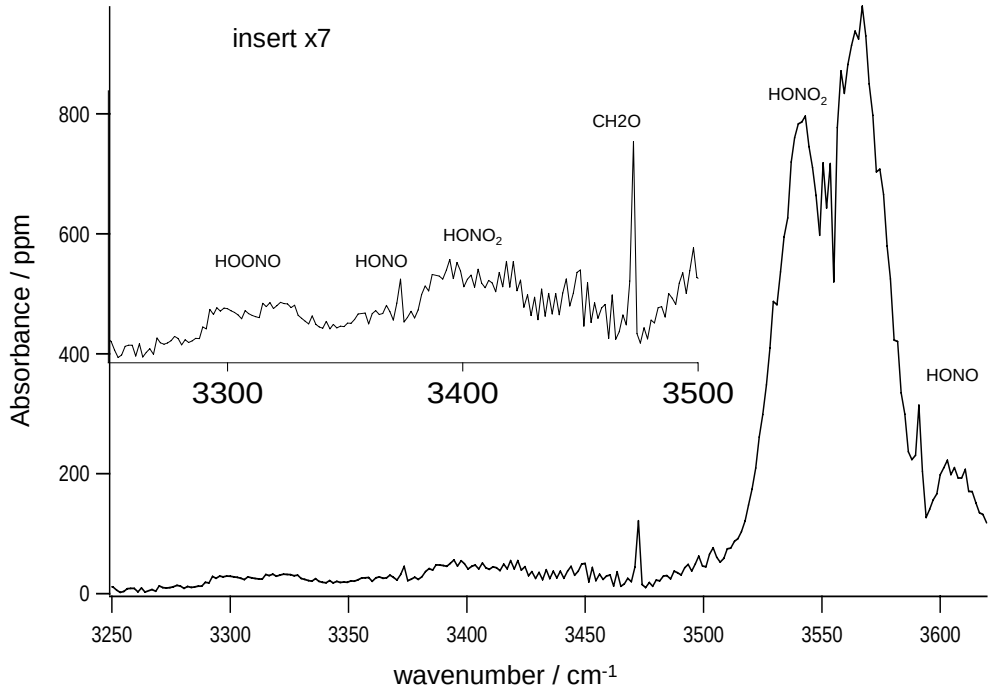


**Figure 3.11. IR-CRDS spectrum of the products of the reaction OH + $NO_2$ using $O(^1D)$ + $CH_4$ as the OH source. The spectrum shown has the background with the no excimer photolysis subtracted and has been converted to absorbance units assuming $L_{cav}$ = 50 cm and $L_s$ = 6 cm.**

The signal-to-noise ratios in the spectra shown above were typical for most data. Data taken above 700 torr had more noise. This was symptomatic of a general degradation of the sensitivity of our apparatus under these conditions. Because our mirrors seal to the flow tube by pressing against an O-ring, the alignment of the mirrors depended upon the pressure gradient across the mirrors. For experiments near 1 atm, this pressure gradient did not exist and the optical cavity became unstable. Data taken with $SF_6$ as a bath gas were also quite noisy, presumably due to aerosols present in the $SF_6$. An example spectrum with $SF_6$ is shown in Figure 3.12. The data shown were taken with 330 torr total pressure and 200 torr $SF_6$. We see that the general features of the component spectra are still discernable, but much noisier.

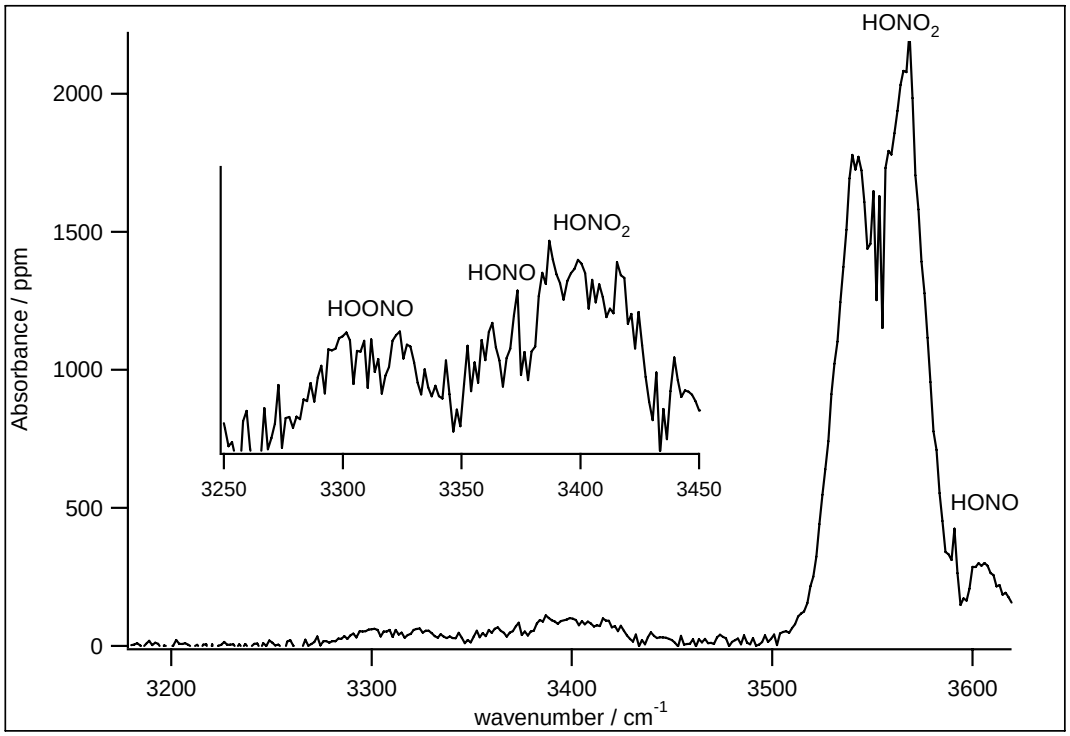


**Figure 3.12. IR-CRDS spectrum of the products of the reaction OH + $NO_2$ using $O(^1D)$ + $H_2$ as the OH source and with 200 torr $SF_6$ added as a bath gas. The spectrum shown has the background with the no excimer photolysis subtracted and has been converted to absorbance units assuming $L_{cav}$ = 50 cm and $L_s$ = 6 cm.**

## 3.3.2 Fits and Integration

HOONO and $HONO_2$ absorbances were obtained by scaling reference spectra to fit their $\nu_1$ bands in our data spectra. Due to spectral congestion, reference spectra for the HONO bands and other nitric acid bands in this region were also used in the fits. The reference spectra used are shown in Figure 3.13. The reference spectra were all collected using our CRDS apparatus so that the instrument resolution would be identical. Reference spectra were mapped onto one *x*-axis so they could be summed and compared to the observed spectra.

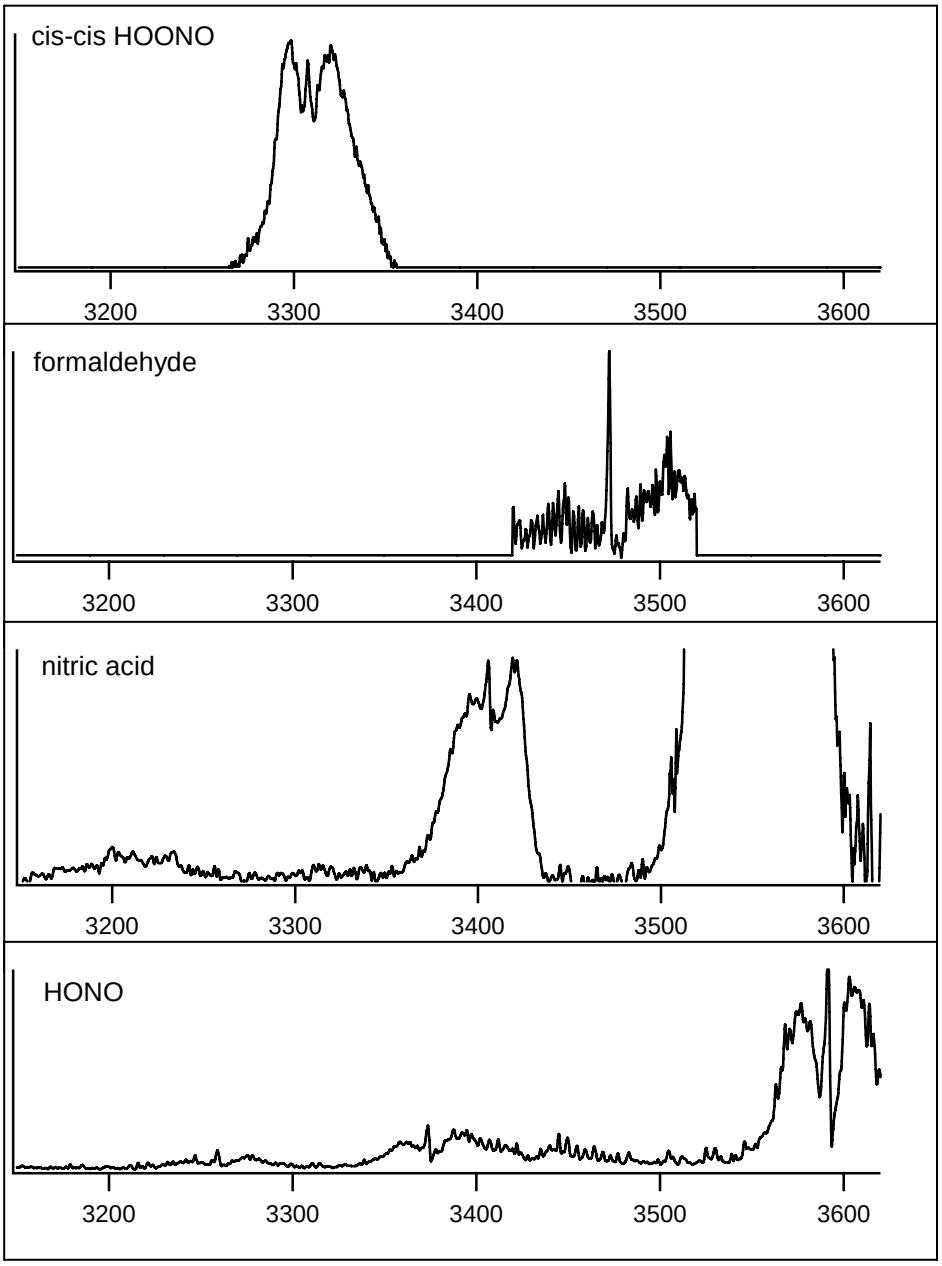


**Figure 3.13. Reference spectra used to fit measured CRDS product spectra.**

The details of how these spectra were generated are included elsewhere in this thesis. The HOONO reference spectrum was taken from the work described in Bean et al. [7]. The nitric acid reference spectrum was taken from the work described in Chapter 2. The nitric acid $\nu_1$ band, off scale in Figure 3.13, was scaled independently from the

other nitric acid peaks. Several $\nu_1$ $HONO_2$ reference spectra were used to account for variation in peak shape with pressure. No other peaks demonstrated a noticeable variation in shape with pressure, indicating that the CRDS artifacts observed for the $\nu_1$ $HONO_2$ band were negligible for the other observed bands.

Using an automated least-squared program to scale the reference spectra was found to be unreliable. Presumably this method failed due to the large stepsize of our data spectra and small shifts in our experimental *x*-axis. As a result, fitting of observed spectra was accomplished by manually scaling reference spectra using IGOR. Fitting of the $HONO_2$ and HOONO peaks were done separately.

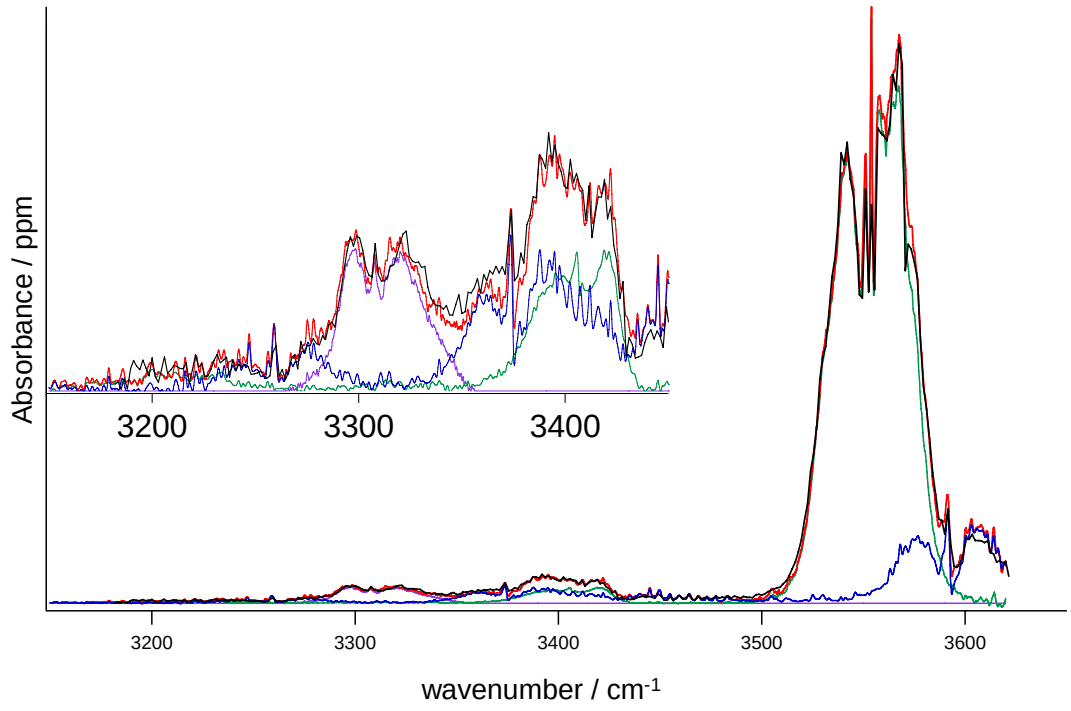


**Figure 3.14. CRDS spectrum of photolysis products (black), fit with spectral components due to $HONO_2$ (green), HONO (blue), and HOONO (purple). The sum of the various components is shown in red.**

Fitting of the HOONO spectrum was done by focusing on the region from 3150 to 3500 $cm^{-1}$. A sample fit for this region is shown in Figure 3.14. The fitting was generally done with the following procedure. First the nitric acid spectrum was scaled to fit the $2\nu_2$ band around 3420 $cm^{-1}$. Second, the HONO spectrum was scaled to fit the $2\nu_2$ bands. Generally, scaling to the P-branch of *cis*-HONO (3230 $cm^{-1}$), with the least interference from other species, provided a good fit to HONO throughout the spectrum. At this point, the signal to the red of *cis*-HONO was checked for a nonzero baseline. Typical baseline offsets were small, $(1/\tau\text{-}1/\tau_0)_{3180} \approx 2000$, relative to the spectral features, $(1/\tau\text{-}1/\tau_0)_{3300} \approx 15000$. If needed, a constant was added to the data spectrum to compensate for the offset and then the $HONO_2$ and HONO spectra were re-scaled.

The HOONO spectrum was then scaled to match the data spectrum from 3285 to 3335 $cm^{-1}$. Small adjustments were then made to the HONO and HOONO spectra to get the best match between the simulated and data spectra. For all spectra it was possible to get the simulated and experimental spectra to match for the HOONO P- and Q-branches as well as the red side of the R-branch. The fits were uniformly poor, however, in the region to the blue of the HOONO R-branch, as will be discussed below (section 3.3.3). The HOONO absorbance was then obtained by having IGOR integrate the HOONO reference spectrum from 3250 to 3350 $cm^{-1}$ using the "print areaxy" command.

The procedure for fitting the nitric acid $\nu_1$ peak focused on the region from 3480 to 3620 $cm^{-1}$. In this case, the only significant spectral interference was the $\nu_1$ peak of HONO and so only the $HONO_2$ and HONO reference spectra were scaled. As described in Chapter 2, the observed $\nu_1$ band shape changes with pressure. Therefore, each data spectrum was fit with a nitric acid $\nu_1$ reference spectrum taken at a similar pressure.

Typically, the HONO spectrum was scaled first to match the observed signal at 3610 $cm^{-1}$. The nitric acid spectrum was then scaled to get the best fit throughout the P- and R-branches. The Q-branch could not be reliably used due to the small number of points sampling this region in our data spectra. Unlike in the HOONO region, baseline offsets had a negligible influence on fits to the much larger $HONO_2$ peaks. Once the best fits had been achieved, the $HONO_2$ absorbance was obtained by having IGOR integrate the $HONO_2$ reference spectrum from 3480 to 3620 $cm^{-1}$ using the "print areaxy" command.

This fitting procedure, while not time efficient, yielded good fits to all data. Possible sources of uncertainty in our derived absorbances (assuming no errors in our reference spectra) were noise in our data spectra, spectral congestion, baseline offsets, and judgment errors on the part of the fitter. Noise and spectral congestion will be discussed for HOONO only, since these were negligible sources of uncertainty in the $HONO_2$ absorbance. The typical signal-to-noise ratio for the P-branch of our HOONO data spectrum was ≈10 (2σ). The region used to set the HOONO scaling included 30 points. If we assume our noise scales as $N^{-1/2}$, then our signal-to-noise for the fit region as a whole was ≈55. This leads to an uncertainty of 2% (2σ).

Uncertainty due to spectral overlap was minimized due to the weighting of HOONO fits toward the P-branch. In this case, only the $2\nu_2$ band of *cis*-HONO impacted the HOONO absorbance. The sensitivity of our HOONO absorbance to the HONO band was evaluated by re-fitting data spectra with different HONO scaling. Due to the small amount of spectral overlap, varying the HONO scaling by ±20% yielded a negligible change in the best-fit HOONO scaling. The uncertainty in our HONO scaling is on the

same order as the uncertainty in HOONO (≈5%) and thus spectral congestion from HONO makes a negligible contribution to the overall uncertainty in our HOONO fits.

Evaluating the uncertainty from correcting baseline offsets is difficult, in large part, because the source of these offsets is still not understood. Offsets only appeared when the ozone absorber was present and appeared to be constant over the range scanned. The offsets could be positive or negative and therefore were unlikely due to absorption by an unknown secondary product. The magnitude of the offsets varied from day to day, implying that cavity alignment may have had some impact. My guess is that some photoaccoustic or heating effect caused a small variation in the cavity when the excimer was on. The resulting small change in the "excimer on" ringdowns relative to the "excimer off" ringdowns led to $1/\tau$ values that could be either larger or smaller. If we assume that adding a constant to each data spectrum to account for its offset was valid, then a similar uncertainty analysis to that described in the previous paragraph yields an uncertainty from the baseline correction of about 5% for data with the largest offsets.

This fitting procedure relied on my judgment rather than a least-square analytical function. While every attempt was made to obtain an optimal fit, it is possible personal bias on my part introduced further error. An attempt to quantify this error was made by making the largest and smallest fits I would deem "reasonable." When compared to my "best" fit values, the full range of reasonable fits typically spanned only ±5%. For particularly noisy spectra, this could be as large as ±10%. This is similar to the uncertainty expected based on the noise of the spectra discussed above. It is possible that some component of this error should be treated as systematic. For example, perhaps my eye systematically gives more weight to noise above the mean signal. My re-analysis of

the fits showed no evidence of this, however, and so this was treated as a random uncertainty.

The total uncertainty in an individual branching ratio measurement from fitting spectra can be estimated by combining all of the uncertainties discussed above: noise in the data spectra, spectral interference, baseline correction, and judgment errors. I have assumed these uncertainties were random and uncoupled and therefore added them in quaduture. An estimate of the uncertainty in a single branching ratio measurement from the spectral fitting was 7%-11% depending on the amount of noise in the HOONO region.

### 3.3.3 Stretch-Torsion Coupling

The relative populations in the ground state, $P_{\mathrm{Rel}}$, were calculated from the data in table 3.3 assuming a Boltzmann distribution,

$$P_{\mathrm{Rel}} = \exp\left(\frac{-(E - ZPE)}{k_{\mathrm{B}} * T}\right).$$

The blue shift of each sequence band was calculated by comparing the $\nu_1$=1←0 transition frequencies for states with torsional excitation to the transition frequency of the ground state.

The partition function, $Q$,

$$Q = \sum_{\text{all states}} P_{\mathrm{Rel}} = 1.64,$$

was used calculate what fraction of the total $\nu_1$=1←0 absorbance is included in the HOONO reference spectrum used for integration.

$$f_{included} = \frac{\sum_{\text{included states}} P_{\text{Rel}}}{Q}$$

Our measured *cis-cis* HOONO absorbances can then be corrected to represent the total HOONO $\nu_1$ absorption through a simple correction factor,

$$Abs_{\text{true}} = Abs_{\text{obs}} * \left( \frac{1}{f_{\text{included}}} \right) = Abs_{\text{obs}} * F_{Boltz} .$$

From looking at the blue shifts in Table 3.2, for most sequence bands it is clear whether or not they qualify as "included states" for our calculation of $f_{\text{included}}$. In addition to the fundamental, the first two states with population only in $\nu_8$ clearly do not shift the absorption frequency outside our reference HOONO spectrum. Most other states clearly do. The two states that are unclear are the first HOON torsion ($\nu_9$=1,$\nu_8$=0), and the first combination band (1,1). The predicted blue shifts of these bands of about 45 $cm^{-1}$ places them right at the edge of HOONO reference spectrum. This can be seen graphically in Figure 3.15.

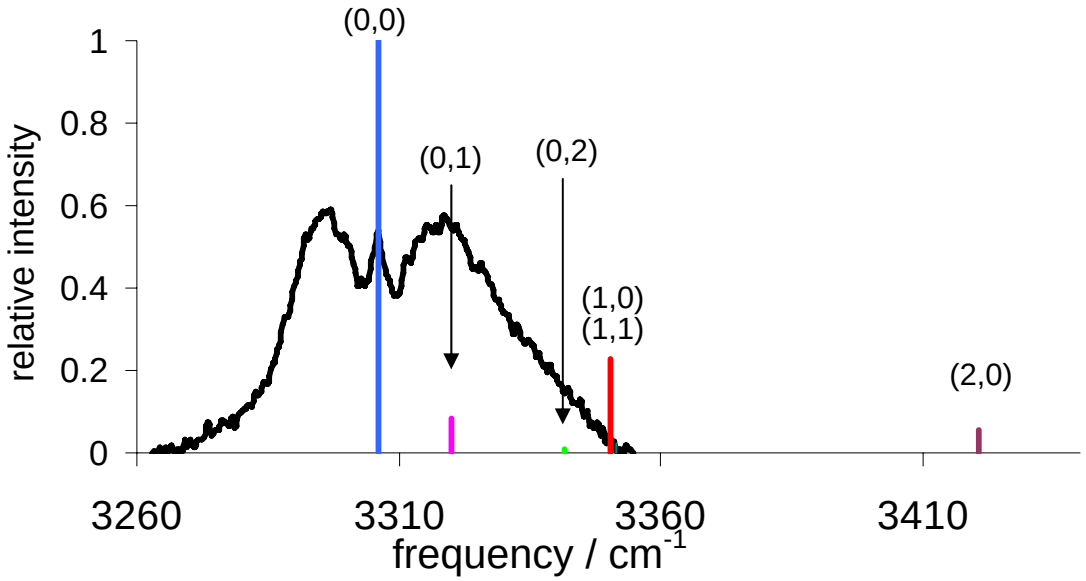


**Figure 3.15. Positions and relative intensities of the lowest calculated HOONO OH stretch transitions with population in torsional modes. Transitions are labeled with the number of torsional quanta as ($\nu_9$, $\nu_8$). The HOONO spectrum used to fit our CRDS product spectra is shown for comparison.**

Pending a more detailed spectroscopic analysis, three values of $F_{\text{Boltz}}$ were calculated. The lower limit of 1.21 was obtained assuming (1,0) and (1,1) were fully contained within our reference spectrum. The upper limit of 1.48 was obtained assuming those two sequence bands were completely outside our reference spectrum. It is likely that some fraction of these bands was included in our reference spectrum and that $F_{\text{Boltz}}$ lies between these limits. Assuming that half of those two states was accounted for by our reference HOONO spectrum yields $F_{\text{Bolt}} = 1.33$.

This correction factor is larger than that derived from the two-dimensional picture (1.25) that only looked at the influence of $\nu_9$. This increase has two sources: (1) the energies of the lowest $\nu_9$ states are lower, leading to a greater population in states that

cause large blueshifts and (2) combination bands add new populated states that have significant blueshifts.

We now look at the more recent attempt to measure the HOONO spectrum, including the intensity to the blue. Figure 3.16 shows the three spectra taken for this purpose (0.2 $cm^{-1}$ stepsize) along with the average of the three. Figure 3.17 shows the fit to this spectrum used to subtract contributions from HONO and $HONO_2$. The residual, presumably the spectrum of HOONO, is shown offset in the upper portion of Figure 3.17. We see outside the main *cis-cis* HOONO peak there is clearly spectral intensity around 3370 $cm^{-1}$ that cannot be subtracted out with either HONO or $HONO_2$. Using this new HOONO spectrum to re-fit branching ratio data led to consistently better fits in the region to the blue of HOONO (see example in Figure 3.18).

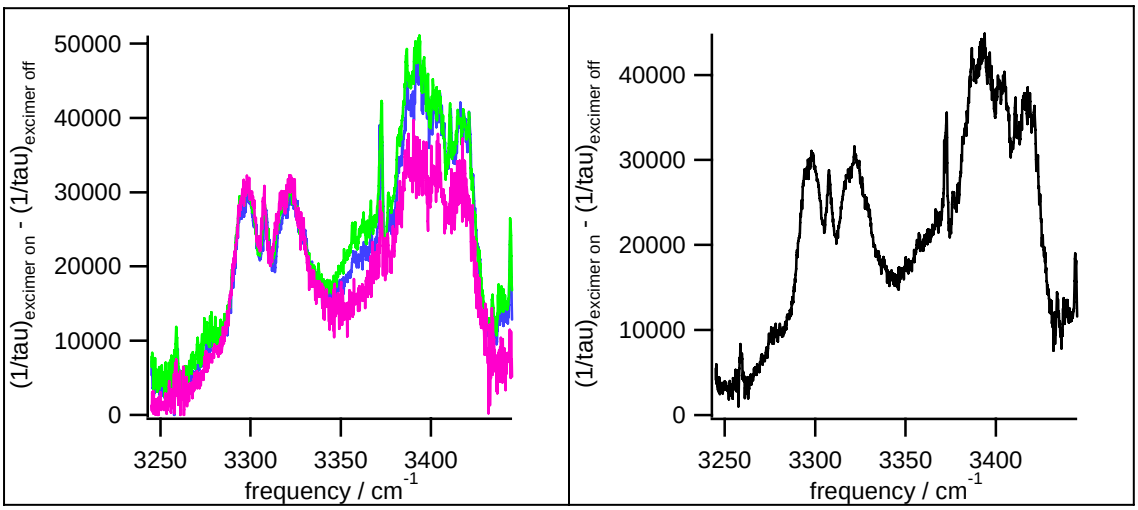


**Figure 3.16. Three spectra used to search for spectral features due to torsionally-excited HOONO. Spectra shown were taken at 0.2 $cm^{-1}$ step size and have the background without photolysis subtracted. The average of the three spectra is shown on the right.**

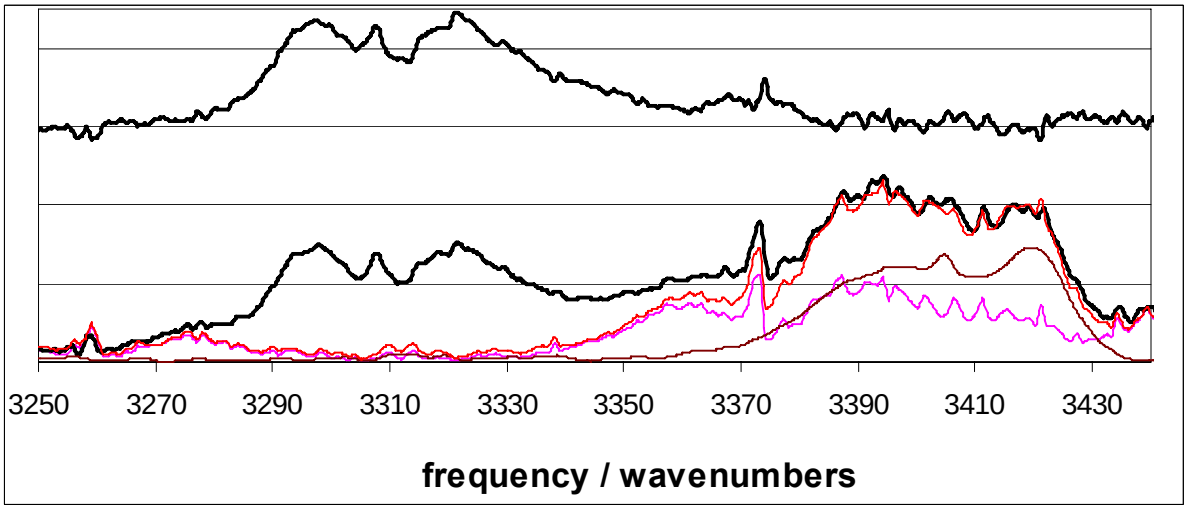


**Figure 3.17. Average product spectrum from Figure 3.16 (black) shown along with reference spectra used for subtraction of HONO (pink) and $HONO_2$ (brown). The sum of the fit spectra are shown in red. The residual, presumably the spectrum of HOONO, is shown above.**

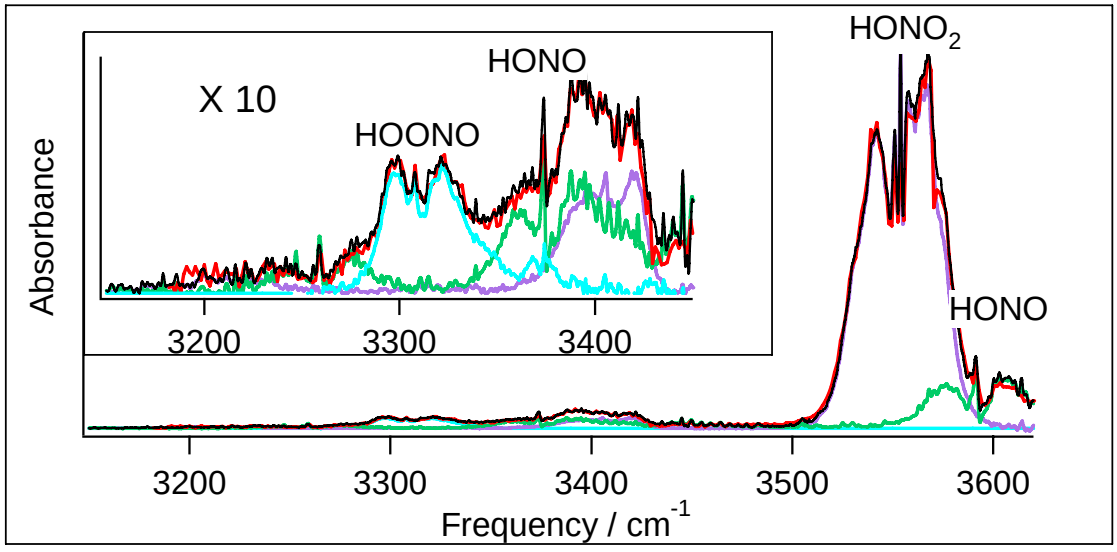


**Figure 3.18. Re-fit of some branching ratio data (red) usng the new HOONO spectrum (blue) along with reference spectra for $HONO_2$ (purple), and HONO (green). The sum of these spectra (black) match the observed spectrum well at all frequencies.**

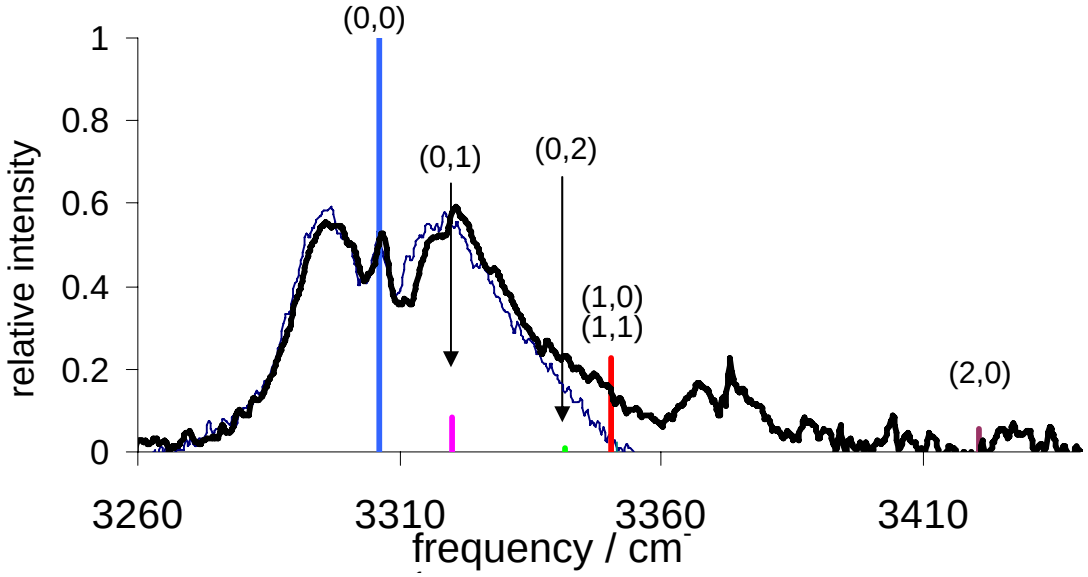


**Figure 3.19. New measured HOONO spectrum from Figure 3.17 (thick line) compared with positions and relative intensities of the lowest calculated HOONO OH stretch-torsion transitions. Transitions are labeled with the number of torsional quanta as ($v_9$, $v_8$). The HOONO spectrum used to fit our CRDS product spectra is shown for comparison (thin line).**

The newly measured HOONO spectrum is shown along with the positions of the calculated transitions of torsionally excited HOONO in Figure 3.19. We still do not capture any transitions shifted above 3380 $cm^{-1}$. The shape from 3250 to 3380 $cm^{-1}$ indicates that the new spectrum includes the (1,0) and (1,1) sequence bands that were the largest source of uncertainty in our derivation of $F_{Boltz}$ above. The ratio of integrated absorbance for the two HOONO spectra is $A_{new}/A_{old} = 1.20$. If we assume that the (2,0) state and all others shifted more than this state are not included in the new spectrum, then our correction factor becomes

$$F_{Boltz} = \frac{A_{new}}{A_{old}} * \left( \frac{\sum_{(0,0)\text{-}(1,1)} P_{Rel}}{Q} \right) = 1.20 * 1.21 = 1.45 .$$

If instead the (2,0) state is included in the new spectrum this would decrease to 1.37. This 5% change gives an estimate of the uncertainty in this correction factor. These

numbers are in good agreement with *ab initio* correction factors calculated without using the new spectrum. My best estimate of the correction factor is $F_{\mathrm{Boltz}}$=1.41±0.07.

### 3.3.4 Branching Ratio

As described above, the branching ratio for each spectrum was calculated with eq 3.1.

$$\mathrm{BR} = \frac{k_{1b}}{k_{1a}} = \frac{\int Abs_{\mathrm{HOONO}}}{\int Abs_{\mathrm{HONO_2}}} \times E_{\mathrm{HONO_2}} \times F_{Boltz} \times \frac{I_{\mathrm{HONO_2}}}{I_{\mathrm{HOONO}}} = \frac{\int Abs_{\mathrm{HOONO}}}{\int Abs_{\mathrm{HONO_2}}} \times E_{\mathrm{HONO_2}} \times 1.41 \times 2.71$$

where $E_{\mathrm{HONO_2}}$ is the pressure-dependent correction to the nitric acid absorbance, $F_{\mathrm{Boltz}}$=1.41 is the correction for torsionally excited HOONO, and the ratio of integrated cross sections $I_{\mathrm{HONO2}}/I_{\mathrm{HOONO}}$ has been calculated to be 2.71. The raw data and corrections leading to the individual branching ratio measurements are shown in Table 3.4. A plot of the full data set of branching ratios as a function of pressure is shown in Figure 3.20.

**Table 3.4. Pressures, areas, and correction factors used to calculate branching ratios. Pressures are in Torr, areas are from integrated spectra in ($1/\tau$-$1/\tau_0$).**

| Date | scan | OH source | Pbar | Peff | HOONO area | $HONO_2$ area | $E_{HONO2}$ | BR |
|---|---|---|---|---|---|---|---|---|
| 17-Aug-05 | 2 | H2 | 25 | 17.6 | 3.30E+05 | 1.41E+07 | 2.32 | 0.039 |
| 17-Aug-05 | 1 | H2 | 25 | 17.6 | 2.73E+05 | 1.41E+07 | 2.32 | 0.032 |
| 11-Aug-05 | 6 | H2 | 25 | 19.4 | 5.12E+05 | 2.13E+07 | 2.29 | 0.040 |
| 11-Aug-05 | 1 | H2 | 25 | 19.5 | 3.50E+05 | 2.03E+07 | 2.28 | 0.029 |
| 11-Aug-05 | 4 | H2 | 25 | 20.9 | 4.65E+05 | 2.24E+07 | 2.26 | 0.035 |
| 22-Aug-05 | 11 | H2 | 35 | 26.3 | 6.63E+05 | 2.11E+07 | 2.19 | 0.055 |
| 22-Aug-05 | 13 | H2 | 35 | 26.3 | 5.30E+05 | 2.21E+07 | 2.19 | 0.042 |
| 17-Aug-05 | 6 | H2 | 50 | 32.2 | 6.04E+05 | 2.37E+07 | 2.13 | 0.046 |
| 17-Aug-05 | 5 | H2 | 50 | 39.3 | 7.55E+05 | 2.42E+07 | 2.07 | 0.058 |
| 11-Aug-05 | 7 | H2 | 50 | 40.7 | 7.33E+05 | 2.58E+07 | 2.06 | 0.053 |
| 11-Aug-05 | 2 | H2 | 50 | 40.9 | 5.49E+05 | 2.34E+07 | 2.05 | 0.044 |
| 17-Aug-05 | 3 | H2 | 75 | 53.7 | 6.60E+05 | 2.23E+07 | 1.97 | 0.057 |
| 17-Aug-05 | 4 | H2 | 75 | 53.7 | 7.99E+05 | 2.54E+07 | 1.97 | 0.061 |
| 3-May-05 | 10 | H2 | 70 | 54.0 | 5.98E+05 | 2.09E+07 | 1.97 | 0.056 |

| | | | | | | | | |
|---|---|---|---|---|---|---|---|---|
| 11-May-05 | 9 | CH4 | 57.4 | 57.4 | 4.68E+05 | 1.39E+07 | 1.95 | 0.066 |
| 11-Aug-05 | 3 | H2 | 75 | 59.0 | 6.64E+05 | 2.69E+07 | 1.94 | 0.049 |
| 2-Mar-05 | 10 | H2 | 71 | 64.1 | 1.12E+06 | 4.55E+07 | 1.91 | 0.049 |
| 11-Aug-05 | 10 | H2 | 75 | 65.0 | 7.79E+05 | 3.10E+07 | 1.91 | 0.050 |
| 14-Apr-05 | 1 | H2 | 95 | 71.3 | 7.87E+05 | 2.33E+07 | 1.88 | 0.068 |
| 2-May-05 | 13 | H2 | 100 | 73.9 | 6.49E+05 | 2.28E+07 | 1.87 | 0.058 |
| 2-May-05 | 9 | H2 | 100 | 74.4 | 5.82E+05 | 1.93E+07 | 1.87 | 0.062 |
| 2-May-05 | 10 | H2 | 100 | 74.4 | 5.41E+05 | 1.81E+07 | 1.87 | 0.061 |
| 2-May-05 | 14 | H2 | 100 | 74.6 | 5.92E+05 | 2.11E+07 | 1.87 | 0.057 |
| 2-May-05 | 8 | H2 | 100 | 76.0 | 9.31E+05 | 3.29E+07 | 1.86 | 0.058 |
| 9-May-05 | 5 | H2 | 100 | 76.2 | 5.34E+05 | 2.05E+07 | 1.86 | 0.053 |
| 2-May-05 | 15 | H2 | 100 | 78.2 | 7.10E+05 | 2.78E+07 | 1.85 | 0.053 |
| 9-May-05 | 6 | H2 | 100 | 78.6 | 5.23E+05 | 1.99E+07 | 1.85 | 0.054 |
| 17-Aug-05 | 7 | H2 | 100 | 79.9 | 8.00E+05 | 2.52E+07 | 1.85 | 0.066 |
| 17-Aug-05 | 8 | H2 | 100 | 79.9 | 8.00E+05 | 2.45E+07 | 1.85 | 0.068 |
| 11-May-05 | 8 | CH4 | 80 | 80.0 | 6.51E+05 | 1.93E+07 | 1.85 | 0.070 |
| 2-May-05 | 7 | H2 | 100 | 80.1 | 9.13E+05 | 3.13E+07 | 1.85 | 0.060 |
| 2-May-05 | 16 | H2 | 100 | 80.5 | 9.70E+05 | 3.68E+07 | 1.84 | 0.055 |
| 9-May-05 | 4 | H2 | 100 | 81.3 | 6.95E+05 | 2.42E+07 | 1.84 | 0.060 |
| 9-May-05 | 1 | H2 | 100 | 81.5 | 4.71E+05 | 1.25E+07 | 1.84 | 0.078 |
| 2-May-05 | 5 | H2 | 100 | 81.9 | 6.68E+05 | 2.37E+07 | 1.84 | 0.059 |
| 2-May-05 | 6 | H2 | 100 | 81.9 | 6.81E+05 | 2.37E+07 | 1.84 | 0.060 |
| 2-May-05 | 3 | H2 | 100 | 82.0 | 6.99E+05 | 2.52E+07 | 1.84 | 0.058 |
| 2-May-05 | 4 | H2 | 100 | 82.0 | 6.68E+05 | 2.39E+07 | 1.84 | 0.058 |
| 2-May-05 | 2 | H2 | 100 | 82.0 | 6.99E+05 | 2.52E+07 | 1.84 | 0.058 |
| 2-May-05 | 1 | H2 | 100 | 82.2 | 7.76E+05 | 2.65E+07 | 1.84 | 0.061 |
| 9-May-05 | 7 | H2 | 100 | 84.4 | 7.48E+05 | 2.43E+07 | 1.83 | 0.064 |
| 9-May-05 | 2 | H2 | 100 | 84.6 | 7.24E+05 | 2.62E+07 | 1.83 | 0.058 |
| 9-May-05 | 3 | H2 | 100 | 84.6 | 5.79E+05 | 1.83E+07 | 1.83 | 0.066 |
| 3-May-05 | 1 | H2 | 100 | 86.6 | 7.48E+05 | 2.21E+07 | 1.82 | 0.071 |
| 11-Aug-05 | 8 | H2 | 100 | 89.7 | 8.79E+05 | 2.96E+07 | 1.81 | 0.063 |
| 11-Aug-05 | 9 | H2 | 100 | 91.1 | 6.73E+05 | 2.49E+07 | 1.81 | 0.057 |
| 30-Mar-05 | 13 | H2 | 103 | 94.6 | 5.30E+05 | 1.84E+07 | 1.79 | 0.062 |
| 16-Feb-05 | 17 | H2 | 100 | 96.0 | 5.89E+05 | 1.66E+07 | 1.79 | 0.076 |
| 22-Apr-05 | 4 | CH4 | 100 | 100.0 | 9.05E+05 | 2.84E+07 | 1.78 | 0.069 |
| 22-Apr-05 | 7 | CH4 | 100 | 100.0 | 4.50E+05 | 1.19E+07 | 1.78 | 0.081 |
| 22-Apr-05 | 6 | CH4 | 100 | 100.0 | 8.77E+05 | 2.76E+07 | 1.78 | 0.068 |
| 22-Apr-05 | 5 | CH4 | 100 | 100.0 | 7.30E+05 | 2.33E+07 | 1.78 | 0.067 |
| 20-Apr-05 | 5 | CH4 | 102 | 102.0 | 9.62E+05 | 3.04E+07 | 1.77 | 0.068 |

| | | | | | | | | |
|---|---|---|---|---|---|---|---|---|
| 20-Apr-05 | 6 | CH4 | 102 | 102.0 | 9.62E+05 | 2.76E+07 | 1.77 | 0.075 |
| 14-Apr-05 | 10 | H2 | 150 | 102.4 | 1.07E+06 | 4.00E+07 | 1.77 | 0.058 |
| 14-Apr-05 | 7 | H2 | 200 | 111.4 | 1.02E+06 | 2.99E+07 | 1.74 | 0.075 |
| 11-May-05 | 1 | CH4 | 116 | 116.0 | 5.91E+05 | 1.60E+07 | 1.73 | 0.082 |
| 2-Mar-05 | 17 | H2 | 151.4 | 148.3 | 8.40E+05 | 2.62E+07 | 1.65 | 0.074 |
| 10-Aug-05 | 1 | H2 | 200 | 150.4 | 1.26E+06 | 4.06E+07 | 1.65 | 0.072 |
| 10-Aug-05 | 2 | H2 | 200 | 151.4 | 1.39E+06 | 4.68E+07 | 1.65 | 0.069 |
| 10-Aug-05 | 3 | H2 | 200 | 151.4 | 1.05E+06 | 3.28E+07 | 1.65 | 0.074 |
| 10-Aug-05 | 4 | H2 | 200 | 151.5 | 8.74E+05 | 2.53E+07 | 1.65 | 0.080 |
| 10-Aug-05 | 6 | H2 | 200 | 152.2 | 1.37E+06 | 4.26E+07 | 1.65 | 0.075 |
| 10-Aug-05 | 5 | H2 | 200 | 152.7 | 8.74E+05 | 2.66E+07 | 1.64 | 0.076 |
| 3-May-05 | 6 | H2 | 180 | 167.5 | 5.73E+05 | 1.83E+07 | 1.62 | 0.074 |
| 6-Oct-05 | 8 | H2 | 514 | 169.4 | 1.89E+06 | 6.01E+07 | 1.61 | 0.075 |
| 6-Oct-05 | 4 | H2 | 515 | 169.9 | 1.68E+06 | 6.04E+07 | 1.61 | 0.066 |
| 17-Feb-05 | 17 | H2 | 200 | 187.6 | 1.65E+06 | 4.85E+07 | 1.58 | 0.082 |
| 30-Mar-05 | 3 | H2 | 225 | 192.9 | 6.40E+05 | 2.50E+07 | 1.57 | 0.062 |
| 6-Oct-05 | 6 | H2 | 513 | 193.6 | 2.36E+06 | 7.19E+07 | 1.57 | 0.080 |
| 11-Oct-05 | 11 | H2 | 510 | 196.1 | 2.03E+06 | 5.95E+07 | 1.57 | 0.083 |
| 18-Apr-05 | 6 | CH4 | 200 | 200.0 | 7.66E+05 | 2.47E+07 | 1.56 | 0.076 |
| 11-May-05 | 12 | CH4 | 200 | 200.0 | 7.69E+05 | 1.91E+07 | 1.56 | 0.098 |
| 18-Apr-05 | 3 | CH4 | 200 | 200.0 | 1.01E+06 | 3.34E+07 | 1.56 | 0.074 |
| 18-Apr-05 | 1 | CH4 | 200 | 200.0 | 9.60E+05 | 2.97E+07 | 1.56 | 0.079 |
| 18-Apr-05 | 4 | CH4 | 200 | 200.0 | 8.06E+05 | 2.95E+07 | 1.56 | 0.067 |
| 20-Apr-05 | 12 | CH4 | 201 | 201.0 | 1.00E+06 | 2.96E+07 | 1.56 | 0.083 |
| 20-Apr-05 | 11 | CH4 | 201 | 201.0 | 7.35E+05 | 2.26E+07 | 1.56 | 0.080 |
| 11-Oct-05 | 7 | H2 | 505 | 209.5 | 2.13E+06 | 5.38E+07 | 1.55 | 0.098 |
| 11-Oct-05 | 13 | H2 | 515 | 217.6 | 1.97E+06 | 5.20E+07 | 1.53 | 0.094 |
| 11-Oct-05 | 9 | H2 | 510 | 219.5 | 2.57E+06 | 6.99E+07 | 1.53 | 0.092 |
| 2-Mar-05 | 4 | H2 | 230 | 222.0 | 1.14E+06 | 3.90E+07 | 1.53 | 0.073 |
| 2-Mar-05 | 7,8 | H2 | 233 | 224.9 | 1.33E+06 | 4.21E+07 | 1.52 | 0.079 |
| 14-Apr-05 | 3 | H2 | 300 | 225.5 | 1.07E+06 | 2.83E+07 | 1.52 | 0.095 |
| 6-Oct-05 | 3 | H2 | 520 | 229.3 | 1.68E+06 | 5.49E+07 | 1.52 | 0.077 |
| 11-Oct-05 | 5 | H2 | 510 | 232.4 | 1.91E+06 | 5.51E+07 | 1.51 | 0.087 |
| 3-May-05 | 4 | H2 | 252 | 237.1 | 7.96E+05 | 2.14E+07 | 1.51 | 0.094 |
| 22-Aug-05 | 3 | H2 | 350 | 256.9 | 8.21E+05 | 2.26E+07 | 1.48 | 0.094 |
| 22-Aug-05 | 1 | H2 | 350 | 274.7 | 6.32E+05 | 1.61E+07 | 1.46 | 0.103 |
| 29-Aug-05 | 1-2 | H2 | 500 | 282.3 | 1.26E+06 | 4.03E+07 | 1.45 | 0.082 |
| 14-Apr-05 | 5 | H2 | 400 | 294.7 | 1.28E+06 | 3.79E+07 | 1.44 | 0.090 |
| 6-Oct-05 | 2 | H2 | 515 | 304.2 | 1.68E+06 | 5.44E+07 | 1.43 | 0.083 |

| | | | | | | | | |
|---|---|---|---|---|---|---|---|---|
| 11-May-05 | 6 | CH4 | 305 | 305.0 | 1.05E+06 | 2.53E+07 | 1.43 | 0.111 |
| 20-Apr-05 | 1 | CH4 | 305 | 305.0 | 1.01E+06 | 2.97E+07 | 1.43 | 0.091 |
| 20-Apr-05 | 2 | CH4 | 305 | 305.0 | 1.11E+06 | 3.10E+07 | 1.43 | 0.096 |
| 11-Oct-05 | 3 | H2 | 518 | 335.5 | 2.27E+06 | 6.00E+07 | 1.40 | 0.103 |
| 3-May-05 | 8 | H2 | 351 | 335.6 | 7.17E+05 | 2.03E+07 | 1.40 | 0.097 |
| 3-May-05 | 7 | H2 | 357 | 335.7 | 1.20E+06 | 3.28E+07 | 1.40 | 0.100 |
| 30-Mar-05 | 4 | H2 | 405 | 343.0 | 2.60E+05 | 8.93E+06 | 1.39 | 0.080 |
| 11-Oct-05 | 8 | H2 | 525 | 343.0 | 2.24E+06 | 5.38E+07 | 1.39 | 0.114 |
| 30-Mar-05 | 5 | H2 | 410 | 347.1 | 5.20E+05 | 1.77E+07 | 1.39 | 0.081 |
| 23-Aug-05 | 1-3 | CH4 | 350 | 350.0 | 1.59E+06 | 3.80E+07 | 1.39 | 0.115 |
| 6-Oct-05 | 5 | H2 | 515 | 358.5 | 3.94E+06 | 9.99E+07 | 1.38 | 0.109 |
| 2-Mar-05 | 9 | H2 | 373 | 363.1 | 1.76E+06 | 5.06E+07 | 1.38 | 0.097 |
| 11-Oct-05 | 2 | H2 | 520 | 383.8 | 2.07E+06 | 4.96E+07 | 1.36 | 0.117 |
| 3-May-05 | 2 | H2 | 408 | 394.3 | 9.95E+05 | 2.35E+07 | 1.35 | 0.120 |
| 11-May-05 | 10 | CH4 | 400 | 400.0 | 9.48E+05 | 2.40E+07 | 1.34 | 0.112 |
| 20-Apr-05 | 9 | | 400 | 400.0 | 1.30E+06 | 3.26E+07 | 1.34 | 0.113 |
| 20-Apr-05 | 10 | CH4 | 400 | 400.0 | 1.22E+06 | 2.91E+07 | 1.34 | 0.119 |
| 11-Oct-05 | 6 | H2 | 525 | 414.1 | 1.87E+06 | 4.53E+07 | 1.33 | 0.118 |
| 29-Aug-05 | 5-8 | H2 | 500 | 417.0 | 1.31E+06 | 4.02E+07 | 1.33 | 0.094 |
| 6-Oct-05 | 7 | H2 | 513 | 418.3 | 3.00E+06 | 7.91E+07 | 1.33 | 0.109 |
| 11-Oct-05 | 10 | H2 | 510 | 423.9 | 1.76E+06 | 3.79E+07 | 1.33 | 0.134 |
| 11-Oct-05 | 12 | H2 | 515 | 424.7 | 1.64E+06 | 3.72E+07 | 1.33 | 0.127 |
| 29-Aug-05 | 9 | H2 | 500 | 429.6 | 2.62E+06 | 6.75E+07 | 1.32 | 0.112 |
| 6-Oct-05 | 1 | H2 | 523 | 431.3 | 1.68E+06 | 4.94E+07 | 1.32 | 0.098 |
| 14-Apr-05 | 2 | H2 | 510 | 433.2 | 1.13E+06 | 3.20E+07 | 1.32 | 0.102 |
| 29-Aug-05 | 11 | H2 | 500 | 433.3 | 2.02E+06 | 6.37E+07 | 1.32 | 0.092 |
| 29-Aug-05 | 11 | H2 | 500 | 433.3 | 2.43E+06 | 6.37E+07 | 1.32 | 0.111 |
| 11-Oct-05 | 1 | H2 | 515 | 434.0 | 1.97E+06 | 4.13E+07 | 1.32 | 0.138 |
| 11-Oct-05 | 4 | H2 | 525 | 439.5 | 1.91E+06 | 4.37E+07 | 1.32 | 0.127 |
| 29-Aug-05 | 4 | H2 | 500 | 447.7 | 2.56E+06 | 6.04E+07 | 1.31 | 0.124 |
| 29-Aug-05 | 10 | H2 | 500 | 452.0 | 2.49E+06 | 6.09E+07 | 1.31 | 0.120 |
| 3-May-05 | 11 | H2 | 490 | 477.3 | 8.55E+05 | 2.04E+07 | 1.29 | 0.124 |
| 14-Apr-05 | 6 | H2 | 605 | 495.4 | 1.49E+06 | 3.53E+07 | 1.28 | 0.126 |
| 11-May-05 | 2 | CH4 | 501 | 501.0 | 6.57E+05 | 1.45E+07 | 1.27 | 0.136 |
| 2-Mar-05 | 12 | H2 | 512 | 503.1 | 1.18E+06 | 2.63E+07 | 1.27 | 0.135 |
| 20-Apr-05 | 4 | CH4 | 505 | 505.0 | 1.47E+06 | 3.13E+07 | 1.27 | 0.141 |
| 20-Apr-05 | 3 | CH4 | 505 | 505.0 | 1.40E+06 | 3.26E+07 | 1.27 | 0.129 |
| 2-Mar-05 | 13 | H2 | 522 | 510.4 | 9.80E+05 | 2.51E+07 | 1.27 | 0.118 |
| 30-Mar-05 | 6 | H2 | 610 | 516.0 | 1.21E+06 | 3.28E+07 | 1.27 | 0.111 |

| | | | | | | | | |
|---|---|---|---|---|---|---|---|---|
| 22-Aug-05 | 6 | H2 | 750 | 518.6 | 1.99E+06 | 4.89E+07 | 1.26 | 0.123 |
| 30-Mar-05 | 8 | H2 | 614 | 519.4 | 8.96E+05 | 2.19E+07 | 1.26 | 0.124 |
| 22-Aug-05 | 5 | H2 | 750 | 519.9 | 2.46E+06 | 6.05E+07 | 1.26 | 0.123 |
| 11-May-05 | 3 | CH4 | 520 | 520.0 | 8.17E+05 | 1.82E+07 | 1.26 | 0.136 |
| 22-Aug-05 | 8 | H2 | 750 | 521.1 | 1.44E+06 | 3.72E+07 | 1.26 | 0.117 |
| 4-Aug-05 | 4 | H2 | 700 | 538.3 | 1.80E+06 | 3.89E+07 | 1.25 | 0.141 |
| 4-Aug-05 | 5 | H2 | 700 | 538.3 | 2.15E+06 | 4.71E+07 | 1.25 | 0.139 |
| 4-Aug-05 | 6 | H2 | 700 | 538.3 | 2.59E+06 | 5.70E+07 | 1.25 | 0.139 |
| 4-Aug-05 | 3 | H2 | 700 | 539.0 | 2.16E+06 | 5.06E+07 | 1.25 | 0.130 |
| 14-Apr-05 | 9 | H2 | 700 | 565.9 | 1.33E+06 | 3.39E+07 | 1.24 | 0.121 |
| 3-May-05 | 5 | H2 | 582 | 566.8 | 9.55E+05 | 2.14E+07 | 1.24 | 0.138 |
| 14-Apr-05 | 8 | H2 | 700 | 567.1 | 1.51E+06 | 3.72E+07 | 1.24 | 0.126 |
| 20-Apr-05 | 13 | CH4 | 605 | 605.0 | 1.37E+06 | 3.28E+07 | 1.22 | 0.131 |
| 20-Apr-05 | 14 | CH4 | 605 | 605.0 | 1.69E+06 | 3.62E+07 | 1.22 | 0.147 |
| 11-May-05 | 11 | CH4 | 606 | 606.0 | 9.49E+05 | 2.19E+07 | 1.22 | 0.136 |
| 30-Mar-05 | 10 | H2 | 730 | 614.3 | 1.12E+06 | 2.80E+07 | 1.21 | 0.126 |
| 30-Mar-05 | 11 | H2 | 732 | 615.8 | 1.00E+06 | 2.43E+07 | 1.21 | 0.130 |
| 3-May-05 | 9 | H2 | 654 | 639.4 | 8.28E+05 | 1.99E+07 | 1.20 | 0.133 |
| 14-Apr-05 | 4 | H2 | 770 | 639.9 | 1.50E+06 | 3.35E+07 | 1.20 | 0.143 |
| 20-Apr-05 | 8 | CH4 | 710 | 710.0 | 1.44E+06 | 3.43E+07 | 1.17 | 0.137 |
| 20-Apr-05 | 7 | CH4 | 710 | 710.0 | 1.62E+06 | 3.32E+07 | 1.17 | 0.160 |
| 11-May-05 | 7 | CH4 | 716 | 716.0 | 8.41E+05 | 1.72E+07 | 1.16 | 0.161 |
| 23-Aug-05 | 4-6 | CH4 | 750 | 750.0 | 2.10E+06 | 4.85E+07 | 1.15 | 0.144 |
| 3-May-05 | 3 | H2 | 770 | 752.0 | 7.96E+05 | 1.78E+07 | 1.15 | 0.149 |

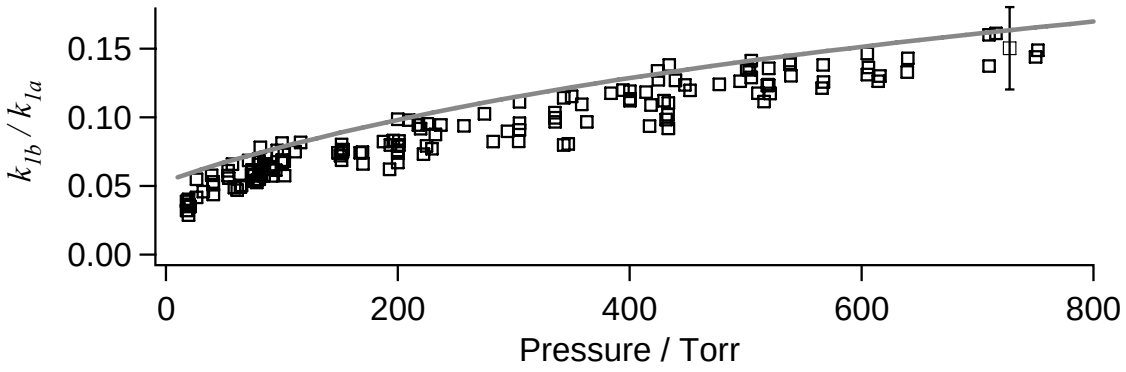


**Figure 3.20. Branching ratio data taken as a function of pressure. A representative 2σ error bar has been added to the point at 750 torr. The solid grey line represents the branching ratio obtained from the modeling fit of Golden et al. [49].**

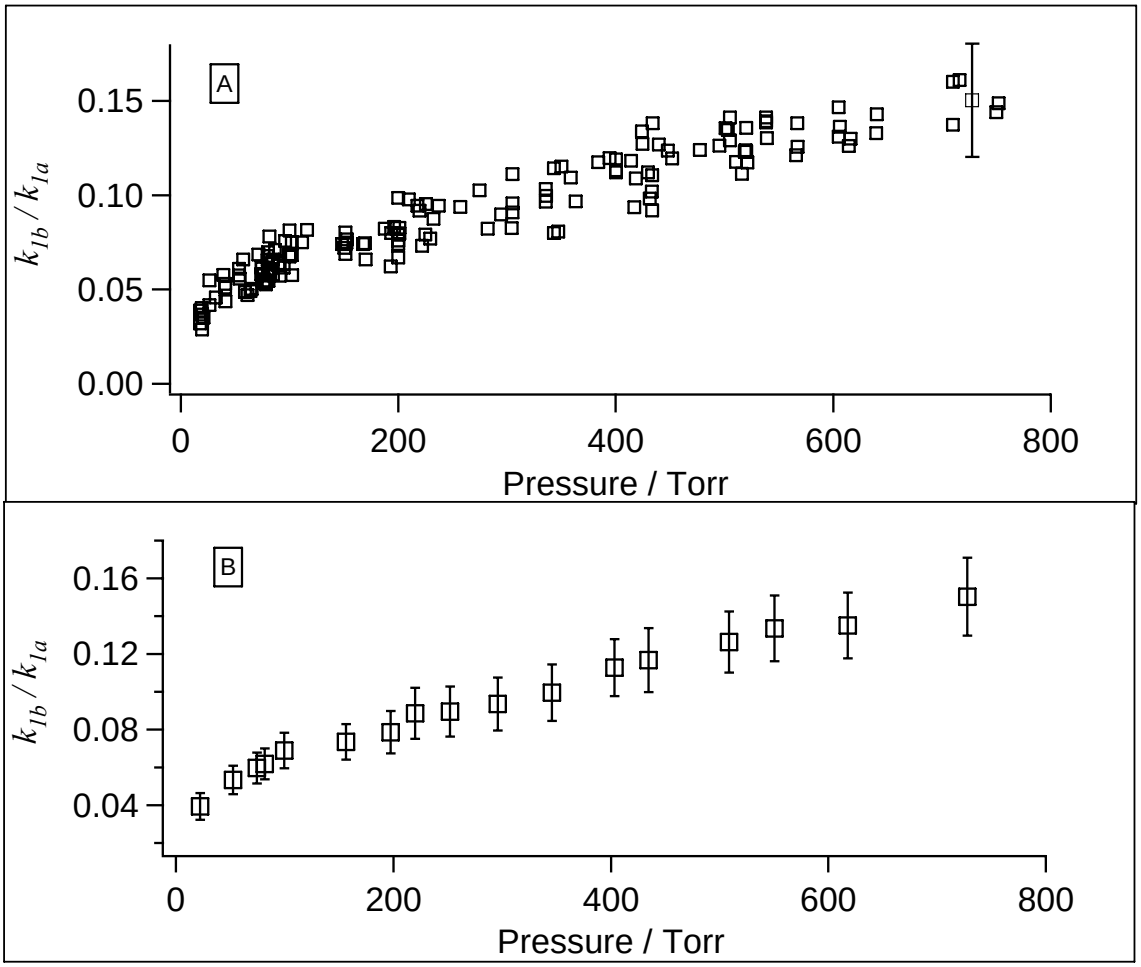


**Figure 3.21. Branching ratio data as a function of pressure. All data is shown in (a). A representative 2σ error bar has been added to the point at 750 torr. Data have been binned into groups and averaged in (b).**

In addition to the random experimental uncertainty represented by the scatter in the Figure 3.20 data, significant systematic uncertainties exist. The largest of these are uncertainties in the calculated ratio of intensities $E_{\mathrm{HONO2}}$ and $F_{\mathrm{Boltz}}$, estimated to be 5% each. These systematic uncertainties have been added to the estimated 7%-11% random uncertainty to give the overall 2σ uncertainty. An error bar representing this uncertainty in a single measurement has been included in Figure 3.21(a). The random uncertainty in the branching ratio at a given pressure is reduced, however, by the large amount of data

taken. Figure 3.21(b) shows the average of the data from Figure 3.21(a) binned into several pressure bins. The error bars shown combine the standard deviation of the mean for the data averaged combined with the systematic uncertainties. The HOONO branching ratio varies significantly with pressure, increasing from 0.039 ± 0.008 at 20 torr to 0.150 ± 0.025 at 760 torr.

## *3.4 Discussion*

### 3.4.1 Comparison With Past Results

#### 3.4.1.1 Stretch-Torsion Coupling

We can compare our calculated torsional energy levels to past calculations using only a 2D potential [45, 46]. The $\nu_9$ energy levels have now been calculated thrice by us and once by Amit Sinha's group, each with slightly different methods. The resulting energies and energies relative to the calculated zero-point energy are shown in Figure 3.22.

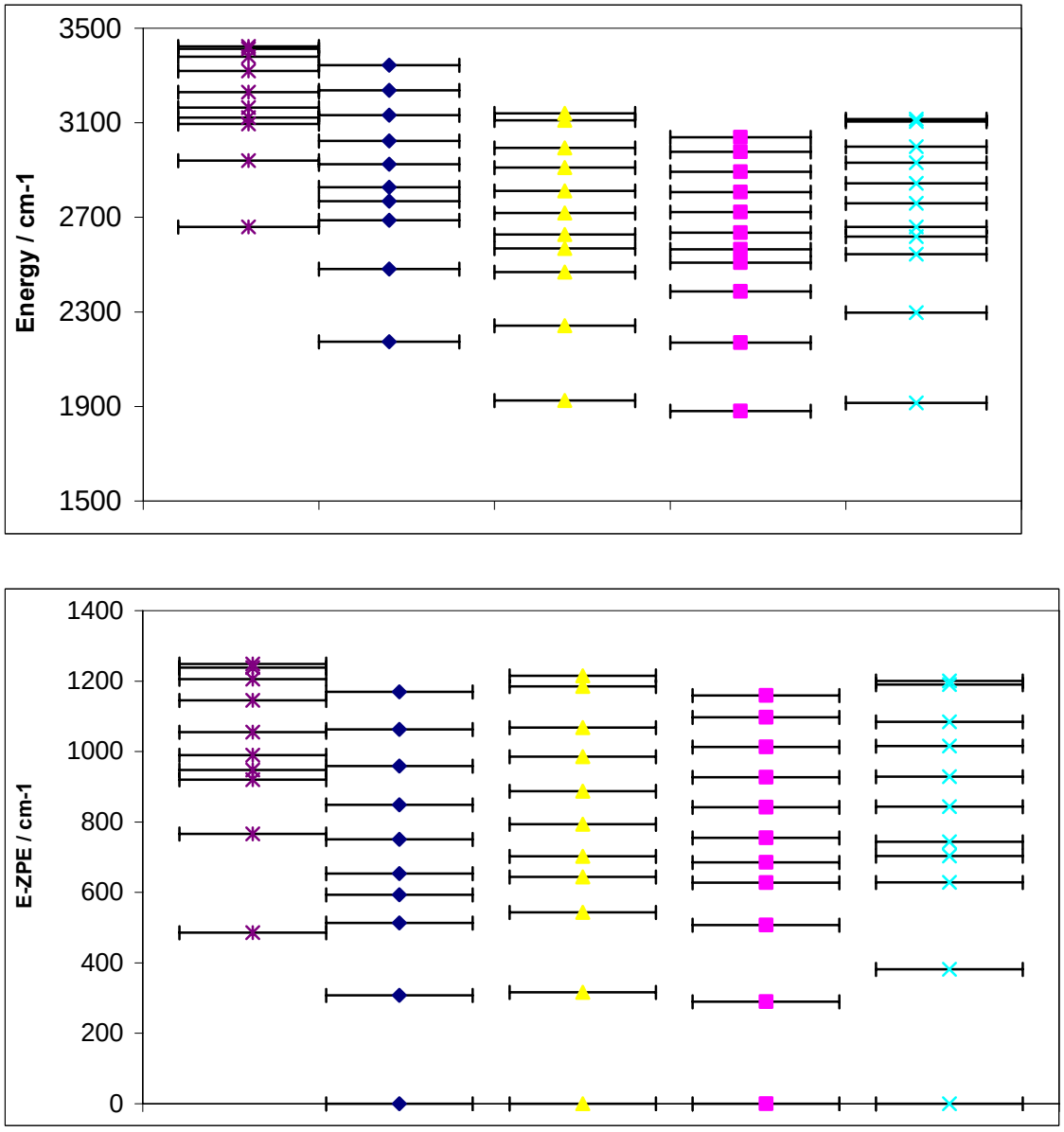


**Figure 3.22. Comparison of calculated HOONO torsion energy levels. All results are for $\nu_1$=0. From left to right: current results with $\nu_8$>0 (purple stars), current results with $\nu_8$=0 (blue diamonds), 2D results on minimum energy path along our 3D potential (yellow triangles), 2D calculations from Matthews et al.[45] with heavy atom geometries relaxed (pink squares), and 2D calculations from McCoy et al. with the heavy atoms fixed[46]. The bottom panel shows the energies relative to the zero-point energy.**

We see that the relative energies of the $\nu_9$ levels when some flexibility of the heavy atoms is included (the middle three sets of points) are very similar. Explicitly adding the coupling to $\nu_8$ does not make a large change the $\nu_9$ levels relative to those of

Matthews et al. [75]. It does, however, add eight levels with $\nu_8 \neq 0$ less than 1200 $cm^{-1}$ above the ZPE.

I make two observations about the above data: (1) the $\nu_9$ levels from our 3D potential are close to those from the best 2D potentials, even as high as 1200$cm^{-1}$ above the ZPE and (2) above the highest torsional level we currently have from the 3D potential, the McKoy et al. results indicate the levels increase fairly rapidly in energy. Therefore, while we currently have only calculated torsional states up to 1300 $cm^{-1}$ in energy using the 3D potential, we would expect torsional states higher in energy to have rapidly diminishing Boltzmann populations. As a result, we expect our future calculations of higher-energy states to have a negligible impact on the calculations of $F_{\text{Boltz}}$ described in Section 3.3.3.

#### 3.4.1.2 Branching Ratio

The most direct comparison of the results presented here are to the results we previously published in Bean et al. [7]. Before this comparison can be made, however, the results presented in Bean et al. must be revised to account for our improved knowledge of the spectroscopy involved. In Bean et al. we assumed $E_{\text{CRDS}} = 0.85$ and included no correction for torsionally excited HOONO absorption. We also now believe the ratio of cross sections to be 5% lower. Revisions of the published data plots are included with a re-print of the original paper in Appendix A. The published value of 0.075±0.020 at 298 K and 20 torr ($P_{\text{eff}}$ = 14 torr($N_2$)) should be revised to 0.047±0.013. This value and our current measurement of 0.039 ± 0.008 at 20 torr and 298 K agree within the uncertainty of each measurement. We might have expected the adjusted Bean

et al. value to be lower than our current measurement due to its lower effective pressure, but it is difficult to evaluate whether this is true given the large uncertainties involved.

Comparisons to other prior measurements are more tenuous. The extreme pressures and temperatures of Hippler et al. make a direct comparison with these results meaningless. We can say that our results qualitatively agree with their measurement of $k_{1b}/k_{1a}$ = 0.15 at 430 K and 5 bar He [60] since we would expect the branching ratio to increase with pressure and decrease with temperature. D'Ottone et al. measured $k_{1b}/k_{1a}$ = 0.10±0.03 at 413 K and 400 torr He [59]. Again it is difficult to make a quantitative comparison, but this result generally agrees with our data.

Our measured pressure-dependence can also be compared to the modeling studies. For ease of comparison, the branching ratio obtained by Golden et al. [49] and Hippler et al. [47] have been superimposed with our data and previous measurements in Figure 3.23.

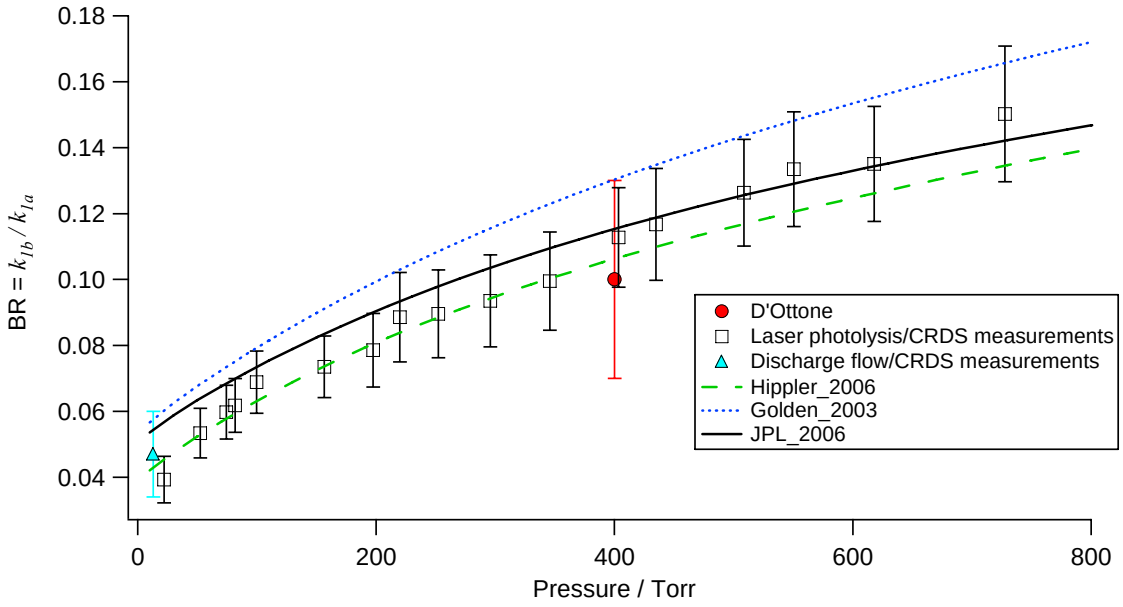


**Figure 3.23. Comparison of current branching ratio measurements with prior data from Bean et al. [7] and D'Ottone et al. [59], modeling results from Golden et al. [49] and Hippler et al. [47], and the current JPL kinetics data evaluation.**

The general shape of our data agrees with the results of both modeling studies. Our results at low pressure agree better with the results of Hippler et al.. It is unclear whether the published branching ratio in Bean et al impacted the results of Golden et al. and caused their low-pressure branching ratio to be increased. At pressures above 400 torr our data lie between the two modeled results. The older modeling results of Matheu and Green [66] and Troe [67] are qualitatively similar in shape but differ quite substantially in the magnitude of their branching ratios under these conditions. Our measurements above 400 torr actually agree reasonably well with the branching ratio derived from the current JPL data evaluation, although the general shape of the branching ratio over the entire pressure range does not.

### 3.4.2 Atmospheric Implications

Based on our branching ratio measurements, we recommend a nitric acid yield ($\Phi = k_{1a} / k_{1a}+k_{1b}$) at 1 atm and 298 K of

$$\Phi_{HONO_2}\left(298\ \text{K}, 1\ \text{atm}\right) = 0.87 \pm 0.03 .$$

Because HOONO redissociates rapidly under atmospheric conditions, the significant HOONO branching ratio we observe acts to lower the critical rate constant $k_{1a}$ and reduce the efficiency of R1 as a sink for $HO_x$ and $NO_x$. Specifically, $k_{1a}$ should be obtained from measurements of the total rate constant $k_1$ under these conditions from the expression

$$k_{1a} = \Phi_{HONO_2} \times k_1 .$$

This has important implications for our understanding of photochemical smog production. The primary effect of lowering $k_{1a}$ is an increase the lifetime of $HO_x$ and $NO_x$, resulting in greater ozone production per unit emission of these species. A recent analysis by Martien and Harley evaluated the sensitivity of modeled ozone outputs to nearly 900 model parameters [4]. In their models of 8-hour peak ozone for Rubidoux, CA (east of Los Angeles) they found that the most influential rate constant for ozone production in their model was $k_{1a}$. The only input parameter with a larger influence on ozone concentrations was the emissions inventory for $NO_x$.

They calculated a seminormalized sensitivity of modeled ozone to $k_{1a}$ of -50 ppb in polluted areas of eastern Los Angeles [4]. A 13% reduction in $k_{1a}$ due to HOONO production would therefore result in a 7 ppb increase in modeled ozone concentrations. This effect would not be limited to areas of extreme pollution, however. An earlier study by Tonnesen found that a 20% decrease in $k_{1a}$ would result in a 6%-16% increase in

ozone concentrations in typical urban conditions and even a 2%-6% increase in ozone concentrations for typical rural conditions [3]. The Tonnesen study also found that a downward adjustment of $k_{1a}$ would change the relative effectiveness of $NO_x$ vs. volatile organic carbon emission control strategies. The direct impact of a 10%-15% HOONO yield on photochemical models would therefore be significant. $k_{1a}$ is also an important parameter in deriving the ozone-forming potentials of hydrocarbons and therefore an adjustment of this value may have secondary impacts upon model outputs.

Another important secondary impact of these branching ratio measurements will be to reduce the uncertainty in the rate constants associated with reaction 3.1a. As discussed above, the two major kinetics data evaluations disagree on the parameters used to describe the pressure dependence of $k_{1a}$ and give large error bars to their parameters. The resulting discrepancy at 1 atm of greater than 10% and the 30% uncertainties are both large for a reaction of such importance. A critical review of photochemical models by Russell and Dennis found that the uncertainty in $k_{1a}$ contributed a significant fraction to the uncertainty in ozone predictions under all conditions [76]. Much of the evaluation uncertainty stems from the prior lack of data on the HOONO branching ratio. The pressure-dependent branching ratio reported here should therefore not only change ozone concentrations from photochemical models, but also reduce this uncertainty in these concentrations.

# 4 Reaction Pathways of Alkoxy radicals

## *4.1 Introduction*

Volatile organic hydrocarbons (VOCs) are released into the atmosphere in large quantities from both anthropogenic and biogenic sources. Once in the troposphere, VOCs are degraded through oxidation initiated by reaction with radicals or photolysis. In these oxidative processes, alkoxy radicals (RO) are often a key intermediate that can react further via one of several mechanisms. The branching ratios of the various pathways determine the distribution of final oxidation products, and therefore impact the extent to which emitted VOCs contribute to the formation of ozone, smog, and secondary organic aerosols.

The oxidation of alkanes (denoted RH here) provides the simplest example of alkoxy radical chemistry. In the presence of $NO_x$, alkoxy radicals are formed from alkanes in the troposphere predominantly by the following mechanism:

$$RH + \bullet OH \longrightarrow R\bullet + H_2O, \qquad \text{Reaction 4.1}$$

$$R\bullet + O_2 \xrightarrow{M} RO_2\bullet, \qquad \text{Reaction 4.2}$$

$$RO_2\bullet + NO \longrightarrow RO\bullet + NO_2. \qquad \text{Reaction 4.3}$$

The $NO_2$ formed in this process undergoes photolysis in the troposphere (<425 nm) to yield O atoms that subsequently react with $O_2$ to generate ozone. Alkoxy radicals react further via one of three mechanisms: α-hydrogen abstraction by $O_2$ to form a carbonyl and $HO_2$, unimolecular isomerization involving a 1,5-hydrogen shift via a cyclic

transition state, or unimolecular dissociation via β-scission. These three reactions for the *n*-butoxy radical (a primary alkoxy radical) and the 2-pentoxy radical (a secondary alkoxy radical) are shown below.

*n*-butoxy: $O_2$

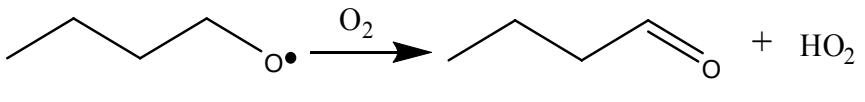


Reaction 4.4

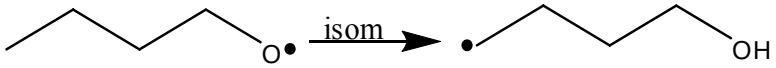


Reaction 4.5

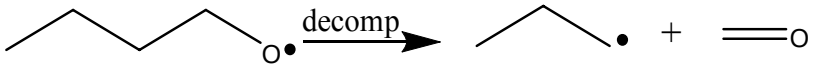


Reaction 4.6

2-pentoxy:

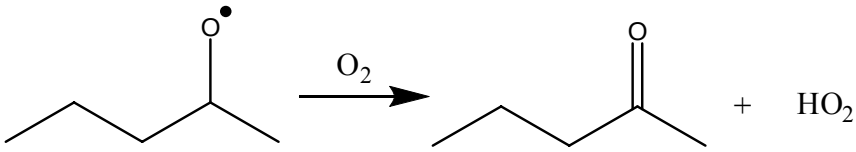


Reaction 4.7

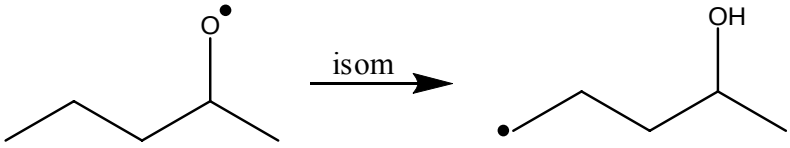


Reaction 4.8

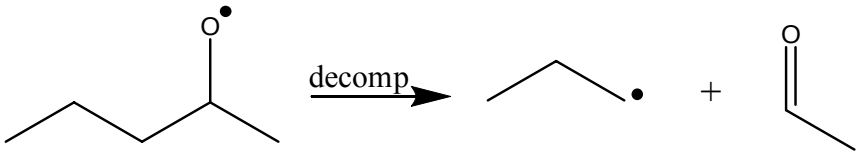


Reaction 4.9

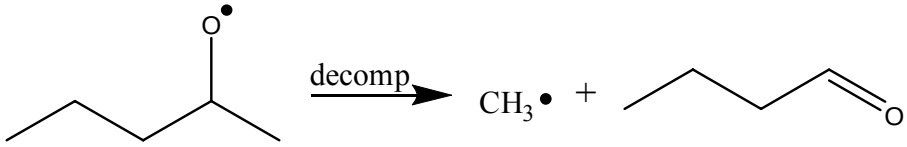


Reaction 4.10

The potential energy surface over which these reactions proceed for the *n*-butoxy radical is shown in Figure 4.1. The branching ratio for each of these pathways depends critically upon the structure of the alkoxy radical. All alkoxy radicals containing an α-hydrogen can undergo reaction with $O_2$. While the rate constant for reaction with $O_2$, $k_{O2}$, has been observed to vary slightly with temperature and the structure of the alkoxy radical, measurements of $k_{O2}$ have generally yielded values within a factor of two of $1\times10^{-14}$ $cm^3$ $molec^{-1}$ $s^{-1}$ at 298 K [77, 78]. Variations in $k_{isom}$ and $k_{decomp}$ with pressure, temperature, and molecular structure are much larger, spanning many orders of magnitude because of the significant barriers involved and differences in the densities of states.

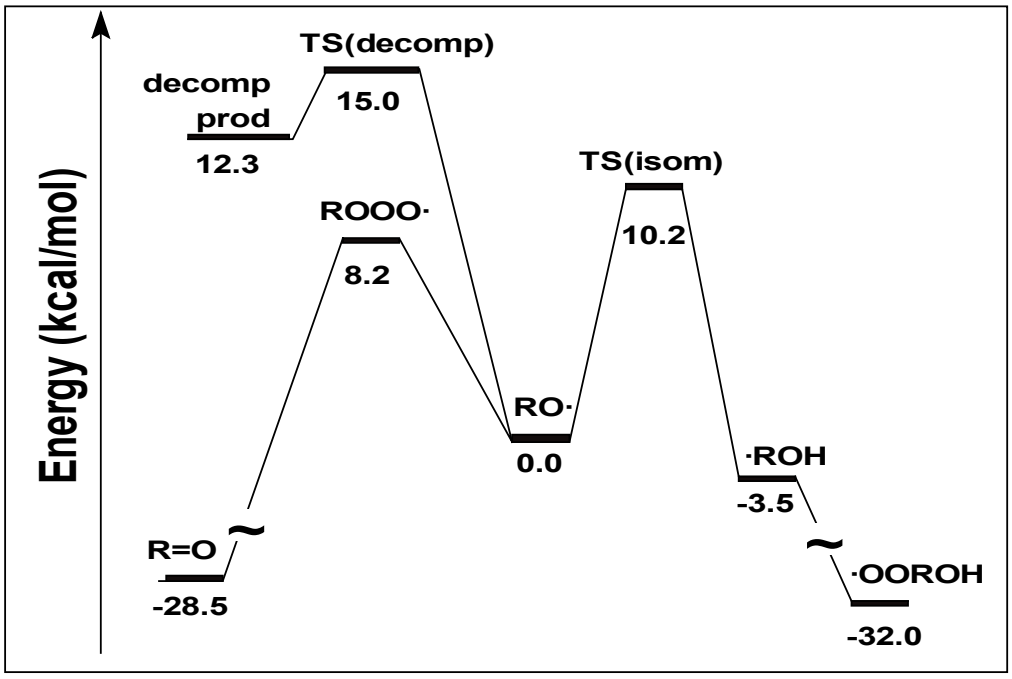


**Figure 4.1. Energy diagram for the decomposition (top left), reaction with $O_2$ (bottom left), and isomerization reactions (right) of *n*-butoxy radicals. Energies for the isomerization and decomposition are taken from Somnitz and Zellner [79, 80] at the modified G2(MP2,SVP) level of theory, while energies for the reaction with $O_2$ are taken from Jungkamp et al.[81] at the B3LYP/6-311+G(3df,2p)//B3LYP/6-31G(d,p) level of theory. All energies listed are relative to the *n*-butoxy radical.**

Only alkoxy radicals that can form a 6-membered ring transition state have a sufficiently low barrier for unimolecular isomerization to be atmospherically relevant [82-86]. The isomerization rate increases when the product is a secondary or tertiary alkyl radical, due to a lowering of the barrier to reaction [82]. Unimolecular decomposition is an available pathway for all alkoxy radicals. Similar to isomerization, the rate of unimolecular decomposition has a strong structural relationship. The rate increases when the transition state is stabilized through substitution at the α- or β-carbon.

The reaction pathways of alkoxy radicals have been the subject of many studies, both experimental and theoretical. Several reviews are available [77, 78, 82, 87-89]. For molecules with all three reaction pathways "open", isomerization and reaction with $O_2$ dominate under atmospheric conditions. Isomerization has been a particularly difficult process to study experimentally due to the wide range of values of $k_{isom}$ and the fast secondary chemistry. In molecules that cannot form a 6-membered ring, isomerization is too slow to compete with reaction with $O_2$ or decomposition. In molecules that can form a 6-membered ring, isomerization generally occurs on the timescale of microseconds or less. As opposed to reaction with $O_2$ or decomposition, isomerization also has no stable product that can be detected long after reaction occurs. As a result, the isomerization of alkoxy radicals has not yet been observed directly. This results in a major uncertainty in the kinetics of alkoxy radicals.

Many previous studies of $k_{isom}$ have focused on the simplest alkoxy radicals that can undergo isomerization: *n*-butoxy and 1- and 2-pentoxy. Under conditions relevant to the lower atmosphere (300K, 1 bar, 21% $O_2$) the lifetime for reaction with $O_2$ is on the order of 20 μs. Previous relative rate measurements have estimated the lifetimes for

isomerization under these conditions to be on the order of 5 μs for reaction 4.5 and 3 μs for reaction 4.8. The decomposition reactions have been estimated to occur on longer timescales: on the order of 1 ms for reaction 4.6 and 100 μs for reaction 4.9. As a result, isomerization and reaction with $O_2$ are expected to be the dominant fates for these alkoxy radicals.

Most previous experimental measurements have been conducted in static smog chambers or slow-flow gas kinetic cells in which the concentration of the end products were measured [83, 85, 86, 90-95]. Alkoxy radicals were produced through generation of the corresponding alkyl radical followed by reactions 4.2-4.3 or by UV photolysis of the corresponding alkyl nitrite. The relative rate constants for isomerization to reaction with $O_2$ ($k_{isom}/k_{O2}$) were estimated by measuring the concentrations of end products as a function of oxygen pressure. Often, several reaction pathways can generate the same products, and so it can be difficult to deduce reaction mechanisms by relying on end-product data [81].

In the presence of $O_2$, the hydroxyalkyl radicals formed in reactions 4.5 and 4.8 rapidly associate with $O_2$ to form a hydroxy peroxy radical.

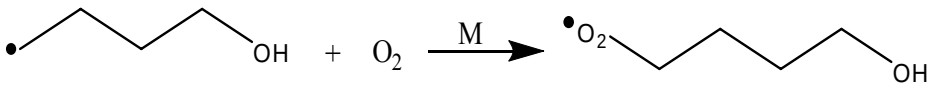


Reaction 4.10

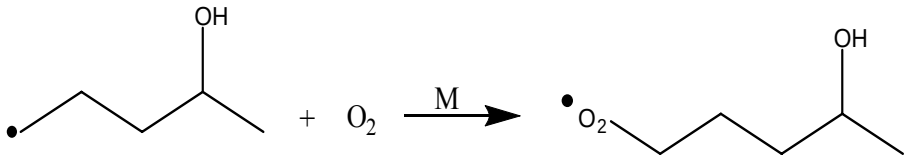


Reaction 4.11

Under lower atmospheric conditions, this association reaction occurs on the order of 50 ns. Most prior experiments have included NO. In this case the products of

reactions 4.10 and 4.11 react with NO via reaction 4.3 to generate a secondary alkoxy radical. This secondary alkoxy radical can also undergo reaction via several pathways, leading to a large variety of possible end-products as well as end products that can be generated by many different pathways. Hein et al. [96] made the only measurement of $k_{isom}$ that did not rely on end product analysis. They measured the secondary production of OH and $NO_2$ using laser-induced fluorescence and then fit their observed time profiles using a kinetic model. This measurement still relied upon an accurate knowledge of secondary kinetics and was limited to low pressures (P = 50 mbar).

An additional concern in studying the reaction pathways of alkoxy radicals is the possibility of preparing vibrationally excited alkoxy radicals. Hot alkoxy radicals result from excess nitrite photolysis energy or the exothermicity of reaction 4.3. Some of this energy is distributed in the vibrational modes of the alkoxy radicals. Vibrationally hot alkoxy radicals could undergo prompt isomerization (reaction 4.12) or prompt decomposition (reaction 4.13) before becoming thermalized by collisional energy transfer:

$$RCH_2O\bullet^* \rightarrow \bullet RCH_2OH \qquad \text{Reaction 4.12}$$

$$RCH_2O\bullet^* \rightarrow \bullet R' + CH_2O \qquad \text{Reaction 4.13}$$

Two previous experiments have addressed the role of hot alkoxy radicals. Geiger et al. prepared *n*-butoxy radicals from 254 nm photolysis of a *n*-butyl iodide/$O_2$/NO/$N_2$ mixture, and noted that their observed oxygen dependence on $k_{isom}/k_{O2}$ was best explained by the presence of 10%-20% hot butoxy radicals [97]. Cassanelli et al. prepared *n*-butoxy radicals by photolyzing *n*-butyl nitrite at 370 ± 10 nm (FWHM) and estimated a 10% yield of product due to nonthermal prompt isomerization [95].

In contrast to previous studies, the experiments described here directly detect the primary isomerization products of *n*-butoxy and 2-pentoxy radicals. Alkoxy radicals were generated through the UV photolysis of the corresponding alkyl nitrites. Product spectra were then taken using infrared cavity ringdown spectroscopy (CRDS). CRDS utilizes a high finesse optical cavity to measure very small absorbances and is an increasingly popular method for monitoring trace species [8, 98, 99]. While other studies have detected products on timescales of minutes to hours after initiating the reaction, our CRDS spectrometer afforded detection of reaction products 10-100 μs after the generation of alkoxy radicals. Additionally, the high sensitivity of CRDS enabled us to work with low concentrations of alkoxy radicals and NO ($[RO]=[NO]\approx10^{14}$ molecules$\times$cm$^{-3}$). This minimized the generation of secondary alkoxy radicals from reaction 4.3 and possible RO + RO side reactions. As a result, we have been able to make the first direct measurements of the products of alkoxy radical isomerization.

Our measurements were made with a slow-flow cell coupling laser photolysis for the generation of alkoxy radicals and pulsed infrared CRDS for the detection of the OH-stretch band formed from the isomerization reactions 4.5 and 4.8. Since these reactions were too fast for us to measure the isomerization kinetics directly, we measured the relative rate $k_{isom}/k_{O2}$ by measuring the primary isomerization product concentration as a function of $O_2$ concentration. The measurement of products on short timescales has also allowed us to evaluate the role of prompt unimolecular reactions in our system.

## 4.2 Experimental Methods

These experiments were the continuation of a project started by Eva Garland. The general experimental method used in the experiments described here was the same as for the first generation of experiments described in her thesis [20]. The main challenge found in her early work was poor signal to noise due to low photolysis yields and large background due to photolysis precursors. We have made improvements in these areas through a more powerful excimer and a new photolysis cell designed to minimize dead volume and UV scatter.

Our experimental setup consisted of a slow-flow cell in which alkyl nitrite precursors were photolyzed with an excimer laser to generate alkoxy radicals. These experiments were performed at a pressure of 670 torr, with mixtures of $O_2$ and $N_2$ used as bath gases. The experimental repetition rate was 10 Hz, and the gas mixture was flushed through the cell every 70 ms, so that a fresh gas sample was probed with each laser pulse.

The reaction products were probed with IR-CRDS. Pulsed infrared radiation was generated with an optical parametric amplifier (OPA) at the difference frequency between the outputs of a doubled YAG (532 nm) and a tunable dye laser (approximately 630 nm). The time between the photolysis and the detection was varied from 0 to 100 μs in order to obtain the time profile of product formation. The time resolution of the detection was limited by the ringdown time. Approximately 40 μs of the ringdown curve were used to generate an exponential fit for which the 1/*e* time was approximately 3-5 μs. Spectra were collected by averaging 16 shots with the excimer on and then 16 shots with the excimer off at each wavelength. The signal with the excimer off (no alkoxy radical

formation) was subtracted to eliminate background from precursor gases and changing mirror reflectivity.

We employed this setup to measure the infrared spectra of alkoxy radical reaction products. Spectra were recorded from 3400 to 3700 $cm^{-1}$, and the OH stretch in this region was used to identify the products from the isomerization pathway. As shown in reactions 4.4-4.11, isomerization is the only pathway of alkoxy radicals that is expected to yield products containing a hydroxyl group. The observed OH stretch peak was also monitored as a function of $O_2$ concentration to measure the rate of isomerization of alkoxy radicals relative to the rate of their reaction with $O_2$, $k_{isom}/k_{O2}$.

### 4.2.1 Generation of Alkoxy Radicals

Alkoxy radicals were generated *in situ* from their nitrite precursors with the output beam from an excimer laser (Lambda Physik LPX 200) at either 254 nm or 351 nm:

$$RONO + h\nu \rightarrow RO\bullet + NO. \qquad \text{Reaction 4.14}$$

Alkyl nitrites were introduced to the cell by bubbling nitrogen through a bubbler kept at 0 $^{o}C$. The concentration of alkyl nitrites was determined by an absorption measurement of the helium/alkoxy nitrite flow at 254 nm. The cross section of methyl nitrite at 254 nm is $1 \times 10^{-18}$ $cm^2$, and the cross section for the other alkyl nitrites is expected to be similar. Alkyl nitrite concentrations in the reaction cell were kept as low as possible (on the order of $10^{16}$ $cm^{-3}$) to minimize spectral interference from their broad absorption of infrared radiation in the 3300-3750 $cm^{-1}$ range.

The butyl nitrite precursors were purchased from Aldrich (95% purity). 2-pentyl nitrite was synthesized from pentanol in aqueous sodium nitrite, using a modification of the synthesis of 1-butyl nitrite described in *Organic Syntheses vol. 2* [100]. Briefly, a cold mixture of sulfuric acid and 2-pentanol was added slowly to a cold aqueous solution of sodium nitrite. The crude product was distilled to reduce the amount of excess residual pentanol. Based on FTIR spectra of the distilled 2-pentyl nitrite, the ratio of 2-pentyl nitrite to 2-pentanol was 8/1. Nitrogen and oxygen were used as bath gases, and the relative ratios of these gases in the reaction cell were used in the determination of the ratio of $k_5/k_4$. Gas flow rates were measured with mass flowmeters (Omega, Edwards) calibrated volumetrically. Gases were mixed in a glass cross 5 cm upstream from the photolysis region. Typical experimental conditions are listed in Table 4.1.

**Table 4.1. Typical experimental conditions for alkoxy radical isomerization studies.**

| | |
|---|---|
| $N_2$ Purge Flow–Left Mirror | 650 sccm |
| $N_2$ Purge Flow–Right Mirror | 650 sccm |
| $N_2$ Bubbler Flow | 225 sccm |
| $N_2$ Dilution Flow | 0–6000 sccm[a] |
| $O_2$ Dilution Flow | 0–6000 sccm[a] |
| Cell Pressure | 670 torr |
| Temperature | 295 K |
| Residence Time | 70 ms |
| Optical Cell Length | 55 cm |
| Photolysis Window Length | 6 cm |
| Excimer Energy at 351 nm | 200 mJ/pulse |
| $\Delta\tau/\tau$ | 0.4% |

**a The sum of the $N_2$ and $O_2$ dilution flows was kept constant at 6000 sccm.**

Most experiments were performed while operating the excimer laser at 351 nm. At this wavelength, the typical output energy was 200 mJ / pulse. The output beam, initially 3 cm × 1 cm, was focused vertically and expanded radially so that the resulting

beam at the cell was 6 cm × 0.3 cm, collimated in the vertical axis and slightly divergent horizontally. The flux of photons entering the cell was $1.0 \times 10^{17}$ photons $cm^{-2}$ resulting in approximately 1% photolysis of the nitrite precursors ($\sigma_{351} = 8 \times 10^{-20}$ $cm^2$).

Experiments with the excimer laser operating at 248 nm were performed previously by Eva. For these experiments, the output beam was focused vertically and expanded radially so that the resulting beam at the cell was 10 cm × 0.5 cm. The typical output energy was 125 mJ / pulse, resulting in approximately 5% photolysis of the nitrite precursors ($\sigma_{351} = 1.3 \times 10^{-18}$ $cm^2$) [20].

The timing of the excimer and YAG lasers was controlled by digital delay generators (SRS model DG535 and EG&G Princeton Research Model 9650). This set the time delay between the preparation of reactants (via photolysis) and the detection of products with cavity ringdown spectroscopy. Data were collected in two modes: frequency spectra were obtained by holding the photolysis-probe delay fixed (typically at 100 μs) and scanning in frequency space, while kinetics scans were obtained by holding the IR wavelength fixed and varying the photolysis-probe delay. In both cases ringdown traces were collected at each point with the excimer on and with the excimer off. The frequency-dependent background of precursor gases and mirror reflectivity could then be subtracted.

### 4.2.2 CRDS Detection

A schematic of the apparatus is shown in Figure 4.2. The gas kinetics cell consisted of a 7 cm × 1 cm metal rectangular tube, coated with a fluoropolymer (FluoroPel PFC 801A/coFS) to minimize reactions at the walls. Fused silica windows of

6 cm length were placed on two sides of the cell to allow light from an excimer laser to pass through. The cell was coupled to ringdown mirrors via Teflon blocks containing ports for introducing reactant gases and measuring the cell pressure. For gas flow cell dimensions and assembly details see appendix B.

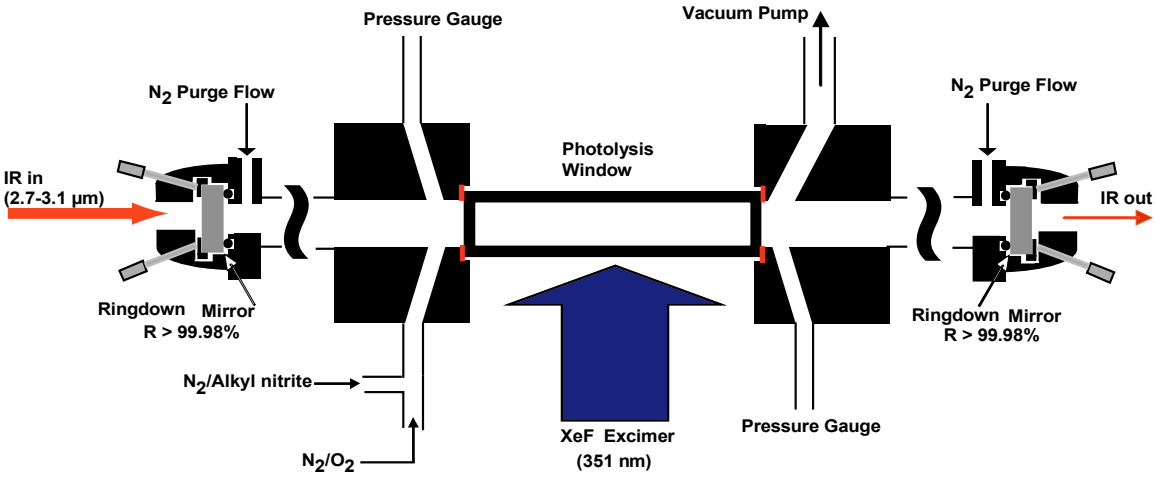


**Figure 4.2. Diagram of the UV photolysis / gas kinetics cell. Experiments were conducted at 670 torr and 295 K. Typical residence time for the gases was 70 ms.**

Details of the cavity ringdown apparatus are given in Chapter 1. For these experiments, the purge volume consisted of 24-cm long glass tubes connected to the ringdown mirror mounts and the Teflon blocks via Ultra-torr adapters. Ringdown data were collected for 40 μs after the Nd:YAG laser fired, at a rate of 50 MSa $s^{-1}$. Ringdown traces from 16 shots were averaged and then fit to an exponential decay using a Levenberg-Marquardt algorithm. Typical background ringdown times were on the order of 7 μs. The standard deviation of successive ringdown times obtained for an empty cell was typically 0.4%, giving a minimum detectable absorbance of 2.6 ppm per pass $Hz^{-½}$. In the presence of the alkyl nitrite precursor, typical ringdown times were on the order of

3 μs. The standard deviation of successive ringdown times was typically 0.4%, giving a minimum detectable absorbance of 6.1 ppm per pass $Hz^{-½}$.

### 4.2.3 Relative Kinetics Measurements

We have measured an absorption feature in the infrared we attribute to the initial product of isomerization. We have used this spectral feature to measure the relative rate of isomerization to reaction with $O_2$ at 298 K. This was accomplished by measuring the decrease in the absorbance of this feature as a function of $O_2$. From this, $k_{isom}/k_{O2}$ was derived.

## *4.3 Results*

### 4.3.1 Chemistry

Photolysis of the alkyl nitrites in the UV leads to prompt dissociation on the excited state surface.

$$RONO + h\nu \rightarrow RO\bullet + NO\bullet \qquad \text{Reaction 4.14}$$

The nascent products RO• and NO• appear on timescales of <1ps. At the laser fluences used at 351 nm, we expect $[RO\bullet] \approx 2\times10^{14}$ molecules×$cm^{-3}$ (~1% photolysis of the precursors). Based on rate constants from the literature, isomerization for *n*-butoxy and 2-pentoxy radicals occurs on time scales of ~5 μs and ~2 μs, respectively [82],

$$RO\bullet \rightarrow HOR\bullet\ , \qquad \text{Reactions 4.5, 4.8}$$

while decomposition occurs on time scales of ~50 ms. At the low concentrations used, recombination reactions of RO• with NO• or RO• ,

$$RO\bullet + RO\bullet \rightarrow ROOR, \text{ other products,} \qquad \text{Reaction 4.15}$$

$$RO\bullet + NO\bullet \rightarrow RONO, \qquad \text{Reaction 4.16}$$

are approximately two orders of magnitude slower than isomerization. Thus, isomerization or the competing reaction with $O_2$ to form $HO_2$ and the respective aldyehyde or ketone will be the dominant fate of the alkoxy radicals. The next question is then the identity of the observed bands.

In the absence of $O_2$ the fate of the isomerization products, the hydroxy-alkyl radicals HOR•, is either recombination with NO• or self-association.

$$HOR\bullet + HOR\bullet \rightarrow (HOR)_2 \qquad \text{Reaction 4.17}$$

$$HOR\bullet + NO\bullet \rightarrow HORNO \qquad \text{Reaction 4.18}$$

If we assume that the HOR• + HOR• association reactions are in the high pressure limit with a gas kinetic rate constant $2\times10^{-11}$ $cm^3s^{-1}$, then the initial lifetime is 130 μs. At 100 μs, approximately 50% of the HOR• radicals will have recombined. The high pressure rate coefficient for association with NO is expected to be approximately $3\times10^{-12}$ $cm^3s^{-1}$. Thus, at 100 μs approximately 50% of the observed OH signal will come from HOR• monomers, with the remainder having dimerized to form a 1,8-octyl diol. Less than 4% as RONO and a similar small percentage may have undergone hydrogen abstraction to form butanol and a hydroxy-butene. We therefore assign these peaks both to the δ-hydroxy alkyl radicals and to their immediate reaction products.

In the presence of $O_2$, the hydroxyl-alkyl radicals HOR• will associate to form peroxy radicals HOROO• with a rate coefficient of roughly $7\times10^{-12}$ $cm^3s^{-1}$ [36],

$$HOR\bullet + O_2 + M \rightarrow HOROO\bullet , \qquad \text{Reaction 4.2}$$

although there is probably a minor channel to form $HO_2$ and a hydroxylated alkene. At 1 torr of $O_2$, the pseudo-first-order lifetime is 5 μs. Assuming that the rate constant for the

HOROO• self reaction is comparable to that for *n*-$C_4H_9O_2$ self-reaction ($4\times10^{-13}$ $cm^3$ $s^{-1}$ [101]), no appreciable reaction will occur in less than 1 ms. For all but the lowest $O_2$ pressures used in this experiment, all spectra observed at 100 μs in the presence of $O_2$ will be those of the hydroxyl peroxyl radicals.

### 4.3.2 Spectra

Figure 4.3 shows a series of infrared spectra obtained following the photolysis of alkyl nitrite precursors. All spectra shown were taken with a photolysis-probe delay of 100 μs and have had the background signal in the absence of photolysis subtracted. We see that the nitrite precursors and contaminants therein contributed significant background, roughly 10 times the signal due to products. This background was much worse for our synthesized 2-pentyl nitrite, presumably due to larger contamination due to remaining pentanol. We see that the signal to noise was much better for the n-butyl nitrite photolysis, but that in both cases a peak can be clearly distinguished in the OH stretch region. Spectra were collected while varying the photolysis-probe delay from 5 μs to 100 μs, and in all cases the spectra were identical, indicating that all peaks appear promptly, on timescales shorter than the time resolution of our experiment (5 μs). As a result, the observed features are all due to the alkoxy radicals or their immediate reaction products.

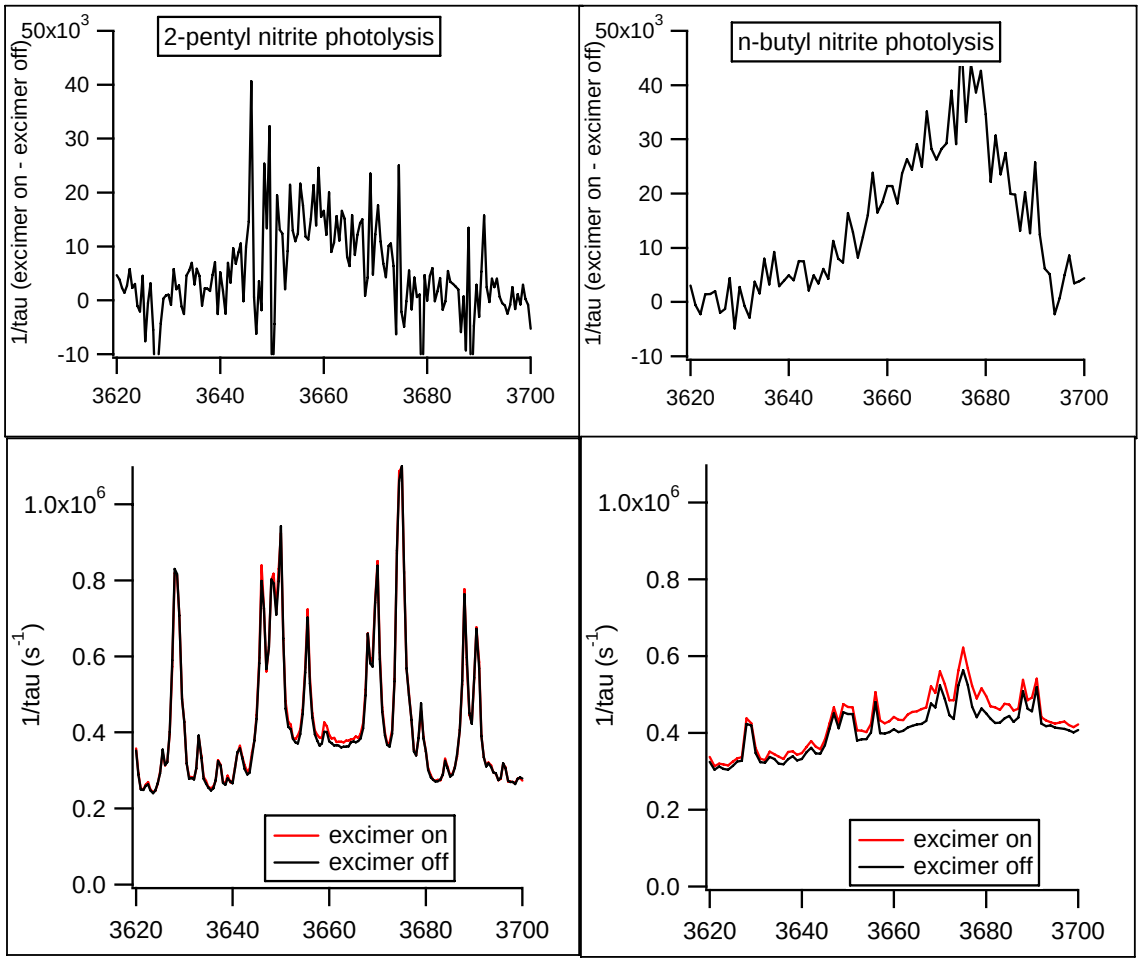


**Figure 4.3. Representative CRDS spectra of products formed 100 μs after photolysis. Raw data with and without the excimer photolysis are shown on the bottom while the top shows the subtraction of the two.**

An attempt was made to maximize the signal to noise by reducing precursor concentrations and increasing the UV flux. This was beneficial to a point, but eventually resulted in unintended negative consequences. Figure 4.4 shows the peak signal following n-butyl nitrite photolysis as a function of photolysis-probe delay. Standard time profiles are shown on the left. On the right are time profiles taken with the photolysis beam focused tightly to increase photon flux. While the peak signal appeared to be larger with the focused excimer, we also saw very large time-dependent peaks in the

signal. These peaks were shown to be independent of frequency and were attributed to photoaccoustic destabilization of the optical cavity. Following the observation of these photoaccoustic peaks, the photolysis cell was found to have black soot on the walls coincident with the transmission path of the excimer. Subsequent experiments were conducted with a more diffuse excimer beam to prevent this "burning" of the nitrites onto the windows.

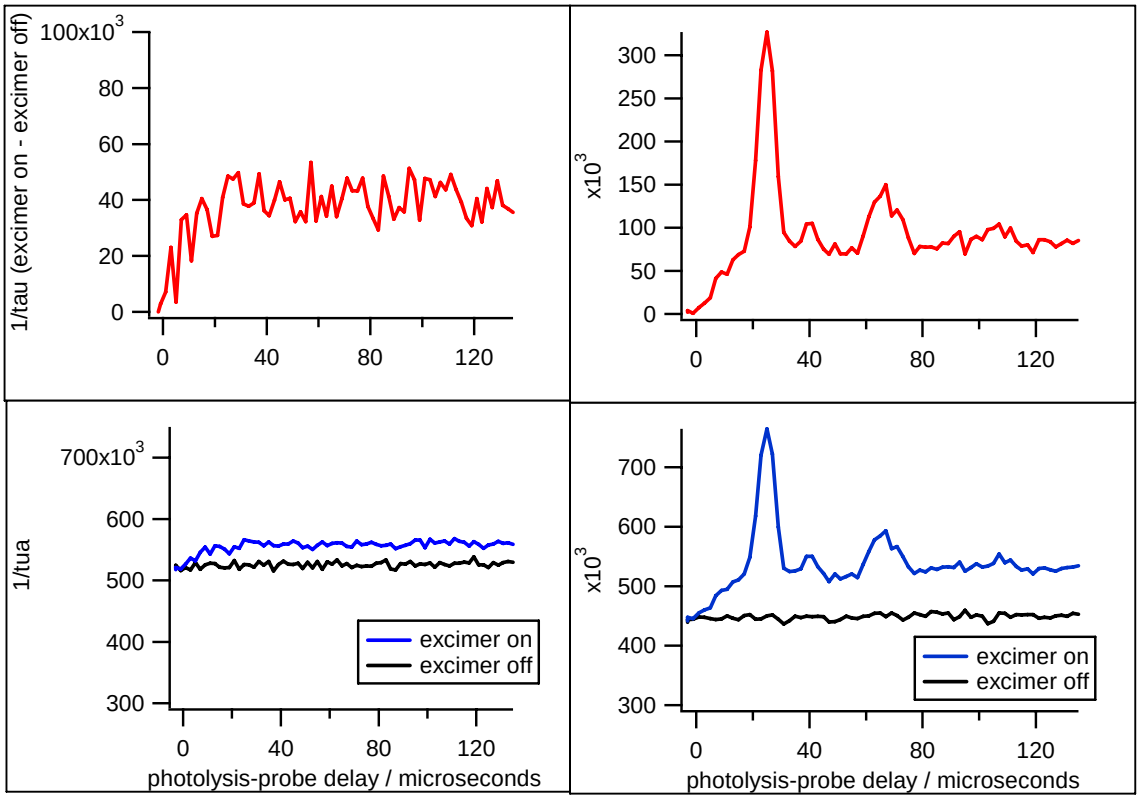


**Figure 4.4. CRDS signals at 3680 cm$^{-1}$ as a function of photolysis-probe delay. The left two panels were taken using our standard UV beam profile. The right two panels were taken with the UV profile focused tightly in the vertical direction.**

Figure 4.5, Figure 4.6, and Figure 4.7 all show the average of many spectra in this region to improve the signal to noise. Figure 4.5 shows the IR spectra of products formed following the generation of four different alkoxy radicals: *n*-butoxy, 2-pentoxy, isobutoxy, and *tert*-butoxy. All radicals were produced from photolysis of the

corresponding alkyl nitrites at 351 nm in the absence of $O_2$. Following photolysis of *n*-butyl nitrite and 2-pentyl nitrite, a clear peak is observed in the OH-stretch region at 3675 $cm^{-1}$. This peak does not appear following the photolysis of isobutyl nitrite or *tert*-butyl nitrite.

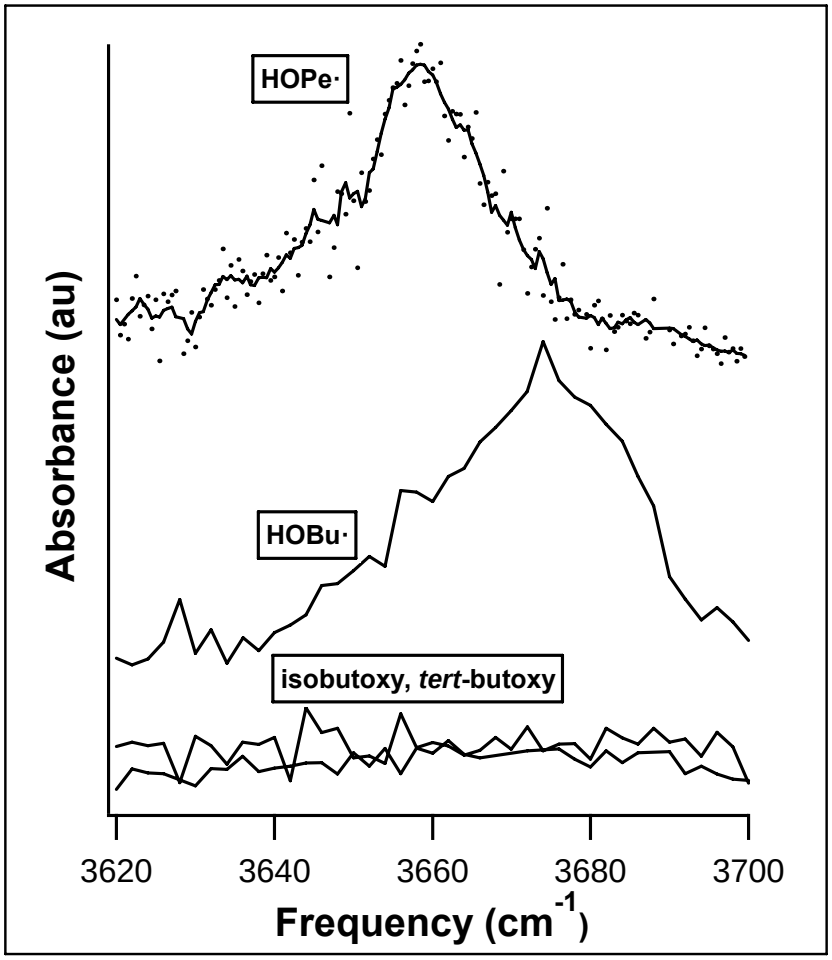


**Figure 4.5. OH stretch infrared spectra of the isomerization products of 2-pentoxy (δ-hydroxy-*n*-pentyl, top) and of *n*-butoxy (δ-hydroxy-*n*-butyl, middle). The product spectra following the generation of isobutoxy and *tert*-butoxy radicals (bottom) show no absorption features above our background noise.**

The shapes and positions of the peaks observed from *n*-butoxy and 2-pentoxy products are nearly identical to the OH-stretch bands found in the infrared spectra of *n*-butanol and 2-pentanol, respectively (Figure 4.6). As expected, we only observe the

alcohol OH-stretches from alkoxy radicals that are long enough to undergo a 1,5-hydrogen shift, and these peaks appear on the very fast timescales we would expect for unimolecular isomerization. Using literature values for $k_{isom}/k_{O2}$ and taking the OH absorption cross section of the isomerization products to be equivalent to *n*-butanol ($7.5 \times 10^{-20}$ $cm^{-2}$) [102] we estimate that the concentration of OH-containing isomerization products was approximately $1.5\times10^{14}$ molecules$\times cm^{-3}$. This is consistent with our estimate of the nitrite photolysis yield.

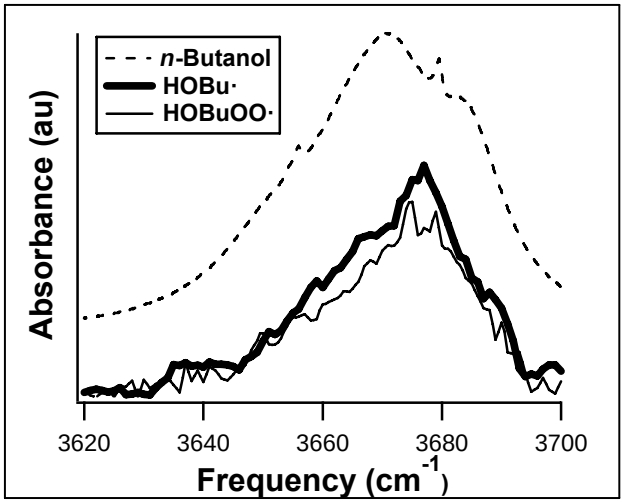


**Figure 4.6. Hydroxy stretch infrared spectra of *n*-butanol (top), the butoxy isomerization product (δ-hydroxy-*n*-butyl, middle), and the butoxy isomerization product in the presence of $[O_2] = 1\times10^{19}$ molecules$\times cm^{-3}$ (δ-hydroxy-*n*-butyl peroxy, bottom).**

Figure 4.6 compares three spectra: the photolysis products of *n*-butyl nitrite in the absence of $O_2$, the photolysis products of *n*-butyl nitrite in the presence of $O_2$, and the IR spectrum of butanol [103]. At our $O_2$ concentrations ($[O_2] = 1\times10^{19}$ molecules$\times cm^{-3}$), the initial δ-hydroxy-*n*-butyl isomerization product will associate with $O_2$ faster than the detection time of our experiment. We therefore assign the peak at 3675 $cm^{-1}$ in the

presence of $O_2$ to the δ-hydroxybutyl peroxy radical. We see that the presence of the peroxy group has minimal impact on the shape or position of the OH stretch band.

### 4.3.3 Prompt Isomerization and Decomposition

Figure 4.7 shows the IR spectrum of products formed following the photolysis of *n*-butyl nitrite at two UV wavelengths: 248 nm and 351 nm. In addition to the OH stretch peak, a second absorption feature is observed in the spectrum taken following photolysis at 248 nm. The feature centered at 3565 $cm^{-1}$ matches the position and band shape of the $2\nu_2$ band of formaldehyde, one of the products of unimolecular decomposition. Assuming a δ-hydroxy-*n*-butyl cross section similar to that of *n*-butanol, we estimate a 60% yield of decomposition upon photolysis at 248 nm. The observation of a significant decomposition yield was not expected based on estimates of the thermal rate constants. The photolysis spectrum obtained following 351 nm photolysis shows no evidence of formaldehyde. For typical experimental conditions, the minimum detectable limit for HCHO is $7 \times 10^{12}$ molecules×$cm^{-3}$. Since typical values of $[C_4H_9O]$ were $2 \times 10^{14}$ molecules×$cm^{-3}$, an upper limit of 5% of butoxy radicals undergo dissociation when butyl nitrite is photolyzed with 351 nm radiation. We therefore believe this formaldehyde is evidence of nonthermal (prompt) decomposition of *n*-butoxy radicals formed with a large amount of internal energy following photolysis at 248 nm.

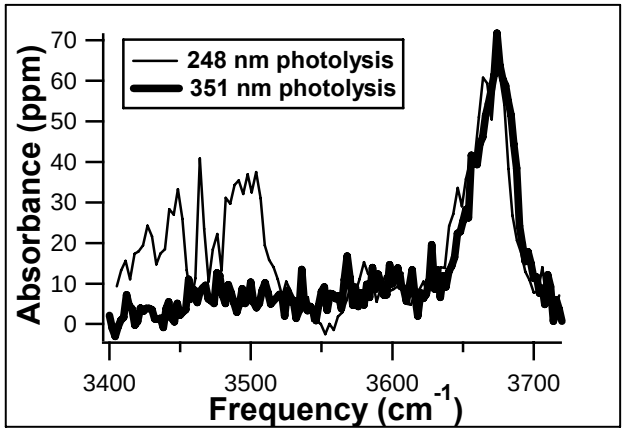


**Figure 4.7. Infrared spectra of the photolysis products of *n*-butyl nitrite at 248 nm and 351 nm. The peak at 3470 cm$^{-1}$ is assigned to formaldehyde, formed through prompt decomposition of the alkoxy radicals when generated through photolysis at 248 nm.**

While we see no evidence of prompt decomposition at 351 nm, it is still possible that prompt isomerization occurs, since the barrier for isomerization is calculated to be 5 kcal mol$^{-1}$ lower than that for decomposition [79, 80]. Since both prompt and thermal isomerization are expected to occur on timescales faster than our kinetic resolution, there is no direct method for us to measure the amount of prompt isomerization. However, if a significant fraction of our isomerization product was formed nonthermally, we would expect that to impact our relative rate measurement, as will be discussed in the next section. In order to minimize the impact of prompt unimolecular processes on our relative rate measurements, all kinetics data were taken using 351 nm as the photolysis wavelength.

### 4.3.4 Relative-Rate Measurements

Attempts to measure the δ-hydroxy-*n*-butyl and δ-hydroxy-*n*-pentyl formation kinetics revealed that the isomerization occurred faster than the time resolution of our apparatus, yielding a lower limit for $k_{isom}$ of $2 \times 10^5$ s$^{-1}$. We therefore measure the rate of

unimolecular isomerization relative to the rate of reaction with oxygen, $k_{isom} / k_{O2}$ by measuring the yield of isomerization product as a function of oxygen concentration. By using the steady state approximation (assuming that $k_{decomp} << k_{isom}$) and solving for 1/[ROH], it can be shown that

$$\frac{1}{[ROH]} = \frac{k_{O_2}[O_2]}{k_{isom}[RO]} + \frac{1}{[RO]}. \qquad \text{Equation 4.1}$$

[ROH] is the concentration of isomerization product, [RO] is the concentration of alkoxy radicals and $[O_2]$ is the oxygen concentration. The branching ratio $k_{isom}/k_{O2}$ can be obtained by plotting 1/[ROH] vs. $[O_2]$ and taking the ratio of the intercept to the slope.

Data were taken by varying $[O_2]$ and rapidly scanning (3620-3700 $cm^{-1}$ at 0.5 $cm^{-1}$ steps) over the OH stretch peak. [ROH] was then obtained by fitting each spectrum to a previously obtained reference spectrum (10 averaged scans, 0.5 $cm^{-1}$ step size) and estimating [ROH] from the height of the peak at 3675 $cm^{-1}$. Data taken in sets of seven to ten $O_2$ concentrations were analyzed separately to minimize the impact of long-term drift in precursor concentrations or laser fluence upon our $k_{isom}/k_{O2}$ determinations. Multiple sets of data (14 sets for *n*-butoxy, 5 sets for 2-pentoxy) were obtained and analyzed according to the aforementioned procedure. Plots of 1/[ROH] vs. $[O_2]$ for *n*-butoxy and 2-pentoxy taken at 670 torr are shown in Figure 4.8 and Figure 4.9. At high oxygen concentrations, [HOR] decreased linearly as $[O_2]$ increased, consistent with the competition of the isomerization and $O_2$ reaction pathways.

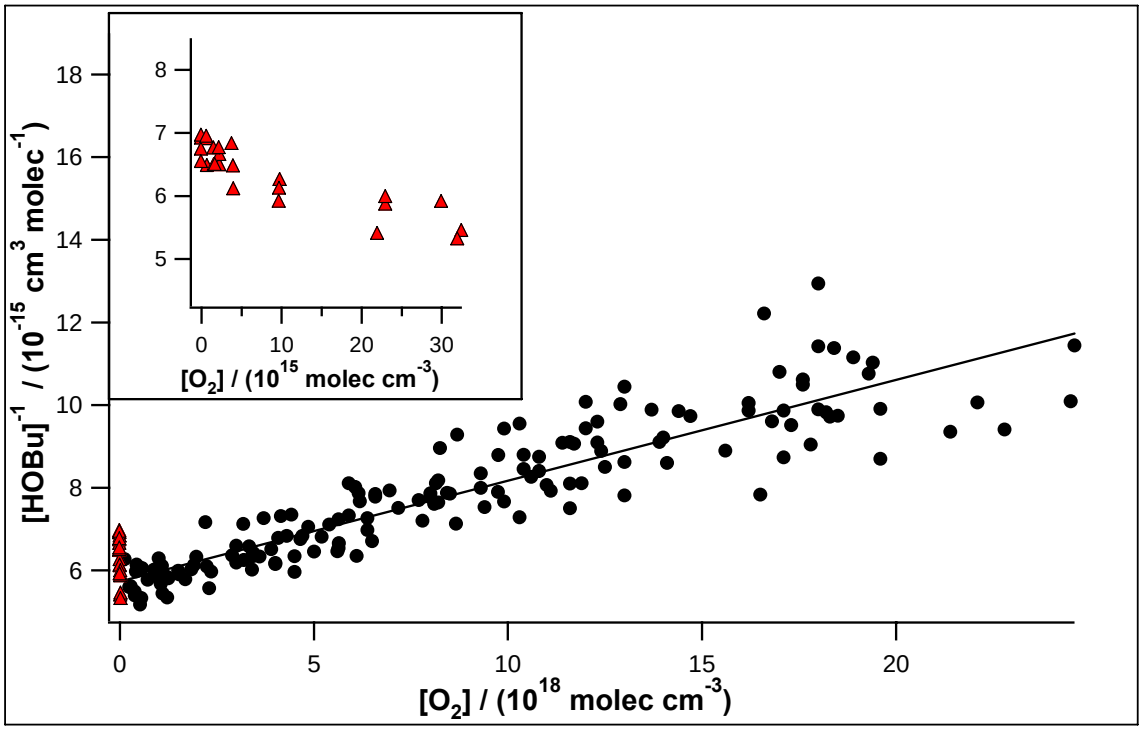


**Figure 4.8. Measurements of 1/[HOROO•] plotted as a function of [$O_2$] for *n*-butoxy. [HOROO•] were calculated from the strength of the OH-stretch infrared peak. Individual data sets have been scaled to [*n*-butoxy] = $2 \times 10^{14}$ molecules×cm$^{-3}$ at [$O_2$] = 0. Data above [$O_2$]=$1\times10^{17}$ cm$^{-3}$ show the expected decrease in [HOROO•] with [$O_2$]. The inset shows an apparent decrease in [$HOC_4H_8OO\cdot$] with [$O_2$] at very low [$O_2$] as discussed in the text. Only the data with [$O_2$] > $5 \times 10^{16}$ molecules×cm$^{-3}$ were used in the linear fit to determine $k_{isom}/k_{O2}$. Slope = $(2.4 \pm 0.2) \times 10^{-34}$ cm$^6$, intercept = $(5.7 \pm 0.2) \times 10^{-15}$ cm$^3$, $k_{isom}/k_{O2} = (2.3 \pm 0.2) \times 10^{19}$ cm$^{-3}$. All errors are reported to 2σ.**

Data taken at very low oxygen concentration (shown as an inset to Figure 4.8) exhibited anomalous behavior; The apparent [HOR] decreased with lower [$O_2$]. At [$O_2$] < $5\times10^{16}$ cm$^{-3}$ the lifetime for this addition becomes comparable to our detection time. This anomalous behavior is therefore likely related to the addition of $O_2$ to the initially formed hydroxyalkyl radicals. One possible explanation is that the apparent decrease in [HOR] is due to a change in the OH stretch cross section in the presence of the peroxy group. An increase of only ≈ 10% in the cross section upon addition of the peroxy group would be required to explain our data. An alternate explanation for our data could be

that, if the initially formed hydroxyalkyl radicals are not rapidly converted to the hydroxyalkyl peroxy radicals, a small fraction re-isomerize back to the alkoxy radical. Calculations on the energetics of *n*-butoxy reactions (Figure 4.1) indicate that the isomerization channel is only slightly exothermic. Using Somnitz and Zellner's calculated $\Delta H_{isom}$ for *n*-butoxy (-3.4 kcal $mol^{-1}$) [79], the ratio of isomerization product to remaining alkoxy [·ROH]/[RO·] is 311.

Regardless of the mechanism, an accurate value of $k_{isom}/k_{O2}$ should be obtained when $[O_2]$ is high enough to ensure rapid conversion of hydroxyalkyl radicals to hydroxyalkylperoxy radicals. As a result, only data with $[O_2] > 5\times10^{17}$ $cm^{-3}$ were used to determine $k_{isom}/k_{O2}$. Each set was normalized to an initial alkoxy radical concentration of $2 \times 10^{14}$ $cm^{-3}$ and then fit using a linear least squares regression. The fits obtained in this way were not statistically different than if the sets were fit individually and then averaged. Because prompt isomerization will increase the value of $k_{isom}/k_{O2}$, this leads to asymmetric error bars. Thus, the results we report are $k_{isom}/k_{O2} = 2.3(+0.2, -0.5) \times 10^{19}$ for *n*-butoxy, and $k_{isom}/k_{O2} = 3.3(+0.4, -0.7) \times 10^{19}$ for 2-pentoxy. All errors are stated to $2\sigma$, and the increased uncertainty for 2-pentoxy stems from the smaller number of data sets.

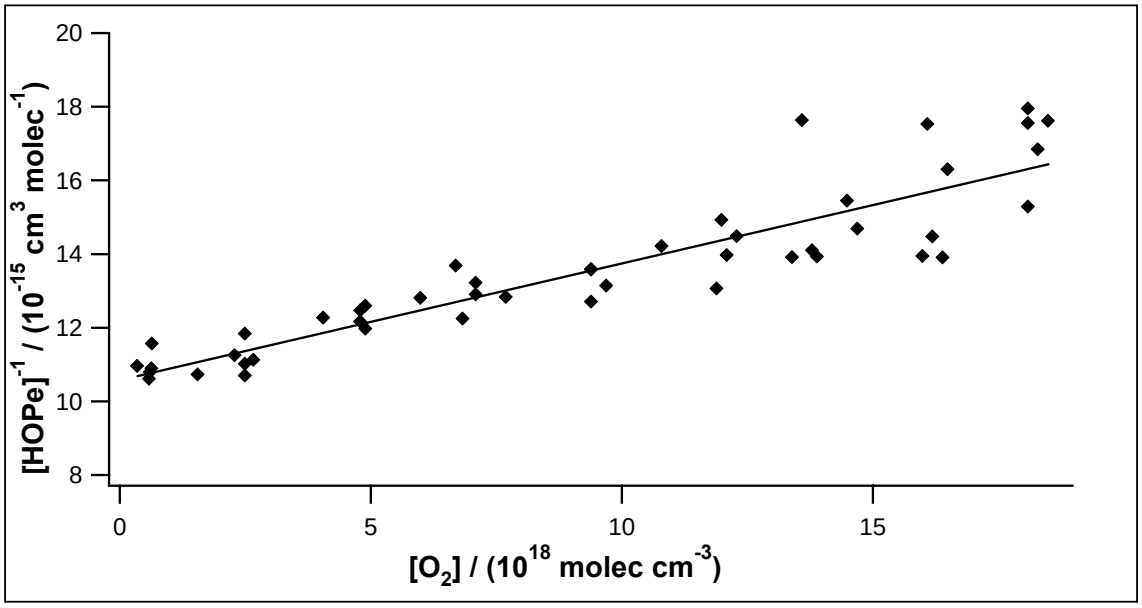


**Figure 4.9. Measurements of 1/[HOROO•] plotted as a function of [$O_2$] for 2-pentoxy. [HOROO•] were calculated from the strength of the OH-stretch infrared peak. Individual data sets have been scaled to [2-pentoxy] = $1 \times 10^{14}$ molecules×cm$^{-3}$ at [$O_2$] = 0. Slope = $(3.2 \pm 0.2) \times 10^{-34}$ cm$^6$, intercept = $(1.06 \pm 0.02) \times 10^{-14}$ cm$^3$, $k_{isom}/k_{O2} = (3.3 \pm 0.4) \times 10^{19}$ cm$^{-3}$. All errors are reported to 2σ.**

Several data sets were taken replacing all $N_2$ with Ar to observe the impact of the collision partner. The Ar data sets resulted in values of $k_{isom}/k_{O2}$ that were statistically indistinguishable from the $N_2$ data, indicating that 670 torr lies near the high-pressure limit of the termolecular falloff curve in agreement with RRKM calculations [104].

We can now re-evaluate the possible influence of prompt isomerization on these measurements. When the possibility of prompt isomerizaiton is included in eq 4.1, the expression for [$C_4H_8OH$] becomes

$$\frac{1}{[ROH]_{tot}} = \frac{k_{O_2}[O_2] + k_{isom}}{k_{isom}\left([RO] + [ROH]_p\right) + k_{O_2}[O_2][ROH]_p}, \qquad \text{Equation 4.2}$$

where $[ROH]_p$ is the amount of product formed through the prompt isomerization channel.

We see from eq 4.2 that a significant yield of prompt isomerization product would lead to a nonlinear dependence of 1/[•ROH] on [$O_2$]. This provides a method for us to quantify the extent of prompt isomerization. We first assumed no prompt isomerization in order to determine the ratio $k_{isom}/k_{O2}$ as described above. Using a literature value for $k_{O2}$ of $1\times10^{-14}$ cm$^3$ molecule$^{-1}$ s$^{-1}$, we calculate $k_{isom}$ [82]. The value of the intercept from our data plot was used as 1/[RO]. We then compared the residual sum of squares (RSS) for our linear fit to the RSS of a fit using eq 4.2 for various values of $[ROH]_p$. An upper bound on the amount of prompt isomerization was estimated by the value of $[ROH]_p$ that led to a doubling of the linear fit RSS. Based on this analysis, $[ROH]_p < 0.07 \times [ROH]_{total}$ for *n*-butoxy, and $[ROH]_p < 0.05 \times [ROH]_{total}$ for 2-pentoxy. This translates to a possible systematic overestimation of $k_{isom}/k_{O2}$ of $0.3 \times 10^{19}$ for *n*-butoxy, and $0.3 \times 10^{19}$ for 2-pentoxy due to prompt isomerization, or a 15% error.

## 4.4 Discussion

We have made the first observation of the hydroxylated isomerization products of *n*-butoxy and 2-pentoxy radicals. The observed spectra are likely due to a mixture of the initial hydroxyl alkyl radical, the hydroxyl peroxy radical formed from addition of $O_2$ and some secondary OH-containing species. Nevertheless, the size of the OH peak can be used as a proxy for the isomerization yield. By measuring the variation in the peak magnitude as a function of $O_2$ concentration, we have measured the relative rate $k_{isom}/k_{O2}$. Our values for $k_{isom}/k_{O2}$ are compared with previous measurements in Table 4.2. Our measurements are unique in the literature in that they directly probe the isomerization

products microseconds after their formation, minimizing possible interference from secondary chemistry.

**Table 4.2. Comparison of $k_{isom}/k_{O2}$ for *n*-butoxy and 2-pentoxy to previous measurements**

| | $k_{isom}/k_{O2}$ ($10^{19}$ cm$^{-3}$)[a] | Molecule Detected | Method | *p* (torr) | Ref |
|---|---|---|---|---|---|
| ***n*-butoxy** | **2.3 (+0.2/-0.5)** | **δ-hydroxy-*n*-butyl peroxy** | **slow flow, CRDS** | **670** | **This work** |
| | 1.95 ± 0.4 | butanal and 4-hydroxy butanal | static, FTIR | 700 | Cassanelli, 2006 [94] |
| | 1.5 ± 0.5 | butanal | static, GC | 760 | Cox, 1981 [91] |
| | 1.9 ± 0.4 | butanal | static, FTIR | 700 | Niki,1981 [86] |
| | 2.1 ± 0.5 | butanal | slow Flow, GC | 760 | Cassanelli, 2005 [95] |
| | 1.8 ± 1.1 | butanal | slow Flow, GC | 760 | Cassanelli, 2005 [95] |
| | 0.25 ± 0.19 | OH and NO2 | fast flow, LIF | 38 | Hein, 1999 [96] |
| | 1.8 ± 0.6 | butanal | static, FTIR | 760 | Geiger, 2002 [97] |
| | | | | | |
| **2-pentoxy** | **3.3 (+0.4/-0.7)** | **δ-hydroxy-*n*-pentyl peroxy** | **slow flow, CRDS** | **670** | **This work** |
| | 3.1[b] | 2-pentone | static, GC | 700 | Atkinson, 1995 [83] |

a All uncertainties are 2σ  b Uncertainty is a factor of 2

Previous experimental studies of the *n*-butoxy radical at 1 atm have obtained values for $k_{isom}/k_{O2}$ ranging from $1.5\times10^{19}$ to $2.2\times10^{19}$ cm$^3$ molec$^{-1}$ [86, 90, 91, 94-96]. A recent report on "Evaluated kinetic and photochemical data for atmospheric chemistry" reports a preferred value of $2.1\times10^{19}$ for $k_{isom}/k_{O2}$ at 298 K and 1 bar pressure, assuming $k_{O2}$ of $1.4\times10^{-14}$ cm$^3$ molec$^{-1}$ s$^{-1}$ [88].

Our measured value for $k_{isom}/k_{O2}$ is approximately 50% larger for 2-pentoxy radicals than for the *n*-butoxy radicals. This is in agreement with the lower barriers for isomerization of the 2-pentoxy radical seen in calculations [80]. We are only aware of one previous measurement of the 2-pentoxy isomerization kinetics in which Atkinson et al. measured the end products from the photo-oxidation of pentane in a smog chamber

[83]. Their product analysis was complicated by the presence of all three possible pentoxy radicals, resulting in a reported uncertainty of a factor of two. Our measured $k_{isom}/k_{O2}$ is consistent with Atkinson et al., but has much smaller error bars.

# 5 Appendix A: Spectroscopy of *cis-cis* HOONO and the $HOONO/HONO_2$ Branching Ratio in the Reaction $OH+NO_2+M$; Discharge Flow Studies

## *5.1 Previously Published Results*

# Cavity Ringdown Spectroscopy of *cis-cis* HOONO and the HOONO/$HONO_2$ Branching Ratio in the Reaction OH + $NO_2$ + M

**Brian D. Bean,[†] Andrew K. Mollner, Sergey A. Nizkorodov,[‡] Gautham Nair, and Mitchio Okumura***

*Arthur Amos Noyes Laboratory of Chemical Physics, MC 127-72, California Institute of Technology, Pasadena, California 91125*

**Stanley P. Sander***

*NASA Jet Propulsion Laboratory, MC 183-901, California Institute of Technology, Pasadena, California 91109*

**Kirk A. Peterson**

*Department of Chemistry, Washington State University, Pullman, Washington 99164-4630*

**Joseph S. Francisco**

*Department of Chemistry, Purdue University, West Lafayette, Indiana 47907A*

*Received: February 17, 2003; In Final Form: June 27, 2003*

The termolecular association reaction OH + $NO_2$ + M was studied in a low-pressure discharge flow reactor, and both $HONO_2$ and HOONO products were detected by infrared cavity ringdown spectroscopy (IR-CRDS). The absorption spectrum of the fundamental $\nu_1$ band of the *cis-cis* isomer of HOONO (pernitrous or peroxynitrous acid) was observed at 3306 $cm^{-1}$, in good agreement with matrix isolation studies and ab initio predictions. The rotational contour of this band was partially resolved at 1 $cm^{-1}$ resolution and matched the profile predicted by ab initio calculations. The integrated absorbances of the $\nu_1$ bands of the *cis-cis* HOONO and $HONO_2$ products were measured as a function of temperature and pressure. These were converted to product branching ratios by scaling the experimentally observed absorbances with ab initio integrated cross sections for HOONO and $HONO_2$ computed at the CCSD(T)/cc-pVTZ level. The product branching ratio for *cis-cis* HOONO to $HONO_2$ was 0.075 ± 0.020($2\sigma$) at room temperature in a 20 Torr mixture of He/Ar/$N_2$ buffer gas. The largest contribution to the uncertainty is from the ab initio ratio of the absorption cross sections, computed in the double harmonic approximation, which is estimated to be accurate to within 20%. The branching ratio decreased slightly with temperature over the range 270 to 360 K at 20 Torr. Although *trans-perp* HOONO was not observed, its energy was computed at the CCSD(T)/cc-pVTZ level to be $E_0 = +3.4$ kcal/mol relative to the *cis-cis* isomer. Statistical rate calculations showed that the conformers of HOONO should reach equilibrium on the time scale of this exeriment. These results suggested that essentially all isomers had converted to *cis-cis* HOONO; thus, the reported branching ratio is a lower bound for and may represent the entire HOONO yield.

## Introduction

The free radical chain termination reaction

$$OH + NO_2 + M \rightarrow HONO_2 + M \qquad (1)$$

is important in oxidation chemistry throughout the lower atmosphere. Radicals in both the $HO_x$ and $NO_x$ families mediate the destruction of ozone in the stratosphere and are central to the formation of photochemical smog in the troposphere.[1,2] Reaction 1 reduces the concentrations of these species by converting them into the stable reservoir species nitric acid. The rate of reaction 1 has important consequences for tropospheric ozone production and photochemical smog. In polluted urban airsheds with high ratios of $NO_x$ to volatile organic compounds (VOC), the rate of reaction 1 is one of the single most influential parameters determining peak ozone mixing ratios.[3,4] At high enough $NO_x$ levels, urban ozone levels decrease with increasing $NO_x$, because elevated $NO_x$ levels reduce OH concentrations through reaction 1 and lead to reduced VOC oxidation rates. Tonnesen[5] has shown that model predictions of ozone production can be almost inversely proportional to changes in the rate coefficient for reaction 1 under these conditions. This negative feedback complicates ozone attainment strategies, which must often balance regulation of VOC vs $NO_x$ emissions. Furthermore, the uncertainty in the rate of reaction 1 is the major contribution to model uncertainties in predicted ozone at high $NO_x$ levels. This uncertainty propagates to scales such as the Maximum Incremental Reactivity, a measure of the ozone-

* Corresponding Authors. E-mail (Okumura): mo@its.caltech.edu. E-mail (Sander): Stanley.P.Sander@jpl.nasa.gov.
† Current address: Department of Chemistry, University of Wisconsin-Madison, Madison, WI 53706.
‡ Current address: Department of Chemistry, University of California at Irvine, Irvine, CA 92697.

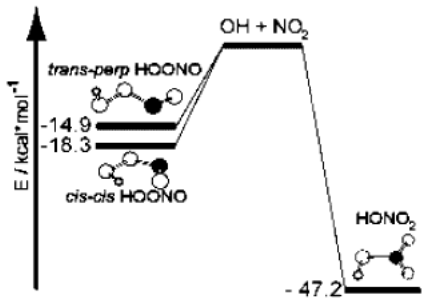


**Figure 1.** Energy level diagram of the reaction OH + $NO_2$. The *cis-cis* and *trans-perp* isomers of HOONO are shown. Energies for HOONO are from CCSD(T) calculations.

forming potential of individual VOCs.[6,7] In the stratosphere, both $HO_x$ and $NO_x$ radicals are involved in catalytic cycles that deplete ozone. Reaction 1 couples these catalytic cycles, and is one of several key reactions that lead to a more complex dependence of stratospheric ozone on $NO_x$ levels. Sensitivity analyses have shown that differences in recommended rates for reaction 1 have a significant effect on mid-latitude ozone concentrations.[8]

Despite extensive studies over a wide range of temperatures and pressures,[9−26] significant uncertainties remain at atmospherically relevant pressures and temperatures. Much attention has recently focused on the yield for a second minor product channel

$$OH + NO_2 + M \rightarrow HOONO + M \qquad (2)$$

producing HOONO (peroxynitrous or pernitrous acid), a weakly bound isomer of nitric acid. The NASA Panel for Data Evaluation[27] and the IUPAC Gas Kinetic Data Evaluation[28,29] summarize the current evidence for this channel, but neither source currently makes a recommendation for its inclusion in atmospheric models. A significant branching fraction into channel 2 is of importance in the atmosphere. Formation of HOONO would reduce the efficiency of the OH + $NO_2$ + M reaction as a sink for OH and $NO_2$ radicals, because HOONO would rapidly dissociate or photolyze back to reactants.

While Leighton[30] had suggested the existence of the HOONO channel in the gas phase, Robertshaw and Smith[9] first proposed that a significant HOONO yield could resolve a discrepancy in the pressure dependence of reaction 1. The effective bimolecular rate constant $k_1$ has an anomalous falloff curve; the observed high-pressure rate constant $k_1^\infty$ is significantly larger than the high-pressure limit extrapolated from low-pressure data. The discrepancy can be removed if the HOONO channel is insignificant at low pressures, but becomes comparable to the $HONO_2$ channel at high pressures. Golden and Smith[31] modeled the OH + $NO_2$ reaction and showed that the high- and low-pressure data could be described quantitatively by statistical models that included HOONO. Hippler et al.[32] have recently revised the high-pressure rate constants in He and $N_2$ downward by ≈30%, but the discrepancy remains.

An energy level diagram illustrating these two channels is shown in Figure 1. At low pressures, the initial HOONO association adduct will redissociate more quickly than $HONO_2$ due to the former's lower density of states, and bound HOONO will be formed in low yields. At high pressures, the weakly bound complex will be stabilized rapidly and the HOONO yield could be comparable to, or even exceed, the $HONO_2$ yield.

Golden and Smith,[31] Matheu and Green,[33] and Troe[34] have modeled the pressure and temperature dependence of $k_1$ and $k_2$. Since the submission of this paper, there has been a new set of master equation calculations by Golden, Barker, and Lohr.[35] While all sets of calculations suggest that HOONO formation should compete with the $HONO_2$ channel in the reaction OH + $NO_2$, the resulting branching ratios at 1 atm and 298 K vary from > 1% (Matheu and Green), to 2.5% (Troe), to 30% (Golden and Smith). However, rate constants, falloff curves, and product yields cannot be calculated quantitatively from first principles, because our knowledge of the transition states, relaxation processes, and potential surfaces (especially for HOONO formation) is too limited. These models rely to some extent on fitting experimental data, and thus may not accurately predict branching ratios without direct measurements of HOONO.

There have been extensive calculations[36−45] of the energetics and conformations of peroxynitrous acid. From MP2 calculations, McGrath and Rowland found three stable forms of HOONO, the *cis-cis*, *cis-trans*, and *trans-perp* isomers (distinguished by the HOON and OONO torsional angles). However, recent results at the highest levels of theory (QCISD(T)/cc-pVTZ) indicate that only the *cis-cis* and *trans-perp* conformations are stable stationary points.[46] The best purely theoretical estimate of the O−O bond energy of *cis-cis* HOONO is $\Delta_2H_0$ = −19.8 kcal/mol at the CCSD(T)/CBS limit with corrections.[44] This estimate is based on the computed $\Delta_fH_0^0(NO_2)$, which is in error by 1.5 kcal/mol. A perhaps more accurate assessment, based on $\Delta_fH_0^0$ (*cis-cis* HOONO) − $\Delta_fH_0^0(HONO_2)$ = 29.0 kcal/mol, gives $\Delta_2H_0$ = −18.3 kcal/mol. In either case, this binding energy is large enough to expect that *cis-cis* HOONO will be a relatively stable molecule at room temperature (see Figure 1). The energy of the *trans-perp* isomer is computed to be 1−3.2 kcal/mol above the *cis-cis* form. The transition state for isomerization between these isomers, the *perp-perp* isomer, has an MP2 energy (including ZPE correction) of 11.4 kcal/mol relative to the *cis-cis* isomer.[37]

HOONO has been studied extensively in the condensed phase, though the most direct spectroscopic studies come from matrix-isolation work. Lee and colleagues[47−50] reported vibrational and UV absorption spectra of HOONO trapped in rare gas matrixes. The observed infrared bands matched frequencies and intensities predicted by ab initio calculations for the *cis-cis* and *trans-perp* isomers. The *cis-perp* isomer is predicted to have vibrational frequencies similar to those of the *trans-perp* isomer, but it was ruled out on the basis of intensity patterns.

In the gas phase, two earlier attempts at infrared absorption spectroscopy failed to detect HOONO. Burkholder et al.[51] attempted to prepare HOONO in a fast-flow multipass cell using a variety of methods ranging from microwave discharge to direct synthesis with $H_2O_2$ and $NOBF_4$. They estimated an upper limit for HOONO yield of 5% based on sensitivity arguments, and an $HONO_2$ yield of 75% + 25%/−10% from mass balance. More recently, Dransfield et al.[52] attempted to detect HOONO formed by reaction 1 with reaction modulation FTIR spectroscopy, but found no unidentified bands that could be assigned to HOONO in the range 700−3200 $cm^{-1}$. They estimated an upper limit for HOONO of 3−4% based on mass balance arguments.

Direct evidence for formation of HOONO in the gas phase by reaction 2 has been reported only recently. In 2001, Donahue et al.[53] described a series of $^{18}OH$ isotopic scrambling experiments that supported the existence of reaction 2 and led to an estimate of the low-pressure branching ratio of $k_2^\circ/k_1^\circ$= 0.17 at room temperature. Nizkorodov and Wennberg[54] then reported

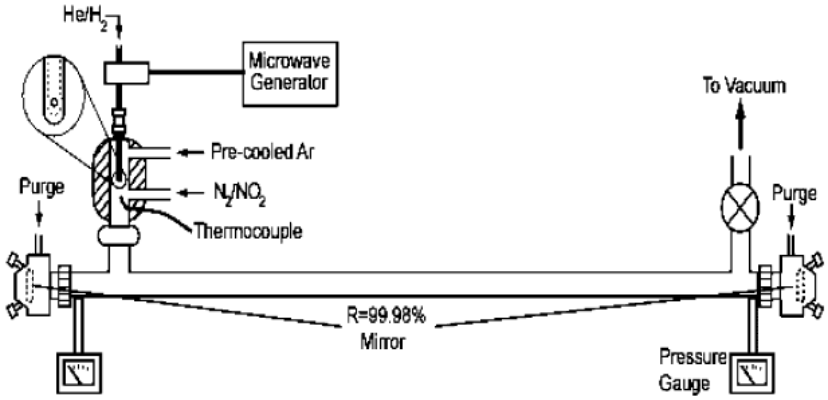


**Figure 2.** Overview of the experimental apparatus. A microwave discharge is used to produce H atoms that are introduced into an Ar flow through the injector tip (exploded view), which then mixes with an $NO_2/N_2$ flow. The H atoms react by $H + NO_2 \rightarrow OH + NO$ to form OH radicals. The OH radicals react with $NO_2$ to form HOONO and $HONO_2$, within 1 cm. Infrared absorption spectra of products are detected downstream in the ringdown cavity, formed by two high-reflectivity mirrors (dashed lines, $R = 99.98\%$ at 2.8 $\mu$m).

the first spectroscopic observation of gas-phase HOONO from the reaction of OH and $NO_2$. They observed the $2\nu_1$ overtone spectrum of HOONO formed in a low-pressure discharge flow cell using action spectroscopy, detecting OH by LIF after predissociation of the overtone-excited molecules. They observed several bands which they tentatively assigned to the isomers of HOONO and combination bands. They estimated that the HOONO yield was 5 ± 3% at 253 K and 20 Torr. In 2002, Hippler et al.[32] reported kinetic evidence for channel 2. They observed a biexponential decay in the OH LIF signal in the reaction OH + $NO_2$ at 5−100 bar and 430−475 K, which they modeled as rapid loss of OH by reactions 1 and 2, followed by slower decomposition of HOONO by the reverse rate $k_{-2}$. They found the enthalpy of reaction 2 at this temperature range to be $\Delta H_2(0) = -19.8$ kcal/mol, in good agreement with the theoretical predictions of the *cis-cis* HOONO dissociation energy $D_0$.

In principle, the branching ratio between reactions 1 and 2 can be measured by infrared absorption spectroscopy of both HOONO and $HONO_2$, but the difficulty of detecting HOONO at such low concentrations ($<10^{12}$ cm$^{-3}$) has been compounded by possible spectral interference from the high concentrations of $HONO_2$ and $NO_2$. However, the lowest energy isomer, *cis-cis* HOONO, can be distinguished from $HONO_2$ in the 3 $\mu$m region, because the OH stretch is significantly red-shifted relative to that of $HONO_2$. Ab initio calculations indicate that this shift arises from a hydrogen-bonding interaction between the H atom and the terminal O atom which occurs only in the *cis-cis* conformation (see Figure 1).[36,37] Lo and Lee observed this band at 3285 cm$^{-1}$ in Ar matrix.[55] In contrast, they observed the $\nu_1$ band of the *trans-perp* isomer at 3563.4 and 3545.7 cm$^{-1}$ (different substitution locations), nearly coincident with the OH stretch of nitric acid at 3550.0 cm$^{-1}$.

In this work, we report a joint experimental/theoretical study to measure the *cis-cis* HOONO-to-$HONO_2$ branching ratio from the reaction OH + $NO_2$ + M, which we denote $k_2(c-c)/k_1$, in a low-pressure discharge flow reactor. We have exploited the high sensitivity of infrared cavity ringdown spectroscopy (IR-CRDS) to observe directly the absorption spectra of *cis-cis* HOONO as well as $HONO_2$ in the 3 $\mu$m region. The branching ratio can be determined from the integrated intensities of the OH stretch modes of both species with the aid of ab initio vibrational band strengths calculated at the QCISD and CCSD(T)/cc-pVTZ level. Finally, we perform statistical calculations to predict the rate that the *trans-perp* HOONO isomer converts to the *cis-cis* form and compute the *trans-perp* HOONO energy. From these results, we infer that the observed *cis-cis* yield most likely represents the total HOONO yield.

## Experiment

An overview of the experimental apparatus is shown in Figure 2. The flow cell comprised two regions, a discharge flow reactor in which the OH + $NO_2$ reaction took place, and a long path spectroscopic detection region. In the reaction region, hydrogen atoms were formed by microwave discharge and thermalized by injection into a flow of pre-cooled argon. This gas was then mixed with $NO_2$ seeded in $N_2$ to produce OH radicals by the reaction

$$H + NO_2 \rightarrow OH + NO \qquad (3)$$

with $NO_2$ in excess. The OH products of reaction 3 then reacted with the $NO_2$. The resulting mixture of products flowed into the detection region, where they were detected by infrared absorption from 2.6 to 3.4 $\mu$m using cavity ringdown spectroscopy. Experiments were performed over the pressure range 5 to 40 Torr and the temperature range 240 to 360 K.

The cell was constructed of Pyrex and quartz, and the interior walls were coated with halocarbon wax to minimize wall reactions. The entire system was evacuated by a 52-cfm mechanical pump through a stopcock and an $LN_2$-trapped foreline. Two capacitance pressure transducers were located at either end of the detection region to verify constant pressure throughout the cell during measurements. All of the gases used in these experiments were UHP grade (99.999%) or higher purity. Six mass flow transducers coupled with needle valves enabled us to vary the flows of the reactant gases as well as the purge flows over the ringdown mirrors. The flows and estimated concentrations of reactants are listed in Table 1. The linear flow velocity was typically 100−200 cm/s, and the total residence time in the cell was typically 200 ms.

**A. OH + $NO_2$ Reaction Region.** H-atoms were produced in a microwave discharge source. $H_2$ was mixed in a 1:200 ratio with He that had been passed through a $LN_2$-cooled zeolite trap to remove condensable impurities. The mixture then flowed through a quartz capillary (4-mm i.d.) in which a discharge was maintained by an Evenson microwave cavity. The capillary extended collinearly into the main reactor cell (2.5-cm i.d.) in

**TABLE 1: Typical Flows and Concentrations for Branching Ratio Measurements**

| species | flow/sccm | concentration/ $cm^{-3}$ (300 K, 20 Torr) |
|---|---|---|
| He | 615 | $2.85 \times 10^{17}$ |
| Ar | 515 | $2.38 \times 10^{17}$ |
| $N_2$ | 242 | $1.12 \times 10^{17}$ |
| $NO_2$ | 13 | $6.0 \times 10^{15}$ |
| $H_2$ | 3 | $1.38 \times 10^{15}$ |

which pre-cooled Ar gas flowed. The discharge gas was injected in jets perpendicular to the Ar flow through small holes near the capillary tip. Turbulent mixing of the discharge gas with the Ar flow ensured an even distribution of H atoms in the reactor and helped to dissipate heat from the discharge.

A mixture of 4% $NO_2$ in $N_2$ by volume (Matheson, certified gravimetrically) was introduced through a 4-mm i.d. inlet approximately 1 cm downstream from the end of the quartz discharge tube. We adjusted the location of the H-atom injection with respect to the $N_2/NO_2$ entrance to allow for the mixing and cooling of the discharge flow, while keeping wall loss of H-atoms to a minimum. At the concentrations used in this experiment, the reaction of H and $NO_2$ was essentially complete within microseconds, while the subsequent association reaction of OH + $NO_2$ + M was complete in $<500$ $\mu$s. Thus, products from reactions 1 and 2 were formed within a few millimeters along the flow, well before the gas entered the spectroscopy region. Although H + $NO_2$ is known to produce high yields of vibrationally excited OH,[56] $NO_2$ is an effective quencher. Furthermore, OH($v$) + $NO_2$ will produce highly excited transient adducts which will not stabilize to form products.

The temperature of the reaction region was measured with a calibrated type "T" thermocouple placed in the center of the reaction zone. The temperature at the point of reaction was slightly higher than the reactor walls, because the $He/H_2/Ar$ mixture had not fully equilibrated. Thermal gradients led to temperature variations of up to $\pm 3°$ C across the reaction region; these uncertainties are reflected in abscissa error bars in the temperature dependence.

**B. Detection of HOONO and $HONO_2$.** Infrared absorption spectra of the reaction products were obtained in a long-path cell situated downstream of the reaction region, 8 cm from the $NO_2$ injection point. Most spectra were recorded in a room-temperature cell (1.9-cm i.d.) which had a cavity length $L$ = 81.5 cm and a sample absorption path length $L_s$ = 51 cm through the reactant gas mixture. The absorption path length $L_s$ was determined by the distance from the gas inlet port to the pump-out port. We occasionally used a second jacketed cell ($L$ = 67 cm, $L_S$ = 32 cm, 2.5-cm i.d., 20 cm distance from the $NO_2$ inlet port), which allowed us to vary the detection cell temperature in order to investigate temperature-dependent wall loss and residence time effects.

Absorption spectra of the reaction products were recorded by pulsed cavity ringdown spectroscopy.[57−59] A mid-infrared laser pulse was injected into an optical cavity made by two high-reflectivity infrared mirrors ($R$ = 99.98%, centered at $\lambda$ = 2.8 $\mu$m, 6 m radius of curvature) sealed to the ends of the detection cell. Each mirror was separated from the main flow of gas by a purge volume approximately 15 cm long. Dry argon flowed over the mirrors (8 sccm over each mirror) and through the purge volumes to protect the mirrors and to minimize losses in reflectivity due to deposition.

We produced tunable (2.6−3.4 $\mu$m) mid-IR in a two-stage, optical parametric amplifier (OPA)[60] by mixing the second harmonic of an Nd:YAG laser and the output of a tunable dye laser in a pair of KTP crystals.[60] The OPA produced an IR beam with energy $E \approx 1$ mJ/pulse and diameter $d \approx 2$ mm after transmission through three filters to remove the residual 532 and 630 nm light. The IR line width was $\Gamma \approx 1$ $cm^{-1}$. The IR wavelength was typically calibrated using the frequencies of known HONO and $HNO_3$ peaks in the spectrum. The IR beam was aligned into the cavity, and the residual beam exiting the cell was focused tightly onto a 1-mm diameter InSb detector (Infrared Associates). Each ringdown trace was amplified and then accumulated with a 300 MHz bandwidth digital oscilloscope with 8-bit digitizer/12-bit averager (Tektronix TDS 320). For each point in a spectrum, typically 32 ringdown traces were averaged by the oscilloscope before transfer to the PC, which then fit the data to a single-exponential function and constant baseline by the Levenberg−Marquardt algorithm.[61]

The ringdown lifetime of radiation trapped in an evacuated optical cavity of length $L$ with mirrors of reflectivity $R$ is $\tau_0 = L/c(1 - R)$, where $c$ is the speed of light.[62−64] Typical empty-cell ring-down times were $\tau_0 \approx 10$ $\mu$s, in good agreement with the stated mirror reflectivity (99.98% at the peak wavelength). In the presence of an absorber, the lifetime is given by $\tau = L/c(1 - R + \alpha L_s)$, where $\alpha = [X]\sigma_X$, $\sigma_X$ is the extinction coefficient of the absorber X, and $L_S$ is the absorption path length through the sample. The measured extinction coefficient is then

$$\alpha = \frac{L}{cL_s}\left(\frac{1}{\tau} - \frac{1}{\tau_0}\right)$$

The possible dependence of the measured extinction coefficient on the concentration of absorber will be discussed in detail below.

Spectra of reaction products were typically recorded by scanning the spectral region of interest with the discharge on and off, and subtracting the two scans. This subtraction eliminated background due to species present in the absence of reaction, as well as to the wavelength-dependent ringdown loss of the mirrors.

We estimated the sensitivity of our CRDS setup from $\Delta\tau$, the minimum detectable change in $\tau$.[63] In a typical run, we found $\Delta\tau/\tau_0 \approx 2\%$ (averaging 32 laser shots), giving a minimum detectable absorption of $\alpha_{min} \approx 1 \times 10^{-7}$ $cm^{-1}$ ($1.8 \times 10^{-7}$ $cm^{-1}$ $\sqrt{Hz}$) for mirrors with reflectivity $R$ = 99.97%. For the detection of $HONO_2$ with the $\nu_1$ band, which has an integrated intensity of $9.5 \times 10^{-18}$ cm/molecule,[65] the minimum detectable concentration of nitric acid was $[HONO_2]_{min} \approx 5 \times 10^{11}$ molecules/$cm^3$ at a single point in the R-branch. Integration over the OH stretching band further improved the sensitivity by roughly $N^{1/2}$, where $N \approx 20$ is the number of data points making up fwhm of the band.

We investigated the effect of the purge gas flow rate on the detection of products. The linear flow velocity of Ar through each of the purged volumes was ≈3 cm/s, or 0.6% of the total flow. We measured both product absorption signals while independently varying the purge flow at the inlet and outlet ends of the detection cell from 0.5% to 9%. There was a gradual decrease (approximately 20%) in the absorption by both $HONO_2$ and HOONO as we increased the purge flow rates to 9%, but the fractional yield of HOONO remained constant. Thus, while some reaction gas mixture entered the purged volume at the flow rates used in this experiment, these gases were flushed out quickly and did not affect branching ratio measurements.

## Computational Methodology

**A. Ab Initio Calculations of Structure, Energetics, and Intensities.** Ab initio electronic structure calculations were

**TABLE 2: Computed Molecular Constants for the *cis-cis* and *trans-perp* Conformational Isomers of HOONO**

| | cis-cis | | | | trans-perp | | |
|---|---|---|---|---|---|---|---|
| | QCISD cc-pVTZ[a] | QCISD(T) cc-pVTZ[a] | CCSD(T) cc-pVTZ | MP2 6-31G(d)[b] | QCISD cc-pVTZ | CCSD(T) cc-pVTZ | MP2 6-31G(d)[b] |
| $\Delta E_0$ (kcal/mol) | | | | | | 3.4 | 2.9[c] |
| $A$ (MHz) | 21726 | 21262 | 21310 | 20900 | 55716 | 54127 | 52576 |
| B | 8133 | 8041 | 8081 | 7949 | 5060 | 4977 | 4902 |
| C | 5917 | 5835 | 5859 | 5759 | 4709 | 4627 | 4550 |
| $\nu_1$ ($cm^{-1}$) | | 3496($a'$) | 3521 | 3547[d] | | 3780 | 3841[e] |
| $\nu_2$ | | 1649($a'$) | 1630 | 1595 | | 1736 | 1720 |
| $\nu_3$ | | 1461($a'$) | 1458 | 1476 | | 1412 | 1408 |
| $\nu_4$ | | 939($a'$) | 969 | 991 | | 992 | 999 |
| $\nu_5$ | | 796($a'$) | 838 | 858 | | 816 | 811 |
| $\nu_6$ | | 618($a'$) | 723 | 776 | | 497 | 443 |
| $\nu_7$ | | 397($a'$) | 419 | 418 | | 366 | 373 |
| $\nu_8$ | | 515($a''$) | 523 | 532 | | 302 | 311 |
| $\nu_9$ | | 363($a''$) | 383 | 360 | | 211 | 219 |

[a] Refs 43,44. [b] McGrath and Rowland, ref 37. [c] MP2/6-311+G(3df,2p), ref 37. [d] Frequencies calculated with the 6-311G(2df,2p) basis set. [e] Frequencies calculated with the 6-311G(d,p) basis set.

performed to predict (a) structures, vibrational frequencies, and energies of the *cis-cis* and *trans-perp* isomers of HOONO, and (b) band intensities of HOONO, $HO_2NO_2$, and $HONO_2$. Calculations were performed with the Gaussian 98[66] and MOLPRO[67] programs. Coupled cluster theory[68] with single and double excitations, with perturbative estimates of connected triples CCSD(T), was used along with the quadratic configuration interaction method (QCISD(T) and QCISD).[69] The QCISD(T) method is correct through fourth-order terms, and it includes the same fifth-order terms as the CCSD(T) method. In the absence of large multireference effects or large single excitation amplitudes, the QCISD(T) method should be very reliable,[69] and its performance is very similar to that of CCSD-(T).[70] The calculations were performed with the Dunning correlation-consistent polarized valence basis sets. The two basis sets used throughout this study are the cc-pVDZ basis set (3s2p1d for C, N, and O; 2s1p for H) and then the cc-pVTZ basis set (4s3p2d1f for C, N, and O; 3s2p1d for H).[71,72] From many benchmark calculations with extended basis sets, the CCSD(T) and QCISD(T) methods have shown that high accuracy can be achieved for the molecular structure and vibrational frequencies.[73,74] Vibrational frequencies were calculated with both the QCISD and CCSD(T) methods. Intensities were calculated with the QCISD method and scaled to estimate the CCSD(T) intensities by the factor 0.968. The scale factor was determined from a calibration set of molecules of well-known intensities and also from calculation of intensities for the calibration set of molecules using the CCSD(T) method. The CCSD(T) intensities were calculated with MOLPRO. The calibration set was HCN, $H_2O$, $CH_4$, and $CH_3O$. A total of 14 intensities were used in the scale factor determination.

**B. Transition Dipole Moment Vector.** Additional calculations were carried out to determine the orientation of the vibrational transition dipole moment for the $\nu_1$ band of HOONO. The electrostatic dipole moment was computed at the B3LYP/cc-pVTZ level using Gaussian 98 for several displacements from equilibrium along the $Q_1$ normal coordinate using the $L$ matrix given at the equilibrium geometry. The resulting dipole vector functions were fit to a polynomial and then numerically integrated over harmonic oscillator wave functions to obtain the three components of the transition dipole matrix element in the principal axis frame.

**C. Calculations of Isomerization Rates.** We computed the formation and isomerization rates of the isomers of HOONO using the program MultiWell.[75,76] We focused in particular on the rate of isomerization from the *trans-perp* isomer to the lower energy *cis-cis* isomer. For the current calculation, we used parameters for the *perp-perp* transition state for rotation of the OONO dihedral angle, which lies between the *trans-perp* and *cis-perp* isomers. The energy of the *perp-perp* isomer was computed at the MP2/6-311G(3df,2p) level with MP2/6-31G-(d) frequencies by McGrath and Rowland (note that the MP2 energies listed in their Table 2 are not corrected for zero-point energy).[37] We employed the *trans-perp* and *cis-cis* vibrational frequencies from the same calculation, but we used our CCSD-(T) calculation of the *trans-perp* energy. We also performed some calculations of the initial branching ratios for reactions 1 and 2, using transition state parameters based on those of Golden and Smith.[31] Energy transfer collisions were described by the single-exponential model[75] with $\alpha = 45$ $cm^{-1} + 0.005$ $E_{upper}(cm^{-1})$, and Lennard-Jones parameters $\epsilon = 180$ K and $\sigma = 4.2$ Å$^2$.

## Results

**A. Spectroscopy of OH + $NO_2$ Products.** Figure 3 shows a room-temperature scan from 3200 to 3700 $cm^{-1}$ taken in 0.2 $cm^{-1}$ steps with the flow cell conditions shown in Table 1. The full-scale spectrum, shown in the inset, is dominated by the $\nu_1$ $HONO_2$ transition. With the discharge off, the $HONO_2$ spectrum was approximately 8−10 times weaker. This small background $HONO_2$ signal, which was always present in the cell during the experiments, arose largely from slow desorption from passivated walls. Several other absorption bands were evident in this region. All of the bands had partially resolved rotational structure. The smaller bands could be assigned to known transitions: the $2\nu_2$ band of $HONO_2$, the $2\nu_2$ and $\nu_1$ bands of both *cis*-HONO and *trans*-HONO, and the $2\nu_3$ transition of $NO_2$. There remained one unidentified band centered at 3306 $cm^{-1}$.

**B. Assignment of the *cis-cis* HOONO Band.** Figure 4 shows the spectrum from 3250 to 3375 $cm^{-1}$ after subtraction of the empty-cell background. The sharp features at 3260 and 3372 $cm^{-1}$ were assigned to the Q-branches of the $2\nu_2$ transitions of *cis*- and *trans*-HONO, respectively. A clearly defined set of P, Q, and R subbands centered at 3306 $cm^{-1}$ was identifiable between these features. We assigned this band to the $\nu_1 = 0 \rightarrow 1$(O−H stretch) transition of *cis-cis* HOONO for the following reasons.

(1) Chemistry. This band was not observed if the discharge was off, even with all reagent gases (Table 1) present. We did not observe any absorption in this region when we recorded experimental reference spectra of either HONO or $HONO_2$

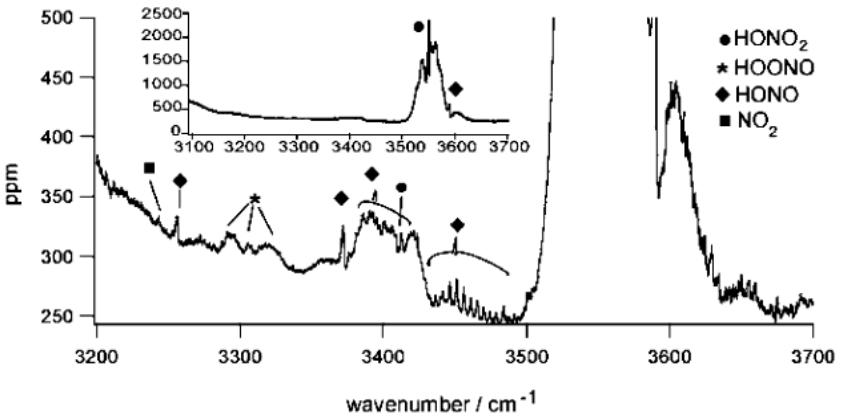


**Figure 3.** Absorption spectrum of the products of OH + $NO_2$ at 20 Torr and 300 K recorded by infrared cavity ringdown spectroscopy. No background has been subtracted; the varying baseline is due to the underlying variations in ringdown mirror reflectivity. The laser line width is 1 $cm^{-1}$ and the step size of the scan is 0.2 $cm^{-1}$. The full scale spectrum, shown in the inset, shows that nitric acid is the dominant product in the reaction OH + $NO_2$. Weaker bands in the magnified scan assigned to known transitions are marked: $HONO_2$ (●), HONO (♦), or $NO_2$ (■). The only unassigned band, at 3306 $cm^{-1}$, is attributed to the $\nu_1$ transition of *cis-cis* HOONO (*).

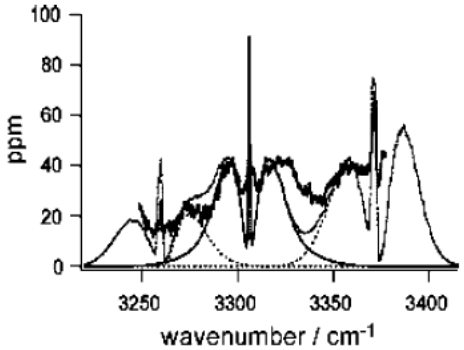


**Figure 4.** Spectrum of the *cis-cis* HOONO $\nu_1$ band and adjacent $2\nu_2$ bands of *cis* and *trans*-HONO, with the ringdown baseline subtracted. The thick line is the experimental data, and the gray line is the sum of three simulated spectra: *cis-cis* HOONO (thin line, centered at 3306 $cm^{-1}$, *cis*-HONO (short dash, 3260 $cm^{-1}$), and *trans*-HONO (long dash, 3372 $cm^{-1}$).

generated from bubbled samples. Furthermore, the band was not present if either $NO_2$ or $H_2$ was removed with the discharge on. We found no detectable spectra of $H_2O_2$ or $HO_2$, which have band origins closer to 3400 $cm^{-1}$, or of $HO_2NO_2$, which has an absorption at 3540 $cm^{-1}$. Thus, this band arose from a reaction product but could not be attributed to any of the primary reactant or product species (HONO, NO, $NO_2$, $HONO_2$) or other conceivable products ($H_2O_2$, $HO_2NO_2$).

(2) Deuterium Substitution. When $D_2$ was substituted for $H_2$ in the discharge flow, the band at 3306 $cm^{-1}$ disappeared but the two adjacent DONO $2\nu_2$ ($NO_2$ stretch overtone bands) were still readily observable. These results indicate that this mode most likely involved a hydride X−H stretch.

(3) Band Position and Intensity. The frequency of the band origin, 3306 $cm^{-1}$, red-shifted relative to the OH stretch of $HONO_2$ by 245 $cm^{-1}$, was in good agreement with the position expected for the *cis-cis* isomer of HOONO from both experiment and theory. The observed band center was close to the 3285 $cm^{-1}$ origin of the $\nu_1$ fundamental of *cis-cis* HOONO observed in matrix isolation experiments; the difference can be accounted for by matrix-induced shifts. It also matched the fundamental position estimated by Nizkorodov and Wennberg,[54] based on their preliminary assignment of a band at 6365 $cm^{-1}$ to the $\upsilon_1 = 0 \rightarrow 2$ overtone transition of *cis-cis* HOONO. Their overtone assignment, taken in conjunction with our observation of the fundamental band, would give $\omega_e = 3430$ $cm^{-1}$ and $\omega_e x_e = 62$ $cm^{-1}$ for the $\upsilon_1$ band of HOONO. This harmonic frequency lies close to $\omega_e = 3521$ $cm^{-1}$, predicted by our CCSD(T)/cc-pVTZ calculations for the *cis-cis* isomer of HOONO. The observed frequency did not match the OH stretch frequencies of the other stable isomer(s) (or of the predicted saddlepoints) of HOONO, all of which have frequencies close to that of nitric acid ($\omega_{exp} = 3550$ $cm^{-1}$).

Finally, the integrated band intensity was approximately 3% of the integrated intensity of the $\nu_1$ band of $HNO_3$. This was consistent with expectations of a relatively low HOONO yield, assuming the two bands had similar absorption cross sections. A quantitative assessment of the HOONO yield is given below.

**C. Ab Initio Calculations.** There have been a number of ab initio calculations on the isomers of HOONO. Here we performed QCISD, QCISD(T), and CCSD(T)/cc-pVTZ calculations on *cis-cis* and *trans-perp* conformers of HOONO, to have a consistent set of high-level spectroscopic constants for the two bound isomers. A third isomer, the *cis-perp* conformation, was not found to be stable. Computational results on the torsional potentials will be reported elsewhere.[46]

Table 2 lists results for the rotational constants and vibrational frequencies of the two isomers, along with a comparison with the MP2 calculations of McGrath and Rowland.[37] The numbering of the normal modes of the *trans-perp* isomer are ordered in descending frequency, while the modes of the *cis-cis* isomer, which has $C_s$ symmetry, are based first on the symmetry $a'$ and then $a''$. In general, the frequencies and rotational constants are close to the MP2 results.

In addition, we report the CCSD(T)/cc-pVTZ energy of the *trans-perp* isomer relative to the lowest energy *cis-cis* geometry to be $\Delta E_0 = +3.4$ kcal/mol, including zero-point correction. The dissociation energy of the *cis-cis* isomer has been reported at a higher level of theory; the best estimate is 18.3 kcal/mol.[44]

To determine the relative yields of HOONO and $HONO_2$, we needed the relative absorption cross sections of the respective fundamental $\nu_1$ transitions. The band strength of nitric acid has been measured, but not that of HOONO. We therefore relied on ab initio intensities computed at equivalent levels of theory

**TABLE 3: Calculated Integrated Intensities for $\nu_1$ (O−H Stretch) Vibrational Transitions in km mol$^{-1}$, and Comparison with Previous Experimental Values**

| | $HONO_2$ | cis-cis HOONO | trans-perp HOONO | $HOONO_2$ |
|---|---|---|---|---|
| QCISD/cc-pVTZ[a] | 98.6 | 34.3 | 50.1 | 52.8 |
| CCSD(T)/cc-pVTZ | 95.4 | 33.2 | 48.6 | 51.2 |
| experiment | 57.0 ± 2.8[b] | | | 36.2 ± 4.4[c] |

[a] Scaled by 0.968 to estimate CCSD(T) intensities (see text). [b] Ref 65. [c] Ref 87.

to determine the ratio of the absorption strengths of *cis-cis* HOONO and $HONO_2$. To estimate the error that may be associated with such a calculation, we also computed the intensity for pernitric acid, $HO_2NO_2$, a molecule of similar composition which, like HOONO, possesses an OH stretch coupled to a peroxide bond.

Table 3 shows the integrated intensities for the OH stretches in HOONO, $HONO_2$, and $HO_2NO_2$ computed with the QCISD-(T)/cc-pVTZ and CCSD(T)/cc-pVTZ methods, as well as a comparison to published values. The QCISD(T) calculations were scaled to estimate the CCSD(T) intensities. While the calculated intensities of $HONO_2$ and $HO_2NO_2$ are greater than the experimental values by 67% and 41%, respectively, the computed $HONO_2$-to-$HO_2NO_2$ intensity ratios are 1.86 at the CCSD(T) level of theory, while the experimental ratio is 1.57. Thus, the computed ratios—though not the absolute magnitudes—agree with experiment to within 18%.

The CCSD(T) calculations gave an intensity ratio of 2.87 for $HONO_2$ to *cis-cis* HOONO, and 1.96 for $HONO_2$ to *trans-perp* HOONO; the scaled QCISD(T) ratios were nearly identical. The integrated absorbance of HOONO must be corrected by this ratio to determine the relative HOONO-to-$HONO_2$ product concentrations. The comparison with pernitric acid suggests that this value should be accurate to within roughly 20%. This estimation of the error is based on a single calibration point; hence, we cannot estimate the statistical uncertainty, but IR absorbances calculated at this level of theory, even within the double harmonic oscillator approximation, are typically accurate to within 20%.[77,78] By estimating the ratio of intensities of similar stretch modes (OH stretches), systematic errors such as anharmonicity are at least partially corrected, though the *cis-cis* HOONO has an apparent hydrogen-bonding interaction not present in either $HONO_2$ or $HO_2NO_2$.

Lower-level B3LYP calculations were performed to predict the orientation of the vibrational transition dipole moment for the $\nu_1 = 0 \rightarrow 1$ transition of *cis-cis* HOONO. The transition dipole moment vector computed as described above was ($\mu_a$, $\mu_b$, $\mu_c$) = (0.041 D, 0.064 D, 0.0 D). This vector differs slightly from the direction of the OH bond. This calculation then predicts a hybrid band with a 2.3:1 ratio in *b*-type to *a*-type character.

**D. Modeling the HOONO $\nu_1$ Band.** With these ab initio predictions, we modeled the expected rotational contours of the $\nu_1$ band of *cis-cis* HOONO using the asymmetric rotor program ASYROT.[79] We made the rigid rotor approximation and used the same set of rotational constants for the *cis-cis* isomer (from the ab initio calculations) for both the upper and lower states, because we had no information on the change in geometry upon excitation of the $\nu_1 = 0 \rightarrow 1$ transition.

To compare the simulation with the 3306 cm$^{-1}$ spectrum, we first had to subtract the contributions to the observed spectrum from the adjacent $2\nu_2$ bands of *cis*-HONO and *trans*-HONO, whose wings overlapped with the HOONO band. We modeled the rotational contours of the HONO bands,[79] using asymmetric rotor constants from high-resolution FTIR data.[80,81]

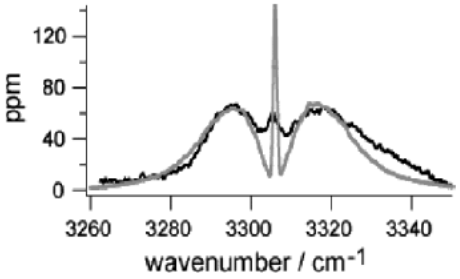


**Figure 5.** Comparison of the experimental *cis-cis* HOONO $\nu_1$ spectrum (with background and HONO $2\nu_2$ overtone bands subtracted) and a simulation (grey line) computed as a hybrid band with ratio $I_b/I_a = 2.3$ using ab initio rotational constants.

The modeled spectra matched reference spectra of HONO taken with this apparatus reasonably well. Figure 4 shows the fit of the modeled *cis*- and *trans*-HONO spectra.

In Figure 5, a scan of HOONO from 3245 to 3380 cm$^{-1}$ taken at 0.2 cm$^{-1}$ steps with the background and HONO contributions subtracted, is compared with the simulation based on the ab initio predictions and a $I_b/I_a$ ratio of 2.3. The simulation is in good agreement with the observed spectrum. We varied the orientation of the transition dipole moment, but found that the spectrum could best be fit as a hybrid band of *a*-type and *b*-type transitions. A range of $I_b/I_a$ values from 1 to 4 was acceptable, because the Q branch blended with the P and R branches, making it difficult to estimate the relative area of the Q branch. This range is consistent with the predicted ratio $I_b/I_a = 2.3{:}1$.

The observed HOONO spectrum has a broader Q branch which partially blends with the P and R branches and a broader R branch shaded to the blue. We attribute these discrepancies to (a) the use of identical upper and lower rotational constants, and (b) contributions from sequence bands, progressions, or hot bands of the low-frequency modes of the loosely bound ring structure. The Q branch, in particular, is not expected to be as sharp as predicted by the simple rigid-rotor approximation, but the relative intensity roughly does match the observed spectrum. Blue-shading of the spectrum may arise from intramolecular hydrogen bond tightening in the vibrationally excited state, leading to a more compact geometry and slightly larger upper state rotational constants. Such effects are well documented in hydrogen-bonded complexes. More important, however, will be the significant population in excited low-frequency vibrations. Our CCSD(T)/cc-pVTZ calculations predict three low-frequency modes—the *a*″ HOON torsion, the *a*″ ONOO torsion, and the *a*′ NOO bend—at 383 cm$^{-1}$, 523 cm$^{-1}$, and 419 cm$^{-1}$, respectively. The OH torsion, in particular, will break the hydrogen bond and lead to substantially blue-shifted sequence bands.

Figure 4 shows the total fit of the summed HOONO and HONO contributions. Together, the three spectra account for most of the extinction in this region. If we assume that the remaining area can be attributed to HOONO sequence bands, we estimate the total HOONO integrated signal to be 14% greater than the area of the simulated spectrum alone. This additional area is primarily on the blue side, and is comparable to the expected contribution from torsionally excited modes. The additional absorption is thus most likely to be due to sequence bands.

**E. Lifetime of HOONO.** The detection of *cis-cis* HOONO was performed at room temperature downstream of the reaction region, well after reactions 1 and 2 were complete. Typical total

residence times were 200 ms; thus, any measurements of absorption by HOONO could only be correlated with HOONO concentration if the HOONO lifetime relative to decomposition at room temperature was significantly longer than 200 ms. We varied the residence time from 75 to 250 ms, but we saw no change in the absolute HOONO signal. If the lifetime of HOONO were $\tau = 200$ ms, we would have expected to see the HOONO signal change by a factor of 1.7 over this time range. Given an uncertainty in HOONO detection of 20%, we estimate that the lifetime must be $\tau > 500$ ms. Thus, we conclude that the HOONO concentration was not changing appreciably over the time scale of this experiment. These conclusions apply as well to mechanisms which might increase *cis-cis* HOONO population, e.g., isomerization of *trans-perp* HOONO to *cis-cis* HOONO during transit through the detection cell.

**F. Characterization of Wall Losses.** In addition to decomposition of *cis-cis*-HOONO, loss of either HOONO or $HONO_2$ on the walls of the cell would result in erroneous product yields. While we saw no significant HOONO loss processes at room temperature, we found small decreases in the HOONO and $HONO_2$ signal at temperatures between 260 and 280 K.

These losses, on the order of 10−20%, increased when a cooled extension was inserted, indicating that some wall deposition or reaction was occurring. At $T < 250$ K, substantial reversible deposition of $HONO_2$ occurred. Our results are in qualitative agreement with unpublished wall loss measurements for HOONO by Fry et al.[82] We therefore limited our HOONO/$HONO_2$ branching measurements to temperatures above 270 K.

**G. Integrated Absorbances of HOONO and $HONO_2$.** Integrated absorbances of the $\nu_1$ bands of both HOONO and $HONO_2$ were obtained by scanning the respective $\nu_1$ bands several times, recording discharge-on and discharge-off spectra, taking the difference, and then summing the runs. The bands were then numerically integrated.

We typically scanned each HOONO spectrum over the range 3250 to 3375 $cm^{-1}$ and fit the observed bands to a composite spectrum from the simulated *cis*-HONO *trans*-HONO, and *cis-cis* HOONO spectra, allowing contributions from each of the three molecules to vary independently. We then used the area under the HOONO curve, scaled to account for the total area of the observed HOONO spectrum in Figure 5, to obtain the integrated HOONO absorption

$$I_{\mathrm{HOONO}} = L_s \int \alpha_{\mathrm{HOONO}}(\nu)\, \mathrm{d}\nu$$

We obtained integrated absorption intensities of nitric acid in a similar manner, scanning from 3490 to 3610 $cm^{-1}$. It was essential to subtract the discharge-off spectrum, as there was a significant amount of background $HONO_2$ accounting for up to 10−15% of the total nitric acid. The spectrum in this region consisted of the main fundamental $\nu_1$ band of $HONO_2$, as well as a sequence band, and a small contribution from the $\nu_1$ band of *trans*-HONO. To obtain the integrated absorption of $HONO_2$, a spectrum of pure bubbled $HONO_2$ of comparable intensity was fit to our spectra and then integrated. We verified that a combination of the bubbled $HONO_2$ and *trans*-HONO spectra adequately represented the observed spectral intensity in the region from 3490 to 3610 $cm^{-1}$.

The magnitude of the $HONO_2$ absorption raised concerns about possible systematic errors in the observed absorbance of the nitric acid spectrum. The peak $HONO_2$ absorption was $\alpha\, l \leq 0.002$ (at the Q branch), so that the spectrum did not appear to be saturated in a single pass. However, the $HONO_2$ spectra were typically 50 times stronger than the HOONO spectra, and the resulting ringdown lifetime was an order of magnitude greater than the baseline ringdown time.

We therefore performed a series of experiments to examine the ringdown spectra of varying concentrations of $HONO_2$ from nitric acid mixed with Ar at 20 Torr. We found that the overall absorption band shape varied slightly with $HONO_2$ concentration. The band shape agreed well with modeled contours at low $HONO_2$ concentrations, but the P and Q branches appeared to decrease relative to the R branch at higher concentrations. Hence, some apparent nonlinearity in the absorption measurement appeared to be occurring.

The use of a low-resolution laser for cavity ringdown spectroscopy may introduce a potential error. As Zalicki and Zare[63] and Yalin and Zare[83] have shown, when the ratio of the absorption bandwidth to laser bandwidth is $V < 100$, the ringdown decay becomes nonexponential. At a given frequency, the laser samples some ensemble of narrow, partially resolved, and unresolved absorption features within the line width of 1 $cm^{-1}$. The total signal is the sum of frequency components $\nu_i$, each contributing a signal with a decay time $\tau_i$ determined by the absorption $\alpha(\nu_i)$. The resulting ringdown signal in general will not be a single exponential. In a typical experiment, the total signal is then a fit to an effective overall decay, which underestimates the absorption. As the spectrum becomes increasingly congested, however, narrow features blend and the lines can become unresolvable. If the spectral features become much wider than the laser line width, the cavity ringdown spectrum should approach the convoluted low-resolution spectrum. Alternatively, Zalicki and Zare also showed that if the absorbance was weak compared to cavity loss, then the integrated intensity—though not the individual line shape—was correct to within 10%. Furthermore, as Hodges et al.[84] have shown, the spectral profile of YAG-pumped dye lasers is not Gaussian, but composed of fluctuating lines at the cavity mode spacing, which tends to ameliorate the underestimation.

The $\nu_1$ band of nitric acid is known to have resolvable Doppler-broadened features, but it is highly congested and has not yet been assigned.[85] In the current experiment, the underlying $HONO_2$ spectrum typically consisted of a set of narrow lines with a Voigt profile from the convoluted Doppler and pressure-broadened line shapes. The ringdown spectra that we recorded possessed partially resolved features.

We therefore determined the deviation of the integrated absorbance measured by CRDS in our branching ratio experiments in a separate experiment, in which we measured the absolute integrated intensity of the $\nu_1$ band as a function of $HONO_2$ concentration. $N_2$ was bubbled through nitric acid and its concentration measured by a 185 nm Hg lamp before dilution with $N_2$ and passage into the CRDS cell. A detailed description of this experiment, as well as simulations of ringdown spectra based on high-resolution spectra of $HONO_2$, will be reported elsewhere.[86] The true integrated intensity was measured at low $HONO_2$ concentrations, and compared to $HONO_2$ absorbance measured at the $HONO_2$ concentrations obtained in the discharge. From these measurements, we concluded that the current branching ratio experiments underestimated the absolute infrared intensity of the $\nu_1$ band of $HONO_2$ by 17%.

In contrast, it is likely that the integrated absorbance of the $\nu_1$ band of *cis-cis* HOONO is correct. First, the HOONO absorption is approximately 10 times less than the mirror loss, thus meeting the criterion of Zalicki and Zare for weak absorption. Second, we expect that this band is highly congested at room temperature. The observed spectrum is relatively

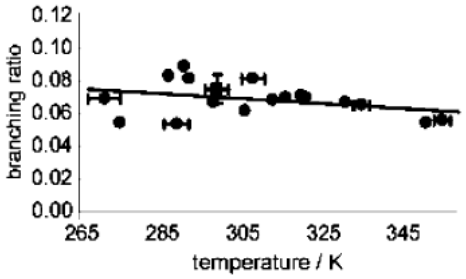


**Figure 6.** Observed ratio of *cis-cis* HOONO to $HONO_2$ products in the reaction OH + $NO_2$ as a function of temperature, at 20 Torr (See Table 1 for gas composition). The experimentally measured ratios of the integrated $\nu_1$ absorption bands were scaled by the computed ratio of absorption cross sections. The abscissa uncertainties are the $2\sigma$ random errors associated with temperature variations. One point (square) was the mean of measurements on several days.

smooth, with no detectable sub-structure. *cis-cis* HOONO is predicted to be an asymmetric rotor with Ray's parameter $\kappa = -0.71$, and the $\nu_1$ band is predicted to be an $a-b$ hybrid. Since the OH bond participates in an intramolecular hydrogen-bond, the rotation−vibration interactions cannot be neglected. Finally, several low-frequency modes, including two torsional modes, will have significant populations that will increase the spectral congestion. HOONO has three modes with harmonic frequencies under 500 $cm^{-1}$, whereas the lowest frequency harmonic mode in nitric acid is slightly below 500 $cm^{-1}$. Under these conditions, the "low-resolution" cavity ringdown spectrum of HOONO is more likely to both reproduce the overall shape of the band and yield the correct integrated absorbance.

**H. Determination of the *cis-cis* HOONO/$HONO_2$ Branching Ratio.** We recorded the integrated absorptions of *cis-cis* HOONO and $HONO_2$ at a variety of reaction temperatures at 20 Torr, and pressures from 4 to 40 Torr at 300 K. While the temperature of the reaction region was varied, all spectroscopic measurements were performed with the detection cell held at room temperature. Thus, the band contours were independent of reaction conditions, and wall losses in the detection region were negligible. Furthermore, as we demonstrated above, the HOONO lifetimes were sufficiently long that HOONO extinction coefficients were unaffected by the residence time. Thus, the column density in the spectroscopy should accurately reflect the product yield. The $HONO_2$ integrated absorption was scaled by 1.17 to correct for the error due to cavity ringdown measurement. The $HONO_2$ concentrations did not vary considerably in the data sets, and we found that use of the same correction factor did not introduce a significant error.

HOONO-to-$HONO_2$ branching ratios were then obtained by weighting the observed absorption intensity ratios by 2.87, the ratio of the ab initio absorption band strengths computed at the CCSD(T)/cc-pVTZ level.

Measurements of the branching ratio were performed at room temperature and 20 Torr on several different days. The variations, most likely arising from source conditions, were ±0.025. Averaging over these results, we determined the 300 K branching ratio to be $k_2(c-c)/k_1 = 0.075 \pm 0.009$, where the quoted uncertainty is the $2\sigma$ standard error of the mean.

Figure 6 shows our measurements of the branching ratio of *cis-cis* HOONO to $HONO_2$ over the temperature range 270 K to 360 K at 20 Torr total pressure. The *cis-cis* HOONO yield appeared to be almost independent of temperature; the slope of the temperature profile was $-1.7(\pm 2.4) \times 10^{-4}$/K ($2\sigma$). The temperatures plotted were from the thermocouple in the reaction region. Typical uncertainties in $T$ due to radial variations of up to ±3 K are shown, but the weak temperature dependence leads to little resulting uncertainty in the yield of HOONO.

**I. Uncertainties.** The scatter in the data shown in Figures 6 is due to random errors that include the effects of (a) noise in the collected spectra; (b) uncertainty in the estimation of the integrated band intensities from fitting the band of HOONO, HONO, and $HONO_2$; and (c) variations in conditions of the reaction region. As discussed above, there is a temperature uncertainty of up to ±3 °C. Our uncertainty in the pressure is 1%. However, the branching ratio depends only weakly on temperature, and thus the error propagated into the branching ratios is negligible.

In addition to the random experimental errors, there are several uncertainties. The largest uncertainty arises from the calculated ratio of absorption cross sections, which we estimate is on the order of 20% on the basis of the difference between the computed and observed ratios of $\nu_1$ band strengths of $HONO_2$ and $HO_2NO_2$. A second uncertainty lies in our correction of the integrated $HONO_2$ absorbance due to the use of the cavity ringdown method. We estimate the error in this correction to be on the order of 10%. Finally, if we conservatively assume that there is resolvable structure in the HOONO spectrum, then the weak absorbance condition of Zalicki and Zare[63] leads to 10% uncertainty in the HOONO intensity. Adding these uncertainties in quadrature to the $2\sigma$ random error of 0.009(12%), we find that the branching ratio for *cis-cis* HOONO vs $HONO_2$ products is

$$k_2(c-c)/k_1 = 0.075 \pm 0.020(2\sigma)$$

at room temperature and 20 Torr of the He/Ar/$N_2$ mixture.

**J. Search for $\nu_1$ Band of *trans-perp* HOONO.** Our spectroscopic measurements in the 3500−3650 $cm^{-1}$ range can also provide a coarse upper bound on the *trans-perp* HOONO concentration. From the matrix isolation studies, the $\nu_1$ band of *trans-perp* HOONO is near 3550 $cm^{-1}$, under the OH stretch of nitric acid. Our calculations predict that this band is 50% weaker than the $\nu_1$ band of $HONO_2$. This band is likely to be a *c*-type transition, because the OH bond lies nearly perpendicular to the plane of the heavy atoms. Thus, the *trans-perp* OH stretch band should exhibit a sharp Q branch that would be readily observed within the $HONO_2$ absorption (unless it lies directly under the $HONO_2$ Q branch). From the absence of any anomalous features or other large discrepancies in the vicinity of the $HONO_2$ spectrum, we infer that the branching fraction of the *trans-perp* isomer is < 20%.

**K. Statistical Calculation of the *trans-perp* → *cis-cis* Isomerization Rate.** We simulated the isomerization process, assuming that these isomers are separated by the transition state with geometry corresponding to the *perp-perp* saddle point computed at the MP2/6-311G(3df,2p) level by McGrath and Rowland.[37] This transition state has an energy of 11.4 kcal/mol relative to the *cis-cis* isomer at the MP2 level, including zero-point energy. For consistency in the density of states calculations, we used their MP2 vibrational frequencies and geometries for all three conformers, *cis-cis*, *trans-perp,* and *perp-perp,* but used our best CCSD(T) estimate for the *trans-perp* energy relative to the energy of *cis-cis* HOONO.

We found that the nascent HOONO molecules establish a rapid ($k > 10^{10}$ $s^{-1}$) microcanonical equilibrium between the two isomers as they are slowly ($k_{collision} \approx 10^8$ $s^{-1}$ at 13 Torr) driven down the internal energy ladder by collisions. Because of its smaller moments of inertia (centrifugal barrier effect) and larger degree of "floppiness", the *trans-perp* isomer has a density

of states comparable to that of the *cis-cis* isomer at energies above the isomerization barrier. Thus, a large fraction of excited HOONO molecules (≈30%) initially fall into the *trans-perp* well. Once the internal energy of the HOONO molecules is below the isomerization barrier, vibrational energy is equilibrated with translations on a microsecond time scale under our experimental conditions. This initial yield of vibrationally thermalized HOONO isomers depends critically on the relative density of states of the two isomers just above the top of the barrier at low pressures. At higher pressures, collisional relaxation may become competitive with isomerization rates.

After the HOONO molecules relax to an initial $c-c/t-p$ population, the *trans-perp* HOONO isomerize on a slower time scale of 0.1−10 ms (over the temperature range of interest), and the $c-c/t-p$ populations approach thermal equilibrium. Using the 11.4 kcal/mol barrier for the *cis-cis* to *trans-perp* isomerization and the 3.4 kcal/mol energy separation between the isomers (both zero-point corrected) and assuming a doubly degenerate reaction path, we find isomerization lifetimes of 0.35 ms and 1.5 ms at 300 and 260 K, respectively. Even with a zero-point corrected *perp-perp* energy of 13.5 kcal/mol and assuming a single reaction path, the lifetime for *trans-perp* relative to isomerization was 18 ms at 300 K. Thus, *trans-perp* HOONO is expected to convert to the lowest energy conformer rapidly relative to the characteristic residence time of products in the flow cell (200 ms). Therefore, the initial yields of the HOONO isomers from OH + $NO_2$ + M, which are difficult to compute, will not be detected in our experiment.

## Discussion

**A. Total HOONO Yield.** The current experiment measures the branching ratio for the formation of one HOONO isomer, the lowest energy *cis-cis* conformation, relative to formation of nitric acid. These results thus put a rigorous lower bound on the total HOONO yield, as other isomers of HOONO may have been formed but were undetected.

Two other HOONO isomers have been predicted, both with OH stretch bands that would overlap with that of nitric acid. Recent calculations conclude that the second lowest energy form, the *cis-perp* isomer, is an inflection point, not a minimum, along the torsional potential about the peroxy bond. This result is consistent with the absence of spectroscopic evidence for the *cis-perp* isomer in matrixes. We consider first the possible formation of the *trans-perp* isomer, whose energy is predicted to be $\Delta E_0 = +3.4$ kcal/mol relative to the *cis-cis* isomer, and then briefly discuss possible problems arising from torsionally excited *cis-cis* HOONO.

Any *trans-perp* HOONO products formed by reaction 2 would most likely isomerize to the *cis-cis* form, because the computed isomerization barrier (11.4 kcal/mol) is predicted to be much lower than the dissociation threshold (18.3 kcal/mol). The absence of any change in the *cis-cis* HOONO abundance with residence time is consistent with one of three hypotheses: (a) the *trans-perp* form equilibrates rapidly with *cis-cis*, prior to entry into the detection volume, (b) no *trans-perp* isomer is formed, or (c) the *trans-perp* isomer isomerizes very slowly compared to the residence time.

Our RRKM calculations with MultiWell support the first scenario, that *trans-perp* isomers rearrange rapidly and are in equilibrium with *cis-cis* HOONO in the detection volume. We calculate that the rate is $>10^3$ $s^{-1}$ at room temperature, and is sufficiently fast, even if the zero-point corrected barrier is as high as 13.5 kcal/mol. Furthermore, the calculations assume that the *perp-perp* conformation is the only transition state, but other pathways may exist.

If isomerization of the *trans-perp* isomer to the *cis-cis* form is indeed rapid compared to the residence time, we can calculate the total yield of HOONO in reactions 1 and 2. From the energetics and frequencies predicted by our CCSD(T) calculations in Table 2, we find $K_{eq}$ (300 K) = [*trans-perp* HOONO]/[*cis-cis* HOONO] = 0.005. Thus, at equilibrium only a negligible fraction the HOONO will be in the *trans-perp* conformation. Even at the highest temperature reported here, the *trans-perp* isomer contributes less than 1.5% to the total population at equilibrium.

While the *cis-perp* isomer is not bound in CCSD(T) calculations,[46] its geometry may be accessed by low ($\upsilon_9 \geq 1$) torsional levels of the NOOH torsion. This torsional motion breaks the intramolecular hydrogen bond, and the large predicted change in the OH vibrational frequency with torsional angle suggests that the sequence bands involving $\upsilon_9$ will be significantly blue-shifted. The excited torsional modes—which may account for 10−30% of the *cis-cis* HOONO population—may be the cause of the intensity on the blue side of the spectrum in Figure 5. However, we cannot rule out that some of the sequence bands cannot be detected within the 3306 $cm^{-1}$ band. Thus, the observed yield obtained from the integrated absorbance of the 3306 $cm^{-1}$ band may underestimate the HOONO yield, though by at most 10−30%. Only detailed modeling of the torsional levels with accurate ab initio potentials, or direct observation of the sequence bands, will allow us to settle this question.

We conclude that the observed *cis-cis* yield accounts for essentially all HOONO formed, i.e., that $k_2/k_1 = 0.075$ at 20 Torr and 300 K for the reaction OH + $NO_2$ + M.

**B. Comparison with Previous Measurements.** Both Burkholder et al. and Dransfield et al. were unable to detect HOONO by FT-IR spectroscopy. Burkholder et al. placed an upper limit of 5% on the HOONO yield,[51] but assumed equal $\nu_1$ cross sections with nitric acid; if our CCSD(T) intensities are used, this upper limit becomes 14%. Our yield also agrees with their $HONO_2$ yield of 75% + 25%/−10% determined from mass balance. Dransfield et al. scanned a wider spectral range under a variety of conditions;[52] they reported an estimate from the mass balance of the HOONO yield to be 0.0 ± 4.1% at 298 K and 60 Torr. Curiously, their published spectra end at 3200 $cm^{-1}$. Our experiments suggest that the concentrations of HOONO in their experiments were near the limits of the reported sensitivities. In addition, their measurements were performed at higher pressures, where HOONO yields may be higher but collisional dissociation will be faster.

Nizkorodov and Wennberg[54] reported a HOONO yield of 5 ± 3% at 253 K and 20 Torr. These measurements were performed under conditions similar to our own, but were based on detection of HOONO alone. Their uncertainty arose because the authors assumed that the HOONO overtone cross-sections were the same as that of $HO_2NO_2$, and that HOONO dissociated with unit quantum efficiency. There was also some uncertainty in the assignment of the peaks, as no rotational structure was resolved. They assigned peaks in a cluster of bands to the $\nu_1$ overtones of the *cis-cis, cis-perp,* and *trans-perp* isomers; more recent results[82] suggest that these are all combination bands, hot bands, and/or Fermi resonances of the *cis-cis* isomer. Given these assumptions, their yield is in quite good agreement with the current findings.

Donahue et al. estimated a low-pressure branching ratio of 0.17 from their isotope exchange measurements, but this estimate is rather weakly constrained by data.[53] Furthermore, since the high-pressure data had not been corrected, they

consequently overestimated $k_2^\infty$ for HOONO, and this discrepancy will have had an impact on their low-pressure extrapolation.

Hippler et al. measured a high-pressure branching ratio in He of 0.33 at 430 K, which fell to 0.15 at 5 bar He.[32] Since HOONO yields are predicted to be further reduced at lower pressures, these results are qualitatively consistent with the present data. They did not estimate rate constants in the low-pressure limit, so a direct comparison would require the pressure and temperature dependences.

Comparisons with the earlier modeling results are more tenuous, since the calculations are sensitive to input parameters. Troe's calculation,[34] for example, may have underestimated the HOONO yield by using too low a binding energy. Matheu and Green[33] attempted to model both forms of HOONO; they find the low-pressure ratio $k_2/k_1 \geq 0.02$. Our results are in good agreement with Golden and Smith,[31] who predict $k_2/k_1 = 0.1$ in the low-pressure limit; this rate was arrived at by multiplying the computed *cis-cis* rate by three to account for the three isomers. Our results are in satisfactory agreement with recent work by Golden, Barker, and Lohr,[35] the most detailed master equation modeling calculations to date. From their fitted parameters, we compute a branching ratio of 0.057 at 13 Torr of $N_2$.

**C. Atmospheric Implications.** The low-pressure branching ratios reported here provide an important constraint on the low-pressure $k_2^0/k_1^0$ branching ratio for models, and are a lower limit on HOONO yields in the atmosphere. The gas mixture, He:Ar:$N_2$, at 20 Torr is equivalent to approximately 13 Torr of dry air after collision efficiencies $\beta$ of the gases are taken into account. The HOONO yield at pressures relevant to the atmosphere will be higher than the yields reported here. Doubling or tripling of this yield could significantly affect atmospheric models. However, while calculations predict that HOONO yields will increase to high levels at atmospheric pressures, one cannot yet predict with full confidence the true falloff curves for HOONO.

Laboratory measurements of reaction 1 generally detect only loss of reactants (typically OH under pseudo-first-order conditions); however, the reported rate coefficient may be either $k_1$ or $(k_1 + k_2)$, depending on whether HOONO has collisionally dissociated on the time scale of the measurements. The implications of the current branching ratio will then depend on the specific experiment.

## Conclusions

This work establishes the formation of HOONO as a minor product channel in the reaction OH + $NO_2$, consistent with recent experimental observations by Donahue,[53] Nizkorodov,[54] and Hippler.[32] Our experiments unambiguously identify HOONO by mid-infrared spectroscopy and provide a direct measure of the branching ratio in the temperature range 270−360 K. We have exploited the sensitive technique of cavity ringdown spectroscopy to detect the absorption spectrum of the $\nu_1$ band of *cis-cis* HOONO, centered at 3306 $cm^{-1}$. The rotational envelope, obtained after subtracting the contributions from the neighboring HONO $\nu_2$ overtones, agrees well with the simulated spectrum derived from high-level ab initio calculations. We determined the HOONO:$HONO_2$ product branching ratio $k_2/k_1$ for the OH + $NO_2$ + M reaction as a function of reaction pressure and temperature from measurements of the integrated absorption of the $\nu_1$ bands of *cis-cis* HOONO and $HONO_2$. These measurements were converted to branching ratios using the ratio of calculated integrated intensities of HOONO and $HONO_2$ bands at the CCSD(T)/cc-pVTZ level. The use of computed cross sections leads to the largest contribution to the uncertainty in the branching ratio. We find a branching ratio of $k_2/k_1 = 0.075 \pm 0.020(2\sigma)$ at room temperature and 20 Torr (He/Ar/$N_2$ buffer gas). This branching ratio decreases weakly with increasing temperature over the range 270−360 K. Although a second isomer of HOONO may be formed, statistical rate calculations show that the higher energy conformer, *trans-perp* HOONO, is expected to isomerize rapidly on the time scale of the current experiment, and will be in its equilibrium abundance, computed to be < 1.5% of the total population. A small fraction of $\nu_9$ (HOON-torsion) excited molecules that access the *cis-perp* geometry may have sequence bands that are significantly blue-shifted and lie under the $HONO_2$ band, and thus be undetected. Thus, the current measurements provide a firm lower bound for and may be a good estimate of the total yield of HOONO.

**Acknowledgment.** This work was supported by NASA Grants NAG5-11657 and NAGW-3911 and the Upper Atmospheric Research and Tropospheric Chemistry Programs. A.K.M. acknowledges support of an NSF Graduate Research Fellowship, G.N. support by a Caltech SURF Fellowship, and G.N. and S.A.N. by the Camille and Henry Dreyfus Postdoctoral Program in Environmental Chemistry. Calculations were supported by the NASA JPL Supercomputing Project. We thank D. M. Golden and J. R. Barker for sharing their results prior to publication and A. Goldman for providing spectral data.

## References and Notes

(1) Perkins, K. K.; Hanisco, T. F.; Cohen, R. C.; Koch, L. C.; Stimpfle, R. M.; Voss, P. B.; Bonne, G. P.; Lanzendorf, E. J.; Anderson, J. G.; Wennberg, P. O.; Gao, R. S.; Del Negro, L. A.; Salawitch, R. J.; McElroy, C. T.; Hintsa, E. J.; Loewenstein, M.; Bui, T. P. *J. Phys. Chem. A* **2001**, *105*, 1521.
(2) Seinfeld, J. H.; Pandis, S. N. *Atmospheric Chemistry and Physics: From Air Pollution to Climate Change*; 1998.
(3) Gao, D. F.; Stockwell, W. R.; Milford, J. B. *J. Geophys. Res.-D* **1996**, *101*, 9107.
(4) Gao, D. F.; Stockwell, W. R.; Milford, J. B. *J. Geophys. Res.-D* **1995**, *100*, 23153.
(5) Tonnesen, G. S. *Atmos. Env.* **1999**, *33*, 1587.
(6) Yang, Y. J.; Stockwell, W. R.; Milford, J. B. *Environ. Sci. Technol.* **1995**, *29*, 1336.
(7) Bergin, M. S.; Russell, A. G.; Milford, J. B. *Environ. Sci. Technol.* **1998**, *32*, 694.
(8) Smith, G. P.; Dubey, M. K.; Kinnison, D. E.; Connell, P. S. *J. Phys. Chem. A* **2001**, *105*, 1449.
(9) Robertshaw, J. S.; Smith, I. W. M. *J. Phys. Chem.* **1982**, *86*, 785.
(10) Westenberg, A. A.; DeHaas, N. *J. Chem. Phys.* **1972**, *57*, 5375.
(11) Anderson, J. G.; Kaufman, F. *Chem. Phys. Lett.* **1972**, *16*, 375.
(12) Anderson, J. G.; Margitan, J. J.; Kaufman, F. *J. Chem. Phys.* **1974**, *60*, 3310.
(13) Harris, G. W.; Wayne, R. P. *J. Chem. Soc., Faraday Trans. 1* **1975**, *71*, 610.
(14) Howard, C. J.; Evenson, K. M. *J. Chem. Phys.* **1974**, *61*, 1943.
(15) Morley, C.; Smith, I. W. M. *J. Chem. Soc., Faraday Trans. 2* **1972**, *68*, 1016.
(16) Anastasi, C.; Bemand, P. P.; Smith, I. W. M. *Chem. Phys. Lett.* **1976**, *37*, 370.
(17) Anastasi, C.; Smith, I. W. M. *J. Chem. Soc., Faraday Trans. 2* **1976**, *72*, 1459.
(18) Atkinson, R.; Perry, R. A.; Pitts, J. N., Jr. *J. Chem. Phys.* **1976**, *65*, 306.
(19) Wine, P. H.; Kreutter, N. M.; Ravishankara, A. R. *J. Phys. Chem.* **1979**, *83*, 3191.
(20) Troe, J. *J. Phys. Chem.* **1979**, *83*, 114.
(21) Forster, R.; Frost, M.; Fulle, D.; Hamann, H. F.; Hippler, H.; Schlepegrell, A.; Troe, J. *J. Chem. Phys.* **1995**, *103*, 2949.
(22) Donahue, N. M.; Dubey, M. K.; Mohrschladt, R.; Demerjian, K. L.; Anderson, J. G. *J. Geophys. Res. D* **1997**, *102*, 6159.
(23) Donahue, N. M.; Demerjian, K. L.; Anderson, J. G. *J. Phys. Chem.* **1996**, *100*, 17855.
(24) Fulle, D.; Hamann, H. F.; Hippler, H.; Troe, J. *J. Chem. Phys.* **1998**, *108*, 5391.

(25) Brown, S. S.; Talukdar, R. K.; Ravishankara, A. R. *Chem. Phys. Lett.* **1999**, *299*, 277.
(26) D'Ottone, L.; Campuzano-Jost, P.; Bauer, D.; Hynes, A. J. *J. Phys. Chem. A* **2001**, *105*, 10538.
(27) DeMore, W. B.; Sander, S. P.; Golden, D. M.; Hampson, R. F.; Kurylo, M. J.; Howard, C. J.; Ravishankara, A. R.; Kolb, C. E.; Molina, M. J. Chemical Kinetics and Photochemical Data for Use in Stratospheric Modeling: Evaluation Number 12. Jet Propulsion Laboratory, 1997.
(28) Atkinson, R.; Baulch, D. L.; Cox, R. A.; Hampson, R. F.; Kerr, J. A.; Rossi, M. J.; Troe, J. *J. Chem. Phys. Ref. Data* **1997**, *26*, 1329.
(29) Atkinson, R.; Baulch, D. L.; Cox, R. A.; Crowley, J. N.; Hampson, R. F.; Kerr, J. A.; Rossi, M. J.; Troe, J. Evaluated kinetic and photochemical data for atmospheric chemistry. In *IUPAC subcommittee on gas kinetic data evaluation for atmospheric chemistry*, 2002.
(30) Leighton, P. A. *Photochemistry of air pollution*; Academic Press: New York, 1961.
(31) Golden, D. M.; Smith, G. P. *J. Phys. Chem. A* **2000**, *104*, 3991.
(32) Hippler, H.; Nasterlack, S.; Striebel, F. *Phys. Chem. Commun. Phys.* **2002**, *4*, 2959.
(33) Matheu, D. M.; Green, W. H., Jr. *Int. J. Chem. Kinet.* **2000**, *32*, 245.
(34) Troe, J. *Int. J. Chem. Kinet.* **2001**, *33*, 878.
(35) Golden, D. M.; Barker, J. R.; Lohr, L. L. *J. Phys. Chem. A*, submitted.
(36) McGrath, M. P.; Francl, M. M.; Rowland, F. S.; Hehre, W. J. *J. Phys. Chem.* **1988**, *92*, 5352.
(37) McGrath, M. P.; Rowland, F. S. *J. Phys. Chem.* **1994**, *98*, 1061.
(38) Tsai, H. H.; Hamilton, T. P.; Tsai, J. H. M.; vanderWoerd, M.; Harrison, J. G.; Jablonsky, M. J.; Beckman, J. S.; Koppenol, W. H. *J. Phys. Chem.* **1996**, *100*, 15087.
(39) Sumathi, R.; Peyerimhoff, S. D. *J. Chem. Phys.* **1997**, *107*, 1872.
(40) Doclo, K.; Rothlisberger, U. *Chem. Phys. Lett.* **1998**, *297*, 205.
(41) Chakraborty, D.; Park, J.; Lin, M. C. *Chem. Phys.* **1998**, *231*, 39.
(42) Jitariu, L. C.; Hirst, D. M. *Phys. Chem. Commun. Phys.* **1999**, *1*, 983.
(43) Li, Y.; Francisco, J. S. *J. Chem. Phys.* **2000**, *113*, 7976.
(44) Dixon, D. A.; Feller, D.; Zhan, C.-G.; Francisco, J. S. *J. Phys. Chem. A* **2002**, *106*, 3191.
(45) Houk, K. N.; Condroski, K. R.; Pryor, W. A. *J. Am. Chem. Soc.* **1996**, *118*, 13002.
(46) Francisco, J. S. Unpublished results.
(47) Cheng, B. M.; Lee, J. W.; Lee, Y. P. *J. Phys. Chem.* **1991**, *95*, 2814.
(48) Chen, W. J.; Lo, W. J.; Cheng, B. M.; Lee, Y. P. *J. Chem. Phys.* **1992**, *97*, 7167.
(49) Lo, W.-J.; Lee, Y. *J. Chem. Phys.* **1994**, *101*, 5494.
(50) Koch, T. G.; Sodeau, J. R. *J. Phys. Chem.* **1995**, *99*, 10824.
(51) Burkholder, J. B.; Hammer, P. D.; Howard, C. J. *J. Phys. Chem.* **1987**, *91*, 2136.
(52) Dransfield, T. J.; Donahue, N. M.; Anderson, J. G. *J. Phys. Chem. A* **2001**, *105*, 1507.
(53) Donahue, N. M.; Mohrschladt, R.; Dransfield, T. J.; Anderson, J. G.; Dubey, M. K. *J. Phys. Chem. A* **2001**, *105*, 1515.
(54) Nizkorodov, S. A.; Wennberg, P. O. *J. Phys. Chem. A* **2002**, *106*, 855.
(55) Lo, W.-J.; Lee, Y. P. *J. Chem. Phys.* **1994**, *101*, 5494.
(56) Irvine, A. M. L.; Smith, I. W. M.; Tuckett, R. P.; Yang, X. F. *J. Chem. Phys.* **1990**, *93*, 3177.
(57) O'Keefe, A.; Deacon, D. A. G. *Rev. Sci. Instrum.* **1988**, *59*, 2544.
(58) Berden, G.; Peeters, R.; Meijer, G. *Int. Rev. Phys. Chem.* **2000**, *19*, 565.
(59) Brown, S. S.; Wilson, R. W.; Ravishankara, A. R. *J. Phys. Chem.* **2000**, *104*, 4976.
(60) Reid, S. A.; Tang, Y. *Appl. Opt.* **1996**, *35*, 1473.
(61) Press:, W. H.; Teukolsky, W. T.; Vetterling, W. T.; Flannery, B. P. *Numerical Recipes in Fortran,* 2nd ed.; Cambridge University Press: Cambridge, 1992.
(62) O'Keefe, A.; Deacon, D. A. G. *Rev. Sci. Instrum.* **1988**, *59*, 2544.
(63) Zalicki, P.; Zare, R. N. *J. Chem. Phys.* **1995**, *102*, 2708.
(64) Romanini, D.; Lehmann, K. K. *J. Chem. Phys.* **1993**, *99*, 6287.
(65) Lange, K. R.; Wells, N. P.; Plegge, K. S.; Phillips, J. A. *J. Phys. Chem. A* **2001**, *105*, 3481.
(66) Frisch, M. J.; Trucks, G. W.; Schlegel, H. B.; Scuseria, G. E.; Robb, M. A.; Cheeseman, J. R.; Zakrzewski, V. G.; Montgomery, J. A., Jr.; Stratmann, R. E.; Burant, J. C.; Dapprich, S.; Millam, J. M.; Daniels, A. D.; Kudin, K. N.; Strain, M. C.; Farkas, O.; Tomasi, J.; Barone, V.; Cossi, M.; Cammi, R.; Mennucci, B.; Pomelli, C.; Adamo, C.; Clifford, S.; Ochterski, J.; Petersson, G. A.; Ayala, P. Y.; Cui, Q.; Morokuma, K.; Malick, D. K.; Rabuck, A. D.; Raghavachari, K.; Foresman, J. B.; Cioslowski, J.; Ortiz, J. V.; Stefanov, B. B.; Liu, G.; Liashenko, A.; Piskorz, P.; Komaromi, I.; Gomperts, R.; Martin, R. L.; Fox, D. J.; Keith, T.; Al-Laham, M. A.; Peng, C. Y.; Nanayakkara, A.; Gonzalez, C.; Challacombe, M.; Gill, P. M. W.; Johnson, B. G.; Chen, W.; Wong, M. W.; Andres, J. L.; Head-Gordon, M.; Replogle, E. S.; Pople, J. A. *Gaussian 98*, A.10 ed.;; Gaussian, Inc.: Pittsburgh, PA, 2001.
(67) Werner, H. J.; Knowles, P. J. "MOLPRO is a package of ab initio programs written with contributions from J. Almlöf, R. D. Amos, A. Bernhardsson, A. Berning, P. Celani, D. L. Cooper, M. J. O. Deegan, A. J. Dobbyn, F. Eckert, S. T. Elbert, C. Hampel, G. Hetzer, T. Korona, R. Lindh, A. W. Lloyd, S. J. McNicholas, F. R. Manby, W. Meyer, M. E. Mura, A. Nicklass, P. Palmieri, K. A. Peterson, R. M. Pitzer, P. Pulay, G. Rauhut, M. Schütz, H. Stoll, A. J. Stone, R. Tarroni, P. R. Taylor, T. Thorsteinsson.," University of Sussex, 2000.
(68) Raghavachari, K.; Trucks, G. W.; Pople, J. A.; Head-Gordon, M. *Chem. Phys. Lett.* **1989**, *157*, 479.
(69) Pople, J. A.; Head-Gordon, M.; Raghavachari, K. *J. Chem. Phys.* **1987**, *87*, 5968.
(70) Lee, T. J.; Rendell; Taylor, P. R. *J. Phys. Chem.* **1990**, *94*, 5463.
(71) Dunning, T. H., Jr. *J. Chem. Phys.* **1989**, *90*, 1007.
(72) Kendall, R. A.; Dunning, T. H., Jr.; Harrison, R. J. *J. Chem. Phys.* **1992**, *96*, 6796.
(73) Martin, J. M. L. *J. Chem. Phys.* **1999**, *100*, 8186.
(74) Bartlett, R. J.; Stanton, J. F. In *Reviews of Computational Chemistry*; Lipkowitz, K. B., Boyd, D. B., Eds.; VCH Publishers: New York, 1994; Vol. 5, p 65.
(75) Barker, J. R. *Int. J. Chem. Kinet.* **2001**, *33*, 232.
(76) Barker, J. R. "MultiWell-1.3.1 software,", 2003.
(77) Galabov, B.; Yamaguchi, Y.; Remington, R. B.; Schaefer, H. F. I. *J. Phys. Chem.* **2002**, *106*, 819.
(78) Thomas, J. R.; DeLeeuw, B. J.; Vacek, G.; Crawford, T. D.; Yamaguchi, Y.; Schaefer, H. F. I. *J. Chem. Phys.* **1993**, *99*, 403.
(79) Judge, R. H.; Clouthier, D. J. *Comput. Phys. Commun.* **2001**, *135*, 293.
(80) Guilmot, J. M.; Melen, F.; Herman, M. *J. Mol. Spectrosc.* **1993**, *160*, 401.
(81) Guilmot, J. M.; Godefroid, M.; Herman, M. *J. Mol. Spectrosc.* **1993**, *160*, 387.
(82) Fry, J.; Nizkorodov, S. A.; Okumura, M.; Wennberg, P. O. In preparation.
(83) Yalin, A. P.; Zare, R. N. *Laser Phys.* **2002**, *12*, 1065.
(84) Hodges, J. T.; Looney, J. P.; van Zee, R. D. *Appl. Opt.* **1996**, *35*, 4112.
(85) Goldman, A.; Rinsland, C.; Perrin, A.; Flaud, J. M. *J. Quant. Spectrosc. Radiat. Transfer* **1998**, *60*, 351.
(86) Mollner, A. K.; Nair, G.; Sander, S. P.; Okumura, M. In preparation.
(87) May, R. D.; Friedl, R. R. *J. Quant. Spectrosc. Radiat. Transfer* **1993**, *50*, 257.

## 5.2 Revisions to Branching-Ratio Results

As described in chapters 2 and 3, our understanding of the spectroscopy used to measure the branching ratio has improved since these results were published. This section briefly describes what revisions should be made to the published data.

The smallest correction is to the calculated ratio of cross sections used. More recent calculations taking into account anharmonicities indicate that this should be changed from 2.87 to 2.71 [73, 74].

Since the publication of Bean et al. we have a much improved understanding of the *cis-cis* HOONO spectrum. In particular, we understand that there is considerable OH stretch intensity blueshifted outside the main peak we used to measure the HOONO absorbance. As described in Chapter 3, our observed HOONO absorbances should have been multiplied by 1.41 to correct for this.

Our assumed correction for nonlinearities in the nitric acid absorbance was significantly too small. We had assumed we could correct our observed nitric acid absorbances by multiplying them by 1.2. As described in detail in Chapter 2, at the low pressures of these experiments we should instead have multiplied by 2.5.

As a result, the Bean et al. results should be corrected using

$$\mathrm{BR}_{\mathrm{new}} = \mathrm{BR}_{\mathrm{published}} \times \frac{2.71}{2.87} \times \frac{1.2}{2.5} \times 1.41 = \mathrm{BR}_{\mathrm{published}} \times 0.64 .$$

The branching ratio at 298K and 13 torr is thus revised from $k_2(c\text{-}c)/k_1 = 0.075 \pm 0.020$ to $k_2(c\text{-}c)/k_1 = 0.048 \pm 0.013$. A revised version of Figure 6 from Bean et al. is shown below.

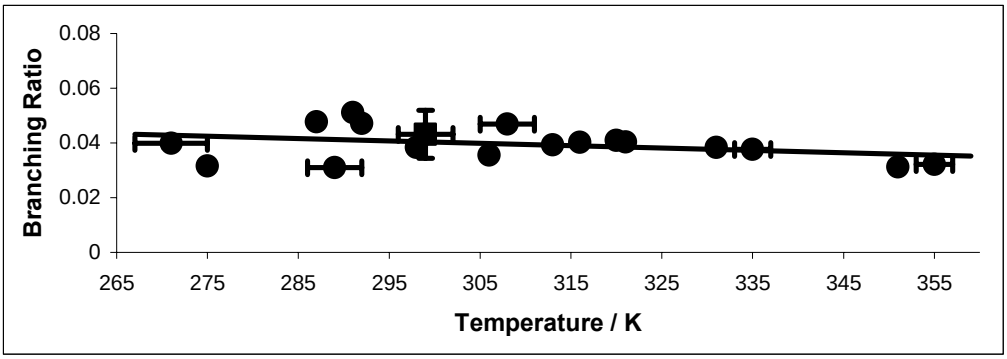


**Figure 5.1 – Corrected ratio of *cis-cis* to $HONO_2$ products in the reaction of OH + $NO_2$ as a function of temperature, at 20 Torr.**

# 6 Appendix B: Experimental Details

## *6.1 Room Temperature Photolysis Cells*

Machine drawings are included of the Teflon blocks and photolysis cells used in photolysis-initiated CRDS studies described in Chapters 4 and 5. Teflon block drawings are courtesy of Brian Bean and were submitted to the machine shop for fabrication. The blocks were coupled to the purge tubes and vacuum line via stainless steel Ultratorr fittings threaded into the Teflon. Initial leaks at the stainless/Teflon interface were sealed by a generous helping of Teflon thread tape. The blocks were coupled the to the gas inlet and pressure gauges by Teflon Swagelock fittings, also threaded into the blocks. These generally seal well, although the Teflon Swagelock parts wear down over the course of repeated tightenings. The seal between the Teflon blocks and the photolysis cell was the most problematic. This was accomplished by fitting the photolysis cells into square grooves in the Teflon blocks and pressing the Teflon blocks together. Often it was found that inserting silicon gaskets between the cell and the Teflon block could improve the seal. With nothing holding the gaskets out they would often deform and be pulled in by the vacuum, breaking the seal. Over time, the Teflon surrounding the square groove was deformed and pressed down into the groove. This made the square groove quite uneven and prevented a seal from being made.

Overall, the design of this cell was certainly functional. Once a good seal was made between the Teflon blocks and the photolysis cell, it would typically last until the cell need to be disassembled. Future cell designs may consider improving upon this seal

mechanism in one of two ways. A thin-walled stainless tube could be inserted inside the silicon gaskets to help them hold shape and resist deformation. This would have the disadvantage of reducing the inside diameter of the CRDS axis, which already can present difficulties for alignment. A compromise would have to be struck with the wall the tube weighing rigidity and inside diameter. The second solution would be to have a round plate welded to the end of the photolysis cells and then create an O-ring seal between this plate and the Teflon blocks. This would certainly seal quite well, but would have the disadvantage of creating significantly more volume containing precursors but not UV photons. This would increase the background for experiments such as the alkoxy experiments described in Chapter 4 and would require faster flow rates to accomplish the same flush duty cycle.

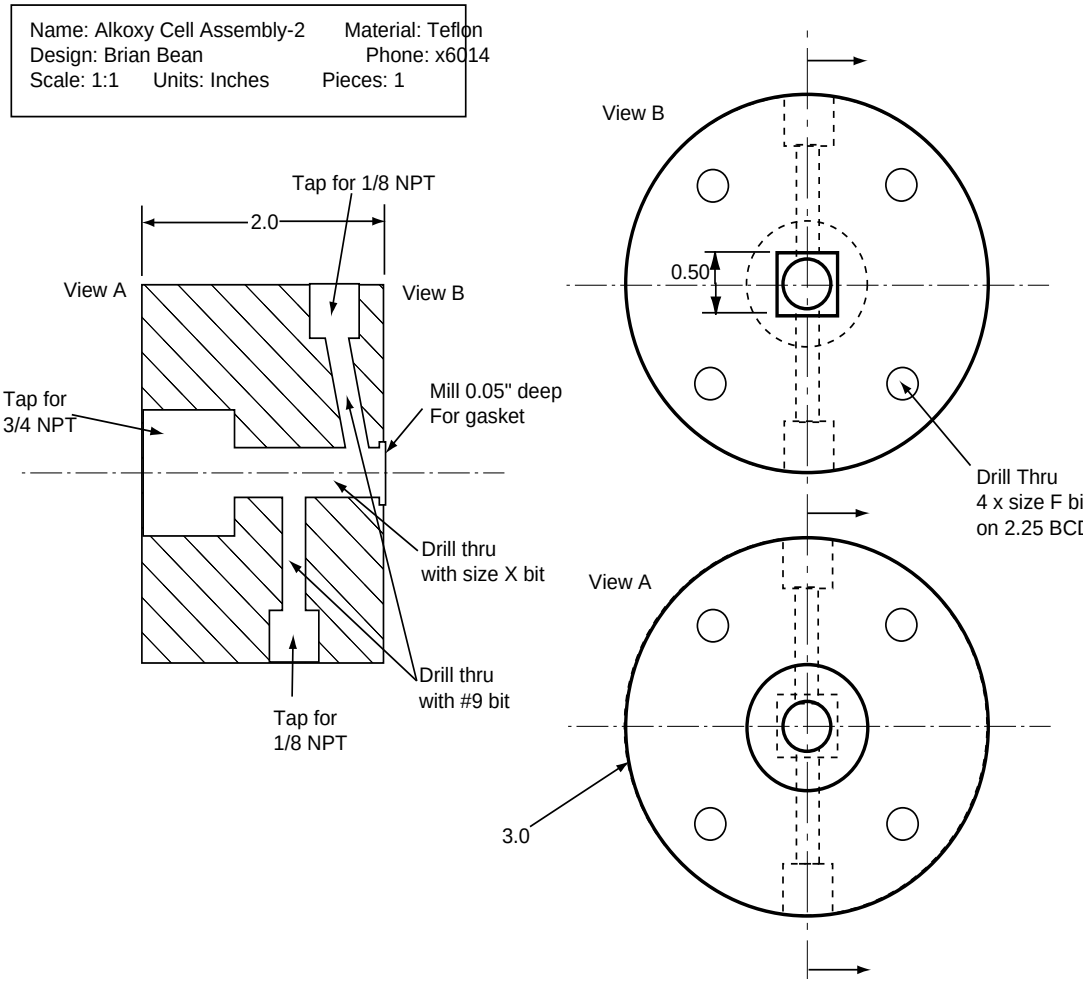


**Figure 6.1. Technical drawing for fabrication of Teflon block for coupling photolysis cell to CRDS mirrors and gas inlets.**

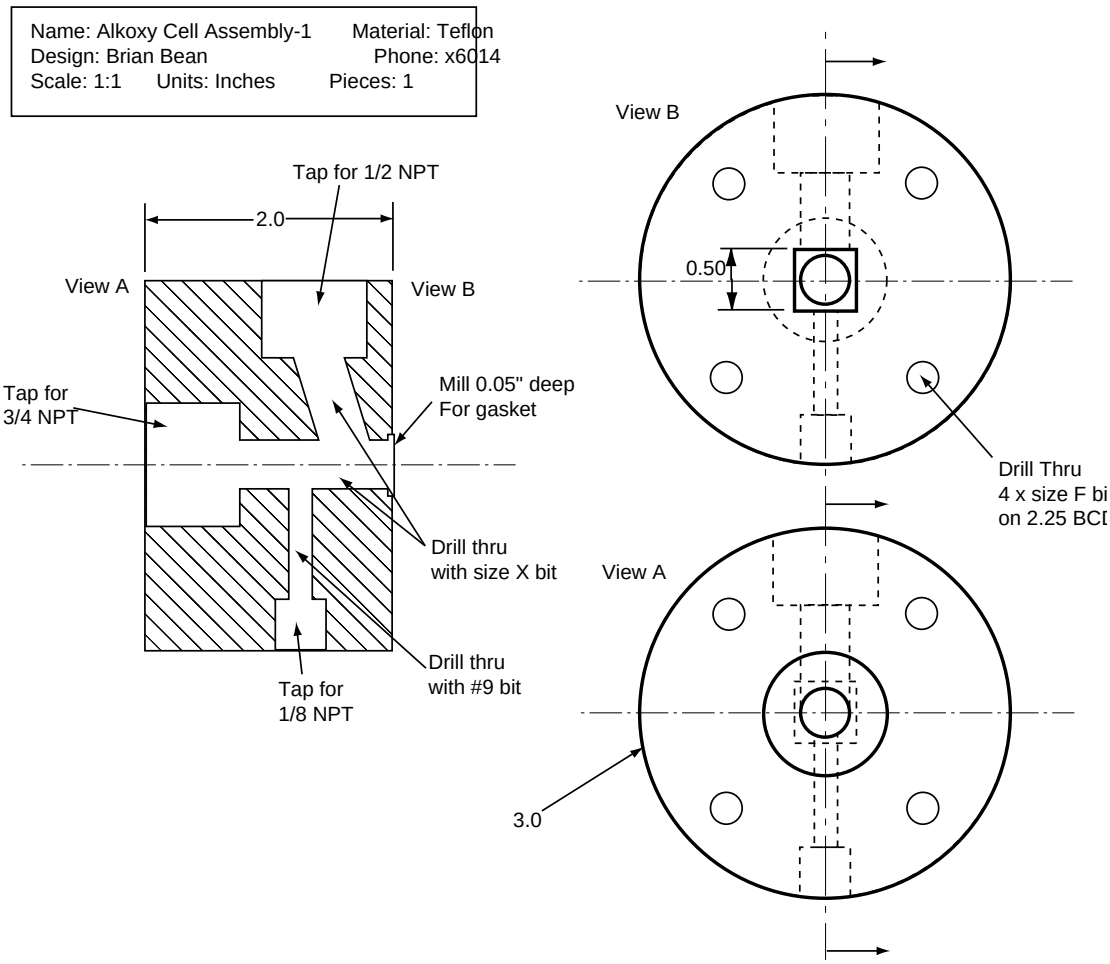


**Figure 6.2. Technical drawing for fabrication of Teflon block for coupling photolysis cell to CRDS mirrors and gas pumpout.**

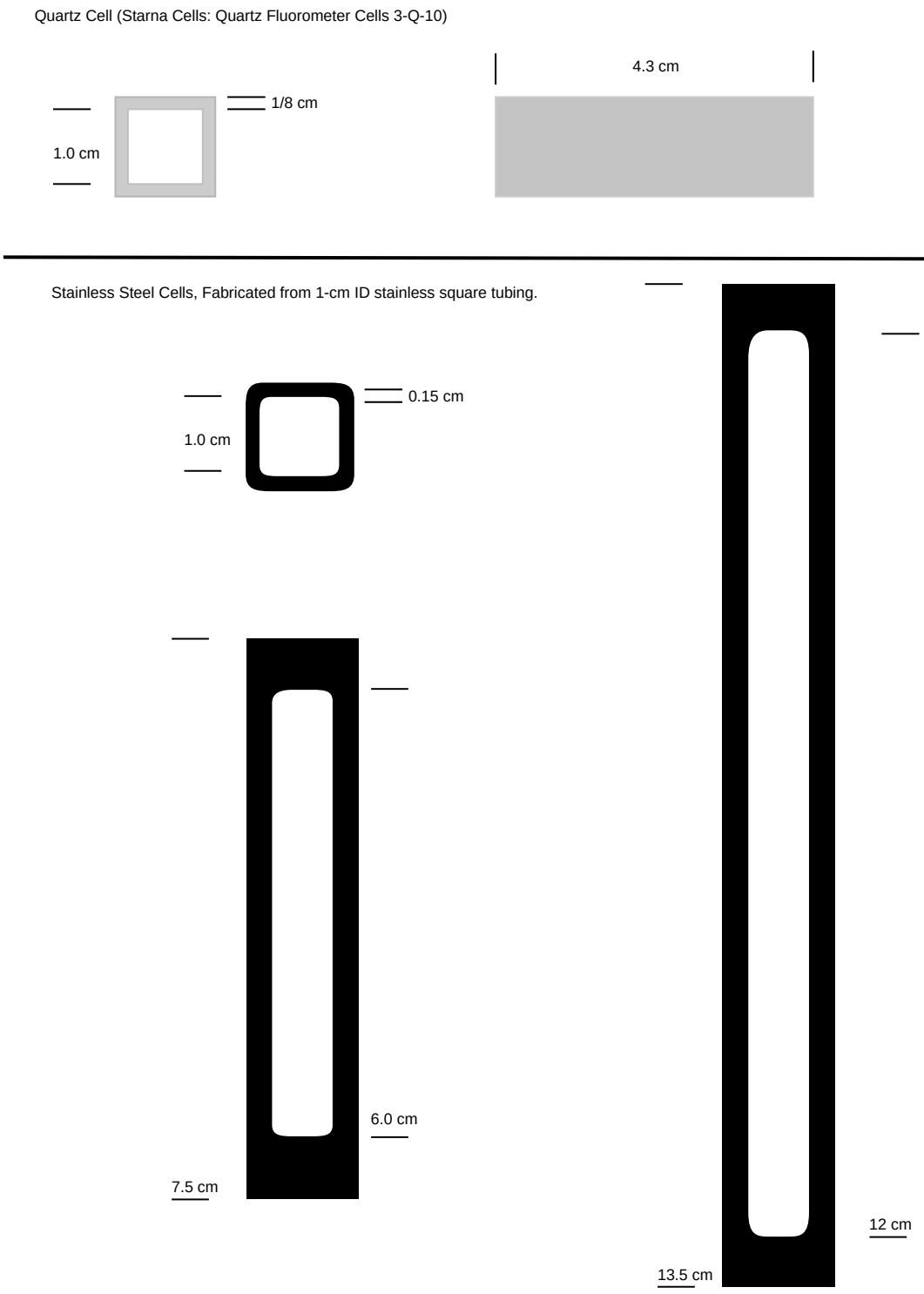


**Figure 6.3. Diagrams of various photolysis cells used.**

## 6.2 184.9 nm Intensity Measurements

The measurement of 184.9 nm intensities from a Hg lamp can be complicated by interference from other wavelengths. This section evaluates this possible interference for the experiments described in Chapter 2. These experiments used a mercury Pen-Ray lamp (UVP) to generate 184.9 nm light. As can be seen in Figure 6.4, these lamps produce many other wavelengths of light in addition to 184.9 nm.

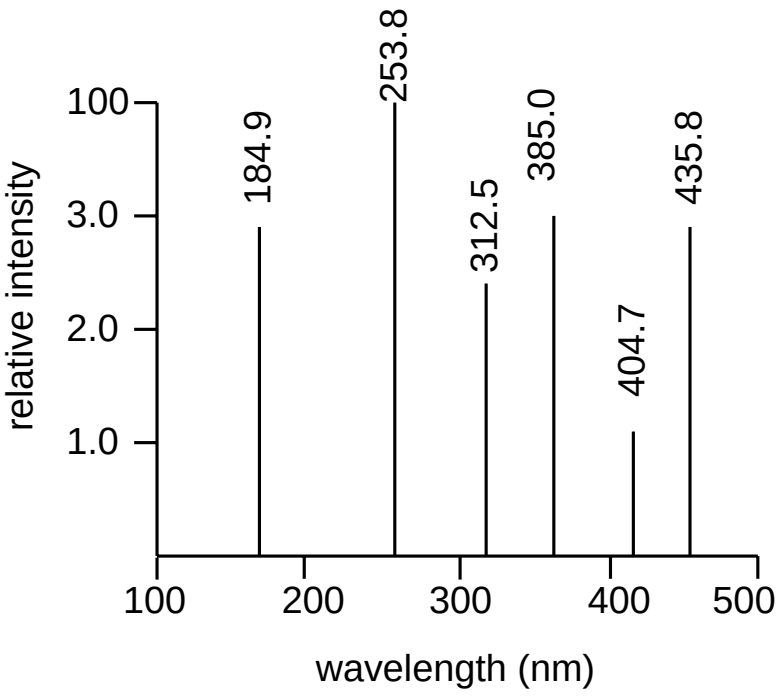


**Figure 6.4. Stated relative line intensities for UVP Hg Pen-Ray lamp.**

Intensity measurements were made with two slightly different detection apparatus. The original apparatus, used for measuring the nitric acid 185 nm cross section, consisted of two custom-made 185 nm interference filters and a PMT with a bi-alkali cathode. Our original concern when making these measurements was leakage from

the most intense emission line at 254 nm ($I_{254} > 30*I_{185}$). This concern was addressed by filling the cell with a few hundred torr of $N_2O$. The cross sections at 185 nm and 254 nm are $1.43\times10^{-19}$ $cm^2$ and $<10^{-23}$ $cm^2$ respectively. The resulting optical depths of >30 at 185 nm and <0.01 at 254 nm allowed for direct measurement of the 254 nm leakage: <2% of the total intensity. This contribution was subtracted from future measurements of the 185 nm intensity.

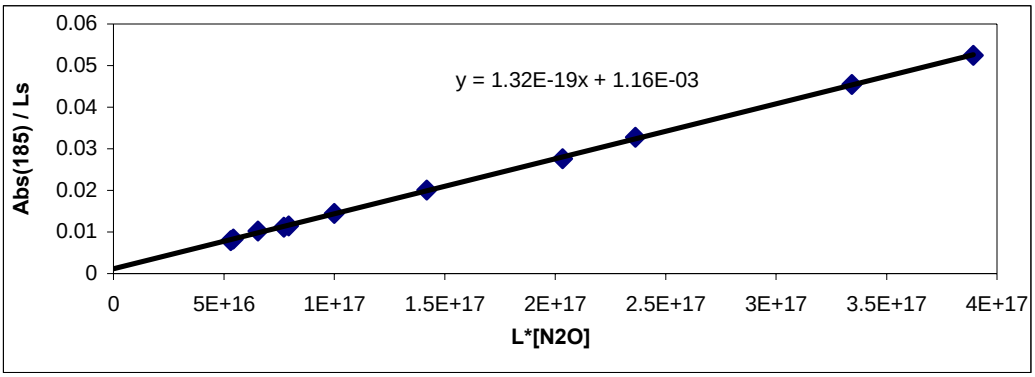


**Figure 6.5. Fit to $N_2O$ Beer's Law Absorbance w/ Hg lamp, double interference filter, and bialkali cathode. $L_s$ = 30.2 cm.**

The Beer's Law absorption as a function of $N_2O$ concentration, with the contribution from 254 nm leakage subtracted, is shown in Figure 6.5. The absorbance was linear over a wide range, and a linear fit to the data yielded an observed cross section of $1.32\times10^{-19}$ $cm^2$. This was about 5% below the literature cross section of $1.43\times10^{-19}$ $cm^2$. We were encouraged by the linearity of the plots and reproducibility of our measured cross section and felt this relatively small discrepancy was within the experimental uncertainty. Our measurements of the nitric acid 185 nm cross section as well as the initial measurements of the IR nitric acid integrated cross section were made using this same apparatus, subtracting the contribution from 254 nm leakage. Our initial linear fit to the data yielded a cross section of $1.53\times10^{-17}$ $cm^2$. Again, this was about 5%

lower than the accepted literature value [25]. This small discrepancy seemed reasonable, especially considering the scatter in nitric acid measurements at such short wavelengths [25-27, 29, 32, 33].

After we finished these initial measurements, the interference filters were lost. Aaron Noell at JPL then used the same for UV measurements of methanol in his cell. The double interference filters were replaced by a commercial 185 nm interference filter (Acton Research Corporation, 24 nm FWHM). Using the bialkali PMT, it was found that leakage by 194 nm light, a mercury emission line not listed in the UVP table shown in Figure 6.4, was an important photon contaminant. The predicted relative intensities (194:185 ratio taken from the CRC) convolved with the filter transmission properties are shown in Table 6.1. The expected relative intensities as observed by the PMT (after the filter) with a bialkali cathode, with fairly constant quantum efficiency, are shown in the column labeled "postfilter intensity." We see that, despite the 194 nm intensity being much smaller than that at 254 nm, the 194 nm light is expected to be a much larger problem due to the properties of the filter. Aaron further reduced the contribution of 194 nm light by a factor of five by switching to a solar-blind CsI PMT. The resulting expected signal as seen by the CsI PMT is also shown in Table 6.1. We see that the contribution from non-185 nm light is expected to be about 5%. The values in Table 6.1 can only be trusted as a rough guide, though, as the specific output characteristics of Pen-Ray lamps vary from lamp to lamp and over the lifetime of the lamp.

**Table 6.1. Expected contribution of various Hg Pen-Ray lamp wavelengths. All values other than wavelengths are relative and unitless.**

| wavelength /nm | Intensity | Filter transmission | postfilter intensity | CsI Response | CsI Signal |
|---|---|---|---|---|---|
| 184.95 | 1000 | 0.18 | 180 | 1 | 180 |
| 194.23 | 300 | 0.15 | 45 | 0.2 | 9 |
| 253.65 | 30000 | 0.0001 | 3 | <0.2? | <0.6? |

When we returned to IR integrated cross section measurements, we used the solar-blind CsI PMT that Aaron had used. Unfortunately, we did not re-measure the nitric acid UV cross section and so do not know if 194 nm contamination influenced this measurement. At the moment, the UV equipment necessary to re-measure this cross section is not available. Instead, I have tried to quantify the contribution of the 194 nm emission from the Pen-Ray lamp to our previous measurement of the nitric acid UV cross section.

The apparatus used was a 160 cm stainless steel Raman cell with UV-transparent windows. The Hg Pen-Ray lamp output was sent through a 10 cm focal length $CaF_2$ lens and a pinhole to collimate the light through the cell. A second pinhole was used at the output window to minimize the collection of photons that reflected within the cell. The same Acton Research 185 nm interference filter described above was used to drastically reduce the detection of 254 nm light. The PMT output was amplified and then sent to an oscilloscope for averaging. The pressure in the cell was measured by a 10K torr MKS Baratron. The experiments consisted of measuring the transmitted intensity as a function of $CO_2$ pressure using both the bialkali and CsI cathode in the PMT and then comparing

the absorbance as a function of pressure for the two. $CO_2$ was chosen because $\sigma_{185} = 13 \times \sigma_{194}$ and because the UV spectrum in this region lacks structure.

Absorbance data as a function of $CO_2$ concentration are shown in Figure 6.6. The data taken with the CsI cathode appeared linear for the range of absorbances measured (Abs $\leq 3$). The fit to this data is almost identical to the literature value of $2.85 \times 10^{-22}$ $cm^2$ [105]. The data taken with the bialkali cathode show obvious curvature, even at absorbances below 0.5. The data can be simulated using only the cross sections at 185 nm and 194 nm. The simulation shown in Figure 6.6 assumes 90% 185 nm and 10% 194 nm and fits the data very well over the entire range of observed absorbances.

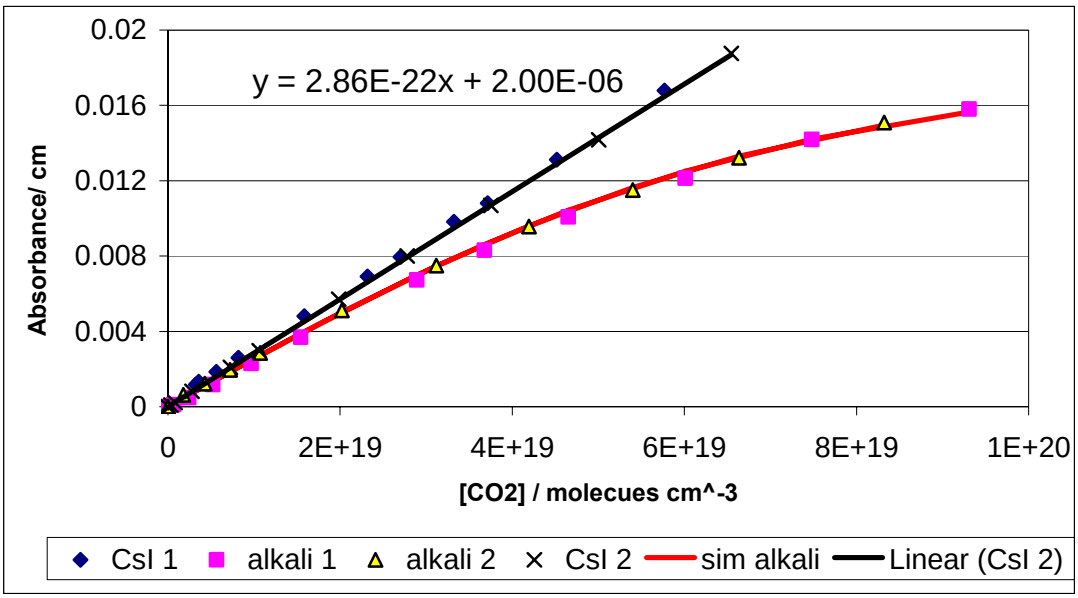


**Figure 6.6. $CO_2$ absorption data taken with two different PMT cathodes. The linear fit to the CsI data is shown in black. A simulation of the bialkali data using observed intensities of 90% 185 nm and 10% 194 nm is shown in orange.**

As Figure 6.6 demonstrates, 184.9 nm intensities taken with the CsI cathode and new filter were likely free from 194 nm contamination. While we cannot re-test the interference filters used in conjunction with the bi-alkali cathode directly, it is likely they

had similar transmission properties to the current filter. Making this assumption, we can use the relative contributions of 185 and 194 nm light derived from Figure 6.6 to correct the intensities measured while measuring $\sigma_{185}$. The observed intensities were therefore corrected to be that of just 185 by

$$I_{185} = I_{obs} - \left[ I_{0,obs} \times 0.095 \times \exp(-\sigma_{194} \times l_s \times [\mathrm{HNO_3}]) \right].$$

This led to very small changes (≈1%) in the intensities and only a 1% increase in our measured $\sigma_{185}$. Because we have had to assume the old filters had similar transmission properties to the new filter, this has been included as an uncertainty in the analysis of our $\sigma_{185}$ measurements described in Section 2.2.2.

## 6.3 Flow Cell Flush Times

In photolysis experiments, it is important to ensure that a fresh gas sample is being photolyzed with each excimer pulse. In this way secondary chemistry and other potential problems stemming from the photolysis of products are eliminated. The group lore when I joined was that, if you calculate the flush time of the photolysis region of the flow cell from the pressure and flowmeter readouts, you should multiply that number by two to get the actual time for a clean gas sample. This was assumed to be the result of diffusion of products into various parts of the cell, which would compete with efficient flushing of the cell.

The nitric acid product from the OH + $NO_2$ photolysis experiments provides a strong spectroscopic measure of "photolysis products." We therefore measured the flush rate directly by monitoring the nitric acid signal as a function of the YAG – Excimer delay time. Figure 6.7 shows data taken at 600 torr and a calculated flush time of 80 ms.

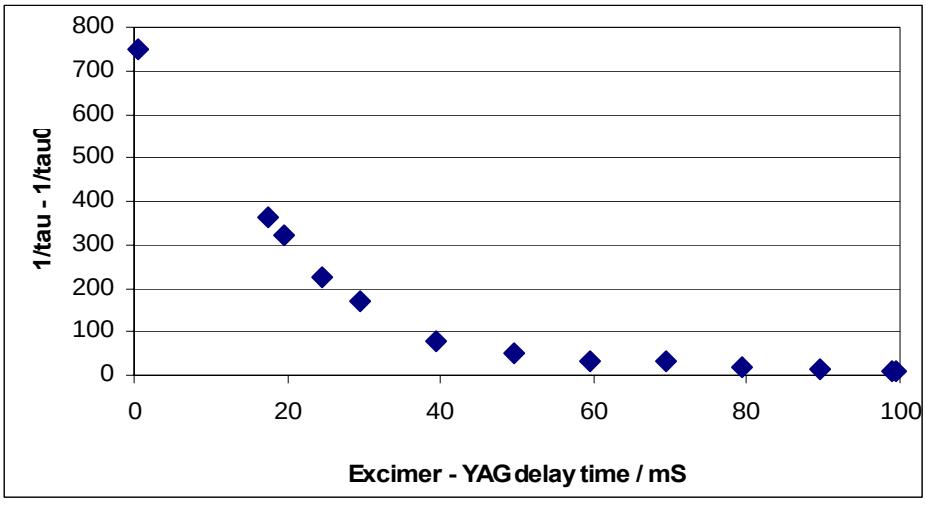


**Figure 6.7 – Nitric acid signal at 3540 $cm^{-1}$ as a function of the Excimer – YAG delay time, for a calculated flush time of 80 mS. The first point shown is taken at the typical delay time for OH + $NO_2$ experiments of 500 µS.**

We see that the initial decrease in nitric acid signal exceeds that predicted by flushing alone, i.e., far less than half the initial nitric acid remains in the probe region 40 ms after the initial photolysis. Presumably this can be explained by diffusion of nitric acid out of the region of the cell being probed by the IR-CRDS. After this initial rapid decay, the signal decays much slower and asymptotes to 1.3% of the signal at 500 μs. Given the notoriety of nitric acid as a very sticky molecule, this remaining signal may more reflect the desorption of nitric acid stuck to the walls of the flow cell than poor flushing of photolysis volume.

Regardless, for our purposes the 1.5% signal at the calculated flush time of 80 ms reflects essentially complete flushing of the photolysis volume. This level of signal was used to determine a minimum flush time (the calculated flush time needed to reduce the signal to 1.5% its initial value at the next excimer shot) at a few different pressures. While this time at 400 torr was about the same as that at 600 torr (88 mS), at 200 torr a faster flush time of about 65 ms was needed. This implies that at lower pressures, diffusion may indeed begin to play an important role and the "factor of two" rule may once again apply. Fortunately, at lower pressures faster flush times are readily achieved.

## 6.4 Mass Flow Transducers

Mass flow transducers (flowmeters) are a critical component of the flow-cell experiments described in this thesis. They enable us to control and precisely know the concentrations of all gases in the cell. This information is critical for any kinetics simulations or cross-section measurements. As implied by their formal name, flowmeters determine mass flow of gas through their sensor. This is accomplished by detecting the heat transferred by a flowing gas, which is directly proportional to the mass flow of the gas. A diagram of the sensors used in Omega flowmeters is shown in Figure 6.8.

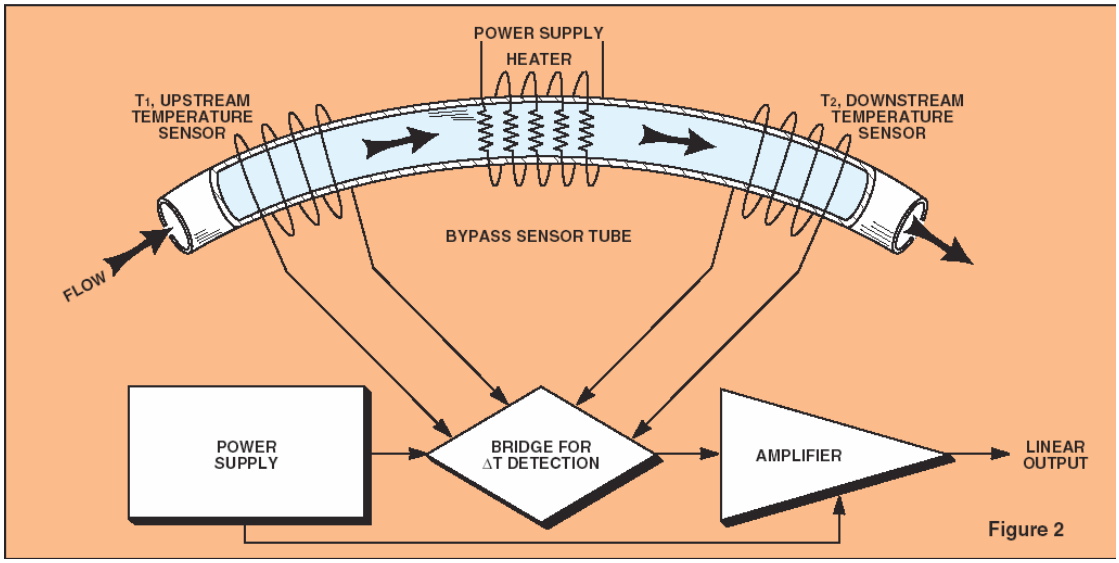


**Figure 6.8. Schematic of mass flow sensor used in Omega Mass Flowmeters. Taken from Omega's Electronic Mass Flowmeters Flow Reference Section http://www.omega.com/toc_asp/frameset.html?book=Green&file=MASS_FLOW_REF**

The temperature difference between the upstream and downstream temperature sensors is converted to a voltage that is linearly related to the mass flow. In order to interpret this voltage, the sensitivity of the flowmeter, given in sccm/volt, must be known

(sccm = standard cubic centimeter = 1cm$^3$ of gas at 70° F and 1 atm). Because the sensor relies on the thermal conductivity of the gas, the sensitivity is gas specific, so the calibration changes when the gas is changed. The calibration for a new gas can be calculated using conversion tables provided in the manuals for each flowmeter.

Sensitivities are provided with any new flowmeter, but should be calibrated upon arrival and re-calibrated periodically. This is accomplished by flowing through calibrated volumes, specifically those included in the calibration kit borrowed from the Sander group at JPL. This kit includes several volumetric cylinders (10, 100, and 1000 cm$^3$) each with a ground glass joint on one end. This joint couples the cylinder to a specialty piece of glassware that introduces soap bubbles to the upstream end of the cylinder. The flow rate is then measured by measuring the time it takes for the soap bubbles to displace the volume of the cylinder. Following corrections for the temperature, pressure, and vapor pressure of water, the flow in standard cubic centimeters is determined and can be plotted as a function of the voltage readout of the flowmeter.

The flowmeters in 17 Noyes were originally all manufactured by Edwards. These all had corrosion-resistant stainless steel bodies, bipolar electrical connections (although of a rather inconvenient design) and were generally robust. Unfortunately, as time has worn on, the sensors in the Edwards flowmeters have begun to go bad. Usually this is a gradually accelerating process of decreasing sensitivity to flow (an increase in the sccm/volt measured when calibrating). This is a serious problem because Edwards left the flowmeter business years ago and, when they left, apparently did not sell their extra sensors or the rights to make them to any other company. As a result, once a flowmeter sensor goes bad, the flowmeter is no longer useable and must be replaced.

So far, the flowmeters that have gone bad have tended to be those for higher flow used for dilution or purge flows of inert gas. As a result, they have been replaced with inexpensive brass-body flowmeters from Omega. These flowmeters must be used *with inert gas only*. Under ideal conditions, these flowmeters seem to work fine. Their sensitivities do not seem to vary between calibrations and the calibration curves are linear, yielding uncertainties in the flow on the order of 0.5%.

However, problems with these Omega flowmeters do exist. First, the power supply is of a positive voltage only. As a result, the flowmeters cannot read any voltage below 0.0 V. This can be and has been a problem when the zero-flow offset is such that the voltage at no flow is not a positive value. When this occurs, there is a range of low flows that will all read zero. In a calibration curve, this is evidenced by a significant positive y-intercept. As a result, it is important to check that the zero-flow reading from the Omega flowmeters is above zero (it is wise to check the value before and after an experiment to account for drift), and then subtract this value from all readings that day.

The more serious issue with the Omega flowmeters stems from the fragility of their electronics. The first time the Omega flowmeters broke, it was clearly my fault. I had been making changes to the power supply and readout box and accidentally reconnected the positive and negative leads backwards. This apparently fried all three Omega flowmeters. It is interesting to note that this did not seem to affect the Edwards flowmeters at all. This does not necessarily imply an inherent problem with the Omega flowmeters, but a better design would have included a fuse or other safety device that would have protected the sensor in case of lab idiot.

The second destruction of flowmeter confirms this. It is generally advised that before you connect or disconnect a flowmeter you turn its power supply off. I would again like to point out that the Edwards flowmeters were connected and disconnected with the power on for years before I joined the group without any drastic consequences. As a result of the shorted electronics mentioned above, I have been very careful to power down the flowmeters before performing any work on them. A recent addition to the lab (who will remain unnamed) changed the gas connections to the flowmeters with the power on. This was just a plumbing job, with no changes to the electronics. After the plumbing was done, one of the Omega flowmeters was broken. Presumably, something touched its nine-pin connector during the job and cased a short. While again this could have been prevented by powering down the flowmeters, relying on these Omega flowmeters that are so prone to breaking is not ideal (in this latter case, we were able to convince them to replace the unit for free, but not without nearly a month of downtime). As a result, I advise switching to a new company when next we need a new flowmeter.

The flowmeter-readout-DIO system is a bit messy, which I believe is a large part of the slow response time of the flowmeter readouts (settling time after changing flow of about ten seconds). The setup could definitely be improved.

**WARNINGS:**

- **With Omega flowmeters, flow ONLY INERT GAS.**
- **Turn power to flowmeters off (power strip mounted to laser table cover) before any work on flowmeters.**
- **Always check calibrations against the previous value to check for sensors that are beginning to fail.**

# 7 Appendix C: CRDS Simulation Programs for Matlab

## *7.1 Introduction*

I cannot give Gautham Nair enough credit for writing these. He did all the legwork on designing the program, wrote a version of the program for C++ and then wrote the original version of these fitting programs. I have made adjustments to the code to for convenience and flexibility, but Gautham should definitely be considered the author of the program. Many thanks also to Kana Takematsu for taking these programs through the motions and helping with the documentation included in this appendix.

It should be noted that after Gautham left for some lesser school in Massachusetts, he wrote some of the programs on a different version of Matlab and there was a small compatibility issue. I worked with Matlab 7.0. To get these programs to work on other versions of Matlab it may be necessary to replace the comma separating output variables of a function with a space i.e. change

```
function [ringspec,simplespec]=
```

to

```
function [ringspec simplespec]=
```

### 7.1.1 Motivation

As described in Chapter 2, pulsed CRDS measurements of spectra with narrow features can have significant errors in the form of incorrect lineshapes and observed integrated absorbances below the true value. These errors stem from fitting observed multi-exponential decays with a single exponential function to extract the decay lifetime

τ. The general goal of these programs is to simulate the expected CRDS signal for a given set of apparatus conditions if the underlying high-resolution spectrum is known. This high resolution spectrum is adjusted by pressure broadening and application of scale factors to take into account species concentration and convert the spectrum from absorbance units to 1/τ.

This spectrum is then convolved with the laser profile to generate the simulated ringdown spectra. At each point in the simulated spectrum, a simulated ringdown decay is produced by summing the individual decays at each frequency weighted by the laser profile, $\sum_i e^{\frac{\alpha_i}{\tau_i}}$, where α is the normalized weighting function for the laser profile. The simulated ringdown decay is then fit with a single exponential function to generate the "experimental" ringdown decay lifetime (1/τ'). This is then repeated for all frequencies in the simulated spectrum. The integrated absorption of the new spectrum and the convolved spectrum without re-fitting the decay, $\sum_i \frac{\alpha_i}{\tau_i}$, can be compared to derive the error in the CRDS spectrum.

The magnitude of the CRDS errors and their sensitivity to various parameters can then be explored. Because there are many parameters which we might be interested in varying systematically, there are several versions of the program each designed to systematically vary an individual parameter. In theory these various programs could be combined into one generalized program, but so far I have found this to be unnecessary.

### 7.1.2 Using MATLAB:

Some general tips for running routines in Matlab. The program files must be contained in the Current Directory shown in Matlab. All saved files will also automatically go to the Current Directory. You can specify any output names you want. Inputs that are arrays or matrices must be pre-existing named items in the Matlab workspace. To run a routine, such as Lorentzbroaden.m broadening the high-resolution spectrum "inputspectrumname" to .05 $cm^{-1}$, you would just type into the command line

outputspectrumname = Lorentzbroaden(0.05, 2.0, inputspectrumname);

and press enter. The semicolon at the end ensures that the output spectrum is not printed to the Command Window. When the program is finished, the new matrix "outputspectrumname" will appear in the Workspace.

WARNING: If you run the program again and do not change the output name, it will be written over without any prompt to warn you!

Comments can be added to any routine by beginning the line with "%".

To save any output matrix to a text file for manipulation in another program, use "save savefilename.out matrixname –ASCII"

When trying to go through the program, it is helpful to generate a fake matrix to manipulate. Just define a matrix ("matrix=…" or [starting point: interval dist: finishing point].) The matrix will appear in the Workspace. If you want to manipulate it, just double click on it. To quickly generate an array (such as a column array of scalefactors for use in SFBatchFixCut.m) you can use

newarrayname = (startnumber:stepsize:endnumber)';

The apostrophe at the end rotates the array from a row to a column. If you want column i of matrix, just write matrixname(:,i). If you want a row, write matrixname(i,:)). If you want to manipulate any matrix (change/add/delete elements), just double click on it.

A flow diagram for the "SFBatchVarCut.m" top-level program to illustrate which programs are interconnected is shown here. The programs are highly modular so that changing and debugging programs is quite simple, even for a novice like me. An arrow indicates a flow of outputs. For example, RingSimVarCutBatch.m calls three different sub-routines, "Gaussiancomb.m", "LMDecdayFitVarCut.m" and "CombDecay3.m". It then uses the information gathered from those sub-routines and sends outputs to "SFBatchVarCut.m". It is important when running a program in Matlab that all needed sub-routines are contained in the Current Directory.

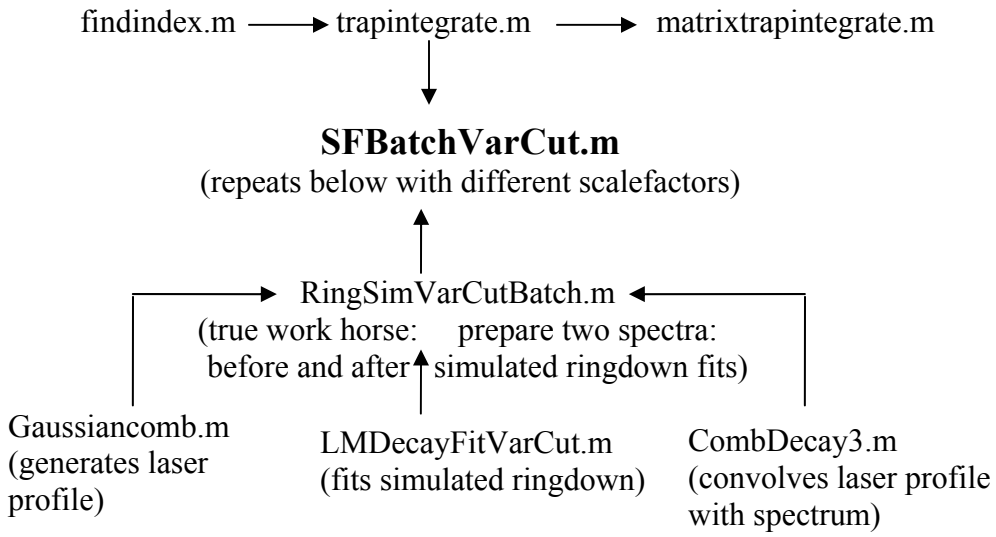

## *7.2 Program Documentation*

Programs are shown below in single-spaced text. If using higher-level programs, sub-routines need to be saved with the titles shown in quotation marks.

### 7.2.1 Common Inputs

**absspectrum** = data spectrum used for simulation. Usually the output of Lorentzbroaden.m

**times** = 1D column array specifying the time axis of the ringdowns. Should reflect the number of points and sample rate of the experiment you are simulating.

**background** = background value for 1/tau. Should be in $s^{-1}$.

**xi,xf** = range of simulated spectrum. (xi-regionwidth) and (xi-regionwidth) should not exceed the range of absspectrum.

**scannedwavenumbers** = 1D column array of frequencies you want in the output spectrum. This is where you would define the stepsize of the spectrum. Could be used to eliminate xi and xf with a short re-program.

**regionwidth** = range in cm^-1 (or whatever units your spectra are in) over which the laser profile will be used to calculate the simulated ringdown at each point. 2*laserfwhm was sufficient in HNO3.

**laserfwhm**=laserfwhm in cm^-1(or whatever units your spectra are in). Treats laser profile as Gaussian (for most simulations assumed to be 1.0 $cm^{-1}$). Actually treats profile as discrete spikes with spacing defined by …

**modespace** = spacing of modes for Gaussian laser profile. Generally assumed to be 0.00666 $cm^{-1}$ we expect from the YAG cavity.

### 7.2.2 "Lorentzbroaden.m"

DESCRIPTION: This program is designed to take a high resolution, Doppler-limited spectrum and convolve it with a Lorentzian lineshape to simulate pressure-broadening.

Reminder: Lorentzian $\frac{1}{\pi}\frac{\frac{1}{2}\Gamma}{(x-x_0)^2+(\frac{1}{2}\Gamma)^2}$

For nitric acid, we found that having regionwidth=2*fwhm was insufficient. If you can spare points at the edge of your spectrum, you should try for at least 4*fwhm.

```
%Inputs
%fwhm=fwhm of Lorentzian profile your are convolving
%regionwidth=total width over which each spectral point will be "spread".
%spectrum=2D matrix containing data spectrum to convolve. Can be imported
%using Matlabs "Import Data" routine. First column must be x-axis
%(frequency units must match fwhm and regionwidth)
% second column can be any arbitrary frequency units.
function broadspec=Lorentzbroaden(fwhm, regionwidth, spectrum);
specspacing=spectrum(2,1)-spectrum(1,1);
convpoints=round(regionwidth/(2*specspacing));

%this initiates the matrices used in the calculation
Npoints=size(spectrum,1);
broadspec=2*ones(Npoints-2*convpoints,2);

%Here is the meat of it. If you wanted to change this to use a different
%shape you would change the second line.
%Motivation for loop: we are going to take each point of the spectrum. Each point is
%going to be treated like a Lorentzian i.e. the intensity assigned to each point is going to
%be redistributed as a Lorentzian. The transformed functions are then going to be
%summed.
for i=(convpoints+1):(Npoints-convpoints)
   lorweights=1./((spectrum((i-convpoints):(i+convpoints),1)-spectrum(i,1)).^2 ...
      +(fwhm/2)^2);
   lorweights=lorweights/sum(lorweights);
   broadspec(i-convpoints,1)=spectrum(i,1);
   broadspec(i-convpoints,2)=sum(spectrum((i-
convpoints):(i+convpoints),2).*lorweights);
end
```

### 7.2.3 "trapintegrate.m"

DESCRIPTION: Used to integrate spectra. Built into the Batch programs below, but can be used for any spectrum in the Workspace that is a 2D matrix with frequency in column 1 and absorbance in column 2. Fairly self explanatory.

```
function trapintegral = trapintegrate(xi,xf,spectrum);
ni = findindex (xi,spectrum); nf = findindex (xf,spectrum);
trapintegral=0.0;
trapintegral=sum(spectrum(ni:(nf-1),2).*(spectrum((ni+1):nf,1)-spectrum(ni:(nf-1),1)));
```

### 7.2.4 "matrixtrapintegrate.m"

DESCRIPTION: Can be used to get the integrals of multiple spectra contained in a 2D matrix where the columns are spectra (such as the outputs from the Batch programs below). **xi** and **xf** should be entered as numbers, **wavelengths** should be a column array such as "scannedwavenumbers" described above, and **spectraonly** should be a matrix with each column as the absorbance points corresponding to the frequencies in "wavelengths".

```
function trapintegrals=matrixtrapintegrate(xi,xf,wavelengths,spectraonly)
trapintegrals=[];
for i=1:size(spectraonly,2)
   trapintegrals=[trapintegrals trapintegrate(xi,xf,[wavelengths,spectraonly(:,i)])];
end
```

### 7.2.5 "Gaussiancomb.m"

DESCRIPTION: Generates a Gaussian shape for use in simulation programs using "laserfwhm", "regionwidth", and "modespace" to describe the laser profile. The "combpattern" output is 2D array describing a Gaussian with 0 as the center point.

```
function combpattern = Gaussiancomb(laserfwhm,regionwidthcm,modespace);

lasersigma=laserfwhm/sqrt(8*log(2));
temp1=0:modespace:regionwidthcm/2;
temp2=-temp1;
temp2(1)=[];
combpoints=[fliplr(temp2) temp1]';
combintensities=exp(-(combpoints.^2)/(2*lasersigma^2));
combpattern=[combpoints combintensities];
```

### 7.2.6 "findindex.m"

DESCRIPTION: Simple program called to give the index number.

```
function n=findindex(x,spectrum)
n=interp1(spectrum(:,1),(1:size(spectrum,1))',x,'nearest');
```

### 7.2.7 "SFBatchFixCut.m" and "SFBatchVarCut.m"

DESCRIPTION: To be used when you want to run several simulations at various "concentrations" (scalefactors). Shown is the program designed to do the ringdown fits cutting a fixed number of points at the start of the simulated ringdown, SFBatchFixCut.m. The program for cutting a fraction of a ringdown for each trace, SFBatchVarCut.m, is identical but calls "RingSimVarCutBatch.m" in the for-loop.

**UNIQUE INPUTS:**

**scalefactors** = 1D column array containing all scalefactors you want used.

NOTE: later in the RingSimFixedCutBatch, the scales factor is multiplied by the arbitrary number 6.024*10^18. If working with known absorbances, it should be possible to change this number so that scaled absorbances represent the expected signal rather than its current arbitrary value.

```
function [ringspecs,simplespecs,integrals,Summary] = SFBatchFixCut (scalefactors, xi,
xf, absspectrum, background, scannedwavenumbers, times, laserfwhm, regionwidth,
modespace);

pringtemp=[];
rringtemp=[];
psimtemp=[];
rsimtemp=[];
ringspecs=[];
simplespecs=[];
Summary=[];
integrals=[];
Npoints=length(scannedwavenumbers);
%length = # of rows in matrix

%this iterates RingSimFixedCutBatch for each scalefactor
for i=1:length(scalefactors)
   [ringspec,simplespec]=RingSimFixedCutBatch(laserfwhm, regionwidth, modespace,
times, scannedwavenumbers, background, scalefactors(i), absspectrum);
```

```
%see later pages for RingSimFixedCutBatch.m.
   ringspecs=[ringspecs ringspec];
%[elements1 elements2] combines the elements into one large array
   simplespecs=[simplespecs simplespec];
   integrals=[integrals [trapintegrate(xi,xf, [scannedwavenumbers ringspec]);...
      trapintegrate(xi,xf, [scannedwavenumbers simplespec])]];
%notice the ";" between the trapintegrates.  This puts the results in two separate rows
%this calculates the integrated absorption for ringsepc and simplespec.
   pringtemp=[pringtemp ringspec(1)];
   rringtemp=[rringtemp ringspec(Npoints)];
   psimtemp=[psimtemp simplespec(1)];
   rsimtemp=[rsimtemp simplespec(Npoints)];
end

%this creates a matrix with columns containing the simulated spectrum
%integral, the integral of the spectrum with no CRDS error, and the first
%and last point in the spectra for both the simulation and with no CRDS
%error (critical for trying to evaluate the error outside the bounds of
%your simulation).
Summary=[integrals' pringtemp' psimtemp' rringtemp' rsimtemp'];
```

### 7.2.8 "ScalefactorBatchCustom.m"

DESCRIPTION: This is the same as SFBatchVarCut.m but it is designed so that any arbitrary laser profile can be used (above routines used Gaussian profile). The normalized laser profile needs to be a pre-existing 2D matrix with the first column as Δ(frequency) with the center of the profile as 0 and the second column the normalized intensity at each value of Δ(frequency).

```
function [ringspecs, simplespecs, integrals, Summary] = ScalefactorBatch (scalefactors,
xi, xf, absspectrum, background, scannedwavenumbers, times, laserprofile);
%in comparison with SFBatchFixCut, laserprofile has replaced inputs laserfwhm,
%regionwidth and modespace.

pringtemp=[];
rringtemp=[];
psimtemp=[];
rsimtemp=[];
ringspecs=[];
simplespecs=[];
Summary=[];
integrals=[];
Npoints=length(scannedwavenumbers);

for i=1:length(scalefactors)
   [ringspec,simplespec]=RingdownSimCustom(laserprofile, times,
scannedwavenumbers, background, scalefactors(i), absspectrum);
%see later pages for RingdownSimCustom.m
   ringspecs=[ringspecs ringspec];
   simplespecs=[simplespecs simplespec];
   integrals=[integrals [trapintegrate(xi,xf, [scannedwavenumbers ringspec]);...
      trapintegrate(xi,xf, [scannedwavenumbers simplespec])]];
   pringtemp=[pringtemp ringspec(1)];
   rringtemp=[rringtemp ringspec(Npoints)];
   psimtemp=[psimtemp simplespec(1)];
   rsimtemp=[rsimtemp simplespec(Npoints)];
end

Summary=[integrals' pringtemp' psimtemp' rringtemp' rsimtemp'];
```

### 7.2.9 "fwhmBatch.m"

DESCRIPTION: Very similar to SFBatch programs above, but you can run a batch of various values of laser fwhm (**laserfwhms**) instead of scalefactors. **widthfactor** is a number which will be multiplied by each laser fwhm to define the "regionwidth" described above.

```
function [ringspecs,simplespecs,integrals,Summary] = fwhmBatch (scalefactor, xi, xf,
absspectrum, background, scannedwavenumbers, times, laserfwhms, widthfactor,
modespace);

pringtemp=[];
rringtemp=[];
psimtemp=[];
rsimtemp=[];
ringspecs=[];
simplespecs=[];
Summary=[];
integrals=[];
Npoints=length(scannedwavenumbers);

for i=1:length(laserfwhms)
   [ringspec,simplespec]=RingdownSim3(laserfwhms(i), laserfwhms(i)*widthfactor,
modespace, times, scannedwavenumbers, background, scalefactor, absspectrum);
   ringspecs=[ringspecs ringspec];
   simplespecs=[simplespecs simplespec];
   integrals=[integrals [trapintegrate(xi,xf, [scannedwavenumbers ringspec]);...
      trapintegrate(xi,xf, [scannedwavenumbers simplespec])]];
   pringtemp=[pringtemp ringspec(1)];
   rringtemp=[rringtemp ringspec(Npoints)];
   psimtemp=[psimtemp simplespec(1)];
   rsimtemp=[rsimtemp simplespec(Npoints)];
end

Summary=[integrals' pringtemp' psimtemp' rringtemp' rsimtemp'];
```

### 7.2.10 "RingSimFixedCutBatch.m" and "RingSimVarCutBatch.m"

DESCRIPTION: Calculates the simulated CRDS spectrum and convolved spectrum for each scalefactor. Shown is RingSimFixedCutBatch.m which uses fits cutting a fixed time period at the start of each ringdown. RingSimVarCutBatch.m uses fits cutting a fraction of a lifetime at the start of each ringdown, and replaces LMdecayfitmodified.m with LMDecayFitVariableCut.m

```
function [ringspec,simplespec]=RingSimFixedCutBatch(laserfwhm, regionwidth,
modespace, times, scannedwavenumbers, background, scalefactor, absspectrum)
combpattern=Gaussiancomb(laserfwhm,regionwidth,modespace);
Nscans=size(scalefactor,1);
Npoints=size(scannedwavenumbers,1);
ringspec=zeros(Npoints,Nscans);
%zeros(m,n) generates m x n matrix with all elements = 0
simplespec=zeros(Npoints,Nscans);
tempdecay=zeros(size(times));
%if zeros(m), creates m x m matrix
simpleinvlifetime=0.0;
tempfitparam=[];

%This does the work of calling Combdecay3.m and LMDecayfitmodified.m for each
%point in the simulated spectra and compiling those numbers for export to
%SFBatchFixCut.m.
for j=1:Nscans
   invlifetimes=[absspectrum(:,1) background + scalefactor(j)* 6.024*10^8*
absspectrum(:,2)];
%creates two column matrix with x and adjusted y.  6.024*10^8 is arbitrary
for i=1:Npoints
   [tempdecay simpleinvlifetime] = CombDecay3 (scannedwavenumbers(i), times,
combpattern, invlifetimes);
%will discuss CombDecay3.m later
   tempfitparam = LMdecayfitmodified (times, tempdecay, tempdecay(1),
simpleinvlifetime);
%will discuss LMdecayfitmodified.m later
   ringspec(i,j)=tempfitparam(2)-background;
   simplespec(i,j)=simpleinvlifetime-background;
%These two outputs will later be called for in the batch files and combined with the
%scanned wavelengths to reconstruct the spectra.
end
end
```

### 7.2.11 "RingdownSim3.m"

DESCRIPTION: This is the first version of the RingdownSim program that is designed for a single set of inputs. The version here uses LMDecayfit.m which fits the full simulated ringdowns. It could easily be modified to use either of the other versions of LMdecayfit by replacing it with the desired version below.

```
function [ringspec,simplespec]=RingdownSim(laserfwhm, regionwidth, modespace,
times, scannedwavenumbers, background, scalefactor, absspectrum)
combpattern=Gaussiancomb(laserfwhm,regionwidth,modespace);
Npoints=size(scannedwavenumbers,1);
ringspec=zeros(Npoints,1);
simplespec=zeros(Npoints,1);
tempdecay=zeros(size(times));
simpleinvlifetime=0.0;
tempfitparam=[];
invlifetimes=[absspectrum(:,1) background+scalefactor*6.024*10^8*absspectrum(:,2)];

for i=1:Npoints
   [tempdecay
simpleinvlifetime]=CombDecay3(scannedwavenumbers(i),times,combpattern,
invlifetimes);
   tempfitparam=LMdecayfit(times,tempdecay,tempdecay(1),simpleinvlifetime);
   ringspec(i)=tempfitparam(2)-background;
   simplespec(i)=simpleinvlifetime-background;
end
```

### 7.2.12 "RingdownSimCustom.m"

DESCRIPTION: This is the version of RingdownSim that can use an arbitrary user-defined laser profile. Otherwise the same as other versions. Currently uses "LMdecayfitVariableCut.m" but could be changed to the Fixcut version.

```
function [ringspec,simplespec]=RingdownSim(laserprofile, times, scannedwavenumbers,
background, scalefactor, absspectrum)
Npoints=size(scannedwavenumbers,1);
ringspec=zeros(Npoints,1);
simplespec=zeros(Npoints,1);
tempdecay=zeros(size(times));
simpleinvlifetime=0.0;
tempfitparam=[];
invlifetimes=[absspectrum(:,1) background+scalefactor*6.024*10^8*absspectrum(:,2)];

for i=1:Npoints
   [tempdecay simpleinvlifetime] = CombDecay3 (scannedwavenumbers(i), times,
laserprofile, invlifetimes);
   tempfitparam = LMdecayfitVariableCut (times, tempdecay, tempdecay(1),
simpleinvlifetime);
   ringspec(i)=tempfitparam(2)-background;
   simplespec(i)=simpleinvlifetime-background;
end
```

### 7.2.13 "Combdecay3.m"

DESCRIPTION: This creates the simulated ringdown decays that will be fit later. It also calculates the signal at each point that would be seen by simply convolving the spectrum with combpattern. This is called by the RingSim programs. Many of the inputs here will be called by index in the main programs.

UNIQUE INPUTS: **cavityinvlifetimes** contains the inverse ringdown lifetimes for given wavenumber input light. First column is wavenumber, second is inverse lifetime ($1/\tau$).

```
function [decay,simpleavg] = CombDecay (centerwavenumber, times, combpattern,
cavityinvlifetimes);

%centerwavenumber is a number (the frequency at which the laser is centered)
%times is a 1d array of desired times to sample the decay (i.e. the
%oscilloscope decay trace data)
%combpattern is a 2d array. It is a simulation of the frequency spectr
%um of the laser shot, assuming wavenumber 0 is the center position.
%The first column is wavenumbers and the second
%column indicates the laser intensity at the corresponding wavenumber.
%cavityinvlifetimes contains the inverse ringdown lifetimes for given wavenumber
%input light. First column is wavenumber, second is inverse (1/e) lifetime.
%decay is the output decay signal and simpleavg is the
%cavity inverse lifetime that would be obtained by simply convolving
%the input spectrum with the comb pattern.

timesize = size (times,1);
decay = zeros (timesize,1);
combsize = size (combpattern,1);
combinvlifetimes = zeros (combsize,1);
combinvlifetimes = interp1 (cavityinvlifetimes(:,1), cavityinvlifetimes(:,2),
combpattern(:,1)+centerwavenumber, 'linear',NaN);
%interp1 is a interpolation (table lookup) function contained in Matlab.
%YI = interp1(X,Y,XI). Sometimes X is left out. This assumes that X=1:N. Note XI
%stands for x interval i.e. if X = 0:10, then XI=0:.25:10.
%Sometimes, after XI, a "method" is chosen in which the interpolation is done. The
%default is linear interpolation. Sometimes after 'method,' the 'extrap" option can be
```

```
%stated.  This chooses a method for extrapolating any elements of XI outside the
interval %spanned by X.  Alternatively, "EXTRAPAVAL" replaces these values with
%EXTRAPVAL.  NaN and 0 are often used for this number.

%Aside:  Interpolation: constructing new data points from discrete set of known data
 %          Extrapolation: find value of function at point x which is outside x_k of function

for i=1:timesize
   decay(i)=sum(combpattern(:,2).*exp(-times(i)*combinvlifetimes));
end
simpleavg=sum(combpattern(:,2).*combinvlifetimes)/sum(combpattern(:,2));
%Notice that the combpattern is normalized here, as the Gaussian was not normalized
%in the subroutine.  The decays generated above will be sent into LMDecayFit programs.
%The decay does not need to be normalized as it is just going to be refit later.
%Multiplying by a constant for normalization will not change the ringdown time.
```

### 7.2.14 "LMDecayFitModified.m"

DESCRIPTION: This actually fits the simulated decay traces using the Levenberg-Marquardt algorithm. I believe the fitting algorithm was taken from Numerical Recipes, but I'm not sure. This particular iteration has a fixed amount of time cut from the beginning of the trace before it is fit.

INPUTS: **fulltimes** is the decay time points (same as **times** from above).

**fulldecsignal** is the decay signal as generated by CombDecay3.m

**inita** initial guess for the amplitude (generally taken as the first point in "fulldecsignal"

**initb** is the initial guess for the lifetime (generally taken from the "simpleinvlifetime" output of CombDecay3.m.

```
function fitparam=LMdecayfit(fulltimes, fulldecsignal, inita, initb)

%This part makes the fit neglect times below a certain threshold

%This is the threshold value, in whatever units your times are in:
%Keep negative if you want it to work just as before.
%Must be changed manually here (does not read from higher-level programs).
tbegin=16e-8;
%This is the code that takes care of the cutting.
tmask=fulltimes>tbegin;
times=fulltimes(tmask);
decsignal=fulldecsignal(tmask);
% The rest of this is fits the remaining points.
chisq=0.0;
ochisq=0.0;
a=0.0;
oa=0.0;
da=0.0;
b=0.0;
ob=0.0;
db=0.0;
lambda=0.001;
beta=zeros(2,1);
```

```
alpha=zeros(2,2);
convergedflag=1;
convergecrit=0.005;
Niterations=1;
Nmax=50;
oa=inita;
ob=initb;
a=oa;
b=ob;
ochisq=sum((decsignal-oa*exp(-ob*times)).^2);

while convergedflag&&(Niterations<Nmax)
   beta=zeros(2,1);
   alpha=zeros(2,2);
   exptemp=exp(-ob*times);
   beta(1)=sum((decsignal-oa*exptemp).*exptemp);
   beta(2)=sum(-oa*times.*(decsignal-oa*exptemp).*exptemp);
   alpha(1,1)=sum(exptemp.^2)*(1+lambda);
   alpha(1,2)=sum(-oa*times.*exptemp.^2);
   alpha(2,1)=alpha(1,2);
   alpha(2,2)=sum(oa^2*times.*times.*exptemp.^2)*(1+lambda);
   da=(alpha(2,2)*beta(1)-alpha(1,2)*beta(2))/(alpha(1,1)*alpha(2,2)-
alpha(1,2)*alpha(2,1));
   db=(alpha(1,1)*beta(2)-alpha(2,1)*beta(1))/(alpha(1,1)*alpha(2,2)-
alpha(1,2)*alpha(2,1));
   a=oa+da;
   b=ob+db;
   chisq=sum((decsignal-a*exp(-b*times)).^2);
   if chisq>ochisq
      lambda=lambda*10;
   else
      lambda=lambda*0.1;
      oa=a;
      ob=b;
      if ((ochisq-chisq)<(chisq*convergecrit))||chisq==0
         convergedflag=0;
      end
      ochisq=chisq;
   end
   Niterations=Niterations+1;
end

fitparam=[a ; b ; Niterations;ochisq];
%Output file gives a = amplitude, b = exponent factor, number of iterations that were
%used in the Levenberg-Marquardt algorithm, and the chi^2 value of the fit.
```

### 7.2.15 "LMDecayFitVariableCut.m"

DESCRIPTION: This is identical to "LMDecayFitModified.m" described above, but a fraction of the decay is cut instead of a fixed amount.

```
function fitparam = LMdecayfitVarCut(fulltimes, fulldecsignal, inita, initb)

%this makes an initial fit, in order to get a guess for the lifetime
tfitparam=LMdecayfit(fulltimes, fulldecsignal, inita, initb);
%This part makes the fit neglect times below a certain threshold
tempa=0.0;
tempb=0.0;
tempa=tfitparam(1);
tempb=tfitparam(2);
%This is the threshold value, in whatever units your times are in:
%Keep negative if you want it to work with no cut.  Currently set to cut
%half of a lifetime.  Needs to be changed manually on the following
%line.
tbegin=0.5*(1/tempb);

%This is the code that takes care of the cutting
tmask=fulltimes>tbegin;
times=fulltimes(tmask);
decsignal=fulldecsignal(tmask);
% This is the end of this part, the rest of the function is as in LMDecayFitModified.m
```

### 7.2.16 "SingledecayVarfitRes.m"/ "SingledecayFixCutRes.m"

DESCRIPTION: These programs are designed to run at a single frequency and allow you to look at the actual ringdowns. The output **decays** is a 3-column matrix with the first column the simulated ringdown, the second column the fit to the simulated ringdown and the third column the residual. Shown in the Varfit version, FixCut is the same but with the LMdecayfit program changed.

```
function [decays,ringinvT,simpleinvT] = SingledecayVarfitRes (laserfwhm, regionwidth,
modespace, times,wavenumber, background, scalefactor, absspectrum)

combpattern=Gaussiancomb(laserfwhm,regionwidth,modespace);
decays=zeros(size(times,1),3);

[decays(:,1),simpleinvT] = CombDecay3(wavenumber,times,combpattern, ...
    [absspectrum(:,1) background+ scalefactor* 6.024*10^8* absspectrum(:,2)]);
fitparam= LMdecayfitVariableCut (times, decays(:,1), decays(1,1), simpleinvT);
decays(:,2)=fitparam(1)*exp(-fitparam(2)*times);
decays(:,3)=(decays(:,1)-decays(:,2));
ringinvT=fitparam(2)-background;
simpleinvT=simpleinvT-background;
```

# 8 References


1. Finlayson-Pitts, B. J. and J. N. Pitts, *Chemistry of the Upper and Lower Atmosphere*. 2000, San Diego, California: Academic Press.
2. Seinfeld, J. H. and S. N. Pandis, *Atmospheric Chemistry and Physics-From Air Pollution to Climate Change*. 1998, New York: John Wiley and Sons.
3. Tonnesen, G. S., "Effects of uncertainty in the reaction of the hydroxyl radical with nitrogen dioxide on model-simulated ozone control strategies". *Atmospheric Environment,* 1999. **33**(10): p. 1587-1598.
4. Martien, P. T. and R. A. Harley, "Adjoint sensitivity analysis for a three-dimensional photochemical model: Application to Southern California". *Environmental Science & Technology,* 2006. **40**(13): p. 4200-4210.
5. Martien, P. T. and R. A. Harley, "Adjoint sensitivity analysis for a three-dimensional photochemical model: Implementation and method comparison". *Environmental Science & Technology,* 2006. **40**(8): p. 2663-2670.
6. Robertshaw, J. S. and I. W. M. Smith, "Kinetics of the hydroxyl + nitrogen dioxide + argon and hydroxyl + nitrogen dioxide + tetrafluoromethane reactions at high total pressures". *Journal of Physical Chemistry,* 1982. **86**(5): p. 785-790.
7. Bean, B. D., A. K. Mollner, S. A. Nizkorodov, G. Nair, M. Okumura, S. P. Sander, K. A. Peterson, and J. S. Francisco, "Cavity ringdown spectroscopy of cis-cis HOONO and the HOONO/HONO2 branching ratio in the reaction OH+NO2+M". *Journal of Physical Chemistry A,* 2003. **107**(36): p. 6974-6985.
8. Berden, G., R. Peeters, and G. Meijer, "Cavity ring-down spectroscopy: Experimental schemes and applications". *International Reviews of Physical Chemistry,* 2000. **19**(4): p. 565-607.

9. Jongma, R. T., M. G. H. Boogaarts, I. Holleman, and G. Meijer, "Trace gas detection with cavity ring down spectroscopy". *Reviews of Scientific Instruments,* 1995. **66**(4): p. 2821-2828.

10. Paldus, B. A. and A. A. Kachanov, "An historical overview of cavity-enhanced methods". *Canadian Journal of Physics,* 2005. **83**(10): p. 975-999.

11. Scherer, J. J., J. B. Paul, A. Okeefe, and R. J. Saykally, "Cavity ringdown laser absorption spectroscopy: History, development, and application to pulsed molecular beams". *Chemical Reviews,* 1997. **97**(1): p. 25-51.

12. Wheeler, M. D., S. M. Newman, A. J. Orr-Ewing, and M. N. R. Ashfold, "Cavity ring-down spectroscopy". *Journal of the Chemical Society - Faraday Transactions,* 1998. **94**(3): p. 337-351.

13. Meijer, G., M. G. H. Boogaarts, R. T. Jongma, D. H. Parker, and A. M. Wodtke, "Coherent cavity ring down spectroscopy". *Chemical Physics Letters,* 1994. **217**(1-2): p. 112-116.

14. Hodges, J. T., J. P. Looney, and R. D. van Zee, "Response of a ring-down cavity to an arbitrary excitation". *Journal of Chemical Physics,* 1996. **105**(23): p. 10287-10288.

15. Hodges, J. T., J. P. Looney, and R. D. van Zee, "Laser bandwidth effects in quantitative cavity ring-down spectroscopy". *Applied Optics,* 1996. **35**(21): p. 4112-4116.

16. O'Keefe, A. and D. A. G. Deacon, "Cavity ring-down optical spectrometer for absorption measurements using pulsed laser sources". *Review of Scientific Instruments,* 1988. **59**(12): p. 2544-2551.

17. Romanini, D. and K. K. Lehmann, "Ring-down cavity absorption spectroscopy of the very weak hydrogen cyanide overtone bands with six, seven, and eight stretching quanta". *Journal of Chemical Physics,* 1993. **99**(9): p. 6287-301.

18. Zalicki, P. and R. N. Zare, "Cavity ring-down spectroscopy for quantitative absorption measurements". *Journal of Chemical Physics,* 1995. **102**(7): p. 2708-2717.

19. Fuelberth, T. M., M.S. Thesis. "The building of an infrared source for use in free radical kinetics important in stratospheric ozone depletion: Cavity ringdown detection", California Institute of Technology, 1997.
20. Garland, E. R., Ph.D. Thesis. "Laboratory studies of atmospheric reactions using infrared cavity ringdown spectroscopy", California Institute of Technology, 2002.
21. Reid, S. A. and Y. Tang, "Generation of tunable, narrow-band mid-infrared radiation through a 532-nm-pumped KTP optical parametric amplifier". *Applied Optics,* 1996. **35**(9): p. 1473-1477.
22. Chackerian, C., S. W. Sharpe, and T. A. Blake, "Anhydrous nitric acid integrated absorption cross sections: 820-5300 cm(-1)". *Journal of Quantitative Spectroscopy & Radiative Transfer,* 2003. **82**(1-4): p. 429-441.
23. Lange, K. R., N. P. Wells, K. S. Plegge, and J. A. Phillips, "Integrated Intensities of O-H Stretching Bands: Fundamentals and Overtones in Vapor-Phase Alcohols and Acids". *Journal of Physical Chemistry A,* 2001. **105**: p. 3481-3486.
24. Phillips, J. A., J. J. Orlando, G. S. Tyndall, and V. Vaida, "Integrated Intensities of OH vibrational overtones in alcohols". *Chemical Physics Letters,* 1998. **296**: p. 377-383.
25. Biaume, F., "Nitric Acid Vapour Absorption Cross-Section Spectrum and its Photodissociation in the Stratosphere". *Journal of Photochemistry,* 1973. **2**: p. 139-149.
26. Burkholder, J. A., R. K. Talukdar, A. R. Ravishankara, and S. Solomon, "Temperature Dependance of the HNO3 UV Absorption Cross Sections". *Journal of Geophysical Research,* 1993. **98**(D12): p. 22937-22948.
27. Johnston, H. and R. Graham, "Gas-phase ultraviolet absorption spectrum of nitric acid vapor". *Journal of Physical Chemistry,* 1973. **77**(1): p. 62-63.
28. Molina, L. T. and M. J. Molina, "UV Absorption Cross-Sections of HO2NO2 Vapor". *Journal of Photochemistry,* 1981. **15**(2): p. 97-108.

29. Okabe, H., "Photodissociation of nitric acid and water in the vacuum ultraviolet; vibrational and rotational distributions of OH". *Journal of Chemical Physics,* 1980. **72**(12): p. 6642-6650.

30. Rattigan, O., E. Lutman, R. L. Jones, R. A. Cox, K. Clemitshaw, and J. Williams, "Temperature-dependent absorption cross sections of gaseous nitric acid and methyl nitrate". *Journal of Photochemistry and Photobiology A-Chemistry,* 1992. **66**(3): p. 313-326.

31. Suto, M. and L. C. Lee, "Photoabsorption and photodissociation of HONO2 in the 105-220nm region". *Journal of Chemical Physics,* 1984. **81**(3): p. 1294-1297.

32. Connell, P. S. and C. J. Howard, "Kinetics study of the reaction HO + HNO3". *International Journal of Chemical Kinetics,* 1985. **17**: p. 17-31.

33. Wine, P. H., A. R. Ravishankara, N. M. Kreutter, R. C. Shah, J. M. Nicovich, and R. L. Thompson, "Rate of reaction of OH with HNO3". *Journal of Geophysical Research,* 1981. **86**(C2): p. 1105-1112.

34. Yalin, A. P. and R. N. Zare, "Effects of laser lineshape on the quantitative analysis of cavity ring-down signals". *Laser Physics,* 2002. **12**: p. 1065-1072.

35. Pine, A. S. and A. Goldman. *private communication*.

36. Sander, S. P., B. J. Finlayson-Pitts, D. M. Golden, R. E. Huie, C. E. Kolb, M. J. Kurylo, M. J. Molina*, et al.*, *Chemical Kinetics and Photochemical Data for Use in Atmospheric Studies, Evaluation Number 15*. 2006, Jet Propulsion Laboratory: Pasadena, CA.

37. Colmont, J., B. Bakri, F. Rohart, and G. Wlodarczak, "Experimental determination of pressure-broadening parameters of millimeter-wave transitions of HNO3 perturbed by N2 and O2, and of their temperature dependences". *Journal of Molecular Spectroscopy,* 2003. **220**: p. 52-57.

38. Schiffman, A. and D. Nesbitt, "Pressure broadening and collisional narrowing in OH(v=1<-0) rovibrational transitions with Ar, He, O2, and N2". *Journal of Chemical Physics,* 1994. **100**(4): p. 2677-2689.

39. Feierabend, K. J., D. K. Havey, and V. Vaida, "Gas phase spectroscopy of HNO3 in the region 2000-8500 cm(-1)". *Spectrochimica Acta Part a-Molecular and Biomolecular Spectroscopy,* 2004. **60**(12): p. 2775-2781.

40. Chen, W. J., W. J. Lo, B. M. Cheng, and Y. P. Lee, "Photolysis of nitric acid in solid nitrogen". *Journal of Chemical Physics,* 1992. **97**(10): p. 7167-73.

41. Cheng, B. M., J. W. Lee, and Y. P. Lee, "Photolysis of nitric acid in solid argon: the infrared absorption of peroxynitrous acid (HOONO)". *Journal of Physical Chemistry,* 1991. **95**(7): p. 2814-17.

42. Lo, W.-J. and Y.-P. Lee, "Ultraviolet absorption of cis-cis and trans-perp peroxynitrous acid (HOONO) in solid argon". *Chemical Physics Letters,* 1994. **229**(4-5): p. 357-361.

43. Lo, W.-J. and Y.-P. Lee, "Infrared absorption of cis-cis peroxynitrous acid (HOONO) in solid argon". *Journal of Chemical Physics,* 1994. **101**: p. 5494-5499.

44. Konen, I. M., I. B. Pollack, E. X. J. Li, M. I. Lester, M. E. Varner, and J. F. Stanton, "Infrared overtone spectroscopy and unimolecular decay dynamics of peroxynitrous acid". *Journal of Chemical Physics,* 2005. **122**(9). 094320.

45. Matthews, J. and A. Sinha, "State-resolved unimolecular dissociation of cis-cis HOONO: Product state distributions and action spectrum in the 2ν(OH) band region". *Journal of Chemical Physics,* 2005. **122**(10). 104313.

46. McCoy, A. B., J. L. Fry, J. S. Francisco, A. K. Mollner, and M. Okumura, "Role of OH-stretch/torsion coupling and quantum yield effects in the first OH overtone spectrum of cis-cis HOONO". *Journal of Chemical Physics,* 2005. **122**(10). 104311.

47. Hippler, H., N. Krasteva, S. Nasterlack, and F. Striebel, "Reaction of OH+NO2: High pressure experiments and falloff analysis". *Journal of Physical Chemistry A,* 2006. **110**(21): p. 6781-6788.

48. Dixon, D. A., D. Feller, C. G. Zhan, and J. S. Francisco, "Decomposition pathways of peroxynitrous acid: Gas-phase and solution energetics". *Journal of Physical Chemistry A,* 2002. **106**(13): p. 3191-3196.

49. Golden, D. M., J. R. Barker, and L. L. Lohr, "Master equation models for the pressure- and temperature-dependant reactions HO+NO2 → HONO2 and HO+NO2 → HOONO". *Journal of Physical Chemistry A,* 2003. **107**(50): p. 11057-11071.

50. Li, Y. M. and J. S. Francisco, "High level ab initio molecular orbital theory study of the structure, vibrational spectrum, stability, and low-lying excited states of HOONO". *Journal of Chemical Physics,* 2000. **113**(18): p. 7976-7981.

51. McGrath, M. P. and F. S. Rowland, "Internal rotation in peroxynitrous acid (ONOOH)". *Journal of Chemical Physics,* 2005. **122**(13). 134312.

52. McGrath, M. P. and F. S. Rowland, "Determination of the barriers to internal rotation in ONOOX (X = H, Cl) and characterization of the minimum energy conformers". *Journal of Physical Chemistry,* 1994. **98**(4): p. 1061-1067.

53. Drouin, B. J., J. L. Fry, and C. E. Miller, "Rotational spectrum of cis-cis HOONO". *Journal of Chemical Physics,* 2004. **120**(12): p. 5505-5508.

54. Li, E. X. J., I. M. Konen, M. I. Lester, and A. B. McCoy, "Spectroscopic characterization of peroxynitrous acid in cis-perp configurations". *Journal of Physical Chemistry A,* 2006. **110**(17): p. 5607-5612.

55. Fry, J. L., S. A. Nizkorodov, M. Okumura, C. M. Roehl, J. S. Francisco, and P. O. Wennberg, "Cis-cis and trans-perp HOONO: Action spectroscopy and isomerization kinetics". *Journal of Chemical Physics,* 2004. **121**(3): p. 1432-1448.

56. Liu, Y. D. and R. G. Zhong, "Theoretical studies on HOONO, HONOO, and HNO3 isomers and their isomerization reactions". *Journal of Molecular Structure-Theochem,* 2006. **765**(1-3): p. 143-149.

57. Zhu, R. S. and M. C. Lin, "Ab initio study of the HO2+NO reaction: Prediction of the total rate constant and product branching ratios for the forward and reverse processes". *Journal of Chemical Physics,* 2003. **119**(20): p. 10667-10677.

58. Zhang, J. Y. and N. M. Donahue, "Constraining the mechanism and kinetics of OH+NO2 and HO2+NOusing the multiple-well master equation". *Journal of Physical Chemistry A,* 2006. **110**(21): p. 6898-6911.

59. D'Ottone, L., D. Bauer, P. Campuzano-Jost, M. Fardy, and A. J. Hynes, "Kinetic and mechanistic studies of the recombination of OH with NO2: Vibrational deactivation, isotopic scrambling and product isomer branching ratios". *Faraday Discussions,* 2005. **130**: p. 111-123.

60. Hippler, H., S. Nasterlack, and F. Striebel, "Reaction of OH+NO2+M: Kinetic evidence of isomer formation". *Physical Chemistry Chemical Physics,* 2002. **4**(13): p. 2959-2964.

61. Donahue, N. M., R. Mohrschladt, T. J. Dransfield, J. G. Anderson, and M. K. Dubey, "Constraining the mechanism of OH+NO2 using isotopically labeled reactants: Experimental evidence for HOONO formation". *Journal of Physical Chemistry A,* 2001. **105**(9): p. 1515-1520.

62. Nizkorodov, S. A. and P. O. Wennberg, "First spectroscopic observation of gas-phase HOONO". *Journal of Physical Chemistry A,* 2002. **106**(6): p. 855-859.

63. Williams, C. F., S. K. Pogrebnya, and D. C. Clary, "Quantum study on the branching ratio of the reaction NO2 + OH". *Journal of Chemical Physics,* 2007. **126**. 154321.

64. Chakraborty, D., J. Park, and M. C. Lin, "Theoretical study of the OH+NO2 reaction: formation of nitric acid and the hydroperoxyl radical". *Chemical Physics,* 1998. **231**(1): p. 39-49.

65. Golden, D. M. and G. P. Smith, "Reaction of OH+NO2+M: A new view". *Journal of Physical Chemistry A,* 2000. **104**(17): p. 3991-3997.

66. Matheu, D. M. and W. H. Green, "A priori falloff analysis for OH+NO2". *International Journal of Chemical Kinetics,* 2000. **32**(4): p. 245-262.

67. Troe, J., "Analysis of the Temperature and Pressure Dependence of the Reaction HO+NO2+M,<-> HONO2+M". *International Journal of Chemical Kinetics,* 2001. **33**(12): p. 878-889.

68. Schofield, D. P. and H. G. Kjaergaard, "Effect of OH internal torsion on the OH-stretching spectrum of cis,cis-HOONO". *Journal of Physical Chemistry A,* 2005. **109**(9): p. 1810-1814.

69. Frisch, M. J., G. W. Trucks, H. B. Schlegel, G. E. Scuseria, M. A. Robb, J. R. Cheeseman, J. Montgomery*, et al.*, *Gaussian 03, Revision C.02*. 2004, Wallingford CT: Gaussian, Inc.

70. Smith, I. W. and M. D. Williams, "Vibrational-relaxation of OH (V=1) and OD(V=1) by HNO3, DNO3, H2O, NO and NO2"*. Journal of the Chemical Society-Faraday Transactions II,* 1985. **81**: p. 1849-1860.

71. Park, C. R. and J. R. Wiesenfeld, "Full characterization of OH product energetics in the reaction of O(1D) with hydrocarbons"*. Journal of Chemical Physics,* 1991. **95**(11): p. 8166-8177.

72. Aker, P. M. and J. J. Sloan, "The initial product vibrational energy distribution in the reaction between O(1D) and H2"*. Journal of Chemical Physics,* 1986. **85**(3): p. 1412-1417.

73. Feierabend, K. J., D. K. Havey, M. E. Varner, J. F. Stanton, and V. Vaida, "A comparison of experimental and calculated spectra of HNO3 in the near-infrared using Fourier transform infrared spectroscopy and vibrational perturbation theory"*. Journal of Chemical Physics,* 2006. **124**(12). 124323.

74. Zhang, X., M. R. Nimlos, G. B. Ellison, M. E. Varner, and J. F. Stanton, "Infrared absorption spectra of matrix-isolated cis, cis-HOONO and its ab initio CCSD(T) anharmonic vibrational bands"*. Journal of Chemical Physics,* 2006. **124**(8). 084305.

75. Matthews, J., A. Sinha, and J. S. Francisco, "Relative vibrational overtone intensity of cis-cis and trans-perp peroxynitrous acid"*. Journal of Chemical Physics,* 2004. **120**(22): p. 10543-10553.

76. Russell, A. and R. Dennis, "NARSTO critical review of photochemical models and modeling"*. Atmospheric Environment,* 2000. **34**(12-14): p. 2283-2324.

77. Orlando, J. J., G. S. Tyndall, and T. J. Wallington, "The atmospheric chemistry of alkoxy radicals"*. Chemical Reviews,* 2003. **103**(12): p. 4657-4689.

78. Atkinson, R. and J. Arey, "Atmospheric degradation of volatile organic compounds"*. Chemical Reviews,* 2003. **103**(12): p. 4605-4638.

79. Somnitz, H. and R. Zellner, "Theoretical studies of unimolecular reactions of C-2-C-5 alkoxy radicals. Part I. Ab initio molecular orbital calculations". *Physical Chemistry Chemical Physics,* 2000. **2**(9): p. 1899-1905.

80. Somnitz, H. and R. Zellner, "Theoretical studies of unimolecular reactions of C-2-C-5 alkoxy radicals. Part II. RRKM dynamical calculations". *Physical Chemistry Chemical Physics,* 2000. **2**(9): p. 1907-1918.

81. Jungkamp, T. P. W., J. N. Smith, and J. H. Seinfeld, "Atmospheric oxidation mechanism of n-butane: The fate of alkoxy radicals". *Journal of Physical Chemistry A,* 1997. **101**(24): p. 4392-4401.

82. Atkinson, R., "Atmospheric reactions of alkoxy and beta-hydroxyalkoxy radicals". *International Journal of Chemical Kinetics,* 1997. **29**(2): p. 99-111.

83. Atkinson, R., E. S. C. Kwok, J. Arey, and S. M. Aschmann, "Reactions of alkoxyl radicals in the atmosphere". *Faraday Discussions,* 1995(100): p. 23-37.

84. Atkinson, R. and S. M. Aschmann, "Alkoxy radical isomerization products from the gas-phase OH radical-initiated reactions of 2,4-dimethyl-2-pentanol and 3,5-dimethyl-3-hexanol". *Environmental Science & Technology,* 1995. **29**(2): p. 528-536.

85. Kwok, E. S. C., J. Arey, and R. Atkinson, "Alkoxy radical isomerization in the OH radical-initiated reactions of C-4-C-8 n-alkanes". *Journal of Physical Chemistry,* 1996. **100**(1): p. 214-219.

86. Niki, H., P. D. Maker, C. M. Savage, and L. P. Breitenbach, "An Ft Ir Study of the Isomerization and O-2 Reaction of Normal-Butoxy Radicals". *Journal of Physical Chemistry,* 1981. **85**(18): p. 2698-2700.

87. Atkinson, R., "Gas-phase tropospheric chemistry of volatile organic compounds .1. Alkanes and alkenes". *Journal of Physical and Chemical Reference Data,* 1997. **26**(2): p. 215-290.

88. Atkinson, R., D. L. Baulch, R. A. Cox, J. N. Crowley, R. F. Hampson, R. G. Hynes, M. E. Jenkin, M. J. Rossi, and J. Troe, "Evaluated kinetic and

photochemical data for atmospheric chemistry: Volume II-Gas phase reactions of organic species". *Atmospheric Chemistry and Physics,* 2006. **6**: p. 3625-4055.

89. Devolder, P., "Atmospheric fate of small alkoxy radicals: recent experimental and theoretical advances". *Journal of Photochemistry and Photobiology A-Chemistry,* 2003. **157**(2-3): p. 137-147.
90. Carter, W. P. L., K. R. Darnall, R. A. Graham, A. M. Winer, and J. N. Pitts, "Reactions of C2 and C-4 Alpha-hydroxy Radicals with Oxygen". *Journal of Physical Chemistry,* 1979. **83**(18): p. 2305-2311.
91. Cox, R. A., K. F. Patrick, and S. A. Chant, "Mechanism of atmospheric photo-oxidation of organic compounds-Reactions of alkoxy radicals in oxidation of normal-butane and simple ketones". *Environmental Science & Technology,* 1981. **15**(5): p. 587-592.
92. Heiss, A. and K. Sahetchian, "Isomerization reactions of the n-C4H9O and n-OOC4H8OH radicals in oxygen". *International Journal of Chemical Kinetics,* 1996. **28**(7): p. 531-544.
93. Dobe, S., T. Berces, and F. Marta, "Gas-phase decomposition and isomerization reactions of 2-pentoxy radicals". *International Journal of Chemical Kinetics,* 1986. **18**(3): p. 329-344.
94. Cassanelli, P., R. A. Cox, J. J. Orlando, and G. S. Tyndall, "An FT-IR study of the isomerization of 1-butoxy radicals under atmospheric conditions". *Journal of Photochemistry and Photobiology A-Chemistry,* 2006. **177**(2-3): p. 109-115.
95. Cassanelli, P., D. Johnson, and R. A. Cox, "A temperature-dependent relative-rate study of the OH initiated oxidation of n-butane: The kinetics of the reactions of the 1-and 2-butoxy radicals". *Physical Chemistry Chemical Physics,* 2005. **7**(21): p. 3702-3710.
96. Hein, H., A. Hoffmann, and R. Zellner, "Direct investigations of reactions of 1-butoxy and 1-pentoxy radicals using laser pulse initiated oxidation: reaction with

O-2 and isomerisation at 293 K and 50 mbar". *Physical Chemistry Chemical Physics,* 1999. **1**(16): p. 3743-3752.

97. Geiger, H., I. Barnes, K. H. Becker, B. Bohn, T. Brauers, B. Donner, H. P. Dorn*, et al.*, "Chemical mechanism development: Laboratory studies and model applications". *Journal of Atmospheric Chemistry,* 2002. **42**(1): p. 323-357.
98. Atkinson, D. B., "Solving chemical problems of environmental importance using cavity ring-down spectroscopy". *Analyst,* 2003. **128**(2): p. 117-125.
99. Vallance, C., "Innovations in cavity ringdown spectroscopy". *New Journal of Chemistry,* 2005. **29**(7): p. 867-874.
100. *Organic syntheses. Collective volume*. 1941, Wiley: New York.
101. Glover, B. G. and T. A. Miller, "Near-IR cavity ringdown spectroscopy and kinetics of the isomers and conformers of the butyl peroxy radical". *Journal of Physical Chemistry A,* 2005. **109**(49): p. 11191-11197.
102. Stein, S. E., J. M. Rukkers, and R. L. Brown, *NIST Standard Reference Database 69*, P. J. Linstron and W. G. Mallard, Editors. 2005, National Institute of Standards and Technology: Gaithersburg, MD (http://webbook.nist.gov).
103. Sharpe, S. W., T. J. Johnson, R. L. Sams, P. M. Chu, G. C. Rhoderick, and P. A. Johnson, "Gas-phase databases for quantitative infrared spectroscopy". *Applied Spectroscopy,* 2004. **58**(12): p. 1452-1461.
104. Somnitz, H. and R. Zellner, "Kinetics and dynamics of multi-channel unimolecular reactions of alkoxyl radicals over an extended range of temperature and pressure. A combined quantum chemical/RRKM dynamical study". *Zeitschrift Fur Physikalische Chemie-International Journal of Research in Physical Chemistry & Chemical Physics,* 2006. **220**(8): p. 1029-1048.
105. Parkinson, W. H., J. Rufus, and K. Yoshino, "Absolute absorption cross section measurements of CO2 in the wavelength region 163-2000 nm and the temperature dependence". *Chemical Physics,* 2003. **290**: p. 251-256.